Université de Montréal

Experimental and numerical study of a magnetic realization of a Bose-Einstein Condensate in a purely organic spin-1/2 quantum magnet (NIT2Py)

par
Reza Moosavi Askari

Département de physique
Faculté des arts et des sciences

Thèse présentée à la Faculté des études supérieures
en vue de l'obtention du grade de Philosophiæ Doctor (Ph.D.)
en Faculté des arts et des sciences

Le 31 août, 2016

Université de Montréal
Faculté des études supérieures

Cette thèse intitulée:

Experimental and numerical study of a magnetic realization of a Bose-Einstein Condensate in a purely organic spin-1/2 quantum magnet (NIT2Py)

présentée par:

Reza Moosavi Askari

a été évaluée par un jury composé des personnes suivantes:

Sjoerd Roorda,	président-rapporteur
Andrea Bianchi,	directeur de recherche
Michel Côté,	codirecteur
François Schiettekatte,	membre du jury
Claude Bourbonnais,	examinateur externe

Thèse acceptée le: ....

RÉSUMÉ

Cette étude porte sur les propriétés magnétiques de cristaux stables à température ambiante composés de molécules organiques à radical libre du nom de NIT2Py. Les mesures de l'aimantation révèlent que chaque molécule a un moment magnétique dû à l'existence d'un électron non apparrié un spin 1/2. Son ordre magnétique est antiferromagnétique. La dépendance du champ issue de la mesure de l'aimantation isothermique à 0.5 K démontre un plateau 1/2 en aimantation. La limite de la phase de la température de champ qui atteint une loi de puissance près d'un point critique quantique, ayant un exposant critique de 1.47 (9), est compatible avec la valeur universelle de 3/2 pour un BEC 3D. La dépendance en température de la chaleur spécifique et l'effet magnétocalorique sont utilisés pour produire un diagramme de phases (H,T). Les phases ordonnées générées par un champ menant à la formation de dômes, ainsi que les niveaux de spins qui se croisent, ont été observées dans le NIT2Py. Ces deux caractéristiques sont des signatures de la réalisation magnétique d'un condensat de Bose-Einstein, et c'est la première fois qu'elles ont été observées dans un aimant quantique purement organique ayant un spin 1/2.

Afin de mieux comprendre ce système, nous proposons ici un modèle hamiltonien de spins basé sur les interactions d'échange-Heisenberg. Pour évaluer les constantes du couplage d'échange (Js), nous utilisons des calculs de pointe pour la structure électronique basée sur la théorie de la fonctionnelle de la densité ; combinés à l'approche de la symétrie brisée, et nous faisons également usage de l'approche de la cartographie énergétique. Ces méthodes nous fournissent les amplitudes des interactions d'échange du système ainsi que leur signe. Les interactions d'échange dominantes sont reliées à trois Js antiferromagnétiques. Un réseau magnétique, composé de la répétition d'un ensemble minimal de Js dominants, doit être construit. En fait, le réseau magnétique le plus approprié pour ce système, celui qui explique le mieux les propriétés magnétiques de NIT2Py, en est un composé de tétramères possédant chacun quatre spins avec deux interactions antiferromagnétiques entre trétramères. En faisant usage de l'approximation du champ moyen, nous pouvons établir un modèle d'aimantation pour le système de tétramères interagissants qui reproduit les propriétés magnétiques du système, comme celle de la saturation à deux niveaux avec un plateau intermédiaire à la mi-saturation. De plus, la diagonalisation exacte de l'hamiltonien de Heisenberg pour un système incluant quatre tétramères est effectuée afin de reproduire l'aimantation ainsi que d'autres propriétés thermodynamiques du système.

Mots clés : cristaux à radicaux libres, aimant quantique organique, hamiltonien de Heisenberg, couplage d'échange, calculs de la structure électronique, théorie de la fonctionnelle de la densité, approche de la symétrie brisée, approche de la cartographie énergétique, plateau 1/2 en aimantation, antiferromagnétique, dimère, tétramère, condensat de Bose-Einstein.

ABSTRACT

The research presented in this thesis focuses on studying the magnetic properties of a purely organic free radical molecule NIT2Py, which can condense into highly stable crystals at room temperature. The magnetization measurements reveal that each molecule carries a magnetic moment due to the existence of a spin-1/2 unpaired electron. The magnetic order is found to be antiferromagnetic (AFM). The field dependence of the magnetization isotherm measurement at 0.5 K shows a 1/2 magnetization plateau. Temperature dependence specific heat and magnetocaloric effect are used to produce the (H,T) phase diagram. In the vicinity of a quantum critical point, the (H,T) phase boundary moves towards a power law with a critical exponent of 1.47(9) that is compatible with the universal value of 1.5 for a 3D BEC. The dome-shaped field-induced ordering phases and the intersecting spin levels observed in NIT2Py are signatures of magnetic realisation of BEC, which is seen for the first time in a purely organic quantum spin-1/2 AFM.

We propose a relevant model spin Hamiltonian based on the Heisenberg exchange interactions. We exploit state-of-the-art electronic structure calculations through density functional theory combined with the broken-symmetry and the energy-mapping approaches to evaluate the exchange coupling constants (Js), which in turn provide us with the sign and strengths of the exchange interactions in the system. The strongest exchange interactions are found to be related to three AFM Js. An appropriate magnetic lattice, which is a repeat pattern of a minimal set of strong Js, is constructed. We found that the magnetic lattice consisting of spin tetramers, each having four spins with two intratetramer AFM interactions, explains the magnetic properties of NIT2Py. By resorting to mean-field approximation, we establish a magnetization model for a system of interacting tetramers, which can reproduce the magnetic properties of the system such as the two-step saturation with an intermediate plateau at half saturated magnetization. Furthermore, an exact diagonalization of the Heisenberg Hamiltonian for a system including four tetramers is carried out, and yields the magnetization and other required thermodynamic properties of the system.

Keywords: Free radical crystal, organic quantum magnet, Heisenberg Hamiltonian, exchange coupling, electronic structure calculation, density functional theory, broken-symmetry approach, energy-mapping approach, 1/2 magnetization plateau, antiferromagnetic, dimer, tetramer, Bose-Einstein condensate.

CONTENTS

LIST OF TABLES

LIST OF FIGURES

LIST OF APPENDICES

LIST OF ABBREVIATIONS

2D	Two dimensional
3D	Three dimensional
AE	All-electron
AFM	Antiferromagnetic
BEC	Bose-Einstein condensate
BFGS	Broyden-Fletcher- Goldfarb-Shanno
BO	Born-Oppenheimer
BS	Broken-symmetry
BZ	Brillouin zone
CI	Configuration Interaction
CW	Curie-Weiss
d-d	dipole-dipole
d-c	double-counting
DFT	Density functional theory
DOS	Density of state
ED	Exact Diagonalization
E_{cut}	Cutoff energy
FHI	Fritz-Haber- Institute
FM	Ferromagnetic
GGA	Generalized-Gradient Approximation
HK	Hohenbergand Kohn
h-c bosons	hard-core bosons
KS	Kohn-Sham
LDA	Local Density Approximation
MCE	Magnetocaloric Effect
MFT	Mean-Field Theory

M-M	Matsubara-Matsuda
MO	Molecular Orbital
MP	Monkhorst and Pack
MPMS	Magnetic Property Measurement System
NC	Norm-Conserving
ngkpt	Number of k-points of MP grid in each of the three dimensions
NN	Nitronyl Nitroxide
PAW	Projector Augmented Waves
PBE	Perdew, Burke and Ernzerhof
p-NPNN	para-Nitrophenyl Nitronyl Nitroxide
POMS	Physical Property Measurement System
QCP	Quantum Critical Point
QE	Quantum Espresso
QMC	Quantum Monte Carlo
SQUID	Superconducting Quantum Interference Device
VMS	Vibrating Sample Magnetometer

To my beloved mother and father

ACKNOWLEDGMENTS

These past six years have been a long road. I have met many kind people along the way that generously gave me their time and collaboration and I wish to warmly thank all those who contributed directly or indirectly to my work.

More specifically, I would like to express my appreciation to my supervisor Dr. Andrea Bianchi for giving me the opportunity to join his research team as a doctoral student in the physics department of University of Montreal. His project proposal inspired me to apply and his thorough experimental knowledge kept me engrossed.

I would like to convey my sincere gratefulness to another professor in the department, my advisor professor Dr. Michel Côté, who mentored me for the theoretical part of my work. Michel's profound knowledge of theoretical physics and electronic structure calculation is one of the pillars of the physic's department upon which enlightenment is built. His patience, thoughtfulness and wisdom are several of his personal qualities that are the most appreciated among the student body, including myself. Michel has been a real mentor and friend for me, always taking the necessary time to answer any and all of my questions, supporting me in my future endeavors, and coaching me beyond the call of duty. It is very hard for me to put in words how much I appreciate Michel. He made me believe in myself again in the middle of my PhD when I had lost motivation. His advice is something that I will always cherish and carry with me throughout my career. He has my full gratitude.

Another person that I feel immensely indebted to is one of my most precious collaborators, Dr. Andres Saul, whose generosity I will remember for many years to come. Andres traveled to Montreal from Marseille to work on the electronic structure calculations, coaching me on the software and possible techniques to use. But even when he was in Marseille, Andres made himself available when necessary, even during his vacation, to answer emails and for a chat via videoconference. He is an extensively skilled professor in this field and I feel honored that he spent such copious amounts of time supporting me in my work.

I would also like to thank contributing chemists Prof. Christian Reber from Univer-

sity of Montreal, Prof. Dominique Juneau from University Claude Bernard Lyon 1 as well as his PhD student Anthony Lannes, for the synthesization of the crystal samples I used for this research. Without their collaboration, our project would simply have not been possible. I would like to thank Anthony Lannes who generously showed me the step by step process of how the synthesization is done.

I wish to take a moment to acknowledge the warmth of several faculty members whose kindness I shall remember: thanks to Dr. Richard Leonelli, the department director, for the kindness he infuses in his support of faculty students, and not to forget his delightful annual corn roasts. Thanks to Anne Gosselin and Lynda Syvrais for giving me a warm, welcoming and inclusive feeling in dealing with administrative affairs.

I would like to thank Dr. Reza Nourafkan for always being ready to share his knowledge and for answering my questions at the end of my PhD.

On a more personal note, I want to thank Guillaume Gélinas for his friendship. He is an anomaly in the physics department. For me, he is one of the most caring people that I have come across. He let me feel warm in this cold world, and I cannot state how much I have appreciated his presence in my life.

Likewise, I would like to express how blessed I feel for the support and constant encouragement I have gotten over the years of my family. My beloved father Majid and mother Azar are the foundation of my success. Their daily absence in my life during the last six years was the sacrifice that I had to make in order to accomplish my dream of earning my doctorate.

I want to thank my uncle Farshid who has a unique, high-spirited character full of merriment, jollity, and has a wonderful sense of humour. Talking to him has always increased my enthusiasm to keep going through arduous times since I started my life in Canada. I am delighted to have him back in my life after 25 years of being separated by distance.

Also, thanks to my affectionate and kind-hearted aunt Ziba and her whole family, and Vahid. They have all accompanied me in their very own way down this long road.

I would like to give my sincere emotions to a lovely lady who showed me consideration, sympathy, and affability from her heart. Thank you Melanie for your thoughtfulness, understanding, and your presence in one of the most stressful and demanding times of my life.

On a final note, I wish to express my deepest regards to the committee that will take the time to review my work: Dr. Michel Côté, Dr. Andrea Bianchi, Dr. Sjoerd Roorda, Dr. François Schiettekatte, and Dr. Claude Bourbonnais.

CHAPTER 1

INTRODUCTION

Today's technological needs have challenged scientists to surpass the borders of traditional atom-based magnets to design new generations of molecule-based magnets that lead to a plethora of prospective technological applications [1–4]. Designing novel magnets that possess magnetic moment and show magnetic ordering despite being void of any metallic element has been a difficult task for scientists ever since magnets have first been studied and employed. Although scientists have proposed theoretical investigations on a new generation of magnets based on molecular crystals of organic free radical, their existence was not experimentally confirmed until recently [5–12].

Indeed, the new generation of magnets is built from organic free radicals that are stable at room temperature and can be condensed into crystals. Organic free radicals used in purely organic magnets are open-shell molecules consisting only of light elements such as H, C, N, and O. Each molecule in those organic magnets possesses a magnetic moment owing to an unpaired electron delocalized in its molecular structure. A magnetic ordering can be achieved in some organic magnets provided that the exchange interaction from overlapping orbitals occurs in the bulk of the material [2].

Magnetism based on atoms in traditional magnets has been restricted to metallic elements belonging either to transition metals or rare earth metals. Magnetism originates from the unpaired electron spins in the d-orbitals of transition metals, and in the f-orbitals of rare earth elements. However, magnetism in organic magnets emanates from the unpaired electron in their p-orbital, which gives unusual properties to them as compared to traditional magnets [4].

To tune the properties of classical magnets, metallurgical methods were needed to change the structure and composition of the material. However, the design and synthesis of a new generation of purely organic magnets are plausible through conventional synthetic organic chemistry techniques. The main limitation in creating molecule-based organic magnets has been the high reactivity of free radicals due to the unpaired electron.

Eventually, the stabilization of free radicals became possible either by adding aromatic rings that increase the delocalization of the unpaired electron or by substituting parts of the molecule with bulky side-groups to protect the radical from undesirable reactions [13].

Although chemists have been more interested in creating organic magnets with ferromagnetic (FM) properties for the purpose of industrial application, physicists have been drawn to finding real systems that experimentally show quantum critical points (QCPs) at finite temperatures in order to shed light on the quantum critical nature of new genuine phase transitions. At the QCP of a many-body quantum system, there is a competition between two ground states with adjacent energies, which gives rise to the formation of exotic quantum phases [14]. Changing certain parameters, such as the application of hydrostatic pressure and the structural modification of the radical molecules by chemical substitution, can tune the way those molecules are oriented with respect to one another and thus change the wavefunction overlap between neighboring molecules. As a consequence, the interactions between the molecules can be modified, and the system can be driven towards a QCP, thereby creating novel quantum phases.

Another characteristic of organic magnets is high isotropic electronic spin as a result of their negligible spin-orbit coupling. The outcome is that the magnetic interactions in organic magnets have little anisotropy [2]. As will be later discussed, owing to the negligible anisotropic interactions, such as the spin-orbit interactions, the uniaxial symmetry of the spin system in organic magnets is maintained down to very low temperature, which makes them better potential materials to experimentally study the realization of Bose-Einstein condensation (BEC) in quantum magnets.

Advancing the technology of magnets by designing purely organic molecule-based magnets with exceptional properties, such as high transparency, high tunability, high flexibility, low temperature organic chemical methodology, low weight, and low environmental pollution is an indispensable target of material science. Organic molecule-based magnetic materials could lead to potential applications in technology such as quantum computing [13], molecular spintronic [15–18] leading to high-density information storage and memory devices [19–21], magneto-optical materials yielding, for instance, optical switching devices [22], superconductors [23, 24], and electronic devices that are flexible and/or transparent [1, 25].

In the challenge to find organic free radicals showing magnetic ordering, some stable organic magnets are noteworthy.

1.1 Nitronyl nitroxide radicals as backbones of organic molecule-based magnets

Galvinoxyl, the first organic compound with a relatively strong ferromagnetic (FM) coupling, was put forth in 1967 [5]. However, this compound does not show magnetic order, and only a low-temperature phase with weak antiferromagnetic (AFM) interactions is observed [26, 27].

In 1973, tanol suberate was reported as the first organic material with an FM ordering [6]. It was later revealed to be an antiferromagnet with a metamagnetic transition, yielding an FM spin alignment [7].

The year 1991 was an important year in the research of organic magnets. FM ordering was observed in [TDAE][C_{60}], TDAE=tetrakis(dimethylamino)ethylene, with a T_c of about 16 K [8]. Additionally, the first genuinely organic magnet with a bulk FM property was reported for the β phase of para-nitrophenyl nitronyl nitroxide (p-NPNN) radical with a T_c of about 0.6 K[9, 10]. p-NPNN radical, shown in Fig. 1.1(a), is a member of the nitronyl nitroxide family, illustrated in Fig. 1.2(a). Nitronyl nitroxide is the most ex-

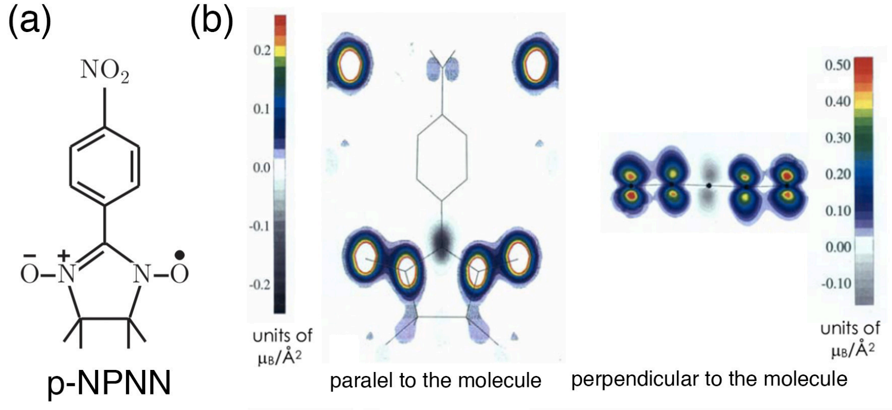

Figure 1.1 – (a) A para-nitrophenyl nitronyl nitroxide (p-NPNN) molecule. (b) Spin density of p-NPNN measured by neutron scattering [28].

tensively studied family of organic free radicals for designing organic magnets because of their advantageous characteristics as compared to other radicals [29, 30]. Nitronyl nitroxide radicals have been used in compounds with metals, like bridging ligands in metal-organic magnets [31, 32], or without metal in purely organic magnets [10, 33].

Interesting magnetic properties result from the unique distribution of the spin density of the unpaired electron in nitronyl nitroxide radicals. The spin density is identically distributed on the two identical N-O atoms of the ONCNO branch of the molecule. Also, there is a small negative spin density on the central carbon due to the spin polarization. As an example, the distribution of spin density measured by neutron scattering for the p-NPNN is illustrated in Fig. 1.1(b) [28].

Nitronyl nitroxide radicals have exceptional stability, which is attributable to their molecular structure that can be manipulated using synthetic organic chemistry techniques. Introducing various substitutes for the -R branch of the nitronyl nitroxide radical, as shown in Fig. 1.2, not only increases the stability of the radicals by delocalizing the unpaired electron over a larger part of the molecule [34], but also results in different magnetic properties. Examples of the various magnetic properties in nitronyl nitroxide radicals are: the crystal of NIT-CN molecules (2-cyano-4,4,5,5-tetramethylimidazoline-1-oxyl-3-oxide) showing an AFM interaction [35], the 5-pyrimidinyl-nitronyl nitroxide molecules exhibiting an FM interaction [36], and the PNNBNO molecules showing a 3D ferrimagnetic system [37].

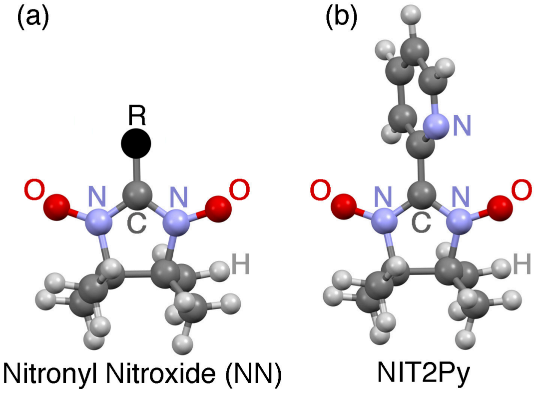

Figure 1.2 – Substituting the -R part in a nitronyl nitroxide molecule (a) by a 2-pyridyl ring yields a NIT2Py molecule (b).

Changing the way the nitronyl nitroxide molecules are stacked in a crystal with respect to one another can also yield different magnetic properties. The structure-magnetism relation in the nitronyl nitroxide crystals is apparent when looking at the β- and γ-phases of the p-NPNN radical. The former, in which the molecules condense into an orthorhombic crystal structure, is subjected to a bulk FM transition at about 0.6 K. The latter, in which the molecules crystallize into a triclinic structure, shows an AFM transition at 0.65 K and 1D FM fluctuations beyond that temperature[38]. Due to the numerous advantageous characteristics of the nitronyl nitroxide family, we chose one of its members as the primary focus of the study presented in this thesis.

1.2 Focus of the research: A purely organic quantum magnet (NIT2Py)

Indeed, this work focuses on a purely organic magnet that is made up of molecules having only C, N, O, and H atoms, and that can be condensed into a crystal. The building blocks of the crystal under study are the free radical molecules that belong the nitronyl nitroxide family. Those molecules are 2- (2'-pyridyl)-4,4,5,5,-tetramethyl-4,5-dihydro-1,H-imidazole-3-oxide-1-oxyl, otherwise known as NIT2Py, having chemical formula $C_{12}H_{16}N_3O_2$. Calculating the total number of electrons corresponding to the 33 atoms in a single NIT2Py molecule $(4 \times 12 + 1 \times 16 + 3 \times 5 + 2 \times 6)$ yields an odd number of electrons, which indicates the presence of an unpaired electron in each of the free radical molecules.

As shown in Fig. 1.2(b), the NIT2Py molecule, is basically a nitronyl nitroxide radical, in Fig. 1.2(a), to which the -R branch is substituted by a 2-pyridyl ring (C_5H_4N). The five-membered nitronyl nitroxide ring [13, 25] is composed of three carbon atoms and two nitrogen atoms. Two of the three carbon atoms are each bound to two methyl groups (CH_3). As for the two nitrogen atoms, each one is connected to an oxygen atom, forming two equal N-O branches. Between the two N-O groups on the five-membered ring is the remaining carbon atom that connects the nitronyl nitroxide ring to the 2-pyridyl ring. The 2-pyridyl ring is an organic heterocyclic compound with a structure analogous to benzene, in which the CH at the second position is replaced by a nitrogen atom. Note that the nitronyl nitroxide and 2-pyridyl are not in the same plane.

Connecting the 2-pyridyl ring to the middle carbon of the five-membered ring of NN increases the delocalization of the unpaired electron over a large part of the NIT2Py molecule, and hence provides the NIT2Py structure with exceptional stability. Also, there is a unique delocalization of an unpaired electron on the two equivalent N and O atoms of the ONCNO branch of the molecules.

Experimental results shed light on another characteristic of NIT2Py, which is the realization of BEC. Until now, BEC has been studied in inorganic quantum magnets [39–41], as well as in some organometallic quantum magnets [42–44]. Also, the observation of BEC in purely organic magnetic material has been, to our knowledge, only limited to a S=1 antiferromagnetically dimerized system, F_2PNNNO [45, 46]. Our research yielded the first magnetic realization of BEC in a S=1/2 spin system with antiferromagnetically coupled tetramers as the basic unit of magnetism.

1.3 Outline of this thesis

In this work, we provide overviews of the theory of magnetism and the theory of electronic structure calculation as a basis for understanding the results of our magnetic measurements on NIT2Py crystals. The complex behaviors, such as a 1/2 plateau observed in the field dependence of the magnetization isotherm, and two dome-shaped regions observed in the phase diagram, motivated us to study this purely organic quantum magnet theoretically, pushing us to develop a model spin Hamiltonian for the NIT2Py system.

The crystal structure of the NIT2Py was determined by X-ray diffraction measurements. However, the magnetic structure of this purely organic crystal is not known. To study the magnetic structure of the NIT2Py system, first the magnetic coupling mechanism between the molecules needs to be known. To achieve this goal, magnetic coupling constants (Js), which shine light on the types and strengths of the magnetic interactions, need to be obtained. We used electronic structure calculations to evaluate the signs and strengths of the magnetic interactions in the NIT2Py system.

Other researchers have used density functional theory (DFT) and broken-symmetry method to calculate the exchange coupling constants in inorganic compounds and metal complexes [47–51]. However, DFT and broken-symmetry method have rarely been applied to the study of purely organic compounds. Here, we evaluate the Heisenberg spin exchanges of NIT2Py using DFT and the broken-symmetry formalism as implemented in the ABINIT package [52] and QUANTUM ESPRESSO [53]. To evaluate the exchange coupling constants, we apply the supercell total energy difference approach and the four-states energy mapping approach. We design a magnetic lattice based on a repeat pattern of a minimal set of the strongest exchange interactions, relevant to the magnetic structure of the NIT2Py system. With the aid of mean-field theory, we consider all the interactions between the magnetic units in the NIT2Py magnetic structure and propose a magnetization formalism that can reproduce the magnetic properties of NIT2Py. Additionally, we carry out the exact diagonalization of a Heisenberg Hamiltonian matrix constructed for the system, and hence obtain the corresponding eigenstates, which in turn yields the magnetization of the system.

CHAPTER 2

THEORETICAL OVERVIEW ON MAGNETISM

The phenomenon of magnetism, as a challenging science, has always solicited people's curiosity. In 1865, James Clerk Maxwell published the original set of four equations concerning electromagnetism, referred as Maxwell's equations [54]. Although Maxwell's equations describe the generation of electric and magnetic fields, the correspondences between them, as well as charges and currents, they do not shed light on the origin of magnetic moments and magnetic order. Magnetic moments are due to spin or orbital degrees of electrons, while the source of magnetic order lies in exchange interactions between the electrons of a magnetic system. In this chapter, the magnetic exchange interaction will be discussed using a dimer system that can be generalized to larger magnetic structures.

2.1 Magnetic moment and magnetization

The magnetic moment, $\boldsymbol{\mu}$, is a fundamental entity in magnetism by which the magnetic properties of a magnetic material can be ascertained. The magnetic moment can be defined based on the variation of the energy of a given system with reference to an applied magnetic field [55],

$$\boldsymbol{\mu} = -\frac{\partial E}{\partial \boldsymbol{B}}. \tag{2.1}$$

Note that the electromagnetic unit (emu) is occasionally utilized as a magnetic moment in the CGS system, where 1 emu=1 erg G^{-1}. Magnetic moment for electrons can originate from the orbital moment L and the spin moment S as

$$\boldsymbol{\mu} = -(\boldsymbol{L} + g\boldsymbol{S})\mu_B, \tag{2.2}$$

where g, in general, is defined as

$$g(J,L,S) = \frac{3}{2} + \frac{1}{2}\left[\frac{S(S+1)-L(L+1)}{J(J+1)}\right]. \tag{2.3}$$

Also, the magnetic moment is quantized in the unit of Bohr magneton given by $\mu_B = \frac{e\hbar}{2m_e c}$ ($\mu_B = 0.927 \times 10^{-20}$erg/G).

The spin-orbit coupling in purely organic molecule-based magnets is negligible due to the exceptional isotropic characteristics of an unpaired electron spin as well as the distribution of the unpaired spin density over a large part of the molecule [2]. Therefore, in the case of organic molecules and solids, the orbital momentum is usually quenched, $\boldsymbol{L} \approx 0$. Then, the total angular momentum (J) can be well approximated by the spin angular momentum [56]. By inserting $J = S$ in Eq. (2.3), the g-factor takes a value of $g = 2$, and the magnetic moment can be obtained by a spin-only value, which is given by

$$\boldsymbol{\mu} \approx -2\boldsymbol{S}\mu_B. \tag{2.4}$$

The next important concept in magnetism which is of experimental interest is magnetization, which is defined as the magnetic moment per unit volume of a compound, $\boldsymbol{M} = \boldsymbol{\mu}/V$, at a given temperature and external magnetic field, $\boldsymbol{H}$. The unit of magnetization in the CGS system is Oersted (Oe) or emu cm^{-3}. Note that one electron per atom is equivalent to an atomic magnetic moment of 1 μ_B [57].

By applying a range of temperatures and external magnetic fields to a magnetic compound, the arrangement of magnetic moments changes and, in turn, the magnetization changes. The magnetic moments favor different arrangements with the neighboring moments, such as parallel or ferromagnetic (FM), and antiparallel or antiferromagnetic (AFM) alignments. In magnetism, obtaining the magnetic field and magnetization is a major challenge.

2.2 Magnetic dipolar interaction

To study the effect of dipole-dipole (d-d) interaction, suppose that two magnetic moments, $\boldsymbol{\mu}_1$ and $\boldsymbol{\mu}_2$, are separated by r. The energy is given by

$$E = \frac{1}{r^3}\left[\boldsymbol{\mu}_1 \cdot \boldsymbol{\mu}_2 - \frac{3}{r^2}(\boldsymbol{\mu}_1 \cdot \boldsymbol{r})(\boldsymbol{\mu}_2 \cdot \boldsymbol{r})\right]. \tag{2.5}$$

If $\boldsymbol{\mu}_1$ and $\boldsymbol{\mu}_2$ are each of the order of 1 μ_B with $r \sim 1$ Å, the energy can be calculated in the order of 1 K. A temperature of 1 K is already larger than the strength of the d-d interaction. As a larger number of materials order at much higher temperatures, the magnetic d-d interaction cannot be considered as the source of ordering in most magnetic materials [56].

Also, in spite of the fact that applying a magnetic field can give rise to some spin polarizations, in the rivalry between the interatomic energies and the external magnetic field, the latter fails. How can we justify the spontaneous magnetization observed in some FM materials even at zero applied magnetic field? For instance, Cobalt (Co), and Iron (Fe) have Curie temperatures of 1388 K and 1043 K respectively, below which they show spontaneous magnetization.

Those facts push us to rethink the origin of magnetic moment and magnetization. In the next section, we will explain why exchange interaction is at the root of these phenomena.

2.3 Exchange interaction

Exchange interaction is the force behind chemical bondings as well as magnetism. Exchange is entirely quantum mechanical and occurs among identical particles such as electrons. It has no classical equivalent. Intriguing is the fact that some daily occurrences as mundane as a magnet posted on the surface of a refrigerator door cannot be profoundly elucidated without quantum mechanics. In general, quantum mechanics is at the heart of all magnetism.

In 1927, a successful model was proposed that accounts for the emergence of hydrogen molecules from hydrogen atoms by quantum mechanics [58]. To understand how this yields magnetism, a simple model, the spin dimer system, is presented that can then be applied to other magnetic superstructures with more spin sites.

A spin dimer consists of two identical $S = 1/2$ spin sites, 1 and 2, with one unpaired electron per site with spins $\boldsymbol{S}_1$ and $\boldsymbol{S}_2$, as shown in Fig. 2.1(a). The total spin is given as $\boldsymbol{S} = \boldsymbol{S}_1 + \boldsymbol{S}_2$. To describe the magnetic interaction between two spins, S_1 and S_2, a Hamiltonian was proposed by Heisenberg, Dirac, and Van Vleck [59–61] as

$$H = J\boldsymbol{S}_1 \cdot \boldsymbol{S}_2. \tag{2.6}$$

This Hamiltonian, known as the Heisenberg spin model, considers localized spins on different sites. It is effective when dealing with well-separated atoms with a fixed number of electrons in each atom, such as in insulators with well-localized wavefunctions. The interaction between spins $\boldsymbol{S}_1$ and $\boldsymbol{S}_2$ in the Heisenberg Hamiltonian is given by the Heisenberg spin exchange interaction J, and depends on the orientation of the spins. If the ground state of the Heisenberg Hamiltonian in Eq. (2.6) is taken into account, there are two possible configurations depending on the value of J. Based on the defined notation in the Hamiltonian of Eq. (2.6), J is positive if the spins are antiparallel, but negative if the spins are parallel [62].

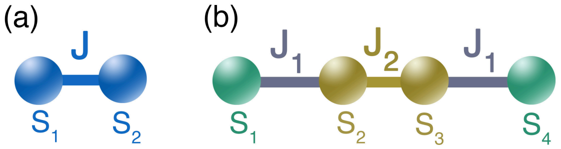

Figure 2.1 – (a) A spin dimer with two coupled S=1/2 and an AFM exchange coupling $J > 0$. (b) a spin tetramer, with four S=1/2 and two different AFM exchange couplings $J_1 > 0$ and $J_2 > 0$.

To find the energy spectrum of this spin dimer Hamiltonian, four basis states are given as $|1\rangle$=$|++\rangle$, $|2\rangle$=$|+-\rangle$, $|3\rangle$=$|-+\rangle$, and $|4\rangle$=$|--\rangle$, in which the first and second components in each state are the z component of the two spins that can either be up or down. Those four vectors, $\{|\varepsilon_1, \varepsilon_2>\}$, are the eigenvectors of S_1^2, S_{1z}, S_2^2, and S_{2z}. So, if operators S_{1z} and S_{2z} act on those states, the results would be $S_{1z}\ |\varepsilon_1,\varepsilon_2 >= \varepsilon_1\frac{\hbar}{2}|\varepsilon_1,\varepsilon_2 >$ and $S_{2z}\ |\varepsilon_1,\varepsilon_2 >= \varepsilon_2\frac{\hbar}{2}|\varepsilon_1,\varepsilon_2 >$. Also, from the general formula for the spin "raising" operator $S_+ = S_x + iS_y$ and spin "lowering" operator $S_- = S_x - iS_y$, one can obtain $S_+\ |+\rangle = 0$, $S_+\ |-\rangle = \hbar|+\rangle$, and $S_-\ |-\rangle = 0$, $S_-\ |+\rangle = \hbar|-\rangle$. Note that to simplify the equations, the angular momentum operators will be calculated in units of $\hbar$, and the $\hbar$ factor will be excluded hereafter. Additionally, the S^2 operator can be defined as

$$\boldsymbol{S}^2 = \boldsymbol{S}_1^2 + \boldsymbol{S}_2^2 + 2\boldsymbol{S}_1 \cdot \boldsymbol{S}_2, \tag{2.7}$$

where, the scalar product of the two spin operators $\boldsymbol{S}_1$ and $\boldsymbol{S}_2$ can be expanded as

$$\begin{aligned}\boldsymbol{S}_1 \cdot \boldsymbol{S}_2 &= S_{1x}S_{2x} + S_{1y}S_{2y} + S_{1z}S_{2z} \\ &= \frac{1}{2}(S_{1+}S_{2-} + S_{1-}S_{2+}) + S_{1z}S_{2z}.\end{aligned} \tag{2.8}$$

To express S_x and S_y in terms of the raising and lowering operators, $S_x = \frac{1}{2}(S_+ + S_-)$ and $S_y = \frac{1}{2i}(S_+ - S_-)$ were used. Inserting Eq. (2.8) in the Hamiltonian of Eq. (2.6) gives the spin dimer Hamiltonian as

$$H = J(\frac{1}{2}(S_{1+}S_{2-} + S_{1-}S_{2+}) + S_{1z}S_{2z}). \tag{2.9}$$

To obtain the energy spectrum of this Hamiltonian, the following 4×4 matrix must be diagonalized

$$H = \begin{pmatrix} \langle 1|H|1\rangle & \cdots & \langle 1|H|4\rangle \\ \vdots & \ddots & \vdots \\ < 4|H|1 > & \cdots & \langle 4|H|4\rangle \end{pmatrix}. \tag{2.10}$$

To calculate each of the 16 elements of the above matrix, the Hamiltonian operator of

Eq. (2.9) acts on each of the four eigenstates as

$$
\begin{aligned}
H\left|+,+\right\rangle &= J\frac{1}{4}\left|+,+\right\rangle, \\
H\left|+,-\right\rangle &= J\frac{1}{2}\left|+,-\right\rangle - J\frac{1}{4}\left|+,-\right\rangle, \\
H\left|-,+\right\rangle &= J\frac{1}{2}\left|+,-\right\rangle - J\frac{1}{4}\left|-,+\right\rangle, \\
H\left|-,-\right\rangle &= J\frac{1}{4}\left|-,-\right\rangle.
\end{aligned}
\tag{2.11}
$$

Then, for example, $\langle +,+|H|+,+\rangle = (1/4)\langle +,+|H|+,+\rangle = (1/4)J$ gives the element in the first column of the first row. The other elements are calculated using the same method, which results in

$$
H = \begin{pmatrix} \frac{1}{4}J & 0 & 0 & 0 \\ 0 & -\frac{1}{4}J & \frac{1}{2}J & 0 \\ 0 & \frac{1}{2}J & -\frac{1}{4}J & 0 \\ 0 & 0 & 0 & \frac{1}{4}J \end{pmatrix}. \tag{2.12}
$$

This matrix consists of three submatrices. Two of those are one-dimensional, and their eigenvalues, $\frac{1}{4}J$, are related to vectors $|++\rangle$ and $|--\rangle$. The eigenvalues associated to the third submatrix can be obtained by diagonalizing the following 2×2 submatrix:

$$
J\begin{pmatrix} \frac{-1}{4} - \lambda & \frac{1}{2} \\ \frac{1}{2} & \frac{-1}{4} - \lambda \end{pmatrix}. \tag{2.13}
$$

By solving $(1-\lambda)^2 - 4 = 0$, we have λ_1=-1 and λ_2=3, which yields the last two eigenvalues as $\frac{1}{4}J$ and $\frac{-3}{4}J$.

However, note that the four basis states initially chosen were deficient in regards to exchange symmetry, because two of the states, $|+-\rangle$ and $|-+\rangle$, are neither symmetric nor antisymmetric upon the exchange of the two identical electrons. Therefore, a more suitable choice for the eigenstates of $\boldsymbol{S}_1 \cdot \boldsymbol{S}_2$ is a linear combination of the two $|+-\rangle$ and $|-+\rangle$ states, as $\frac{1}{\sqrt{2}}\left[\left|+,-\right\rangle + \left|-,+\right\rangle\right]$, which is symmetrical, and $\frac{1}{\sqrt{2}}\left[\left|+,-\right\rangle - \left|-,+\right\rangle\right]$, which is antisymmetrical with respect to the exchange operator. The obtained eigenvalue $\frac{-3}{4}J$ is non-degenerate and related to the vector $\frac{1}{\sqrt{2}}[|+,-\rangle - |-,+\rangle]$, which is known as the singlet state. Furthermore, the eigenvalue $\frac{1}{4}J$ is three-fold degenerate and associated to three vectors, $|+,+\rangle$, $|-,-\rangle$, and $\frac{1}{\sqrt{2}}[|+,-\rangle + |-,+\rangle]$, called the triplet state. If the singlet and triplet states had been chosen as the eigenstates rather than the four vectors of $| \varepsilon_1, \varepsilon_2 >$, the matrix of Eq. (2.10) would already have been diagonal [63].

The eigenvalues of a spin dimer system are given as

$$E_S^{spin} = -\frac{3}{4}J,\ E_T^{spin} = \frac{1}{4}J. \tag{2.14}$$

Now, consider that the atomic orbitals centered at hydrogen atoms A and B are given respectively as ϕ_A and ϕ_B. Then, based on the Heitler-London model, the molecular orbital is formed as

$$\psi(\boldsymbol{r}_1, \boldsymbol{r}_2) = \frac{1}{\sqrt{2}} \left(\phi_A(\boldsymbol{r}_1)\phi_B(\boldsymbol{r}_2) \pm \phi_B(\boldsymbol{r}_1)\phi_A(\boldsymbol{r}_2)\right), \tag{2.15}$$

where the first product indicates that the first electron with the spatial coordinates $\boldsymbol{r}_1$ is found in atom A and the second electron with $\boldsymbol{r}_2$ is around atom B. Also, the ± signs in Eq. (2.15) mean that the spatial wavefunction under the exchange of two identical electrons either remains unchanged, namely symmetric $(+)$ spatial wavefunction, or changes its sign $(-)$, called antisymmetric spatial wavefunctions, which are generally recognized as exchange symmetry [56].

Also, the total wavefunction for two electrons is given as the product of the spatial and spin wavefunctions: $\Psi = \psi(\boldsymbol{r}_1, \boldsymbol{r}_2) \otimes \chi(S_1, S_2)$. The spin wavefunction is defined as

$$\chi(S_1, S_2) = \frac{1}{\sqrt{2}} \left(\alpha(S_1)\beta(S_2) \pm \beta(S_1)\alpha(S_2)\right), \tag{2.16}$$

where α indicates the spin up and β, the spin down. To satisfy the antisymmetric property of the overall wavefunction of two electrons as stated by the Pauli principle, there are two possibilities: if we are dealing with a symmetric spatial part, the spin part must be antisymmetric (i.e. singlet state) or, in the case of an antisymmetric spatial part, the spin part must be symmetric (i.e. triplet state). The difference between the energies of the singlet and triplet states of a dimer in Eq. (2.14) is given by

$$E_T^{spin} - E_S^{spin} = \frac{1}{4}J - (-\frac{3}{4}J) = J. \tag{2.17}$$

Therefore, the energy splitting of the singlet-triplet states of a dimer corresponds to the spin exchange constant J of this system. If the result is $J > 0$, then the singlet state is favored ($E_S < E_T$) and the interaction described by Eq. (2.6) leads to an antiparallel (AFM) spin coupling. However, if $J < 0$, the triplet state is preferred ($E_T < E_S$) and a parallel (FM) spin coupling occurs.

Two electrons on one atom mostly yield a $J < 0$, which indicates a triplet state and, consequently, an antisymmetric spatial wavefunction. The outcome is two electrons staying apart to minimize the Coulomb repulsion. If two electrons are located on the two nearest atoms, a mixture of atomic states, one located on one atom and another on the other atom, results in a joint state, namely the molecular orbital. Then, the spatial wavefunction is either symmetric, a bonding orbital, or antisymmetric, an antibonding orbital. The energy of the antibonding state is larger than that of the bonding state, as shown in Fig. 2.2. In a hydrogen molecule, the singlet state is favored with two electrons in the bonding state [56].

Bear in mind that the sign and degree of exchange interaction between the spins are essential to design new molecular magnets. This exchange interaction is a quantum mechanical phenomenon, which is caused by overlapping of wavefunctions of the electrons in neighboring molecules in molecule-based magnets. As it is complex to examine the magnetic properties of radical pairs in the crystal solids directly, the pairwise interaction in Eq. (2.6) can be employed on all of the neighboring free radical molecules carrying unpaired electron spins. Therefore, Heisenberg model between two spins in a spin dimer can be generalized to a general spin Hamiltonian $\boldsymbol{H}_s$, called the Heisenberg Hamiltonian, by summing over all of the radical pairs, as shown in Eq. (2.18). The Heisenberg Hamiltonian provides us with a practical way to study the magnetic properties of free

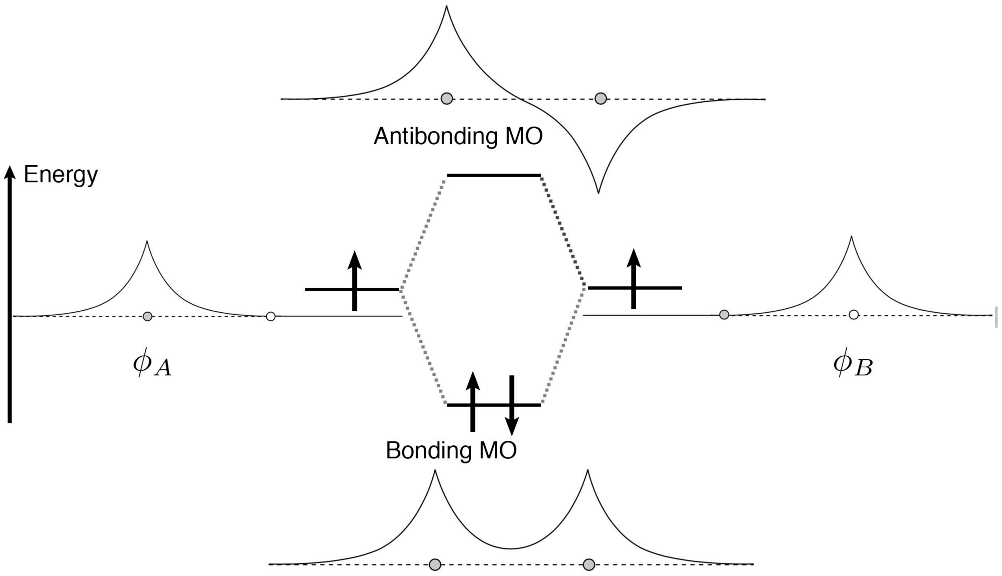

Figure 2.2 – Two atomic orbitals for atom A and B are shown on the left and right along with the corresponding wave function ϕ_A and ϕ_B respectively. Each of those atomic orbitals contains one electron. A bonding and an antibonding molecular orbital (MO) are created respectively by the sum and difference of those atomic orbitals. In the bonding MO, the spatial part of the wave function is symmetric, which results in an antisymmetric spin part. However, the spatial part of the antibonding MO is antisymmetric, and its spin part is symmetric. The energy of the bonding MO is lower than the antibonding MO, and thus the singlet state is favored. This representation can be used to show the molecular orbitals of H_2 being formed from two H atomic orbitals [57].

radical pairs in the crystal solids [56].

$$\boldsymbol{H}_s = \sum_{i>j} J_{ij} \boldsymbol{S}_i \cdot \boldsymbol{S}_j, \tag{2.18}$$

where $\sum_{i>j}$ means that the summation is limited to the spin pairs. Also, J_{ij} is the exchange interaction between the i and j spins. Note that, in this spin Hamiltonian, the electronic characteristics such as the Coulomb interaction and hopping are mapped into spin variables [57].

2.4 Magnetic susceptibility

The relation between the magnetization $\boldsymbol{M}$ of a magnetic material and the applied magnetic field $\boldsymbol{H}$ is given by

$$\chi = \frac{\partial M}{\partial H}, \tag{2.19}$$

where χ is the magnetic susceptibility. Magnetization is a vector, applied magnetic field is an axial vector, and susceptibility is a tensor. However, χ can be diagonal depending on the selection of axes of the reference system. χ can be considered as a scalar if the magnetic material is isotropic [64].

However, in a weak magnetic field, a linear relationship is valid between $\boldsymbol{M}$ and $\boldsymbol{H}$, which is expressed by a well-known equation as

$$\mathbf{M} = \chi \mathbf{H}. \tag{2.20}$$

The overall magnetic susceptibility of a material consists of diamagnetic and paramagnetic contributions, $\chi = \chi_{\mathrm{Dia}} + \chi_{\mathrm{Para}}$. The sign of total magnetic susceptibility determines if the magnetic material is dominated by paramagnetism ($\chi > 0$) or diamagnetism ($\chi < 0$). Diamagnetism is a quantum mechanical phenomenon existing to some extent in all materials and it gives rise to a small negative magnetic susceptibility independent of temperature. By applying an external magnetic field to a material, the atomic current loops generated by the orbital motion of the core electrons changes in such a way that the induced magnetic field opposes the applied field. The diamagnetic contribution of the magnetic susceptibility is significant in delocalized π systems, such as in a benzene molecule. Applying a magnetic field to the benzene ring induces a current that, due to very itinerant π electrons, passes around the benzene ring. Because the benzene ring's diameter is much larger than that of the atom, the resulting χ_{Dia} in that delocalized π system is greater than the atom[56].

However, the paramagnetic contribution to the total magnetic susceptibility, which corresponds to the unpaired electron in magnetic materials with empty shells, is substantially stronger than the diamagnetic contribution. In the absence of an external magnetic field, the magnetic moments of the unpaired electrons of the neighboring molecules are randomly aligned and can be approximated as free spins due to weak interactions between them. Then, by employing an external magnetic field, these magnetic moments start to align in the direction of the applied field, and magnetization in the paramagnetic material appears. As the magnitude of the applied magnetic field increases, so does the extent of the alignment of the spins and, consequently, the induced magnetization. But, increasing the temperature renders the alignment of spins more random, and hence the magnetization decreases. Thus, the magnetization of a magnetic material is contingent on the external magnetic field and temperature [56].

2.5 Magnetization of non-interacting magnetic moments

The magnetization density of a quantum mechanical system with a uniformly applied magnetic field B and at zero temperature is given by

$$M(B,T=0) = -\frac{1}{V}\frac{\partial E_0(B)}{\partial B}, \tag{2.21}$$

where V is the volume of the system and E_0 is the ground-state energy. At a given temperature, the magnetization density can be expressed in terms of thermal equilibrium average of the magnetization of every excited state as

$$M(B,T) = \frac{\sum_n M_n(B)e^{-\beta E_n}}{\sum_n e^{-\beta E_n}}, \tag{2.22}$$

where $\beta = \frac{1}{k_B T}$ is the thermodynamic beta, $k_B = 1.38064 \times 10^{-16}$ ergK^{-1} is the Boltzmann constant, and $E_n(B)$ is the total energy of state n. Also, the magnetization density $M_n(B)$ is defined as

$$M_n(B) = -\frac{1}{V}\frac{\partial E_n(B)}{\partial B}. \tag{2.23}$$

In the thermodynamical form, we can express M as

$$M = -\frac{1}{V}\frac{\partial F}{\partial B}, \tag{2.24}$$

where F is the free energy and is designated as

$$F = -\frac{1}{\beta}\ln Z. \tag{2.25}$$

The partition function, Z, is obtained through

$$Z = \sum_{n} e^{-\beta E_n}, \tag{2.26}$$

where the sum goes over all the states of system n. Note that by means of the partition function, the other thermodynamic properties of the system can be derived. So, the energy of the system is given by

$$E = -\frac{\partial}{\partial \beta}\ln Z. \tag{2.27}$$

Subsequently, the specific heat is obtained by

$$C_V = -\beta\frac{\partial E}{\partial \beta}\frac{1}{T}. \tag{2.28}$$

Substituting Z in Eq. (2.25) with Eq. (2.26) yields

$$F = -\frac{1}{\beta}\ln(\sum_{n} e^{-\beta E_n}). \tag{2.29}$$

If we assume that only the lowest-lying spin multiplet plays a part in statistical mechanical sums, then the free energy of Eq. (2.30) for a single spin is given by

$$F = -\frac{1}{\beta}\ln\sum_{S_z=-S}^{S} e^{-\beta g \mu_B S_z B}. \tag{2.30}$$

Based on the general formula for the sum of a geometric series as $\sum_{k=a}^{b} r^k = \frac{r^a - r^{b+1}}{1-r}$ with $r \neq 1$, then Eq. (2.30) becomes

$$\sum_{S_z=-S}^{S} e^{-\beta g \mu_B B S_z} = \frac{e^{\beta g \mu_B B S} - e^{-\beta g \mu_B B (S+1)}}{1 - e^{-\beta g \mu_B B}}. \tag{2.31}$$

Multiplying the numerator and denominator of the fraction in Eq. (2.31) by $e^{1/2\beta g \mu_B B}$, and by using the result to replacing the sum over the partition function in Eq. (2.30), we obtain

$$\begin{aligned} F &= -\frac{1}{\beta} \ln \frac{e^{\beta g \mu_B B (S+\frac{1}{2})} - e^{-\beta g \mu_B B (S+\frac{1}{2}))}}{e^{\frac{1}{2}\beta g \mu_B B} - e^{-\frac{1}{2}\beta g \mu_B B}}, \\ &= -\frac{1}{\beta} \ln \frac{2\sinh(\beta g \mu_B B (S+\frac{1}{2}))}{2\sinh(\frac{\beta g \mu_B B}{2})}. \end{aligned} \tag{2.32}$$

The magnetization of N non-interacting magnetic moments in a volume V can be attained based on Eq. (2.24) as

$$M = \frac{N}{V} g \mu_B \left\{ (\frac{2S+1}{2}) \coth(\beta g \mu_B B (\frac{2S+1}{2})) - \frac{1}{2} \coth(\beta g \mu_B B \frac{1}{2}) \right\}. \tag{2.33}$$

If $x = \beta g \mu_B S B$, then

$$M = \frac{N}{V} g \mu_B S B_S(x), \tag{2.34}$$

where $B_S(x)$ is known as the Brillouin function and is described as

$$B_S = \frac{2S+1}{2S} \coth(\frac{2S+1}{2S} x) - \frac{1}{2S} \coth(\frac{1}{2S} x). \tag{2.35}$$

Substituting the Brillouin function in Eq. (2.34) with Eq. (2.35), the magnetization of non-interacting $S = 1/2$ spins is given by

$$M = 2\coth(2\frac{\mu_B}{k_B T} B) - \coth(\frac{\mu_B}{k_B T} B). \tag{2.36}$$

The magnetization of non-interacting magnetic moments in Eq. (2.36) as a function of applied magnetic field is shown in Fig. 2.3. When the applied magnetic field is large and the temperature is low, the magnetization does not follow the linear proportionality, and it approaches a saturation magnetization, $M_{sat} = Ng\mu_B S$.

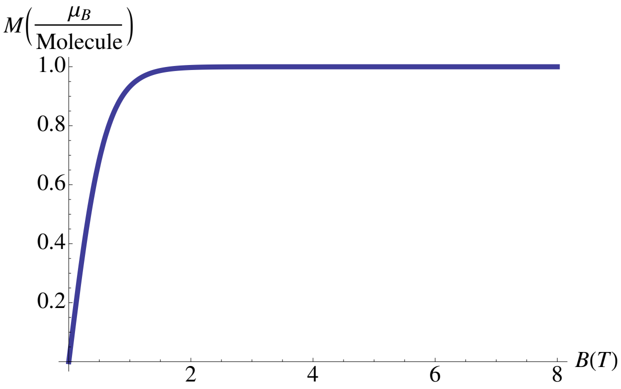

Figure 2.3 – The magnetization is illustrated as a function of applied magnetic field for a system of non-interacting spins at temperature 0.4 K. By increasing the field, the magnetization saturates at $1\mu_B$.

In the high temperature limit where $k_B T \gg \mu_B B$, the Brillouin function in Eq. (2.35) becomes

$$\begin{aligned} B_S &= \frac{2S+1}{2S}\left(\frac{2S}{2S+1}\frac{1}{x} + \frac{1}{3}\frac{2S+1}{2S}x\right) - \frac{1}{2S}\left(2S\frac{1}{x} + \frac{1}{3}\frac{1}{2S}x\right) \\ &= \frac{1}{3}\frac{S+1}{S}x, \end{aligned} \tag{2.37}$$

where expansion $\coth(x) \approx \frac{1}{x} + \frac{x}{3} + \ldots$ for the small x was used. By replacing $B_S(x)$ in Eq. (2.34) with Eq. (2.37), and also considering $x = \beta g \mu_B S B$, the magnetization for non-interacting spins in the high temperature limit is obtained as

$$M = \frac{N}{V}\frac{g^2\mu_B^2}{3}\frac{1}{k_B T}S(S+1)B. \tag{2.38}$$

Additionally, the magnetic susceptibility for weak magnetic fields is obtained by substituting M in Eq. (2.20) with Eq. (2.38) as

$$\chi = \frac{N}{V}\frac{g^2\mu_B^2}{3}\frac{1}{k_BT}S(S+1). \tag{2.39}$$

Note that magnetic susceptibility can be written as

$$\chi = \frac{N}{V}\frac{\mu_{eff}^2}{3k_BT}, \tag{2.40}$$

in which the effective moment of this non-interacting spin system is given by

$$\mu_{eff} = g\mu_B\sqrt{S(S+1)}. \tag{2.41}$$

The effective moment indicates the spin S and the number of unpaired electrons in a magnetic centre. By defining Curie's constant as $C = \frac{N}{V}\frac{g^2\mu_B^2 S(S+1)}{3k_B}$, Eq. (2.39) becomes $\chi = \frac{C}{T}$, which is known as Curie's law and is valid only for weak magnetic fields or high temperatures. Curie's constant is related to the effective moment by $C = \frac{N}{V}\frac{\mu_{eff}^2}{3k_B}$.

2.6 Magnetic order

In section 2.3, we discussed the FM and AFM interactions employing spin exchange interactions between the magnetic moments of neighboring atoms of a spin dimer system. In this section, we will study the FM and AFM magnetic ground states resulting from those magnetic interactions. In an FM ground state, all the neighboring magnetic moments have a parallel alignment, as opposed to an AFM ground state with an antiparallel alignment. By use of mean-field (MF) approximation, we will study the effect of magnetic interactions between a given magnetic moment and all the adjacent neighbors by replacing those interactions with an effective MF.

At high temperatures, the magnetic susceptibility is given by the Curie-Weiss (CW) law as

$$\chi = \frac{C}{T-\theta}, \tag{2.42}$$

where θ is the Weiss temperature. Based on the so-called MF theory, θ is linked to the exchange energy by

$$\theta = \frac{S(S+1)}{3k_B}\sum_n z'_n J'_n, \tag{2.43}$$

where the sum extends over all the nearest neighbors of a given spin. J'_n represents the spin exchange constant related to the n^{th} neighbor, and z' shows the number of neighboring spins linked to the given spin through J'_n [62]. In a magnetic material, θ establishes the energy scale of the magnetic interactions as it is the algebraic sum of the Js in that magnetic system. If $\theta = 0$, the material is paramagnetic, has no spin-spin correlations, and its spin orientations are random. However, at temperature $T \sim |\theta|$ and provided that there is no magnetic frustration, the system begins to deviate from the CW law and exhibits a long-range order close to $|\theta|$. The sign of θ shows the net exchange interaction: either $\theta > 0$ indicates a dominant FM exchange interaction, or $\theta < 0$ manifests a dominant AFM exchange interaction.

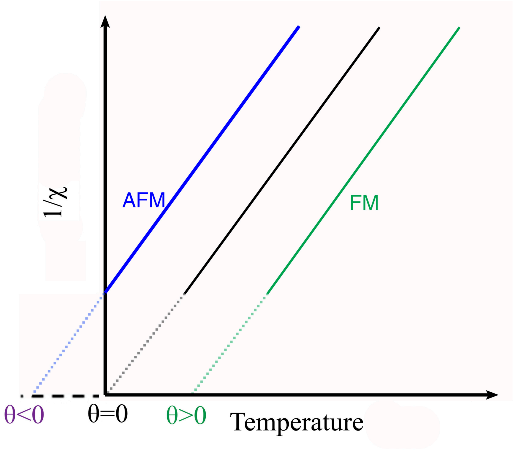

Figure 2.4 – The temperature dependence of the inverse of magnetic susceptibility. Intersection of $1/\chi(T)$ and the positive or the negative part of the temperature axis indicates respectively dominant FM or AFM interactions.

As shown in Fig. 2.4, by plotting the inverse of susceptibility as a function of temperature, $1/\chi(T)$, and fitting it to the CW law, θ is obtained by the intersect on the temperature axis. Large exchange interactions can be obtained if there is a substantial deviation of the $1/\chi(T)$ plot in the low temperatures from the linear CW law at high temperatures. By decreasing the temperature until $T_c \sim |\theta|$, the paramagnetic states become less stable than some ordered states. Based on the MF theory for ferromagnetism, the approximate ratio of $|\theta|/T_c \sim 1$ indicates a transition to a long-range ordered state, in which T_c is the critical temperature [65]. Nevertheless, in the case of antiferromagnetism, this ratio is more complicated and dependent on the magnetic structure of the system. An arbitrary condition was suggested as a criterion for a system to show spin-frustration if $|\theta|/T_N > 6$, where T_N is the Neel temperature below which a 3D AFM ordering occurs [62]. Spin frustration happens in some magnetic materials having particular lattice structures. The magnetic moments in the lattice structure of a frustrated magnet are arranged in such a way that simultaneous minimization of the energies of all the magnetic exchange interactions is not possible, and hence, a long-range magnetic order may not happen. As the temperature drops towards zero in a frustrated magnet, spin fluctuations can be caused due to the occurrence of a high number of low-energy states [66]. However, a 3D long-range order can occur in the low-temperature magnetic ground state of a magnet provided that there is no compelling spin frustration and that the magnetic moments are interacting in three directions [65].

2.6.1 Magnetic specific heat and entropy

Specific heat as a function of temperature can provide us with information regarding the phase transitions in a magnetic material at low temperatures. Evidence for the existence of a 3D long-range AFM order in a magnetic material is a sharp λ-like peak in the specific heat as a function of temperature. In general, the specific heat consists of different contributions such as of phonons (i.e., vibrations of the lattice), spins, and conduction electrons. But in insulating magnets, the electronic contribution can be ignored, and only the phonon contribution needs to be subtracted from the total specific heat. The phonon contribution C_{ph} can be determined by the Debye model [67] from which the general form at low temperatures is given by the following integral

$$C_{\mathrm{ph}} = 9Nk_B \left(\frac{T}{\Theta_D} \right)^3 \int_0^{\frac{\Theta_D}{T}} \frac{x^4 e^x}{(e^x - 1)^2} dx, \tag{2.44}$$

where $x = \frac{\hbar\omega}{k_B T}$, and Θ_D is known as the Debye temperature [68]. Usually, an approximated version of this Debye model is used at even lower temperatures, $T \ll \frac{\Theta_D}{10}$, as

$$C_{\mathrm{ph}} = \frac{12\pi^4 N k_B}{5} \left(\frac{T}{\Theta_D} \right)^3, \tag{2.45}$$

which is known as Debye-T^3 law.

Bear in mind that a broad maximum in a magnetic specific heat is an anomaly known as Schottky anomaly, and is different than the phase transition identified by a sharp peak. A Schottky anomaly in the specific heat is observed for a system containing multiple discrete energy levels. For the simplest case with two levels, at very high temperatures both states are identically occupied following the Boltzmann distribution, and hence it is difficult to alter the energy of the system. At very low temperatures, it is hard to change the energy of the system because all the magnetic moments are aligned with the applied magnetic field, and the energy is insufficient to excite transitions from the ground state [56]. However, at the $k_B T \sim \mu_B B$ temperature, the transitions between two quantum states become possible, and the Schottky anomaly occurs. The specific heat of a Schottky anomaly is given by

$$C_{Sh} = Nk_B \frac{e^{\Delta_\varepsilon/T}}{(1 + e^{\Delta_\varepsilon/T})^2} \left(\frac{\Delta_\varepsilon}{T} \right)^2, \tag{2.46}$$

where Δ_ε is the energy between the two levels. Another parameter of magnetic ordering is magnetic entropy. Entropy, given by $S = -(\partial F/\partial T)_B$, measures the disorder in a system. A lowering of the temperature decreases the magnetic entropy, which increases the ordering of spins in a magnetic material. At high temperatures, the magnetic entropy amounts to the total entropy of a paramagnetic system of spins S, given by $S_{mag} = Rln(2S + 1)$, where $R = 8.314$ J/mol K. Experimentally, the magnetic entropy change is obtained by the integral of the measured magnetic specific heat as a function of temperature as

$$S_{mag} = \int \frac{C_{mag}}{T} dT. \tag{2.47}$$

2.7 Magnetization of non-interacting dimers

Applying an external magnetic field (B) results in three Zeeman split levels for the energy level corresponding to the triplet state, E_T in Eq. (2.14). However, the singlet state, E_S in Eq. (2.14) is unaffected by the magnetic field. So, the energy of different states of the dimer system with Zeeman splitting is given by

$$\begin{aligned} E_S(S=0, S_z=0) &= -\frac{3}{4}J \\ E_T(S=1, S_z=-1) &= \frac{1}{4}J + g\mu_B B, \\ E_T(S=1, S_z=0) &= \frac{1}{4}J, \\ E_T(S=1, S_z=1) &= \frac{1}{4}J - g\mu_B B. \end{aligned} \tag{2.48}$$

As shown in Fig. 2.5, there is an energy gap between the singlet ground state and the lowest excited triplet state of a spin dimer with an AFM spin couplings J. The S_z branch of the triplet state decreases linearly when applying magnetic field due to the Zeeman effect. In weak applied magnetic fields, the energy of the lowest level of the triplet state, $S_z = 1$, is still higher than the energy of the singlet ground state. As illustrated in Fig. 2.5(a), at temperatures lower than a given critical temperature, the thermal energy is not sufficient to populate the $S_z = 1$ level, and in turn, the AFM spin dimer is a spin-gapped system. However, by increasing the external magnetic field until reaching a critical field, B_c, the $S_z = 1$ level of the triplet state crosses the singlet state, as shown in Fig. 2.5(b). The intersection between the $S_z = 1$ of triplet excited state and the singlet-ground state occurring at B_c leads to the degeneracy of the two levels. In that case, the spin dimer system acts as an integer-spin ($S = 1$) system, in which the spin dimers can occupy the same lowest-energy quantum state which provides the magnetic realization of the Bose-Einstein Condensate (BEC). So, in spite of the fact that the spin dimers are not interacting, the magnetic system undergoes a 3D long-range order. Consequently, the applied magnetic field closes the magnetic energy gap and then it induces magnetic long-rang order. To study the behavior of the magnetization of such an AFM spin dimer, first the partition function of the system is evaluated. The partition function is obtained for its total number of spins, N, by using Eq. (2.26), as such

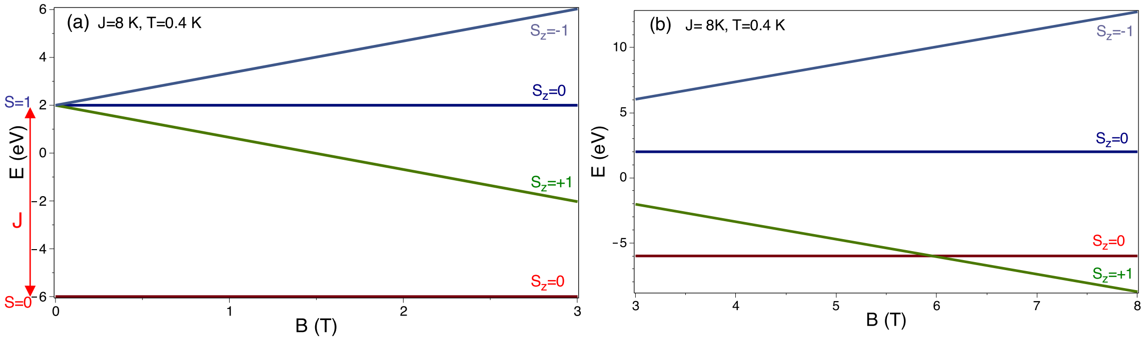

Figure 2.5 – The energy spectrum of a spin dimer with two S=1/2 spins and an AFM spin exchange $J = 8$ K in Eq. (2.48) at T=0.4 K under (a) a weak applied magnetic field, and (b) a strong applied magnetic field.

$$\begin{aligned} Z &= \left[e^{\frac{3}{4}\beta J} + e^{-\frac{1}{4}\beta J}(e^{\beta g \mu_B B} + 1 + e^{-\beta g \mu_B B})\right]^N, \\ &= \left[e^{\frac{3}{4}\beta J} + e^{-\frac{1}{4}\beta J}(1 + 2\cosh(\beta g \mu_B B))\right]^N. \end{aligned} \tag{2.49}$$

Subsequently, the free energy of the system is obtained through Eq. (2.25)

$$F = -N\frac{1}{\beta} ln[e^{\frac{3}{4}\beta J} + e^{-\frac{1}{4}\beta J}(1 + 2\cosh(\beta g \mu_B B))]. \tag{2.50}$$

Finally, the magnetization of the system of non-interacting dimers is reached by substituting the F in Eq. (2.24) with the free energy of the system in Eq. (2.50):

$$M = \frac{N}{V}\frac{2g\mu_B(\sinh(\beta g \mu_B B))}{e^{\beta J} + (1 + 2\cosh(\beta g \mu_B B))}. \tag{2.51}$$

In Fig. 2.6, the magnetization of the aforementioned spin dimer, as a function of applied magnetic field based on Eq. (2.51), is shown for different temperatures. In general, the horizontal region of the magnetization as a function of an applied magnetic field is called the magnetization plateau. As illustrated in Fig. 2.6, the magnetization of the spin dimer at very low temperatures is zero until it reaches a critical applied field, B_c. The region of $B < B_c$ with $M = 0$ is called the zero magnetization plateau. The $B < B_c$ region in Fig. 2.5 indicates the area where the system cannot reach the lowest excited triplet state. But by augmenting the applied magnetic field larger than the critical field, $B > B_c$, the magnetization gradually increases until it attains a saturation magnetization, M_{sat} at 1 μ_B.

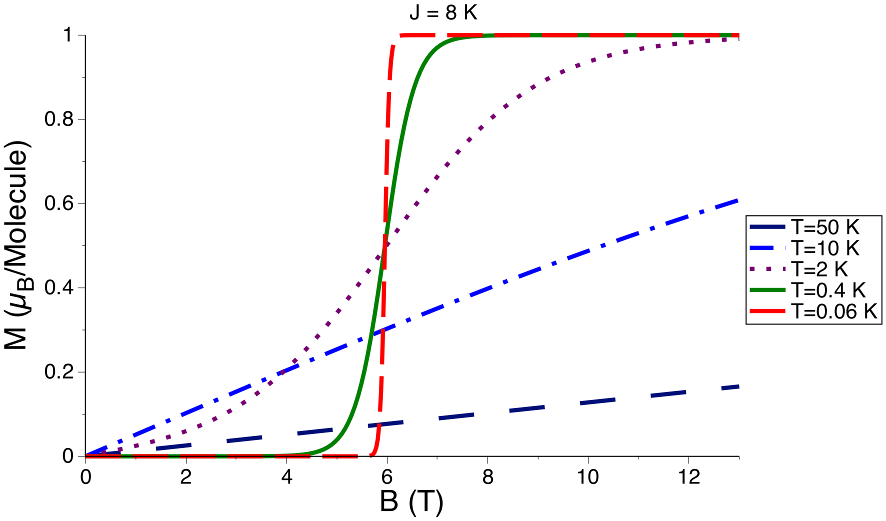

Figure 2.6 – Magnetization of an AFM S=1/2 spin dimer in Eq. (2.51) for J=8 K shown as a function of the applied magnetic field at various temperatures.

2.8 Spin tetramer

As the energy spectrum and magnetization of non-interacting dimers are understood, the concept can be applied to obtain the energy levels and the magnetization of larger magnetic units such as spin tetramers. We will now discuss spin tetramers as a backdrop for explaining the experimental data of NIT2Py.

2.8.1 Energy of different states in a spin tetramer

A spin tetramer magnetic unit consists of four interacting spin angular momenta, $\boldsymbol{S}_1$, $\boldsymbol{S}_2$, $\boldsymbol{S}_3$, and $\boldsymbol{S}_4$, in which the total spin of the system is written as $\boldsymbol{S} = \boldsymbol{S}_1 + \boldsymbol{S}_2 + \boldsymbol{S}_3 + \boldsymbol{S}_4$. Exchange coupling constant J_1 is associated to the interaction between $\boldsymbol{S}_1$ and $\boldsymbol{S}_2$, and between $\boldsymbol{S}_3$ and $\boldsymbol{S}_4$, whereas J_2 is related to the interaction between $\boldsymbol{S}_2$ and $\boldsymbol{S}_3$, as shown in Fig. 2.1(b). As based on a given number of spins, the total number of states as well as the number of singlet, triplet, and other states in a spin system can be determined. For example, by adding four $S = \frac{1}{2}$ spins in a tetramer, the numbers between $S = S_1 + S_2$ and $|S_2 - S_1|$ in integer steps give the spin S as 1, 0, 1, 0. Adding up those spins yields S as 2, 1, 0, 1, 1, 0, which translates into two singlets ($S = 0$), three triplets ($S = 1$), and one quintuplet ($S = 2$). Then, by multiplying the number of multiplicity of a certain state to $(2S + 1)$ and by summing up the results, the total number of states in a tetramer is $2 \times (2 \times 0 + 1) + 3 \times (2 \times 1 + 1) + 1 \times (2 \times 2 + 1) = 16$.

The Hamiltonian of the spin tetramer is given by

$$H = J_1(\boldsymbol{S}_1 \cdot \boldsymbol{S}_2 + \boldsymbol{S}_3 \cdot \boldsymbol{S}_4) + J_2(\boldsymbol{S}_2 \cdot \boldsymbol{S}_3), \tag{2.52}$$

where the scalar product between the spins can be written the same way as in Eq. (2.8), which results in

$$\begin{aligned} H = J_1[\frac{1}{2}(S_{1+}S_{2-} + S_{1-}S_{2+}) + S_{1z}S_{2z} + \frac{1}{2}(S_{3+}S_{4-} + S_{3-}S_{4+}) + S_{3z}S_{4z}] \\ +J_2(\frac{1}{2}(S_{2+}S_{3-} + S_{2-}S_{3+}) + S_{2z}S_{3z}). \end{aligned} \tag{2.53}$$

Because each of these four spins in a spin tetramer can take two values, spin up or down, the total number of states is $4^2 = 16$. Therefore, a 16×16 matrix needs to be diagonalized in order to acquire the eigenvalues of the different states of the system as given in Eq. (2.54).

$$\begin{pmatrix} \langle 1|H|1\rangle & \langle 1|H|2\rangle & \langle 1|H|3\rangle & \cdots & \langle 1|H|16\rangle \\ \langle 2|H|1\rangle & \langle 2|H|2\rangle & \langle 2|H|3\rangle & \cdots & \langle 2|H|16\rangle \\ \vdots & \vdots & \vdots & \ddots & \vdots \\ \langle 16|H|1\rangle & \langle 16|H|2\rangle & \langle 16|H|3\rangle & \cdots & \langle 16|H|16\rangle \end{pmatrix}_{16\times 16}, \tag{2.54}$$

where those 16 different states are $|1\rangle$=$|+,+,+,+\rangle$, $|2\rangle$=$|+,+,+,-\rangle$, $|3\rangle$=$|+,+,-,+\rangle$, $|4\rangle$=$|+,-,+,+\rangle$, $|5\rangle$=$|-,+,+,+\rangle$, $|6\rangle$=$|+,+,-,-\rangle$, $|7\rangle$=$|+,-,+,-\rangle$, $|8\rangle$=$|+,-,-,+\rangle$, $|9\rangle$=$|-,+,+,-\rangle$, $|10\rangle$=$|-,+,-,+\rangle$, $|11\rangle$=$|-,-,+,+\rangle$, $|12\rangle$=$|+,-,-,-\rangle$, $|13\rangle$=$|-,+,-,-\rangle$, $|14\rangle$=$|-,-,+,-\rangle$, $|15\rangle$=$|-,-,-,+\rangle$, $|16\rangle$=$|-,-,-,-\rangle$.

To calculate each component of the matrix of Eq. (2.54), the Hamiltonian of Eq. (2.53) must first act on each of those 16 states. For example, to calculate the element in the first column of the first row, $\langle 1|H|1\rangle$, the Hamiltonian acts on the state $|+,+,+,+\rangle$ as

$$\begin{aligned} H\,|+,+,+,+\rangle &= J_1[(\frac{1}{2}(0)+\frac{1}{4}\,|+,+,+,+\rangle)+(\frac{1}{2}(0)+\frac{1}{4}\,|+,+,+,+\rangle)] \\ &\quad +J_2((\frac{1}{2}(0)+\frac{1}{4}\,|+,+,+,+\rangle)) = (\frac{1}{2}J_1+\frac{1}{4}J_2)\,|+,+,+,+\rangle). \end{aligned} \tag{2.55}$$

Then, $\langle 1|H|1\rangle$=$\frac{1}{2}J_1+\frac{1}{4}J_2$. All the remaining elements of the matrix are derived using the same method and those derivations can be consulted in Annex II. Consequently, the resulted matrix is given in Eq. (2.57).

$$\begin{pmatrix}
\tfrac12 J_1+\tfrac14 J_2 & 0 & 0 & 0 & 0 & 0 & 0 & 0 & 0 & 0 & 0 & 0 & 0 & 0 & 0 & 0 \\
0 & \tfrac14 J_2 & \tfrac12 J_1 & 0 & 0 & 0 & 0 & 0 & 0 & 0 & 0 & 0 & 0 & 0 & 0 & 0 \\
0 & \tfrac12 J_1 & -\tfrac14 J_2 & \tfrac12 J_2 & 0 & 0 & 0 & 0 & 0 & 0 & 0 & 0 & 0 & 0 & 0 & 0 \\
0 & 0 & \tfrac12 J_2 & -\tfrac14 J_2 & \tfrac12 J_1 & 0 & 0 & 0 & 0 & 0 & 0 & 0 & 0 & 0 & 0 & 0 \\
0 & 0 & 0 & \tfrac12 J_1 & \tfrac14 J_2 & 0 & 0 & 0 & 0 & 0 & 0 & 0 & 0 & 0 & 0 & 0 \\
0 & 0 & 0 & 0 & 0 & \tfrac12 J_1-\tfrac14 J_2 & \tfrac12 J_2 & 0 & 0 & 0 & 0 & 0 & 0 & 0 & 0 & 0 \\
0 & 0 & 0 & 0 & 0 & \tfrac12 J_2 & -\tfrac12 J_1-\tfrac14 J_2 & \tfrac12 J_1 & \tfrac12 J_1 & 0 & 0 & 0 & 0 & 0 & 0 & 0 \\
0 & 0 & 0 & 0 & 0 & 0 & \tfrac12 J_1 & -\tfrac12 J_1+\tfrac14 J_2 & 0 & \tfrac12 J_1 & 0 & 0 & 0 & 0 & 0 & 0 \\
0 & 0 & 0 & 0 & 0 & 0 & \tfrac12 J_1 & 0 & -\tfrac12 J_1+\tfrac14 J_2 & \tfrac12 J_1 & 0 & 0 & 0 & 0 & 0 & 0 \\
0 & 0 & 0 & 0 & 0 & 0 & 0 & \tfrac12 J_1 & \tfrac12 J_1 & -\tfrac12 J_1-\tfrac14 J_2 & \tfrac12 J_2 & 0 & 0 & 0 & 0 & 0 \\
0 & 0 & 0 & 0 & 0 & 0 & 0 & 0 & 0 & \tfrac12 J_2 & \tfrac12 J_1-\tfrac14 J_2 & 0 & 0 & 0 & 0 & 0 \\
0 & 0 & 0 & 0 & 0 & 0 & 0 & 0 & 0 & 0 & 0 & \tfrac14 J_2 & \tfrac12 J_1 & 0 & 0 & 0 \\
0 & 0 & 0 & 0 & 0 & 0 & 0 & 0 & 0 & 0 & 0 & \tfrac12 J_1 & -\tfrac14 J_2 & \tfrac12 J_2 & 0 & 0 \\
0 & 0 & 0 & 0 & 0 & 0 & 0 & 0 & 0 & 0 & 0 & 0 & \tfrac12 J_2 & -\tfrac14 J_2 & \tfrac12 J_1 & 0 \\
0 & 0 & 0 & 0 & 0 & 0 & 0 & 0 & 0 & 0 & 0 & 0 & 0 & \tfrac12 J_1 & \tfrac14 J_2 & 0 \\
0 & 0 & 0 & 0 & 0 & 0 & 0 & 0 & 0 & 0 & 0 & 0 & 0 & 0 & 0 & \tfrac12 J_1+\tfrac14 J_2
\end{pmatrix}. \tag{2.56}$$

The diagonalization of the matrix in Eq. (2.57) yields 16 eigenvalues: two are non-degenerate and related to two singlet states (E_{S1} and E_{S2}) with a total spin of $S = 0$; three are three-fold degenerate and associated to three triplet states (E_{T1}, E_{T2}, and E_{T3}) with a total spin of $S = 1$; and one is five-fold degenerate and corresponds to a quintuplet (E_{Q1}) with a total spin of $S = 2$.

Those two singlets, three triplets, and one quintuplet states are given as

$$\begin{aligned}
E_{S1} &= -\frac{1}{2}J_1 - \frac{1}{4}J_2 + \frac{1}{2}\sqrt{4J_1^2 - 2J_1J_2 + J_2^2)}, \\
E_{S2} &= -\frac{1}{2}J_1 - \frac{1}{4}J_2 - \frac{1}{2}\sqrt{4J_1^2 - 2J_1J_2 + J_2^2)}, \\
E_{T1} &= -\frac{1}{2}J_1 + \frac{1}{4}J_2, \\
E_{T2} &= -\frac{1}{4}J_2 + \frac{1}{2}\sqrt{J_1^2 + J_2^2}, \\
E_{T3} &= -\frac{1}{4}J_2 - \frac{1}{2}\sqrt{J_1^2 + J_2^2}, \\
E_{Q1} &= \frac{1}{2}J_1 + \frac{1}{4}J_2.
\end{aligned} \tag{2.57}$$

2.8.2 Magnetization of non-interacting Tetramer

In the presence of an external magnetic field, the triplet and quintuplet states in Eq. (2.57) of a spin tetramer system with four *S*=1/2 spins and two AFM exchange couplings undergo Zeeman splitting. So, each of the three triplet states splits into three levels, and the quintuplet state into five levels. However, the two singlet states stay unaffected. The energy of each of those 16 levels is given by

$$\begin{aligned}
E_{S1}(S=0,S_z=0) &= -\frac{1}{2}J_1-\frac{1}{4}J_2+\frac{1}{2}\sqrt{4J_1^2-2J_1J_2+J_2^2}),\\
E_{S2}(S=0,S_z=0) &= -\frac{1}{2}J_1-\frac{1}{4}J_2-\frac{1}{2}\sqrt{4J_1^2-2J_1J_2+J_2^2}),\\
E_{T1,1}(S=1,S_z=-1) &= -\frac{1}{2}J_1+\frac{1}{4}J_2+g\mu_BB,\\
E_{T1,2}(S=1,S_z=0) &= -\frac{1}{2}J_1+\frac{1}{4}J_2,\\
E_{T1,3}(S=1,S_z=+1) &= -\frac{1}{2}J_1+\frac{1}{4}J_2-g\mu_BB,\\
E_{T2,1}(S=1,S_z=-1) &= -\frac{1}{4}J_2+\frac{1}{2}\sqrt{J_1^2+J_2^2}+g\mu_BB,\\
E_{T2,2}(S=1,S_z=0) &= -\frac{1}{4}J_2+\frac{1}{2}\sqrt{J_1^2+J_2^2},\\
E_{T2,3}(S=1,S_z=+1) &= -\frac{1}{4}J_2+\frac{1}{2}\sqrt{J_1^2+J_2^2}-g\mu_BB,\\
E_{T3,1}(S=1,S_z=-1) &= -\frac{1}{4}J_2-\frac{1}{2}\sqrt{J_1^2+J_2^2}+g\mu_BB,\\
E_{T3,2}(S=1,S_z=0) &= -\frac{1}{4}J_2-\frac{1}{2}\sqrt{J_1^2+J_2^2},\\
E_{T3,3}(S=1,S_z=+1) &= -\frac{1}{4}J_2-\frac{1}{2}\sqrt{J_1^2+J_2^2}-g\mu_BB,\\
E_{Q1,1}(S=2,S_z=-2) &= \frac{1}{2}J_1+\frac{1}{4}J_2+2g\mu_BB,\\
E_{Q1,2}(S=2,S_z=-1) &= \frac{1}{2}J_1+\frac{1}{4}J_2+g\mu_BB,\\
E_{Q1,3}(S=2,S_z=0) &= \frac{1}{2}J_1+\frac{1}{4}J_2,\\
E_{Q1,4}(S=2,S_z=+1) &= \frac{1}{2}J_1+\frac{1}{4}J_2-g\mu_BB,\\
E_{Q1,5}(S=2,S_z=+2) &= \frac{1}{2}J_1+\frac{1}{4}J_2-2g\mu_BB. \qquad (2.58)
\end{aligned}$$

In Fig. 2.7(a), the energy levels of Eq. (2.58) corresponding to the two $S=0$ singlet states, three Zeeman split levels ($S_z=-1$, $S_z=0$, and $S_z=1$) of each of the three $S=1$ spin triplets, as well as the five Zeeman split levels ($S_z=-2$, $S_z=-1$, $S_z=0$, $S_z=1$, and $S_z=2$) of an $S=2$ quintuplet of a spin tetramer with two AFM spin couplings of J_1 =4 K and J_2=8 K are shown at T=0.4 K. The lowest excited triplet state has a

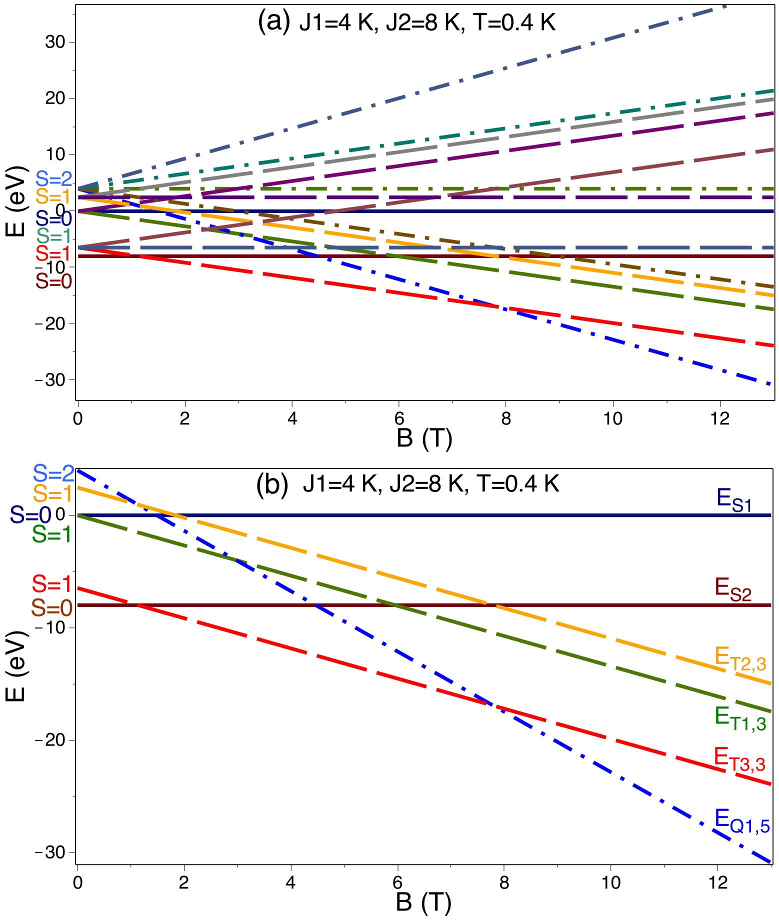

Figure 2.7 – Influence of applied magnetic field on the energy levels of a spin tetramer in Eq. (2.58) with AFM couplings J_1=4 K and J_2=8 K at a very low temperature of 0.4 K. (a) Energy levels of the two S=0 singlet states, the three S=1 triplet states each including three Zeeman split levels, and the energy of the quintuplet state with five Zeeman split levels as given in Eq. (2.58). (b) Evolution of the lowest-energy spin levels of the singlets, triplets, and quintuplet states with applied magnetic field.

gap above the singlet ground state. That lowest excited triplet state has an energy gap relative to the quintuplet excited state. For the sake of clarity, only the lowest Zeeman split level of each of the two singlets, three triplets, and the quintuplet states is exhibited in Fig. 2.7(b). In the presence of an applied magnetic field, the lowest branches, $S_z = 1$ levels, of the three triplet states and the $S_z = 1$ and $S_z = 2$ levels of the quintuplet state decrease linearly as a consequence of the Zeeman effect. At the first critical field of B_{c1}, the $S_z = 1$ level of the lowest-energy triplet state with the energy $E_{T3,3}$ crosses the singlet ground state, and therefore closes the zero-field gap between them. By increasing the applied magnetic field up to a second critical field of B_{c2}, the $S_z = 2$ level of the quintuplet state with $E_{Q1,5}$ intersects with the $S_z = 1$ level of the lowest-energy triplet state having $E_{T3,3}$. As a consequence, the zero-field spin gap between them is closed. For $B > B_{c2}$, the $S_z = 2$ level of the quintuplet state becomes lower in energy than the $S_z = 1$ level of the lowest-energy triplet state. Therefore, the spin tetramer system acts like a BEC system with integer-spin $S = 2$ in which the spin tetramers can occupy the same lowest-energy quantum state.

In the next step, the effect of the external magnetic field on the magnetization of a spin tetramer system is studied. Considering the energies of those 16 states, the partition function of the system with N spins can be obtained through Eq. (2.26) as

$$\begin{aligned}
Z = [&e^{-\beta(-\frac{1}{2}J_1-\frac{1}{4}J_2)}(e^{-\frac{\beta}{2}\sqrt{4J_1^2-2J_1J_2+J_2^2}}+e^{\frac{\beta}{2}\sqrt{4J_1^2-2J_1J_2+J_2^2}})\\
&+e^{-\beta(-\frac{1}{2}J_1+\frac{1}{4}J_2)}(e^{\beta g\mu_B B}+1+e^{-\beta g\mu_B B})\\
&+e^{-\beta(-\frac{1}{4}J_2+\frac{1}{2}\sqrt{J_1^2+J_2^2})}(e^{\beta g\mu_B B}+1+e^{-\beta g\mu_B B})\\
&+e^{-\beta(-\frac{1}{4}J_2-\frac{1}{2}\sqrt{J_1^2+J_2^2})}(e^{\beta g\mu_B B}+1+e^{-\beta g\mu_B B})\\
&+e^{-\beta(\frac{1}{2}J_1+\frac{1}{4}J_2)}(e^{2\beta g\mu_B B}+e^{\beta g\mu_B B}+1+e^{-\beta g\mu_B B}+e^{-2\beta g\mu_B B})]^N,
\end{aligned}\tag{2.59}$$

which can be simplified to

$$\begin{aligned}
Z = [&e^{-\beta(-\frac{1}{2}J_1-\frac{1}{4}J_2)}(2\cosh(\frac{\beta}{2}\sqrt{4J_1^2-2J_1J_2+J_2^2}))\\
&+(1+2\cosh(\beta g\mu_B B))\left(e^{-\beta\frac{1}{4}J_2}(e^{\beta\frac{1}{2}J_1}+e^{-\beta\frac{1}{2}J_1})+e^{\beta\frac{1}{4}J_2}(e^{\beta\frac{1}{2}\sqrt{J_1^2+J_2^2}}+e^{-\beta\frac{1}{2}\sqrt{J_1^2+J_2^2}})\right)\\
&+e^{-\beta(\frac{1}{2}J_1+\frac{1}{4}J_2)}2\cosh(2\beta g\mu_B B))]^N.
\end{aligned}\tag{2.60}$$

By using the relation $e^x + e^{-x} = 2\cosh x$, Eq. (2.61) leads to

$$\begin{aligned}Z = {} & [e^{-\beta(-\frac{1}{2}J_1 - \frac{1}{4}J_2)}(2\cosh(\frac{\beta}{2}\sqrt{4J_1^2 - 2J_1J_2 + J_2^2})) \\ & + (1 + 2\cosh(\beta g\mu_B B))\left(e^{-\beta\frac{1}{4}J_2}(2\cosh(\beta\frac{1}{2}J_1)) + e^{\beta\frac{1}{4}J_2}(2\cosh(\beta\frac{1}{2}\sqrt{J_1^2 + J_2^2}))\right) \\ & + e^{-\beta(\frac{1}{2}J_1 + \frac{1}{4}J_2)}2\cosh(2\beta g\mu_B B))]^N. \end{aligned} \tag{2.61}$$

Finally, the partition function can be written as

$$Z = [A_1' + A_2'(1 + 2\cosh(\beta g\mu_B B)) + A_3' 2\cosh(2\beta g\mu_B B)]^N, \tag{2.62}$$

where, A_1', A_2', and A_3' are given by

$$\begin{aligned} A_1' &= e^{-\beta(-\frac{1}{2}J_1 - \frac{1}{4}J_2)}2\cosh(\frac{\beta}{2}\sqrt{4J_1^2 - 2J_1J_2 + J_2^2}), \\ A_2' &= e^{-\beta\frac{1}{4}J_2}2\cosh(\beta\frac{1}{2}J_1) + e^{\beta\frac{1}{4}J_2}2\cosh(\beta\frac{1}{2}\sqrt{J_1^2 + J_2^2}), \\ A_3' &= e^{-\beta(\frac{1}{2}J_1 + \frac{1}{4}J_2)}. \end{aligned} \tag{2.63}$$

Subsequently, the free energy can be obtained by substituting the Z in Eq. (2.25) with the partition function in Eq. (2.63)

$$F = -N\frac{1}{\beta}\ln[A_1' + A_2'(1 + 2\cosh(\beta g\mu_B B)) + A_3' 2\cosh(2\beta g\mu_B B)]. \tag{2.64}$$

Eventually, the magnetization of the non-interacting spin tetramer system can be obtained based on Eq. (2.24) as

$$M = \frac{N}{V}\frac{2g\mu_B\left[A_2'\sinh(\beta g\mu_B B) + 2A_3'\sinh(2\beta g\mu_B B)\right]}{A_1' + A_2'(1 + 2\cosh(\beta g\mu_B B)) + 2A_3'\cosh(2\beta g\mu_B B))}. \tag{2.65}$$

In Fig. 2.8, magnetization as a function of the external magnetic field of a system of non-interacting spin tetramers with two AFM exchange couplings J_1=4 K and J_2=8 K, is shown at various temperatures. At high temperatures, when the applied field is increased, the magnetization also increases in a roughly linear fashion. Additionally, the saturation

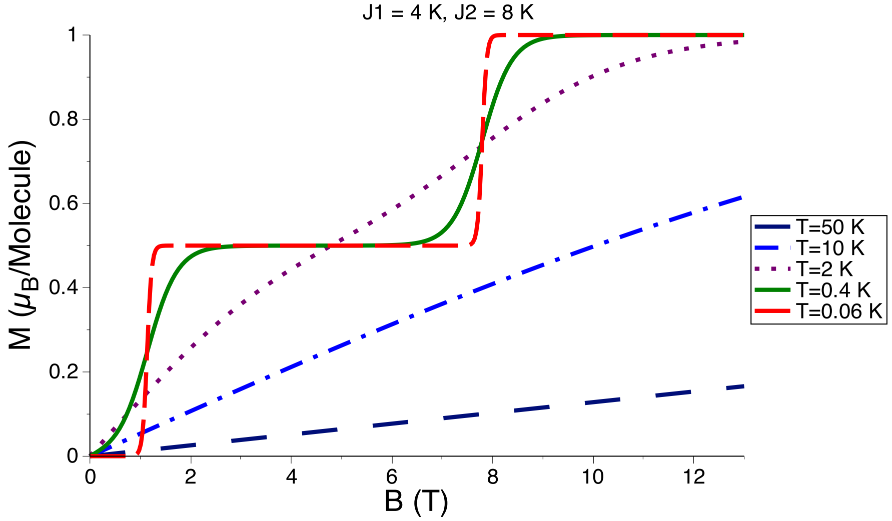

Figure 2.8 – The magnetic field dependence of magnetization of a non-interacting spin tetramer system based on Eq. (2.65) shown at different temperatures for two AFM couplings J_1=4 K and J_2=8 K. The system shows a finite magnetization plateau at 1/2 μ_B.

magnetization at high temperatures, such as at 50 K, is not obtained even at 13 T. On the other hand, when the temperature is lowered, for instance at 2 K, the magnetization increase is no longer linear, and the saturation is attained at approximately 13 T.

Much like what the dimer system showed at temperatures close to 0 K, there are two regions where magnetization stays constant in a finite range of applied magnetic fields. In the first region, $B < B_{c1}$, the magnetization stays at zero; the zero magnetization $M_z = 0$ plateau. The second region, $B > B_{c2}$, where the magnetization saturates at 1 μ_B, is $M_z = 1$ plateau. Also, two other regions exhibit increasing magnetization in magnetic field: the first occurs at B_{c1} where the $S_z = 1$ level of the lowest-energy triplet state crosses the singlet ground state, as seen in Fig. 2.7(b); the second region is at B_{c2} where the $S_z = 2$ level of the quintuplet state passes the $S_z = 1$ level of the lowest-energy triplet state.

As will be discussed in section 2.11 on mapping the spin system onto a system of hared-core bosons, a constant magnetization in a finite range of applied magnetic field points to a constant number of bosons in each site. So, the zero magnetization plateau corresponds to an empty boson in each site, and the $M_z = 1$ plateau, to one boson in each site. In general, intermediate plateaux can appear at half-integer values of the saturation magnetization, and are associated to fractional boson fillings such as 1/8, 1/4, 1/3, and 1/2 [69–71]. In the case of the spin tetramer in Fig. 2.8, there is a magnetization plateau at half-integer value of the saturation magnetization between two critical fields, $B_{c1} < B < B_{c2}$, which is called a 1/2 magnetization plateau.

2.9 Bringing the interactions into play through mean-field theory

Mean-field (MF) theory can be used to study a complex system including all the possible interactions between its magnetic units. In the MF approach, all the interactions with a subsystem of an infinite lattice can be replaced by an effective MF. The subsystem can be an individual spin or a group of spins such as a spin dimer or a spin tetramer. To reach this objective, the model Hamiltonian is written based on the Ising model as

$$H = J' \sum_{\langle i,j \rangle} S_i S_j - g\mu_B \sum_i S_i B, \tag{2.66}$$

where the S_i and S_j are the Ising spins with magnitudes of $+1$ or -1. The exchange interaction with the nearest neighbours is shown by J', where $J' > 0$ indicates an AFM interaction and $J' < 0$ a FM interaction. Note that the summation avoids double-counting interactions and goes over the pairs of nearest neighbouring spins on sites i and j in the lattice. The spin for each site is [72]

$$S_i = \langle S_i \rangle + (S_i - \langle S_i \rangle), \tag{2.67}$$

which means that the spin of each site can be written as the sum of its mean value, $\langle S_i \rangle = m$, and the fluctuations, $\delta S_i = S_i - m$:

$$S_i = m + \delta S_i. \tag{2.68}$$

By substituting the S_i and S_j in Eq. (2.66) with Eq. (2.67), the model Hamiltonian can be written as

$$H = J' \sum_{\langle i,j \rangle} m^2 + m(S_i - m) + m(S_j - m) + \delta S_i \delta S_j - g\mu_B \sum_i S_i B. \tag{2.69}$$

Note that $\sum_{\langle i,j \rangle}$ can be replaced by $\frac{1}{2}\sum_i \sum_{NN}$, in which the coefficient 1/2 is to avoid the double-counting of interactions and NN is the nearest neighbours of i. If the number of nearest neighbours is defined as z', we have

$$H = J' \sum_i (z' m S_i - \frac{z'}{2} m^2) + m(S_j - m) + J' \sum_{\langle i,j \rangle} \delta S_i \delta S_j - g\mu_B \sum_i S_i B. \tag{2.70}$$

Here, the term $J' \sum_{\langle i,j \rangle} \delta S_i \delta S_j$ corresponds to the product of two fluctuation values. In MF approximation, that second order fluctuation is negligible and can be ignored. Thus, the model Hamiltonian can be approximated by an MF Hamiltonian, H_{MF} as

$$H_{MF} = J' \sum_i (z' m S_i - \frac{z'}{2} m^2) + m(S_j - m) - g\mu_B \sum_i S_i B. \tag{2.71}$$

By substituting the dimensionless mean value of spin in Eq. (2.71) with $m = \frac{M}{g\mu_B}$, where M is the magnetization with a dimension, one obtains

$$H_{MF} = g\mu_B \sum_i (J' z' \frac{M}{g^2 \mu_B^2} - B) S_i - N \frac{J' z'}{2} \frac{M^2}{g^2 \mu_B^2}. \tag{2.72}$$

The term in brackets is a combination of the MF produced by neighbouring spins, $J' z' \frac{M}{g^2 \mu_B^2}$, and the applied magnetic field, B. That combination is called an effective MF, h_{eff}, and is written as

$$h_{eff} = J' z' \frac{M}{g^2 \mu_B^2} - B. \tag{2.73}$$

In the following sections, the MF approach is used to include interactions between the magnetic units, such as spin dimers and tetramers.

2.9.1 Magnetization of interacting spin dimers

To study the magnetization of the interacting spin dimers, we must first take into account the energies of the singlet and triplet states of the non-interacting spin dimer in Eq. (2.14). Then, those energies can be written for interacting spin dimers by using the result of the MF Hamiltonian of Eq. (2.72) as

$$\begin{aligned}
E_S &= -\frac{3}{4}J - N\frac{J'z'}{2}\frac{M^2}{g^2\mu_B^2},\\
E_T &= \frac{1}{4}J - N\frac{J'z'}{2}\frac{M^2}{g^2\mu_B^2} - g\mu_B h_{eff},\\
E_T &= \frac{1}{4}J - N\frac{J'z'}{2}\frac{M^2}{g^2\mu_B^2},\\
E_T &= \frac{1}{4}J - N\frac{J'z'}{2}\frac{M^2}{g^2\mu_B^2} + g\mu_B h_{eff},
\end{aligned} \tag{2.74}$$

where J represents the intradimer exchange interaction, and J' is the exchange interaction of a given dimer with the nearest neighbours. As given in Eq. (2.73), h_{eff} includes the effect of the interdimer exchange interactions in the MF level. Those energies of singlet and triplet states of interacting dimers are used to determine the partition function of the system.

The partition function is written based on Eq. (2.26), in which the effect of the total number of N spins is taken into account as

$$Z = \left[e^{N\beta\frac{J'z'}{2}\frac{M^2}{g^2\mu_B^2}} \left(e^{\frac{3}{4}\beta J} + e^{-\frac{1}{4}\beta J} (e^{\beta g\mu_B h_{eff}} + e^{-\beta g\mu_B h_{eff}} + 1) \right) \right]^N . \tag{2.75}$$

By using h_{eff} from Eq. (2.73), and by taking into account the relation $e^x + e^{-x} = 2\cosh x$, the Eq. (2.75) can be written as

$$Z = \left[e^{N\beta\frac{J'z'}{2}\frac{M^2}{g^2\mu_B^2}} \left(e^{\frac{3}{4}\beta J} + e^{-\frac{1}{4}\beta J} \left(1 + 2\cosh\left(\beta g\mu_B \big(J'z'\frac{M}{g^2\mu_B^2} - B \big) \right) \right) \right) \right]^N . \tag{2.76}$$

Subsequently, the free energy of this system can be obtained based on Eqs. (2.25) and

(2.76) as

$$F=-N\frac{J'z'}{2}\frac{M^2}{g^2\mu_B^2}-N\frac{1}{\beta}\ln\left(e^{\frac{3}{4}\beta J}+e^{-\frac{1}{4}\beta J}\left(1+2\cosh\left(\beta g\mu_B\big(J'z'\frac{M}{g^2\mu_B^2}-B\big)\right)\right)\right). \tag{2.77}$$

Consequently, the magnetization of interacting spin dimers is given by substituting the free energy in Eq. (2.24) with Eq. (2.77) as

$$M=-\frac{N}{V}\frac{2g\mu_B\left(\sinh\left(\beta g\mu_B\big(J'z'\frac{M}{g^2\mu_B^2}-B\big)\right)\right)}{e^{\beta J}+\left(1+2\cosh\left(\beta g\mu_B\big(J'z'\frac{M}{g^2\mu_B^2}-B\big)\right)\right)}. \tag{2.78}$$

The magnetization of interacting dimers yielded from Eq. (2.78) is a function of M as well as an applied magnetic field, $M=f(M,B)$, and hence is a non-linear equation. That transcendental equation needs to be solved numerically in order to find the magnetization.

In Fig. 2.9, the magnetization as a function of applied magnetic field for a spin dimer with an AFM intradimer couplings of J=8 K, and AFM interdimer interactions of J'=4 K is shown at different temperatures. When interactions between dimers are introduced in the dimer system discussed in section 2.7, the triplet states disperse into a band of excitations, as shown in Fig. 2.10(a). The resulting magnetic energy gap of the system of interacting dimers, $J_{interdimer}$, is lower compared to the spin gap of a non-interacting dimer, J.

By increasing the applied magnetic field, the excitation energy of the $S_z=1$ level of the triplet state is decreased and intersects with the singlet ground state. For a system of interacting dimers, the intersection between the dispersed $S_z=1$ level of the triplet state, and the singlet state occurs at two critical fields, B_{c1} and B_{c2}, as shown in Fig. 2.10(a). For $B<B_{c1}$, the ground state is only composed of singlet states with zero magnetization. At B_{c1}, the lowest energy S_z=1 excitation of the triplet state and the singlet ground state are intersected resulting in a closing of the gap between those two states and in populat-

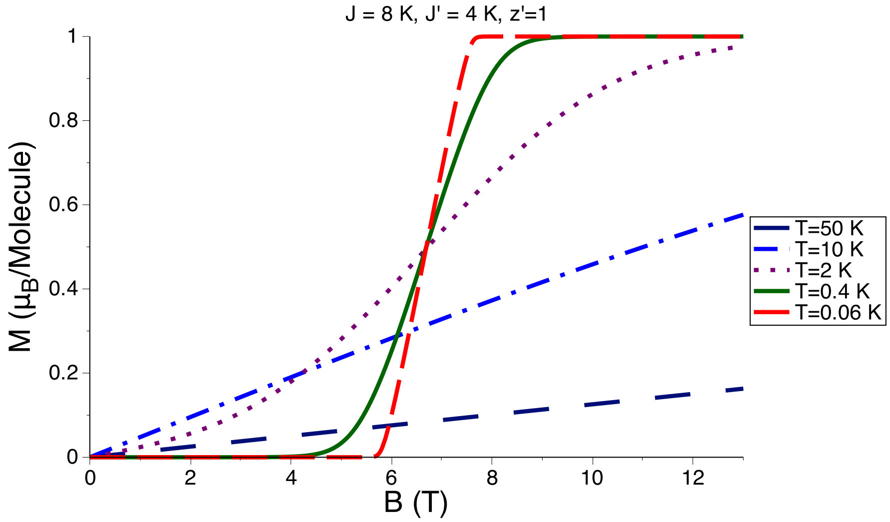

Figure 2.9 – The magnetic field dependence of the magnetization of an antiferromagnetically-coupled dimer system based on Eq. (2.78) shown at different temperatures for an AFM intradimer interaction of J=8 K, and the AFM interdimer interactions of J'=4 K.

ing the ground state with bosons. As bosons can condense in a BEC state, the result is the formation of the BEC of spin triplets, namely BEC of magnons or triplons. Note that the triplet bosonic excitations in an antiferromagnet with spin dimers are called triplons, which are similar to magnons (i.e., the quanta of magnetic excitations), and have the same quantum numbers. So, they are quasiparticles with integer-spin values that follow the bosonic statistics.

The condensate state in the spin language translates into the XY magnetic ordering [73] arising from the transverse spin components perpendicular to the direction of applied field, $\langle S_x \rangle$ and $\langle S_y \rangle$. Furthermore, the total magnetization, M_z, in the direction of the applied field, (i.e., canted XY-AFM ordering), stems from the longitudinal spin component, $\langle S_z \rangle$ [74]. In Fig. 2.10(c), the field-induced ordered phase inside of the $B_{c1} < B < B_{c2}$ region in the phase diagram is dome-shaped. At the first quantum critical point (QCP) at B_{c1}, there is a transition from a quantum paramagnetic phase with no ordering to a canted XY AFM phase with long-range magnetic ordering. The ordered phase continues until the second QCP at B_{c2}. As shown in Fig. 2.10(b), augmenting the applied field increases the magnetization M_z continuously inside the dome region as it

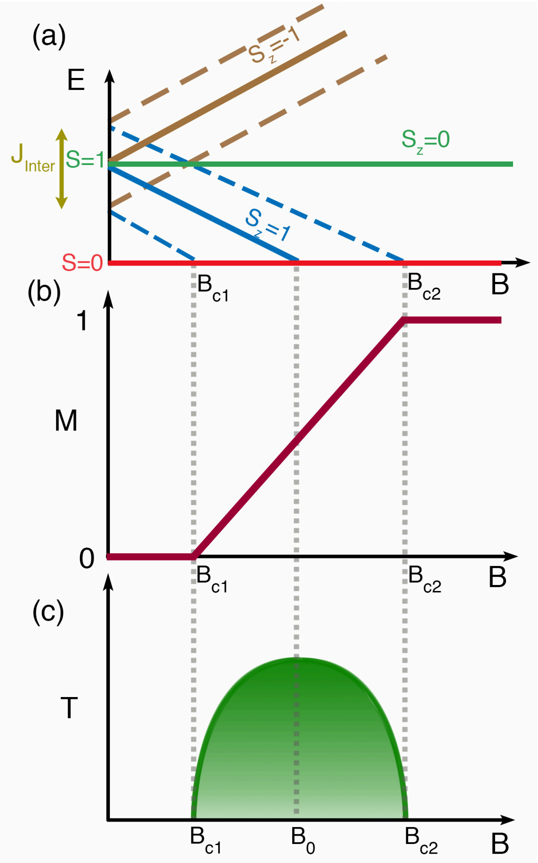

Figure 2.10 – (a) Illustration of the spin levels of the singlet and triplet states of a system of interacting dimers. By introducing the interdimer interactions, the levels are dispersed as bands that evolve in applied magnetic fields. (b) Magnetization as a function of the applied magnetic field at very low temperature. (c) The temperature-magnetic-field phase diagram showing a BEC region between two critical fields, B_{c1} and B_{c2}, where the lowest-energy triplet excitations intersect with the singlet ground state.

populates the ground state with more bosons. The center of the dome is at B_0, which is the field that maximizes the T_N and relates to a point with zero chemical potential $\mu = 0$. The dome is roughly symmetrical around B_0. It relates to the particle-hole symmetry of the mapped Hamiltonian in the bosonic language, as will be seen in section 2.11.

As magnetic moments tend to be polarized in the direction of the applied field, the more the applied field is augmented along the z axis, the more the XY magnetization decreases to B_{c2} where the ordered moment is destroyed ($M_{XY} = 0$) and the moments are completely aligned with the applied field along the z axis, as can be seen in Fig. 2.10(b).

For applied fields higher than B_{c2}, the ground state consists of one triplon per site, and there is a saturation magnetization [74].

Magnetic field-induced quantum phase transition and magnetic ordering have been observed in some non-organic quantum magnets with spin-gapped AFM dimers of S=1/2 spins, such as $TlCuCl_3$ [75–77], and $BaCuSi_2O_6$ [78–80], in which the applied magnetic field closes the zero-field spin gap, and the compound undergoes a magnetic quantum phase transition from the paramagnetic state to a long-range magnetic ordered state, which can be characterized as the BEC of magnons or triplons.

2.9.2 Magnetization of interacting spin tetramers

The MF approach is used to include all the magnetic interactions among the spin tetramers presented in section 2.8.1. The energies of the 16 states of the tetramer can be obtained by using the results of the MF approximation of Eq. (2.72). Those 16 states include two singlet states, three triplet states, E_{T1}, E_{T2}, and E_{T3}, each one splitting into three sub-levels, and also a quintuplet state, E_Q that splits into five sub-levels. So, we have

$$
\begin{aligned}
E_{S1} =& -\frac{1}{2}J_1 - \frac{1}{4}J_2 + \frac{1}{2}\sqrt{4J_1^2 - 2J_1J_2 + J_2^2)} - \frac{NJ'z'}{2}\frac{M^2}{g^2\mu_B^2},\\
E_{S2} =& -\frac{1}{2}J_1 - \frac{1}{4}J_2 - \frac{1}{2}\sqrt{4J_1^2 - 2J_1J_2 + J_2^2)} - \frac{NJ'z'}{2}\frac{M^2}{g^2\mu_B^2},\\
E_{T1,1} =& -\frac{1}{2}J_1 + \frac{1}{4}J_2 - \frac{NJ'z'}{2}\frac{M^2}{g^2\mu_B^2} - g\mu_B h_{eff},\\
E_{T1,2} =& -\frac{1}{2}J_1 + \frac{1}{4}J_2 - \frac{NJ'z'}{2}\frac{M^2}{g^2\mu_B^2},\\
E_{T1,3} =& -\frac{1}{2}J_1 + \frac{1}{4}J_2 - \frac{NJ'z'}{2}\frac{M^2}{g^2\mu_B^2} + g\mu_B h_{eff},\\
E_{T2,1} =& -\frac{1}{4}J_2 + \frac{1}{2}\sqrt{J_1^2 + J_2^2} - \frac{NJ'z'}{2}\frac{M^2}{g^2\mu_B^2} - g\mu_B h_{eff},\\
E_{T2,2} =& -\frac{1}{4}J_2 + \frac{1}{2}\sqrt{J_1^2 + J_2^2} - \frac{NJ'z'}{2}\frac{M^2}{g^2\mu_B^2},\\
E_{T2,3} =& -\frac{1}{4}J_2 + \frac{1}{2}\sqrt{J_1^2 + J_2^2} - \frac{NJ'z'}{2}\frac{M^2}{g^2\mu_B^2} + g\mu_B h_{eff},\\
E_{T3,1} =& -\frac{1}{4}J_2 - \frac{1}{2}\sqrt{J_1^2 + J_2^2} - \frac{NJ'z'}{2}\frac{M^2}{g^2\mu_B^2} - g\mu_B h_{eff},\\
E_{T3,2} =& -\frac{1}{4}J_2 - \frac{1}{2}\sqrt{J_1^2 + J_2^2} - \frac{NJ'z'}{2}\frac{M^2}{g^2\mu_B^2},\\
E_{T3,3} =& -\frac{1}{4}J_2 - \frac{1}{2}\sqrt{J_1^2 + J_2^2} - \frac{NJ'z'}{2}\frac{M^2}{g^2\mu_B^2} + g\mu_B h_{eff},\\
E_{Q1,1} =& \frac{1}{2}J_1 + \frac{1}{4}J_2 - \frac{NJ'z'}{2}\frac{M^2}{g^2\mu_B^2} - 2g\mu_B h_{eff},\\
E_{Q1,2} =& \frac{1}{2}J_1 + \frac{1}{4}J_2 - \frac{NJ'z'}{2}\frac{M^2}{g^2\mu_B^2} - g\mu_B h_{eff},\\
E_{Q1,3} =& \frac{1}{2}J_1 + \frac{1}{4}J_2 - \frac{NJ'z'}{2}\frac{M^2}{g^2\mu_B^2},\\
E_{Q1,4} =& \frac{1}{2}J_1 + \frac{1}{4}J_2 - \frac{NJ'z'}{2}\frac{M^2}{g^2\mu_B^2} + g\mu_B h_{eff},\\
E_{Q1,5} =& \frac{1}{2}J_1 + \frac{1}{4}J_2 - \frac{NJ'z'}{2}\frac{M^2}{g^2\mu_B^2} + 2g\mu_B h_{eff}.
\end{aligned}
\tag{2.79}
$$

Here, the intratetramer exchange interactions are given by J_1 and J_2, and the exchange interaction of a given tetramer with the nearest neighbors is represented by J'. Also, the effect of the intertetramer exchange interactions is incorporated using the MF approach as an effective MF, h_{eff}, which is given in Eq. (2.73).

The partition function of the system can be defined based on Eq. (2.26) as

$$\begin{aligned}
Z = e^{N\beta\frac{J'z'}{2}\frac{M^2}{g^2\mu_B^2}} \Big[& e^{-\beta(-\frac{1}{2}J_1-\frac{1}{4}J_2)}\big(e^{-\frac{\beta}{2}\sqrt{4J_1^2-2J_1J_2+J_2^2}}+e^{\frac{\beta}{2}\sqrt{4J_1^2-2J_1J_2+J_2^2}}\big) \\
& + e^{-\beta(-\frac{1}{2}J_1+\frac{1}{4}J_2)}\big(e^{\beta g\mu_B h_{eff}}+1+e^{-\beta g\mu_B h_{eff}}\big) \\
& + e^{-\beta(-\frac{1}{4}J_2+\frac{1}{2}\sqrt{J_1^2+J_2^2})}\big(e^{\beta g\mu_B h_{eff}}+1+e^{-\beta g\mu_B h_{eff}}\big) \\
& + e^{-\beta(-\frac{1}{4}J_2-\frac{1}{2}\sqrt{J_1^2+J_2^2})}\big(e^{\beta g\mu_B h_{eff}}+1+e^{-\beta g\mu_B h_{eff}}\big) \\
& + e^{-\beta(\frac{1}{2}J_1+\frac{1}{4}J_2)}\big(e^{2\beta g\mu_B h_{eff}}+e^{\beta g\mu_B h_{eff}}+1+e^{-\beta g\mu_B h_{eff}}+e^{-2\beta g\mu_B h_{eff}}\big)\Big]^N,
\end{aligned} \tag{2.80}$$

which becomes

$$\begin{aligned}
Z = e^{N\beta\frac{J'z'}{2}\frac{M^2}{g^2\mu_B^2}} \Big[& e^{-\beta(-\frac{1}{2}J_1-\frac{1}{4}J_2)}(2\cosh(\frac{\beta}{2}\sqrt{4J_1^2-2J_1J_2+J_2^2})) \\
& + (1+2\cosh(\beta g\mu_B h_{eff}))\big(e^{-\beta(-\frac{1}{2}J_1+\frac{1}{4}J_2)}+e^{-\beta(-\frac{1}{4}J_2+\frac{1}{2}\sqrt{J_1^2+J_2^2})}+e^{-\beta(-\frac{1}{4}J_2-\frac{1}{2}\sqrt{J_1^2+J_2^2})} \\
& + e^{-\beta(\frac{1}{2}J_1+\frac{1}{4}J_2)}\big)+e^{-\beta(\frac{1}{2}J_1+\frac{1}{4}J_2)}2\cosh(2\beta g\mu_B h_{eff}))\Big]^N.
\end{aligned} \tag{2.81}$$

Subsequently, we have

$$\begin{aligned}
Z = e^{N\beta\frac{J'z'}{2}\frac{M^2}{g^2\mu_B^2}} \Big[& e^{-\beta(-\frac{1}{2}J_1-\frac{1}{4}J_2)}(2\cosh(\frac{\beta}{2}\sqrt{4J_1^2-2J_1J_2+J_2^2})) \\
& + (1+2\cosh(\beta g\mu_B h_{eff}))\left(e^{-\beta\frac{1}{4}J_2}(2\cosh(\beta\frac{1}{2}J_1))+e^{\beta\frac{1}{4}J_2}(2\cosh(\beta\frac{1}{2}\sqrt{J_1^2+J_2^2}))\right) \\
& + e^{-\beta(\frac{1}{2}J_1+\frac{1}{4}J_2)}2\cosh(2\beta g\mu_B h_{eff}))\Big]^N.
\end{aligned} \tag{2.82}$$

Finally, the partition function is written as

$$Z = [A_1' + A_2'\left(1+2\cosh(\beta g\mu_B h_{eff})\right) + A_3' 2\cosh(2\beta g\mu_B h_{eff})]^N. \tag{2.83}$$

where, A'_1, A'_2, and A'_3 are given in Eq. (2.63).

Consequently, the free energy can be obtained by replacing the partition function in Eq. (2.25) with Eq. (2.83):

$$F = -N\frac{1}{\beta}\frac{J'z'}{2}\frac{M^2}{g^2\mu_B^2} - N\frac{1}{\beta}\ln[A'_1 + A'_2\left(1+2\cosh(\beta g\mu_B h_{eff})\right) + A'_3 2\cosh(2\beta g\mu_B h_{eff})]. \tag{2.84}$$

The magnetization of interacting spin tetramers can be attained through substituting the free energy in Eq. (2.24) with Eq. (2.84) as

$$M = -\frac{N}{V}\frac{2g\mu_B\left(A'_2\sinh(\beta g\mu_B(J'z'\frac{M}{g^2\mu_B^2}-B)) + 2A'_3\sinh(2\beta g\mu_B(J'z'\frac{M}{g^2\mu_B^2}-B))\right)}{A'_1 + A'_2\left(1+2\cosh(\beta g\mu_B(J'z'\frac{M}{g^2\mu_B^2}-B))\right) + 2A'_3\cosh(2\beta g\mu_B(J'z'\frac{M}{g^2\mu_B^2}-B))}. \tag{2.85}$$

Note that the effective MF is considered based on Eq. (2.73). The magnetization of interacting tetramers resulted from Eq. (2.85) is a non-linear equation, $M = f(M,B)$. This transcendental equation is solved numerically, and the solutions provide the magnetization of the interacting spin tetramer system. In Fig. 2.11, the resulting magnetization of a spin tetramer with two AFM intratetramer couplings, J_1=4 K and J_2=8 K, and AFM intertetramer interactions of J'=1.5 K, is shown for different temperatures. At very low temperatures, the system shows a 1/2 magnetization plateau.

Fig. 2.12(a) illustrates the lowest-energy $S = 0$ singlet state, the $S_z = 1$ level of the lowest-energy $S = 1$ excited triplet state and the $S_z = 2$ of the $S = 2$ quintuplet state. The $S_z = 1$ level of the lowest-energy triplet state as well as the $S_z = 2$ level of the quintuplet state are represented as bands because of magnetic dispersion in the presence of intertetramer interactions. By increasing the applied magnetic field, the branch of $S_z = 1$ excitation of the lowest-energy triplet is lowered linearly because of the Zeeman effect and crosses the singlet ground state. They intersect at two critical fields, B_{c1} and B_{c2}. As a consequence, the first dome-shaped region occurs between $B_{c1} < B < B_{c2}$,

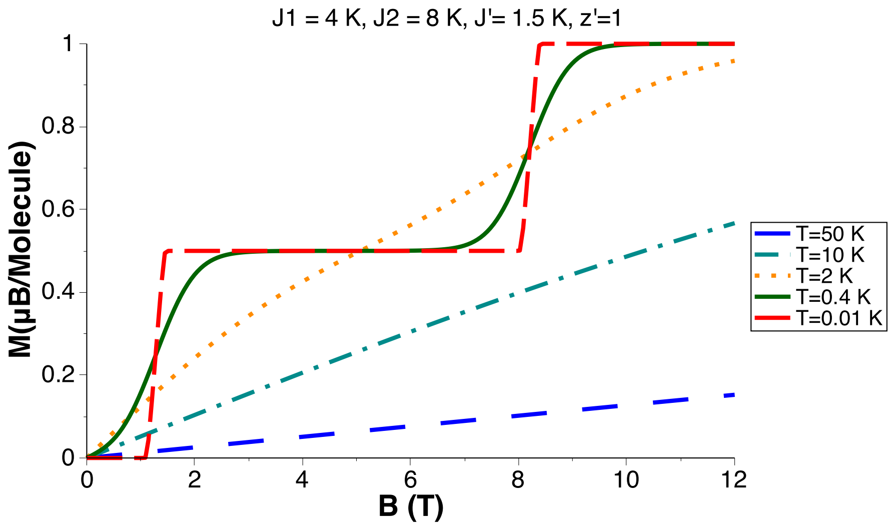

Figure 2.11 – Magnetization as a function of applied magnetic fields shown at various temperatures based on Eq. (2.11), for an interacting spin tetramer system with AFM intratetramer couplings, J_1=4 K and J_2=8 K, and AFM intertetramer interactions, J'=1.5 K.

where the $S_z = 1$ triplets condense into a BEC state, as shown in Fig. 2.12(c). Moreover, the branch of $S_z = 2$ of the quintuplet state decreases linearly in magnetic fields and intersects the $S_z = 1$ of the lowest-energy triplet state in critical fields B_{c3} and B_{c4}. In consequence, the second dome of AFM order appears between $B_{c3} < B < B_{c4}$, where the $S_z = 2$ quintuplets condense into a BEC state.

In the two BEC regions with a long-range magnetic order, the total magnetization in the direction of the applied field, M_z, is continuously increasing in an approximately linear fashion, as exhibited in Fig. 2.12(b). The zero magnetization ($M_z = 0$) plateau, situated below $B < B_{c1}$, and the $M_z = 1$ plateau, located above $B > B_{c4}$, correspond to the regions where an integer number of bosons stays constant in each site. Between those two plateaux, a half-integer plateau with fractional boson fillings exists.

2.10 Exact Diagonalization method

The exact diagonalization of the matrix Hamiltonian gives the eigenstates of a quantum system, which in turn can be used to compute any static or dynamic quantity of the system under study. As discussed in section 2.3, the matrix representation of the Hamil-

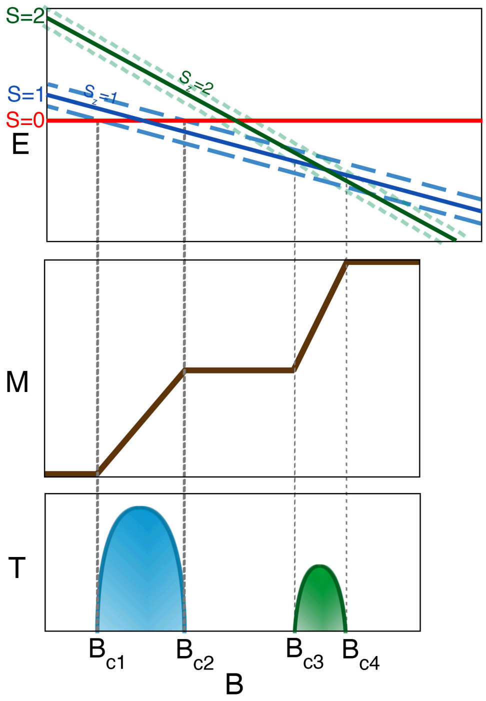

Figure 2.12 – (a) $S = 0$ singlet ground state, $S_z = 1$ branch of lowest-energy triplet state, and $S_z = 2$ level of the $S = 2$ quintuplet state of a system of interacting spin tetramers. By taking the intertetramer interactions into account, the spin levels of a tetramer are dispersed into bands that are evolving in magnetic fields. (b) The magnetization as a function of applied magnetic field exhibiting a plateau at half-integer value of the saturation magnetization. (c) The temperature-magnetic-field phase diagram showing two BEC states: the first, between $B_{c1} < B < B_{c2}$ where the $S_z = 1$ of the lowest-energy triplet state intersects the singlet ground state. The second, between $B_{c3} < B < B_{c4}$ where the $S_z = 2$ level of the quintuplet state crosses the $S_z = 1$ of the lowest-energy triplet state.

tonian is given in Eq. (2.12) for a spin-1/2 dimer ($N = 2$). As the Hamiltonian commutes with the projection along z of the total spin S ($[H, S_z] = 0$), the matrix can be split up into three sub-matrices which are not admixed by the Hamiltonian. Those three sub-matrices are associated with fixed values of the z-component of the total spin S_z as $+1$, -1, and 0. As we will discuss, this symmetry of the Hamiltonian can be taken into account to optimize the numerical calculations in larger systems.

For a finite quantum system having a limited number of spin sites such as the dimer, one can precisely calculate all the eigenstates by numerically diagonalizing the appropriate Hamiltonian matrix. In a system of N $S = 1/2$ spins, the size of the matrix (i.e., the dimension of the Hilbert space) is 2^N. So, one needs to diagonalize a $2^N \times 2^N$ matrix. It is worth mentioning that for the diagonalization of an $M \times M$ matrix Hamiltonian (i.e., the matrix size of $M = 2^N$), the number of operations scales as M^3, and the needed memory to store is M^2. This exponential augmentation with the number of spin sites limits the number of spins N to around 16-20. Other more sophisticated techniques must be used for larger systems [81].

To perform the exact diagonalization of a given matrix Hamiltonian, basis states must be generated. In the case of a S=1/2 system, the basis states are formed by single-spin states $\uparrow_i$ and $\downarrow_i$, $i = 1,\cdots,N$. By taking advantage of the relevant symmetry operations of the system, the spin states can be categorized. Subsequently, states can create blocks labeled by a conserved quantum number, such as for the conservation magnetization in the z direction (m_z). Because $m_z = \sum_{i=1}^{N} S_i^z$ commutes with the Hamiltonian, the block diagonalization of the matrix Hamiltonian can be carried out using magnetization conservation. A block Hamiltonian acting on all states with $m_z = (n_\uparrow - n_\downarrow)/2$ can be constructed, where $n_\downarrow = N - n_\uparrow$. The size of the block for $n_\uparrow$ spins up is: $M = N!/(n\uparrow ! n_\downarrow !)$. Owing to the fact that those blocks can be diagonalized independently from each other, the computational cost is acutely reduced. For example, in the case of four spin tetramers with a total of 16 spin sites (N=16), there are $2^{16} = 65536$ possible basis states. The larger block is the one for $m_z = 0$ with $n_\uparrow = n_\downarrow = 8$, and a block size of $16!/8!8! = 12870$.

To represent the spin states directly in the computer, the ↑ and ↓ in a S=1/2 system are described as bit integer values 1 and 0, respectively. For example, the state $|0\rangle$=$|\downarrow,\downarrow,\downarrow,\cdots,\downarrow\rangle$ is represented by $0\cdots000$ and the state $|1\rangle$=$|\downarrow,\downarrow,\downarrow,\cdots,\uparrow\rangle$ by $0\cdots001$. Representing the basis states as a bit-pattern not only reduces the required memory, but also increases the speed of numerical calculations [82].

To compare the theoretical magnetization with the experimental one, we need to calculate the mean value of the magnetization from the eigenvalues and eigenvectors. If we have 2^N eigenenergies and each one has a definite S_z, the partition function is given by

$$Z = \sum_{i=0}^{2^N-1} e^{-\beta(E_i - g\mu_B S_i^z B)}, \tag{2.86}$$

where N is the number of spin sites in the system. Note that the energy of the system is $\langle E \rangle = -\frac{\partial \ln Z}{\partial \beta}$. The mean value of magnetization at finite T and H is $\langle S_z \rangle = m_z$, in which $\langle S_z \rangle$ is obtained through

$$\langle S_z \rangle = \frac{1}{\beta}\frac{\partial \ln Z}{\partial B} = g\mu_B \frac{\sum_i^{2^N-1} S_i^z e^{-\beta\left(E_i - g\mu_B S_i^z B\right)}}{\sum_i^{2^N-1} e^{-\beta\left(E_i - g\mu_B S_i^z B\right)}}. \tag{2.87}$$

Note that S_i^z is the total magnetization of the state i with energy E_i.

2.11 Bose-Einstein condensate in quantum magnets

The concept of Bose-Einstein Condensation (BEC), proposed by Bose and Einstein in 1924, put forward a new quantum state of matter by showing that bringing the temperature of a non-interacting gas of bosons under a critical value, T_c, would condense them into the lowest-energy quantum state. However, it was not until 1995 that this phenomenon was observed in laser-cooled collections of cold alkali atoms, an experiment that resulted in the three leading scientists, Cornell, Ketterle, and Wieman, obtaining the Nobel prize in physics in 2001 [83]. Although bosonic and cold atoms were discussed to show the BEC state, the concept can be investigated more broadly and extended to other bosonic quasiparticles [74]. As was suggested by Matsubara and Matsuda [84] concerning the transformation between a S=1/2 spin system and a system of hard-core (h-c) bosons, generalizing this exact mapping to systems with higher-spin values allows the quantum magnets to realize the BEC state.

To discuss how the Matsubara-Matsuda (M-M) transformation can be used to map a S=1/2 spin system with $d \geq 2$ where d is the spatial dimensionality of the system, onto a system of h-c bosons, one could look at a hypercubic d-dimensional lattice, in which the S=1/2 spins are coupled with an AFM exchange interaction $J > 0$. In the presence of an applied magnetic field along symmetry axis z, the Heisenberg XXZ Hamiltonian of this system, in which $J = J_x = J_y \neq J_z$, is given by

$$H_{XXZ} = J \sum_{\mathbf{r},\nu} \left(S^x_{\mathbf{r}} S^x_{\mathbf{r}+\mathbf{e}_\nu} + S^y_{\mathbf{r}} S^y_{\mathbf{r}+\mathbf{e}_\nu} + \gamma S^z_{\mathbf{r}} S^z_{\mathbf{r}+\mathbf{e}_\nu} \right) - g_{zz}\mu_B B \sum_{\mathbf{r}} S^z_{\mathbf{r}}, \tag{2.88}$$

where the uniaxial exchange anisotropy parameter is provided by γ, and the gyromagnetic factor in the direction of the z axis is given by g_{zz}. The last term in Eq. (2.88) indicates the Zeeman coupling to an applied magnetic field B.

The M-M transformation is given by

$$S^+_j = b^\dagger_j,\ S^-_j = b_j,\ S^z_j = b^\dagger_j b_j - \frac{1}{2}. \tag{2.89}$$

Here, the creation and annihilation operators of a S=1/2 spin in site j, S^+_j and S^-_j, are mapped respectively onto the creation and annihilation operators of the h-c bosons, $b^\dagger_j$ and b_j. Bear in mind that those h-c bosonic operators satisfy the following commutation relation [85]

$$[b_i, b^\dagger_j] = \delta_{ij}(1 - 2b^\dagger_j b_j). \tag{2.90}$$

The occupation number operator $n_j = b^\dagger_j b_j$ in Eq. (2.90) determines the number of h-c bosons on a certain site, which is either 0 or 1 based on the constraint on the h-c bosonic. The effect of the h-c bosonic constraint contrasts with the usual bosonic operators that allow any number of bosons on a specific site [86]. As will later be seen, an infinite on-site repulsion is added to the Hamiltonian to realize the h-c bosons constraint, and hence to avoid the double or higher occupation of a certain site [73].

By applying the M-M transformation in Eq. (2.89) on the Hamiltonain in Eq. (2.88), one obtains

$$H_{XXZ} = J \left(\sum_{\mathbf{r},\nu} \frac{1}{2}(b^\dagger_{\mathbf{r}} b_{\mathbf{r}+\mathbf{e}_\nu} + b^\dagger_{\mathbf{r}+\mathbf{e}_\nu} b_r) + \gamma(b^\dagger_{\mathbf{r}} b_{\mathbf{r}} - \frac{1}{2})(b^\dagger_{\mathbf{r}+\mathbf{e}_\nu} b_{\mathbf{r}+\mathbf{e}_\nu} - \frac{1}{2}) \right) - g_{zz}\mu_B B \sum_{\mathbf{r}} b^\dagger_{\mathbf{r}} b_{\mathbf{r}}, \tag{2.91}$$

where $b^{\dagger}_{\mathbf{r}} b_{\mathbf{r}} = n^{b}_{\boldsymbol{r}}$ is the occupation number for the h-c bosons, and the chemical potential is given by $\mu = g_{zz}\mu_B B$. So, Eq. (2.91) can be written as

$$H_{XXZ} = \frac{J}{2}\sum_{\mathbf{r},\nu}\left(b^{\dagger}_{\mathbf{r}} b_{\mathbf{r}+\mathbf{e}_{\nu}} + b^{\dagger}_{\mathbf{r}+\mathbf{e}_{\nu}} b_{\mathbf{r}}\right) + \gamma J \sum_{\mathbf{r},\nu}(n^{b}_{\mathbf{r}} - 1/2)(n^{b}_{\mathbf{r}+\mathbf{e}_{\nu}} - 1/2) - \mu \sum_{\mathbf{r}} n^{b}_{\mathbf{r}}. \quad (2.92)$$

The Hamiltonian in Eq. (2.92) commutes with the sum of h-c boson number operator, $\sum_{\boldsymbol{r}} n^{b}_{\boldsymbol{r}}$, and thus it conserves the total number of h-c bosons. So, the Hamiltonian is invariant under the transformation $\widetilde{b}^{\dagger}_{r} = e^{i\varphi} b^{\dagger}_{r}$, which is the global U(1) transformation. It should be mentioned that the uniaxial symmetry, U(1) symmetry, of a spin in site j is given by $\widetilde{S}^{+}_{j} = e^{i\varphi} S^{+}_{j}$. U(1) symmetry represents the continuous symmetry of the spin rotation with an angle of ϕ in the direction of a certain axis, the z axis in this case. Consequently, the conservation of the total number of h-c bosons is related to the global U(1) symmetry of the spin Hamiltonian.

So, the essential quality that distinguishes whether a system of h-c bosons condenses or not is the conservation of the total number of h-c bosons. That quality is preserved when the spin Hamiltonian of a system possesses the uniaxial symmetry. In the case of real quantum magnets, the uniaxial symmetry can be broken by anisotropic interactions, like the spin-orbit interaction in a system with lattice anisotropy or the classical dipole-dipole interaction. As the U(1) symmetry-breaking terms become important at low temperatures, the idea of BEC is an approximation for real magnets. Nevertheless, as discussed in section 2.2, in the case of BEC quantum magnets, which mostly possess small spin values of S=1/2 or 1, the order of d-d interactions, ranging from 10 mK to 100 mK, are considerably lower compared to the order of transition temperatures of BEC, which scale from 1 K to 100 K [73]. Furthermore, because the unpaired electron spin in purely organic quantum magnets has isotropic characteristics and their spin density is distributed over a large part of the molecule, the spin-orbit interactions in those spin systems are negligible [2], which makes them a better experimental representation of BEC down to very low temperatures. Therefore, the BEC model offers an excellent characterization for quantum magnets with uniaxial symmetry-breaking temperatures much lower than the BEC transition temperatures. A list of some quantum magnets with a 3D BEC is presented in the reference [73].

Additionally, based on the M-M transformation in Eq. (2.89), the total number of h-c bosons, $N=\sum_j n_j^b$, is mapped onto the total magnetization in the z direction, $M_z=\sum_j S_j^z$ along with a constant, giving $N=M_z+const$. So, the number conservation of h-c bosons is linked to the conservation of the magnetization in the z direction. Moreover, based on Eq. (2.92), the chemical potential, $\mu = g_{zz}\mu_B B$, is associated with the applied magnetic field, B. As a consequence, B can be used as a tuning parameter to change the number of h-c bosons in quantum magnets. Upon increasing B, the number of h-c bosons can be increased to reach the maximum number of one h-c boson per site at the saturation field given by $B_{sat} = dJ(1+\gamma)/g_{zz}\mu_B$ [73].

Bear in mind that the initial spin Hamiltonian in Eq. (2.88) has time-reversal symmetry, $\mathbf{S}_j \rightarrow -\mathbf{S}_j$ and $B \rightarrow -B$, which results in the Hamiltonian in Eq. (2.92) having particle-hole symmetry (i.e., invariant under $b_{\mathbf{r}}^{\dagger} \rightarrow -b_{\mathbf{r}}$ and $\mu \rightarrow -\mu$). The time-reversal symmetry of the initial Hamiltonian indicates that there are two saturation magnetic fields, $-B_{sat}$ and $+B_{sat}$, in the spin system, as shown in Fig. 2.13. Due to the particle-hole symmetry of H_{XXZ} in Eq. (2.92), the BEC QCPs at the two saturation fields are equal. So, the phase diagram of $S=1/2$ XXZ model in Fig. 2.13 has one saturation field as opposed to the phase diagram of the interacting spin dimers in Fig. 2.10 that has two critical fields, B_{c1} and $B_{c2}=B_{sat}$. The difference is due to a non-zero magnetic gap of the interacting dimer system at zero applied field, which contrasts with the gapless system in the $S=1/2$ XXZ model which has a magnetic order at $B=0$. The magnetic ordered phase at $B=0$ has been observed in the Cs_2CuCl_4 compound with a BEC QCP at the saturation field B_c [87].

By mapping the spin system onto a system of h-c bosons, the ground state of the spin Hamiltonian in Eq. (2.88) for $B \leq -B_{sat}$ with spin state $|\downarrow\rangle$ is related to the state with no h-c boson: $|\downarrow\rangle \leftrightarrow |0\rangle$. Contrarily, the ground state for $B \geq B_{sat}$ with spin state $|\uparrow\rangle$ is associated with the state with one h-c boson in each site: $|\uparrow\rangle \leftrightarrow \prod_{\boldsymbol{r}} b_{\boldsymbol{r}}^{\dagger}|0\rangle$ [73]. The

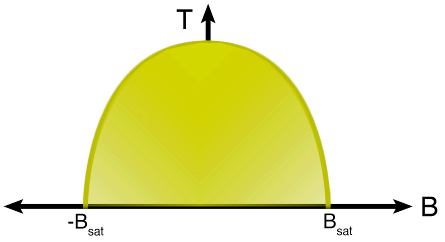

Figure 2.13 – The temperature-magnetic-field phase diagram of the $S = 1/2$ XXZ model showing a BEC state with a single saturation field.

Hamiltonian in Eq. (2.92) can be written in $\boldsymbol{k}$-space as

$$H_{XXZ} = \sum_{\boldsymbol{k}} (\omega_{\boldsymbol{k}} - \tilde{\mu}) \hat{b}^{\dagger}_{\boldsymbol{k}} \hat{b}_{\boldsymbol{k}} + \frac{1}{2L} \sum_{\boldsymbol{k}, \boldsymbol{k'}, \boldsymbol{q}} V_{\boldsymbol{q}} \hat{b}^{\dagger}_{\boldsymbol{k}+\boldsymbol{q}} \hat{b}^{\dagger}_{\boldsymbol{k}-\boldsymbol{q}} \hat{b}_{\boldsymbol{k}} \hat{b}_{\boldsymbol{k'}}, \tag{2.93}$$

where

$$\begin{aligned} \hat{b}^{\dagger}_{\mathbf{k}} &= \frac{1}{\sqrt{L}} \sum_{\mathbf{r}} e^{i\mathbf{k}\cdot\mathbf{r}} b^{\dagger}_{\mathbf{r}}, \\ V_{\mathbf{q}} &= U + 2\gamma J \sum_{v} \cos k_v, \\ \omega_{\boldsymbol{k}} &= J \sum_{v} (1 + \cos k_v), \\ \tilde{\mu} &= g_{zz} \mu_B (B + B_{sat}). \end{aligned} \tag{2.94}$$

As the BEC QCP at both saturation fields are equal, only the $-B_{sat}$ was taken into account in Eq. (2.93). The constraint on h-c bosons is imposed by considering the limit on the on-site repulsion as $U \to \infty$. Also, the dispersion relation at $B = -B_{sat}$ (i.e., $\tilde{\mu}$=0) for $k << 1$ is approximated by $\omega_{\boldsymbol{k}} \simeq Jk^2/2$. In conclusion, the dispersion relation at the QCP at $B = -B_{sat}$ is quadratic, $\omega_k \propto k^2$, which indicates the dynamical exponent of z=2. The QCP associated with this kind of second-order quantum phase transition at $B = -B_{sat}$ is known as BEC QCP. Note that the effective dimension, D, of this BEC QCP is the sum of the spatial dimensionality of the system, d, and the dynamical exponent, z=2, which is given by $D = d + 2$. Therefore, for the BEC QCP, the upper critical dimension is d_c=2, and so the spatial dimension of the system must be $d \geq 2$ to be able to study the interaction term in Eq. (2.93) by MF approach [73].

CHAPTER 3

THEORY OF ELECTRONIC STRUCTURES

The characteristics of a magnetic system are related to the way its electronic energy levels are altered by an external magnetic field. Because the magnetic properties of a molecule-based magnet arise from the open-shell electronic structures of its free radical molecules, a profound understanding of how those electronic structures are formed is essential. The dynamics of the magnetic systems is well reproduced on the basis of the Heisenberg-like spin Hamiltonians. The sign and magnitude of the magnetic interaction between the spins on sites i and j (S_i and S_j) are determined by the Heisenberg spin exchange constant that we refer to as J_{ij}. Using a model Heisenberg spin Hamiltonian consisting of a summation of all those pairwise interactions between different spin sites in the magnetic system under study results in its magnetic energy levels. We use the density functional theory (DFT) [88–90] calculations and broken-symmetry states to evaluate those magnetic interactions. We start by calculating the total energies of different independent spin configurations corresponding to a single cell or various supercells of the system. Then, we examine the signs and magnitudes of the dominant Js by means of energy-mapping analysis. First, the supercell total energy difference mapping [48, 51, 91, 92] is employed, followed by the four-state energy mapping [93]. Once the numerical values of those dominant Js are deduced, the properties of a magnetic system can be studied.

3.1 Wavefunction-free quantum physics

To describe the properties of a solid consisting of nuclei ($\{\boldsymbol{R}_I\}$) and electrons ($\{\boldsymbol{r}_i\}$), the many-body wavefunction, $\Psi(\{\boldsymbol{r}_i\},\{\boldsymbol{R}_I\})$, must be found by solving the Schrödinger equation, $\hat{H}\psi = E\psi$, where the Hamiltonian is given by [94]

$$\hat{H} = -\sum_i \frac{\hbar^2\nabla^2_{\mathbf{R}_i}}{2M_i} + \frac{1}{2}\sum_i\sum_{j\neq i}\frac{Z_iZ_je^2}{|\mathbf{R}_i-\mathbf{R}_j|} - \sum_i \frac{\hbar^2\nabla^2_{\mathbf{r}_i}}{2m_e} + \frac{1}{2}\sum_i\sum_{j\neq i}\frac{e^2}{|\mathbf{r}_i-\mathbf{r}_j|}$$
$$-\sum_i\sum_j\frac{Z_ie^2}{|\mathbf{R}_i-\mathbf{r}_j|}. \tag{3.1}$$

Here, m_e is the electron mass, M_i is the mass of i'th ion and Z_i its atomic number. The first two terms in the Hamiltonian of Eq. (3.1) specific to the nuclei, are the kinetic energy operators and the Coulomb interactions of the nuclei. Whereas the third and fourth terms correspond to the electrons, and are the kinetic energy operators as well as the Coulomb interactions of the electrons. The fifth term is the Coulomb interactions of the electrons with the nuclei. Solving the Schrödinger equation for materials with that Hamiltonian is very challenging, and so a number of approximations have been devised to make it feasible.

The first approximation to simplify this Hamiltonian is the Born-Oppenheimer (BO) approximation. As the positions of the nuclei in space are assumed to be fixed due to the nuclei mass being much heavier than the electrons $M_{nuclei} \gg m_{electron}$, the motion of atomic nuclei and of the electrons in this approximation can be separated. This enables the decoupling of the total wavefunction into the nuclear and the electronic wavefunctions $\Psi(\{\boldsymbol{r}_i\},\{\boldsymbol{R}_I\}) = \Psi(\{\boldsymbol{R}_I\}) \times \Psi(\{\boldsymbol{r}_i\})$ [68].

By assuming the nuclei are static, their kinetic energies, given in the first term in Eq. (3.1), can be omitted. Also, the second term, which is the Coulomb interaction between the nuclei, is treated as a constant that does not influence the solution. Therefore, only the three last terms in Eq. (3.1) need to be addressed. Furthermore, the last term in Eq. (3.1) is related to the Coulomb potential of the nuclei in which the electrons move. That term is known as the external potential, V_{ext}, in DFT. The external potential defines the Hamiltonian (H), and the Hamiltonian gives many different independent electronic wavefunctions, $(\Psi_0, \Psi_1, \Psi_2, \cdots)$. One of those wavefunctions is the ground state wavefunction of the system with which the ground state electronic density can be calculated. It can be shown that, for every external potential, there is a unique ground state wavefunction and vice versa ($V_{ext}(\boldsymbol{r}) \leftrightarrow \Psi_{GS}(\boldsymbol{r})$) [89].

The electronic density of a system with N electrons can be defined as

$$n(\boldsymbol{r}) = N \int d^3r_2 \int d^3r_3 \cdots \int d^3r_N \Psi^*(\boldsymbol{r}, \boldsymbol{r}_2, \cdots, \boldsymbol{r}_N)\Psi(\boldsymbol{r}, \boldsymbol{r}_2, \cdots, \boldsymbol{r}_N). \tag{3.2}$$

By considering an electron in the external field of all the other electrons, the many-electron problem can be simplified to many one-electron problems. So, we suppose that the total wavefunction is written as the product of all of the single particle states, known as Hartree product form [90],

$$\Psi(\boldsymbol{r}_1, \boldsymbol{r}_2 \cdots \boldsymbol{r}_N) = \prod_i \psi_{n_i}(\boldsymbol{r}_i) = \psi_{n_1}(\boldsymbol{r}_1)\psi_{n_2}(\boldsymbol{r}_2) \cdots \psi_{n_N}(\boldsymbol{r}_N). \tag{3.3}$$

The Hartree product form is valid for distinguishable classical particles. However, we have $\psi_{n_1}(\boldsymbol{r}_1)\psi_{n_2}(\boldsymbol{r}_2) \cdots \psi_{n_N}(\boldsymbol{r}_N) \neq -\psi_{n_1}(\boldsymbol{r}_2)\psi_{n_2}(\boldsymbol{r}_1) \cdots \psi_{n_N}(\boldsymbol{r}_N)$, which indicates that the wavefunction is not antisymmetric with respect to the exchange of the coordinates. Thereby, the resulting particles would not be indistinguishable and would not follow the Pauli exclusion principle, as opposed to the characteristics of electrons. To ameliorate the approximate form, one can generate an antisymmetric function by writing a linear combination of Hartree product wavefunctions, which is given as a single Slater determinant form through

$$\Psi(\boldsymbol{r}_1, \cdots, \boldsymbol{r}_N) = \frac{1}{\sqrt{N!}} \begin{vmatrix} \psi_{n_1}(\boldsymbol{r}_1) & \psi_{n_2}(\boldsymbol{r}_1) & \cdots & \psi_{n_N}(\boldsymbol{r}_1) \\ \psi_{n_1}(\boldsymbol{r}_2) & \psi_{n_2}(\boldsymbol{r}_2) & \cdots & \psi_{n_N}(\boldsymbol{r}_2) \\ \vdots & & & \vdots \\ \psi_{n_1}(\boldsymbol{r}_N) & \psi_{n_2}(\boldsymbol{r}_N) & \cdots & \psi_{n_N}(\boldsymbol{r}_N) \end{vmatrix}. \tag{3.4}$$

As an example, from $\Psi(\boldsymbol{r}_1, \boldsymbol{r}_2) = \frac{1}{\sqrt{2}}(\psi_{n_1}(\boldsymbol{r}_1)\psi_{n_2}(\boldsymbol{r}_2) - \psi_{n_1}(\boldsymbol{r}_2)\psi_{n_2}(\boldsymbol{r}_1))$, one can show that, upon exchanging the coordinates of the two electrons, the sign of the total wavefunction changes. Also, if the two electrons are placed in the same quantum state, $n_1 = n_2 = i$, then the total wavefunction would be zero. So, the two electrons obey the Pauli exclusion principle and cannot be found in an identical quantum state [95].

By using the Hartree product form and Slater determinant form, the electronic density can be written with regard to the individual electron wavefunctions as

$$n(\boldsymbol{r}) = \sum_{i}^{N} \psi_i^*(\boldsymbol{r})\psi_i(\boldsymbol{r}) = \sum_{i}^{N} |\psi_i(\boldsymbol{r})|^2 , \tag{3.5}$$

which expresses density as the probability distribution of the wavefunction.

Based on the first theorem of Hohenberg and Kohn (HK) [96], a single density corresponds to a unique wavefunction which means that, if $\Psi \neq \Psi'$, then $n \neq n'$. To prove that statement, one can simply assume that if $\Psi \neq \Psi'$, then $n = n'$, which leads to a contradiction. As a result, $n_{GS}(\boldsymbol{r}) \leftrightarrow \Psi_{GS}(\boldsymbol{r})$, which means that a single density corresponds to a unique wavefunction and vice versa. Consequently, the external potential is uniquely connected to the wavefunction, and the wavefunction is uniquely linked to the density: $V_{ext}(\boldsymbol{r}) \leftrightarrow \Psi_{GS}(\boldsymbol{r}) \leftrightarrow n_{GS}(\boldsymbol{r})$. Thus, the middle step, Ψ_{GS}, can be omitted and the external potential uniquely corresponds to the ground state density of a many-electron system: $V_{ext}(\boldsymbol{r}) \leftrightarrow n_{GS}(\boldsymbol{r})$. So, the external potential, and consequently the total energy, is a unique functional of the density. Note that a functional maps space of functions onto numbers the same way a function can map numbers onto numbers.

The second theorem of HK states that the true ground state electronic density is the one that minimizes the total energy functional. Therefore, a ground state energy can be considered as a unique functional of the ground state electronic density $E_{GS} = E[n_{GS}(\boldsymbol{r})]$. As a consequence, DFT offers wavefunction-free quantum physics by referring to density containing as much information as the wavefunction. Using electronic density rather than the wavefunction provides us with the power to calculate any observable ground-state property of the many-electron system as a unique functional of the density. Thus, a $3N$-dimensional problem of dealing with wavefunction as a function of the position of each electron is reduced to a 3-dimensional problem of dealing with electronic density as only a function of space.

3.2 DFT implemented by Kohn-Sham approach

The Kohn-Sham (KS) approach is a successful approach that has been extensively used to put DFT into practice as an effective single-particle theory. In the KS approach, single-particle orbitals $\phi_i(\boldsymbol{r})$, namely KS orbitals, are taken into account as a particular type of wavefunction. Consequently, the DFT is regarded as a single-particle theory, in spite of the fact that the many-body effects are considered through the exchange-correlation functional, which will be discussed shortly.

The total kinetic-energy functional can be written as $T[n] = T_s[n] + T_c[n]$, which is a combination of the $T_s[n]$ term related to the kinetic energy of the non-interacting single particles with density n, and the $T_c[n]$ term as a pure correlation effect associated with what is left. The exact $T[n]$ as a functional of n is unknown. However, for a system of N non-interacting particles with density n, $T_s[n]$ can be written with respect to the single-particle orbitals $\phi_i(\boldsymbol{r})$ through [89]

$$T_s[n] = -\frac{\hbar^2}{2m}\sum_i^N \int d^3r \phi_i^*(\boldsymbol{r})\nabla^2\phi_i(\boldsymbol{r}). \tag{3.6}$$

One can deduce that $T_s[n] = [\{\phi_i[n]\}]$. In other words, T_s is a functional of the full set of occupied single-particle orbitals ϕ_i, and each of those orbitals is a functional of density n.

The exact energy functional can now be given by

$$E[n] = T[n] + U[n] + V[n] = T_s[\{\phi_i[n]\}] + U_H[n] + E_{xc}[n] + V[n], \tag{3.7}$$

where $U_H[n] = \frac{1}{2}\int d^3r \int d^3r' \frac{n(\boldsymbol{r})n(\boldsymbol{r'})}{|\boldsymbol{r}-\boldsymbol{r'}|}$ is the classical electrostatic energy, namely the Hartree energy, of a system of particles interacting by means of Coulomb interactions. Also, $V[n] = \int d^3rn(\boldsymbol{r})v_{ext}(\boldsymbol{r})$ is the potential energy [90]. $E_{xc}[n]$, called the exchange-correlation energy, is unknown. Because $T_s[\{\phi_i[n]\}]$ is orbital functional, the minimization of energy in Eq. (3.7) with regard to the density cannot be directly executed. As an alternative, a scheme put forward by KS [97] proposes an indirect minimization through

[89]

$$0=\frac{\delta E[n]}{\delta n(\boldsymbol{r})}=\frac{\delta T_s[n]}{\delta n(\boldsymbol{r})}+\frac{\delta V[n]}{\delta n(\boldsymbol{r})}+\frac{\delta U_H[n]}{\delta n(\boldsymbol{r})}+\frac{\delta E_{xc}[n]}{\delta n(\boldsymbol{r})}=\frac{\delta T_s[n]}{\delta n(\boldsymbol{r})}+v_{ext}(\boldsymbol{r})+v_H(\boldsymbol{r})+v_{xc}(\boldsymbol{r}). \tag{3.8}$$

Here, the term $v_{ext}(\boldsymbol{r}) = \delta V[n]/\delta n(\boldsymbol{r})$ is the external potential in which the electrons are moving, and it does not arise from electron-electron interactions. However, the term $\delta U_H[n]/\delta n(\boldsymbol{r})$ gives rise to the Hartree potential, which describes the classical charge-charge interaction, $v_H[n](\boldsymbol{r}) = \int d^3r \frac{n(\boldsymbol{r}')}{|\boldsymbol{r}-\boldsymbol{r}'|}$. Also, $v_{xc}(\boldsymbol{r}) = \delta E_{xc}[n]/\delta n(\boldsymbol{r})$ is the exchange-correlation potential and contains all the many-particle interactions [90].

If one has a system with non-interacting particles in a potential $v_s(\boldsymbol{r})$, then the exchange-correlation and Hartree contributions are canceled out. So, the minimization of the energy $E_s[n]$ with respect to density n results in

$$0=\frac{\delta E_s[n]}{\delta n(\boldsymbol{r})}=\frac{\delta T_s[n]}{\delta n(\boldsymbol{r})}+\frac{\delta V_s[n]}{\delta n(\boldsymbol{r})}=\frac{\delta T_s[n]}{\delta n(\boldsymbol{r})}+v_s(\boldsymbol{r}). \tag{3.9}$$

One can deduce that the identical solution $n(\boldsymbol{r}) \equiv n_s(\boldsymbol{r})$ can be obtained when minimizing the energy in Eq. (3.8) and in Eq. (3.9), provided that

$$v_s(\boldsymbol{r}) = v_{ext}(\boldsymbol{r}) + v_H(\boldsymbol{r}) + v_{xc}(\boldsymbol{r}). \tag{3.10}$$

The Schrödinger equation for this system of non-interacting particles in potential $v_s(\boldsymbol{r})$ is given by

$$\left[-\frac{\hbar^2\nabla^2}{2m}+v_s(\boldsymbol{r})\right]\phi_i(\boldsymbol{r})=\varepsilon_i\phi_i(\boldsymbol{r}), \tag{3.11}$$

which results in the single-particle orbitals ϕ_i. These orbitals can be used to compute the density of the interacting system as

$$n(\boldsymbol{r}) \equiv n_s(\boldsymbol{r}) = \sum_i^N f_i\,|\phi_i(\boldsymbol{r})|^2. \tag{3.12}$$

Here, f_i indicates the occupation of the i'th orbital, which can have a value of 1 (for $i < N$), 0 (for $i > N$), or $0 \leq f_i \leq 1$ (for $i = N$).

The KS equations, given in Eqs. (3.10), (3.11), and (3.12), enable us to calculate the density of a system of interacting particles in potential $v_{ext}(\boldsymbol{r})$ by replacing that calculation by a system of non-interacting particles in potential $v_s(\boldsymbol{r})$. Hence, solving a many-body Schrödinger equation can be substituted with solving a single-body Schrödinger equation.

When solving the KS equations, we are dealing with a non-linear problem because both the Hartree and the exchange-correlation potentials depend on the density (n), which, in turn, depends on the single-particle orbitals (ϕ_i). To solve that non-linear problem and to find the ground state electronic density, we employ a self-consistent cycle of four principal steps. In step 1, a trial density ($n(\boldsymbol{r})$) is chosen. In step 2, the corresponding v_s are computed, and consequently the KS equation in Eq. (3.11 is solved for KS orbitals ϕ_i. In step 3, a new electronic density is calculated from the resulting ϕ_i from step 2 and by using Eq. (3.12). Finally, in step 4, the new calculated density is compared to the initial trial density. If the densities are the same, the true ground state density is obtained. If not, then the process is repeated starting from step 2 with the new calculated density as the input [98]. That cycle continues until obtaining a convergence, such as in the energy.

3.3 DFT calculations

Three DFT aspects must first be determined to carry out DFT calculations: the exchange-correlation (xc) functional, the numerical method, and the computer code.

As discussed before, the first feature, the exact xc functional, is unknown and needs to be approximated in order to make DFT calculations practical. One of the historically important approximations is that of local density approximation (LDA). In LDA, the real inhomogeneous system with density $n(\boldsymbol{r})$ is assumed to be composed of very small elements and, in each of those small elements, the density is approximated to be locally constant. The xc energy of the real inhomogeneous system can be approximately evaluated by calculating the electronic density of each of its elements. This is done by assuming that the role of each element in the xc energy of the inhomogeneous system is approximately equivalent to the homogeneous one with the same density [89]. In 1965, Kohn and Sham [97] proposed the initial xc functional for a particular solid, called homogeneous electron gas (i.e., jellium), in which the atomic nuclei are uniformly distributed in space and electrons have a homogeneous isotropic distribution.

Based on the xc energy defined as $E_{xc}[n] = \int d^3rn(\boldsymbol{r})e_{xc}[n(\boldsymbol{r})]$, the $e_{xc}[n(\boldsymbol{r})]$ is the density xc functional. In the LDA, the xc energy at each point in the real inhomogeneous system is approximately equivalent to the xc energy of a homogeneous electron gas of identical density. So, we have

$$E_{xc}[n] \approx E_{xc}^{LDA}[n] = \int d^3rn(\boldsymbol{r})e_{xc}^{LDA}(n(\boldsymbol{r})), \tag{3.13}$$

where $E_{xc}^{LDA}[n]$ is the local-density approximation of $E_{xc}[n]$. Note that, in that approximation, $e_{xc}^{LDA}(n(\boldsymbol{r}))$ is no longer a functional, but is a function of n at point $\boldsymbol{r}$. For the homogeneous electron gas, the exchange part can be evaluated analytically [99], and the correlation part can be obtained from precise numerical simulations [100]. Furthermore, the xc potential is given by $v_{xc}^{LDA}[n](\boldsymbol{r}) = \delta E_{xc}^{LDA}/\delta n(\boldsymbol{r})$. Although Kohn and Sham had not anticipated in their paper that their guess for the xc functional would result in a meaningful description for real solids, impressively their assumption was later shown to be computationally relevant and works quite well in actual calculations.

As discussed, the density at point $\boldsymbol{r}$ is utilized in LDA. In a real inhomogeneous solid, one is dealing with a spatially changing density $n(\boldsymbol{r})$. So, to improve the accuracy of LDA, it is worthwhile to incorporate the knowledge regarding the spatial variation of density in the functional. For this reason, functionals in the form of

$$E_{xc}^{GGA}[n] = \int d^3rf(n(\boldsymbol{r}), |\nabla n(\boldsymbol{r})|), \tag{3.14}$$

were proposed, which are called generalized-gradient approximations (GGAs) [101]. One of the mostly employed and trusted GGAs is PBE, which is put forward by Perdew, Burke, and Ernzerhof (PBE) in 1996 [102].

The second feature that needs to be specified in a DFT calculation is the numerical basis that is utilized to solve the KS equations [97], such as Projector Augmented Waves (PAW) [103].

Finally, the third feature, the computer code, such as ABINIT [52] or QUANTUM ESPRESSO [53], is required to implement the numerical method in a DFT calculation.

3.3.1 Planewave DFT

Wavefunctions can be described as a linear combination of some basis functions. In planewave DFT, these basis functions are chosen as planewaves. In these planewave DFT calculations, three important characteristics must be chosen wisely: cutoff energy, k-point grid, and pseudopotentials.

In order to discuss cutoff energy (E_{cut}), we first need to briefly review Bloch waves. The electron wavefunctions in a crystal are given by Bloch waves with the form

$$\phi_{n,\boldsymbol{k}}(\boldsymbol{r}) = \exp(i\boldsymbol{k}\cdot\boldsymbol{r})u_{n,\boldsymbol{k}}(\boldsymbol{r}), \tag{3.15}$$

where $u_{n,\boldsymbol{k}}(\boldsymbol{r})$ is the periodic part with the same periodicity as the crystal. Based on the Bloch theorem for a periodic system, the energy eigenstates of an electron in a crystal are given by Bloch waves, $\phi_{n,\boldsymbol{k}}$, where n is the band index and $\boldsymbol{k}$ is the wavevector [55]. Based on the fact that any periodic function can be expanded by a Fourier series, the periodic function in Eq. (3.15), $u_{n,\boldsymbol{k}}(\boldsymbol{r})$, is expanded as

$$\phi_{n,\boldsymbol{k}}(\boldsymbol{r}) = \frac{1}{\sqrt{V_{cell}}}\exp(i\boldsymbol{k}\cdot\boldsymbol{r})\sum_{\boldsymbol{G}} c_{n,\boldsymbol{k}}(\boldsymbol{G})\exp(i\boldsymbol{G}\cdot\boldsymbol{r}), \tag{3.16}$$

where $\boldsymbol{G}$ is a reciprocal lattice vector, and V_{cell} is the volume of the primitive cell. As a consequence, the Bloch wave can be described as the sum of the planewaves with the wavevector $(\boldsymbol{k}+\boldsymbol{G})$, of which the sum runs over an infinite number of reciprocal lattice vectors. However, due to numerical limitations in copping with infinite sums, defining a E_{cut} for the planewave basis is necessary. This planewave E_{cut} is determined for the expansion of Eq. (3.16) as

$$E_{cut} = \frac{1}{2}\left|\boldsymbol{k} + \boldsymbol{G}_{max}\right|^2. \tag{3.17}$$

The number of planewaves as the basis functions is controlled by $\boldsymbol{G}_{max}$ in expansion (3.16), and hence by E_{cut} in Eq. (3.17). The number of planewaves is related to the G_{max} by $N_{PW} \propto V_{cell}G_{max}^3$. Then, by taking into account Eq. (3.17), the number of planewaves is $N_{PW} \propto V_{cell}E_{cut}^{3/2}$. The quality of KS single-electron wavefunctions $\phi_{n,\boldsymbol{k}}(\boldsymbol{r})$ is affected by the number of reciprocal lattice vectors (with a maximum of $\boldsymbol{G}_{max}$), and more commonly by the corresponding planewave E_{cut}. Therefore, an energy convergence test regarding the E_{cut} must be performed to determine its appropriate value [52, 104].

The second concept to be contemplated in a planewave DFT calculation is the choice of the k-point grid. Because any two k-points differing only by a reciprocal lattice vector $\boldsymbol{G}$ are identical $\boldsymbol{k} = \boldsymbol{k} + \boldsymbol{G}$, we have $\phi_{n,\boldsymbol{k}} = \phi_{n,\boldsymbol{k}+\boldsymbol{G}}$ [55]. Therefore, all the discrete Bloch waves take place in the first Brillouin zone (BZ). In the equation of density $n(\boldsymbol{r})$, the sum over the k-points is given by an integral only in the first BZ

$$n(\boldsymbol{r}) = \frac{1}{V_{BZ}} \sum_{n}^{occupied} \int_{BZ} d^3k \left|\phi_{n,\boldsymbol{k}}(\boldsymbol{r})\right|^2, \tag{3.18}$$

where $V_{BZ} = (2\pi^3)/V_{cell}$ is the volume of the BZ and $\phi_{n,\boldsymbol{k}}(\boldsymbol{r})$ are the single-electron KS orbitals. To execute numerical calculations in practice, the integral must be turned into a weighted sum over special k-points: $1/V_{BZ}\int_{BZ} \Rightarrow \sum_{\boldsymbol{k}} \omega_{\boldsymbol{k}_i}$. The k-points and the weights ($\omega_{\boldsymbol{k}_i}$) are selected to recreate the integral as precisely as possible. The Monkhorst and Pack (MP) set of points [105] is commonly used as special k-points. By taking advantage of the symmetries of the BZ, the required number of k-points to obtain a distinctive precision in calculating the integral in Eq. (3.18) is lessened. The MP special points mesh is composed of evenly positioned points in the BZ that are not associated to one another through any symmetry operation. So, establishing an adequately dense $\boldsymbol{k}$-point mesh is essential for the convergence of the results of a self-consistent calculation. An appropriate number of k-points to sample the BZ can be determined by executing the energy convergence tests in a planewave DFT.

The third concept that comes into account in performing a planewave DFT calculation is pseudopotentials. The leading role in the important properties of solids, such as chemical bonding, is played by the valence electrons. However, the core electrons do not participate in those properties as they can be considered relatively frozen in their atomic structure. So, an effective potential, namely pseudopotential, can be used to imitate the influence of the core electrons on the valence electrons in a solid [52, 104]. Using pseudopotentials has many advantages such as a decrease in E_{cut} and an exceptional drop in the number of electrons and wavefunctions in the calculations because only the valence electrons are taken into account [106]. Various GGA (PBE) pseudopotentials are available, such as PAW [103] and norm-conserving (NC) [107]. The NC pseudopotentials have the constraint of maintaining the amount of charge inside a certain cutoff radius (r_c) in order to reconstruct the all-electron (AE) wavefunction. However, the PAW pseudopotentials eliminate the need for that constraint and instead use a compensation charge. As a consequence, the PAW pseudopotentials utilize less planewaves, and a lower E_{cut}, to perform the calculations and result in smoother wavefunctions as compared to the NC pseudopotentials. In the ABINIT package, one has access to a library of pseudopotentials for most of the elements in the periodic table [108].

3.4 Evaluation of exchange coupling constants by electronic structure calculations

As discussed in section 2.3, the difference between the energies of the spin triplet state and the singlet state of a dimer is described by the exchange constant J. In this section, the energy difference between those two states is evaluated by using electronic structure calculation formalism. Suppose that, at first, there is no interaction between two magnetic orbitals ϕ_1 and ϕ_2 shown in Fig. 3.1 (a), which are related to singly occupied atomic orbital at site 1 and site 2, respectively. Then, as a weak interaction is introduced between these two magnetic orbitals, an energy gap $\Delta\varepsilon$ is formed between the two levels of the spin dimer, ψ_1 and ψ_2. These two levels are given by the two linear mixtures of the two magnetic orbitals ϕ_1 and ϕ_2, and can be written as $\psi_1 \approx 1/\sqrt{2}(\phi_1 + \phi_2)$

and $\psi_2 \approx 1/\sqrt{2}(\phi_1 - \phi_2)$. Subsequently, these orbitals result in the spin configurations shown in Fig. 3.1(b). Ψ_T is related to one of the triplet states $|\psi_1\alpha\psi_2\alpha|$, which can be regarded as the lowest triplet state. The spin configurations of the singlet state are shown as $\Psi_{S1}: |\psi_1\alpha\psi_1\beta|$, $\Psi_{S2}: |\psi_2\alpha\psi_2\beta|$, and $\Psi_{S3}: 1/\sqrt{2}(|\psi_1\alpha\psi_2\beta| - |\psi_1\beta\psi_2\alpha|)$. Nevertheless, the lowest singlet state of the system is given by the configuration-interaction wavefunction Ψ_S, which is a roughly equal combination of the two singlet states Ψ_{S1} and Ψ_{S2} shown in Fig. 3.1(b). So, the lowest singlet state of the system is given by $\Psi_S = \lambda_1\Psi_{S1} + \lambda_2\Psi_{S2}$ [62]. Because the ψ_1 and ψ_2 orbitals can be calculated for the triplet state Ψ_T, they can be used to assess the configuration-interaction (CI) energies, E_T^{CI} and E_S^{CI}, corresponding to two electronic states, Ψ_T and Ψ_S, with respect to the electronic Hamiltonian of this system as

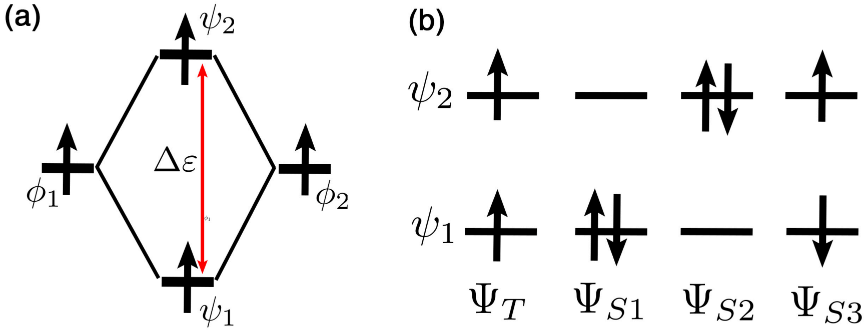

Figure 3.1 – (a) The magnetic orbitals, ϕ_1 and ϕ_2, each occupied by a single unpaired electron, with no interaction between those orbitals. Introducing weak interactions between those two magnetic orbitals yields the levels ψ_1 and ψ_2 of the spin dimer with an energy gap $\Delta\varepsilon$ between them. (b) The wave function of the electron configuration of the $S_z = 1$ triplet state, Ψ_T, as well as the wavefunctions of the three possible configurations of the singlet state, Ψ_{S1}, Ψ_{S2}, and Ψ_{S3}, are exhibited.

$$\boldsymbol{H}_e = \boldsymbol{h}(1) + \boldsymbol{h}(2) + \frac{1}{r_{12}}. \tag{3.19}$$

Here, r_{12} is the distance between electron 1 and electron 2, and $\boldsymbol{h}(1)$ and $\boldsymbol{h}(2)$ are the one-electron energies, including the terms for the kinetic energy and nuclear attraction energy, for each of the electrons. Consequently, the difference between the electronic energies of the triplet and singlet states is given by

$$E_T^{CI} - E_S^{CI} = -2K_{12} + \frac{\Delta\varepsilon}{J_{11} - J_{12}}, \tag{3.20}$$

where the exchange integral, K_{12}, is

$$K_{12} = \langle\phi_1(1)\phi_2(2)|\frac{1}{r_{12}}|\phi_2(1)\phi_1(2)\rangle, \tag{3.21}$$

and the Coulomb repulsions, J_{11} and J_{12}, are

$$\begin{aligned} J_{11} &= \langle\phi_1(1)\phi_1(2)|\frac{1}{r_{12}}|\phi_1(1)\phi_1(2)\rangle, \\ J_{12} &= \langle\phi_1(1)\phi_2(2)|\frac{1}{r_{12}}|\phi_1(1)\phi_2(2)\rangle. \end{aligned} \tag{3.22}$$

The energy difference between the spin triplet state and the spin singlet state of the dimer system in Eq. (2.17) by the Heisenberg spin Hamiltonian of Eq. (2.9) can be mapped onto the configuration-interaction (i.e. electronic) energy difference between the triplet state and the single state calculated by the electronic Hamiltonian of Eq. (3.19). In other words, $E_T^{Spin} - E_S^{Spin} = E_T^{CI} - E_S^{CI}$. Therefore, spin exchange J can be achieved as [62]

$$J = -2K_{12} + \frac{\Delta\varepsilon}{J_{11} - J_{12}}. \tag{3.23}$$

Considering the notation of $J < 0$ for the ferromagnetic exchange and $J > 0$ for the antiferromagnetic one, and the fact that the exchange repulsion K_{12} and the effective on-site repulsion $U_{eff} = J_{11} - J_{12}$ are positive, the total exchange interaction is written as a combination of the ferromagnetic part $J_F = -2K_{12}$ and of the antiferromagnetic part $J_{AFM} = \Delta\varepsilon/(J_{11} - J_{12})$ [62]. What we understand from that conclusion is threefold: (1) that by augmenting the overlap integral, $\Delta\varepsilon$ increases, which leads to a larger J_{AFM}, such as magnetization changing from FM to AFM in some materials when mechanical pressure is applied and hence the overlap integral (hopping integral) increases as the interatomic distances decrease [57]; (2) that if the U_{eff} decreases, J_{AFM} increases; and (3) that by making the exchange integral K_{12} larger, the tendency towards ferromagnetism,

J_F, grows [62].

3.5 Broken-symmetry approach within the DFT framework

As discussed, for a spin dimer, the magnetic energy levels of this system resulting from the exchange interaction among a pair of spins was represented by the Heisenberg spin Hamiltonian $\boldsymbol{H}_s$ in Eq. (2.6) along with the spin exchange coupling constant J. This spin exchange constant J is the difference in the energy of the triplet spin state and the spin singlet state in Eq. (2.17). Subsequently, as explained in section 3.4, mapping the energy levels of the spin Hamiltonian $\boldsymbol{H}_s$ onto those of the electronic Hamiltonian $\boldsymbol{H}_e$, J is described as the difference in the electronic energies of the triplet state and the singlet state in Eq. (3.23). In the case of a general magnetic system, the magnetic energy levels can be considered by generalizing the Heisenberg spin model. As shown in Eq. (2.18), one can achieve that generalization of the Heisenberg Hamiltonian by summing over all the pairwise magnetic interactions using the Heisenberg spin Hamiltonian in Eq. (2.18). Nevertheless, in practice, an analytical specification of the pure eigenstates of the Heisenberg spin Hamiltonian concerning the spin exchange constants and their numerical evaluations, are unfeasible. Moreover, the assessment of the eigenvalue levels of the electronic Hamiltonian for this general magnetic system is impractical [62]. To make those analytical calculations and numerical evaluations practical, Noodleman proposed a different model. His model simplifies the computational endeavors to calculate the Heisenberg exchange coupling constants J by using the difference between the energies of the highest pure spin multiplet and the broken-symmetry state [109]. In order to elaborate on Noodleman's model, we will now re-examine the spin dimer.

As discussed in 2.3, the total wavefunction of a spin dimer system must be antisymmetric. The total wavefunction of the spin singlet is given by

$$\psi(S=0,S_z=0)=\frac{1}{2}\left[\phi_A(\boldsymbol{r}_1)\phi_B(\boldsymbol{r}_2)+\phi_A(\boldsymbol{r}_2)\phi_B(\boldsymbol{r}_1)\right]\left[\alpha(S_1)\beta(S_2)-\alpha(S_2)\beta(S_1)\right], \tag{3.24}$$

where the spatial part is symmetric and the spin part is antisymmetric, hereby giving an antisymmetric total wavefunction. As for the total wavefunction of the triplet state, the total wavefunctions are given by

$$\begin{aligned}
\psi(S=1,S_z=1) &= \frac{1}{\sqrt{2}}\left[\phi_A(\boldsymbol{r}_1)\phi_B(\boldsymbol{r}_2)-\phi_A(\boldsymbol{r}_2)\phi_B(\boldsymbol{r}_1)\right]\alpha(S_1)\alpha(S_2),\\
\psi(S=1,S_z=-1) &= \frac{1}{\sqrt{2}}\left[\phi_A(\boldsymbol{r}_1)\phi_B(\boldsymbol{r}_2)-\phi_A(\boldsymbol{r}_2)\phi_B(\boldsymbol{r}_1)\right]\beta(S_1)\beta(S_2),\\
\psi(S=1,S_z=0) &= \frac{1}{2}\left[\phi_A(\boldsymbol{r}_1)\phi_B(\boldsymbol{r}_2)-\phi_A(\boldsymbol{r}_2)\phi_B(\boldsymbol{r}_1)\right]\left[\alpha(S_1)\beta(S_2)+\alpha(S_2)\beta(S_1)\right].
\end{aligned} \tag{3.25}$$

As previously mentioned, the wavefunctions of non-interacting electrons in the KS system are written as a single determinant formed from a set of KS orbitals, which are obtained by solving Eq. (3.11). The KS single determinant for a spin dimer system is given by

$$\psi_{KS} = \frac{1}{\sqrt{2}}\begin{pmatrix}\phi_A(r_1)\chi_A(S_1) & \phi_A(r_2)\chi_A(S_2)\\ \phi_B(r_1)\chi_B(S_1) & \phi_B(r_2)\chi_B(S_2)\end{pmatrix}. \tag{3.26}$$

The question that arises is: is it possible to write the singlet and triplet states as the single determinant in Eq. (3.26)? To answer this question, we begin by writing the $S_z = 1$ triplet state as the single determinant as such

$$\begin{aligned}
\psi_{KS}(\uparrow\uparrow) &= \frac{1}{\sqrt{2}}\begin{pmatrix}\phi_A(\boldsymbol{r}_1)\alpha(S_1) & \phi_A(\boldsymbol{r}_2)\alpha(S_2)\\ \phi_B(\boldsymbol{r}_1)\alpha(S_1) & \phi_B(\boldsymbol{r}_2)\alpha(S_2)\end{pmatrix}\\
&= \frac{1}{\sqrt{2}}\left[\phi_A(\boldsymbol{r}_1)\phi_B(\boldsymbol{r}_2)-\phi_A(\boldsymbol{r}_2)\phi_B(\boldsymbol{r}_1)\right]\alpha(S_1)\alpha(S_2),
\end{aligned} \tag{3.27}$$

which is equivalent to the $\psi(S=1,S_z=1)$ in Eq. (3.25). The same way, the $S_z=-1$

triplet state is written as a single determinant:

$$\begin{aligned}\psi_{KS}(\downarrow\downarrow) &= \frac{1}{\sqrt{2}}\begin{pmatrix}\phi_A(\boldsymbol{r}_1)\beta(S_1) & \phi_A(\boldsymbol{r}_2)\beta(S_2)\\ \phi_B(\boldsymbol{r}_1)\beta(S_1) & \phi_B(\boldsymbol{r}_2)\beta(S_2)\end{pmatrix}\\ &= \frac{1}{\sqrt{2}}\left[\phi_A(\boldsymbol{r}_1)\phi_B(\boldsymbol{r}_2) - \phi_A(\boldsymbol{r}_2)\phi_B(\boldsymbol{r}_1)\right]\beta(S_1)\beta(S_2),\end{aligned} \tag{3.28}$$

which is equal to $\psi(S = 1, S_z = 1)$ in Eq. (3.25). However, the terms $\frac{1}{\sqrt{2}}[\uparrow\downarrow + \downarrow\uparrow]$ and $\frac{1}{\sqrt{2}}[\uparrow\downarrow - \downarrow\uparrow]$, representing respectively the $S_z = 0$ triplet state and the the singlet state, cannot be written as a single determinant. Thus, it is not possible to calculate the eigenstates of these pure spin states of $S_z = 0$ triplet and the singlet, by employing DFT. To deal with this difficulty, the broken-symmetry states $|BS\rangle$ need to be defined. They are given by

$$\begin{aligned}|BS\rangle &= \alpha(S_1)\beta(S_2) = |\uparrow\downarrow\rangle\,,\\ |BS\rangle &= \beta(S_1)\alpha(S_2) = |\downarrow\uparrow\rangle\,.\end{aligned} \tag{3.29}$$

The energy of these $|BS\rangle$ states can be calculated with regard to the Heisenberg spin Hamiltonian $\boldsymbol{H}_s$ for a spin dimer in Eq. (2.6) as

$$\langle BS|\boldsymbol{H}_s|BS\rangle = -\frac{1}{4}J. \tag{3.30}$$

Bearing that in mind, one can conclude that the energy of a $|BS\rangle$ state has a central position among the energies of the singlet state and of the triplet state, as shown in Fig. 3.2.

Those BS states can be written as single determinant wavefunctions in the form of Eq. (3.26). The BS state $|\uparrow\downarrow\rangle$ is written as

$$\begin{aligned}\psi_{KS}(\uparrow\downarrow) &= \frac{1}{\sqrt{2}}\begin{pmatrix}\phi_A(\boldsymbol{r}_1)\alpha(S_1) & \phi_A(\boldsymbol{r}_2)\alpha(S_2)\\ \phi_B(\boldsymbol{r}_1)\beta(S_1) & \phi_B(\boldsymbol{r}_2)\beta(S_2)\end{pmatrix}\\ &= \frac{1}{\sqrt{2}}\left[\phi_A(\boldsymbol{r}_1)\phi_B(\boldsymbol{r}_2)\alpha(S_1)\beta(S_2) - \phi_A(\boldsymbol{r}_2)\phi_B(\boldsymbol{r}_1)\alpha(S_2)\beta(S_1)\right].\end{aligned} \tag{3.31}$$

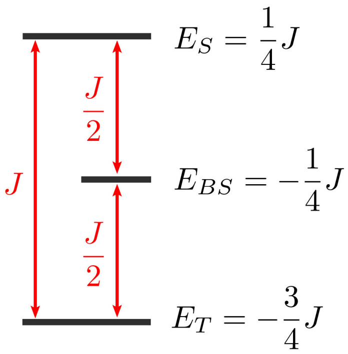

Figure 3.2 – The energy of the broken-symmetry state (E_{BS}) is shown in the middle of the energies of the pure spin states, singlet state (E_S) and triplet state (E_T), of a spin dimer.

Also, the BS state $|{\downarrow\uparrow}\rangle$ is given by

$$\begin{aligned}\psi_{KS}(\downarrow\uparrow) &= \frac{1}{\sqrt{2}}\begin{pmatrix}\phi_A(\boldsymbol{r}_1)\beta(S_1) & \phi_A(\boldsymbol{r}_2)\beta(S_2)\\ \phi_B(\boldsymbol{r}_1)\alpha(S_1) & \phi_B(\boldsymbol{r}_2)\alpha(S_2)\end{pmatrix}\\ &= \frac{1}{\sqrt{2}}\left[\phi_A(\boldsymbol{r}_1)\phi_B(\boldsymbol{r}_2)\beta(S_1)\alpha(S_2) - \phi_A(\boldsymbol{r}_2)\phi_B(\boldsymbol{r}_1)\beta(S_2)\alpha(S_1)\right].\end{aligned} \tag{3.32}$$

It can be shown that those BS states are equal to a combination of the singlet state $\psi(S=0, S_z=0)$ in Eq. (3.29) and of the third state of the triplet $\psi(S=1, S_z=0)$ in Eq. (3.25) as

$$\begin{aligned}\psi_{KS}(\uparrow\downarrow) &= \frac{1}{\sqrt{2}}[\psi(S=0, S_z=0) + \psi(S=1, S_z=0)],\\ \psi_{KS}(\downarrow\uparrow) &= \frac{1}{\sqrt{2}}[\psi(S=0, S_z=0) - \psi(S=1, S_z=0)].\end{aligned} \tag{3.33}$$

Note that the real singlet state as well as the $S_z = 0$ triplet state are eigenstates of the $\boldsymbol{S}^2$ with the eigenvalues of 0 ($S=0$) and 1 ($S=1$) respectively. However, the BS states are not the eigenstates of $\boldsymbol{S}^2$ as they are a mix of the singlet state and of the $S_z = 0$ triplet state. Also, the pure spin states in the maximum spin state S_{max}, namely the high spin states, are defined as

$$\begin{aligned}
|S_{max}\rangle &= \alpha(S_1)\alpha(S_2) = |\uparrow\uparrow\rangle\,, \\
|S_{max}\rangle &= \beta(S_1)\beta(S_2) = |\downarrow\downarrow\rangle\,.
\end{aligned} \tag{3.34}$$

The difference of the spin energy of the $|S_{max}\rangle$ states, calculated for the triplet state in Eq. (2.14) as $(1/4)J$, and of the spin energy of the $|BS\rangle$ states, given in Eq. (3.30) as $(-1/4)J$, is obtained as $E_s(S_{max}) - E_s(BS) = (1/2)J$. This difference between spin energies can be mapped onto the difference between the electronic energies evaluated from DFT calculations, which results in

$$E_{DFT}(S_{max}) - E_{DFT}(BS) = \frac{1}{2}J. \tag{3.35}$$

Note that the $|BS\rangle$ states in Eq. (3.29) are not the eigenstates of the Heisenberg spin Hamiltonian $\boldsymbol{H}_s$ in Eq. (2.6) as opposed to the true eigenstates of the system. As DFT depends on the BS states rather than on the true eigenstates of a magnetic system, the exchange coupling constants of any real magnetic system can be evaluated by using electronic structure calculation through the broken-symmetry formalism and on the basis of energy-mapping approaches. In the next sections, two different energy-mapping approaches are introduced: the supercell total energy differences approach and the four-states energy mapping approach.

3.5.1 Supercell total energy mapping approach

The first method to evaluate the Js in a realistic magnetic material based on DFT and by exploiting the BS states is conducted by first considering diverse collinear spin arrangements of the magnetic moments within a supercell, then by calculating the total energies corresponding to these different spin configurations, and finally by mapping these total energies onto a Heisenberg spin Hamiltonian of the form of [48, 51, 92]

$$\boldsymbol{H} = \boldsymbol{H}_0 + \sum_{i>j} J_{ij} \boldsymbol{S}_i \cdot \boldsymbol{S}_j, \tag{3.36}$$

where $\boldsymbol{H}_0$ represents the spin-independent component of the Hamiltonian. The S=1/2 spin operators related to sites i and j are denoted, respectively, by $\boldsymbol{S}_i$ and $\boldsymbol{S}_j$. J_{ij} represents the exchange coupling constant between these spin operators. Based on the Heisenberg spin Hamiltonian of Eq. (3.36), $J_{ij} > 0$ represents an antiferromagnetic (AFM) spin exchange interaction and $J_{ij} < 0$ a ferromagnetic (FM) one. This Hamiltonian can be written in second quantization as [91]

$$\boldsymbol{H} = \boldsymbol{H}_0 + \sum_{i>j} \frac{J_{ij}}{2} \sum_{\sigma\sigma'} \left[c^{\dagger}_{i\sigma} c_{i\sigma'} c^{\dagger}_{j\sigma'} c_{j\sigma} - \frac{1}{2} c^{\dagger}_{i\sigma} c_{i\sigma} c^{\dagger}_{j\sigma'} c_{j\sigma'} \right], \tag{3.37}$$

where the creation operators and annihilation operators of electrons with spins σ or σ', and the magnetic orbital of sites i or j are introduced. For example, the creation operator for an electron with spin σ' in the magnetic orbital of site j is given by $c^{\dagger}_{j\sigma'}$, and the annihilation operator by $c_{j\sigma'}$. By supposing that the magnetic state $|\alpha\rangle$ of a supercell with the orbital of site i possessing Ising spin $\sigma_i = \pm 1$, we can write this state as

$$|\alpha\rangle = \prod_i c^{\dagger}_{i\sigma_i} |0\rangle . \tag{3.38}$$

Then, the expectation value of the Heisenberg Hamiltonian of Eq. (3.37) can be formulated as an Ising Hamiltonian of the form of

$$\varepsilon_{\alpha}^{DFT} = \langle \alpha | \boldsymbol{H} | \alpha \rangle = \varepsilon_0 + \frac{1}{4} \sum_{i>j} J_{ij} \sigma_i \sigma_j, \tag{3.39}$$

where the spin-independent part of the total energy is designated by ε_0. The energies related to different spin configurations in a supercell can be written with respect to the exchange couplings as:

$$\varepsilon_{\alpha}^{DFT} = \varepsilon_0 + \sum_k a_{\alpha,k} J_k . \tag{3.40}$$

In Eq. (3.40), the second term is called the Ising energy of spin configuration α, and is defined as

$$\varepsilon_{\alpha}(\text{Ising}) = \sum_{k} a_{\alpha,k} J_k, \tag{3.41}$$

in which the sum runs over the number of magnetic couplings, k. Moreover, depending on the spin configuration under study, the coefficients $a_{\alpha,k}$, will represent different integer numbers. Note that α indicates the number of inequivalent configurations. Given the number of equivalent configurations to a certain configuration (i.e. degeneracy) by g_{α}, we have

$$\Sigma_{\alpha} g_{\alpha} = 2^N, \tag{3.42}$$

where N is the number of magnetic moments. In other words, the sum of the degeneracy of the configurations, where the sum runs over the number of configurations, gives the total number of configurations.

Afterwards, in order to calculate the spin-independent part of the total energy, ε_0, a weighted average of the calculated energy in Eq. (3.40) is considered as

$$\frac{1}{2^N} \sum_{\alpha} g_{\alpha} \varepsilon_{\alpha} = \frac{1}{2^N} \varepsilon_0 \sum_{\alpha} g_{\alpha} + \frac{1}{2^N} \sum_{k} \sum_{\alpha} g_{\alpha} a_{\alpha,k} J_k, \tag{3.43}$$

which due to $\sum_{\alpha} g_{\alpha} a_{\alpha k} = 0$ and Eq. (3.42), it is simplified to

$$\varepsilon_0 = \frac{1}{2^N} \sum_{\alpha} g_{\alpha} \varepsilon_{\alpha}. \tag{3.44}$$

Eventually, the exchange couplings can be evaluated numerically by minimizing the deviation of the DFT average energies and Ising energies for all the configurations, which can be fulfilled by a least-squares fitting analysis that includes minimizing the following error function:

$$F = \sum_{\alpha} g_{\alpha} \left(\varepsilon_{\alpha}^{DFT} - \varepsilon_0 - \sum_{k} a_{\alpha,k} J_k \right)^2 . \tag{3.45}$$

The total number of spin configurations depends on the number of magnetic moments of molecules within a defined cell unit. Also, to evaluate the exchange couplings passing the single cell, larger cells, namely supercells, must be created. Supercells are defined by multiplying the single cell in different crystallographic axes. For example, a supercell, $2\times1\times1$, which is created by doubling the single cell along the a axis, includes 16 molecules, and hence the total number of possible spin configurations is $2^{16} = 65536$. However, by taking into account the spin reversal and crystalline symmetries, the number of configurations can be decreased to a certain number of inequivalent configurations.

3.5.2 Four-state energy mapping approach

In addition to the supercell total energy mapping approach explained in section 3.5.1, the four-state energy mapping approach can be employed to evaluate the Heisenberg spin exchange constants. In this approach, the specific exchange coupling constant of a given magnetic system can be evaluated by means of the energies of only four different spin configurations. In those four configurations, four different spin arrangements are considered for the two spin sites from which originates the exchange coupling constant under investigation, and the same alignment is assigned to the remaining spin sites. In the spin Hamiltonian of Eq. (3.36), defining the effective parameter of $J_{ij}^{eff} = S_i S_j J_{ij}$ results in turning the spin vectors $\boldsymbol{S}_i$ and $\boldsymbol{S}_j$ into unit vectors. For instance, in order to find J_{12}^{eff}, the four states energies, as given by E_1 to E_4 in Eq. (3.46), must be calculated. In these four states, four different spin arrangements, $\uparrow\uparrow$, $\uparrow\downarrow$, $\downarrow\uparrow$, and $\downarrow\downarrow$, are considered, in which the first component is the spin sign for S_1 and the second component is the spin sign for S_2. The $\uparrow$ is equivalent to unit vector $(0,0,1)$, which signifies the direction of the spin unit vector along the positive direction of the z axis, and $\downarrow$ to $(0,0,-1)$ along the negative direction. For all the other spin sites, the same spin alignment (i.e. all $\uparrow$ or all ↓, depending on the experimental or low-energy spin states) are considered [62].

$$\begin{aligned}
E_1 &= E\left[S_1 :\uparrow, S_2 :\downarrow, \text{other spin sites} :\uparrow\right], \\
E_2 &= E\left[S_1 :\downarrow, S_2 :\uparrow, \text{other spin sites} :\uparrow\right], \\
E_3 &= E\left[S_1 :\uparrow, S_2 :\uparrow, \text{other spin sites} :\uparrow\right], \\
E_4 &= E\left[S_1 :\downarrow, S_2 :\downarrow, \text{other spin sites} :\uparrow\right]. \qquad (3.46)
\end{aligned}$$

Then, J_{12}^{eff} is evaluated with

$$J_{12}^{eff} = \frac{E_1 + E_4 - E_2 - E_3}{4}. \qquad (3.47)$$

This technique can be extended to all the spin pairs ij corresponding to different spin exchange paths J_{ij}, and hence to evaluate all the exchange couplings in a magnetic system.

CHAPTER 4

MODEL HAMILTONIAN FOR NIT2PY

Constructing an appropriate model Hamiltonian is necessary to provide a magnetic energy spectrum, and to determine the magnetic properties of a system. This chapter will discuss the determination and specification of the spin Hamiltonian relevant to the NIT2Py system. The NIT2Py model Hamiltonian is designed based on the Heisenberg exchange interactions of the system. To begin, a model Hamiltonian is created by the exchange interactions corresponding to the spin contributions of the first nearest neighbors. The Hamiltonian needs to be invariant with respect to all the symmetry operations of the system. It is a powerful tool in order to reduce the number of interactions. Secondly, a more systematic approach is discussed that considers all the possible exchange interactions between magnetic moments based on the symmetry operations of NIT2Py. The general spin Hamiltonians are created for a NIT2Py single cell and supercell. Those general spin Hamiltonians will be employed in chapter 6 to find the signs and magnitudes of the exchange coupling constants (Js) in the single cell and supercell.

4.1 Crystal structure of NIT2Py

NIT2Py compound (see section I.1 of Annex I) was synthesized by a group of collaborating chemists: Professor Christian Reber of University of Montreal, Professor Dominique Juneau and his PhD student Anthony Lannes of the University Claude Bernard Lyon 1. The first crystals were obtained in the form of very fragile, long needle-shaped crystals, as shown in Fig. 4.1(a). Single crystals of NIT2Py were required to perform physical measurements, and so the recrystallization process was carried out several times by changing the parameters, such as the type of solvents and temperature, to obtain large enough single crystals (see section I.3 of Annex I). The successful result was achieved by means of the slow evaporation method, in which the NIT2Py crystals were dissolved in a mixture of dichloromethane and heptane that was then kept in a water bath of 30 C°, which yielded large purple crystals as shown in Fig. 4.1(b). The crystal structure of the resulting large purple single crystals was examined in University of Montreal using an X-ray diffraction measurement with a monocrystal diffractometer from the Bruker company (Microstar X8 PROTEUM), which has a source of FR591 rotating anode. The resulting crystal structure of NIT2Py is in accordance with the published values in the reference [110].

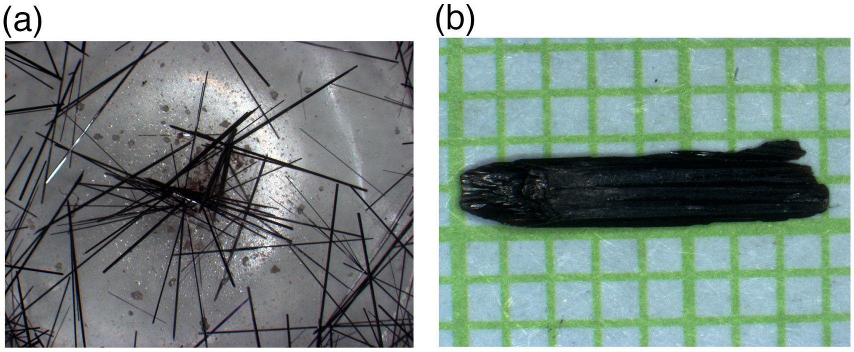

Figure 4.1 – (a) Long needle-shaped crystals of NIT2Py. (b) Large crystal of NIT2Py obtained from a recrystalization process. Note that a NIT2Py crystal grows along the crystallographic *a* axis.

One of our several attempts to recrystallize NIT2Py lead to the discovery a new phase of NIT2Py. By using the X-ray diffraction measurement, we realized that the crystal structure of the new phase, namely β phase, is different than the first phase (see section I.2 of Annex I).

In both the α and β phases, the NIT2Py molecules are condensed into crystals of monoclinic structure with the space group $P2_1/c$. In the α phase, the lattice parameters include the lengths of the cell edges a=6.1471(2) Å, b=30.061(1) Å, and c=12.9583(4) Å, and the angles between them $\alpha = 90.00°$, $\beta = 100.269(2)°$, and $\gamma = 90.00°$. However, in the β phase, the lattice parameters are a=6.2696(2) Å, b=40.3246(14) Å, and c=9.8488(3) Å, and the angles are $\alpha = 90.00°$, $\beta = 99.464(2)°$, and $\gamma = 90.00°$. The two phases have about the same length along the crystallographic a axis, which is determined by X-ray as the direction of the crystal growth. However, the crystallographic c axis is longer in the α phase, and the crystallographic b axis is much longer in the β phase.

In addition, the cell volume is different in the two phases, which is 2356.14(13) Å^3 for the α phase and 2456.1(2) Å^3 for the β phase. Thus, the density of those two phases, defined as the chemical formula weight of NIT2Py, 234.28 g/mol, divided by the cell volume, are not identical.

There are two molecules per asymmetric unit, the smallest unit of the crystal that can reproduce the unit cell through the application of the symmetry operations. However, the alignment of those two molecules in the asymmetric unit of the α and β phases is not identical. The NIT2Py unit cell of each of the α and β phases is composed of 8 molecules, as shown in Fig. 4.2(a) and (b), respectively. The way the NIT2Py molecules are oriented with respect to one another, and hence, the way those molecules are packed in the crystal, are different in each of the phases.

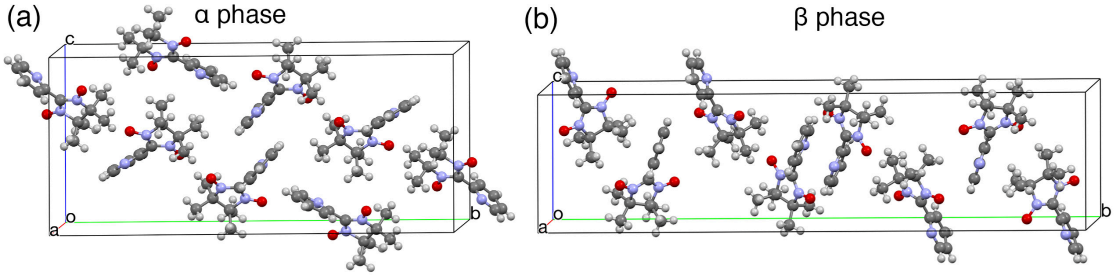

Figure 4.2 – Unit cell of NIT2Py for (a) the α phase and (b) the β phase.

As shown in Fig. 4.3, the alignment of the NIT2Py molecules in the α and β phases are compared along different crystallographic axes. In each molecule, the 2-pyridyl ring is considered as the head of the molecule, and the NN ring as its body. Also the middle carbon atom in the ONCNO branch of each molecule is taken as the reference point to measure the intermolecular distances. As shown in Fig. 4.3(a), when looking at a line of molecules along the c axis, we notice that each molecule has its body perpendicular to the head of the next molecule in the same line, and that they have identical intermolecular distances. In the next parallel line of molecules along the c axis, each pair of molecules with a head to head alignment has a shorter intermolecular distance as compared to the next pair of molecules in the same line having their bodies facing each other and their heads facing opposite directions. However, as shown in Fig. 4.3(b), in the β phase, a group consisting of four lines of molecules has their heads upwards, and another group including the next four lines of molecules has their head downwards.

As shown in Fig. 4.3(e) and (f), in α phase, molecules are creating 2D planes parallel to each other along the crystallographic $(\bar{1}02)$ planes, which is not observed in the β phase.

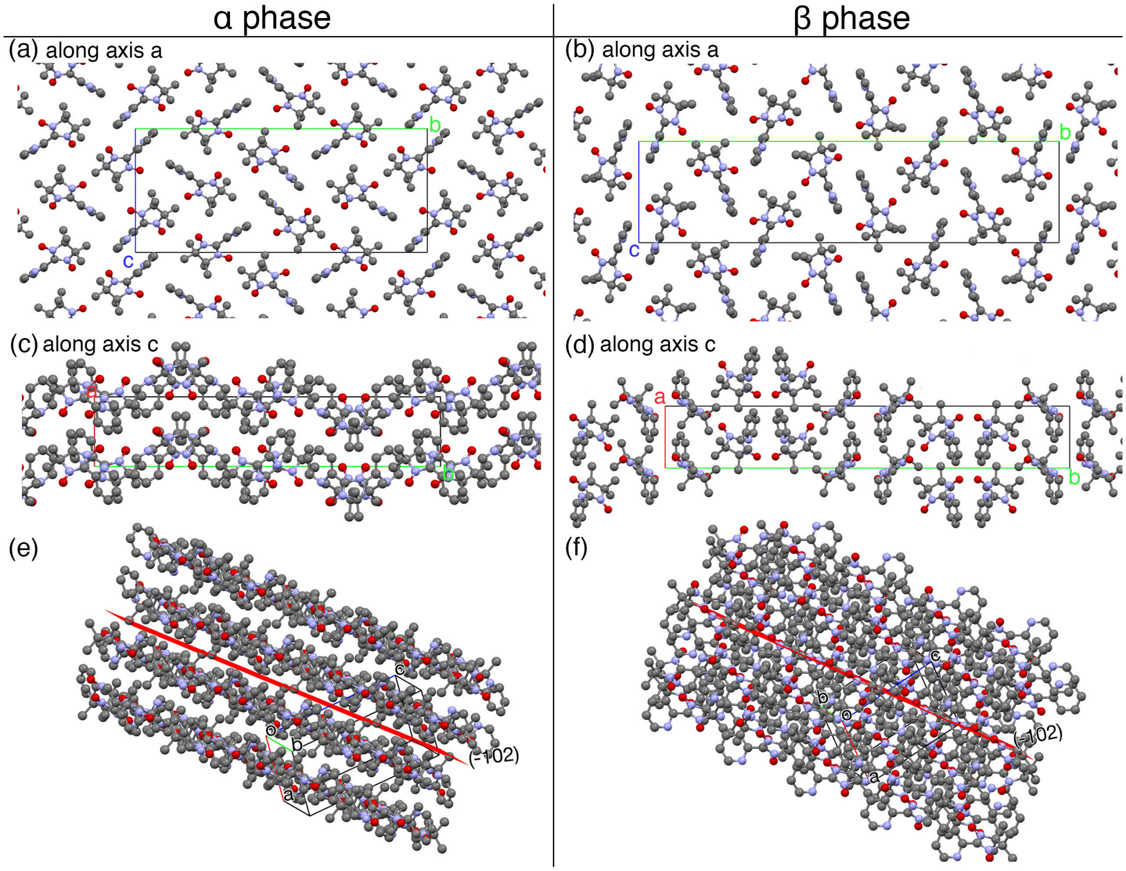

Figure 4.3 – The NIT2Py molecules shown along the a axis for (a) the α phase and (b) the β phase. Also, the way those molecules are oriented along the *c* axis is compared for (c) the α phase (d) the β phase. The molecules create 2D planes in (e) the α phase, but not in (f) the β phase.

As the focus of this research is on the magnetic properties of the α phase, we discuss the symmetry properties and design the spin Hamiltonians for the single cell and supercell of the α phase in the next sections. Thereafter, if the phase type of the NIT2Py is not mentioned, we are referring to the α phase.

4.2 Symmetry properties of NIT2Py

The symmetry properties of the system are studied based on the NIT2Py crystallographic space group and the corresponding symmetry operations. Because those symmetry operations leave the Hamiltonian invariant, one can exploit them to lessen the number of necessary interactions. The NIT2Py space group is $P2_1/c$, with four symmetry operators given in Table 4.I. As shown in Fig. 4.4, the NIT2Py molecules are labeled from 1 to 8 based on the symmetry group relations between them. The relation between the eight molecules can be understood by applying the symmetry operators on each of the two inequivalent molecules in the NIT2Py asymmetric unit, which are labeled as molecules 1 and 5 and are shown respectively in brown and gray in Fig. 4.5. Applying the four possible symmetry operators of the NIT2Py unit cell in Table 4.I to molecule 1 leads to molecules 1, 2, 3, and 4. The same exercise employed on molecule 5 yields

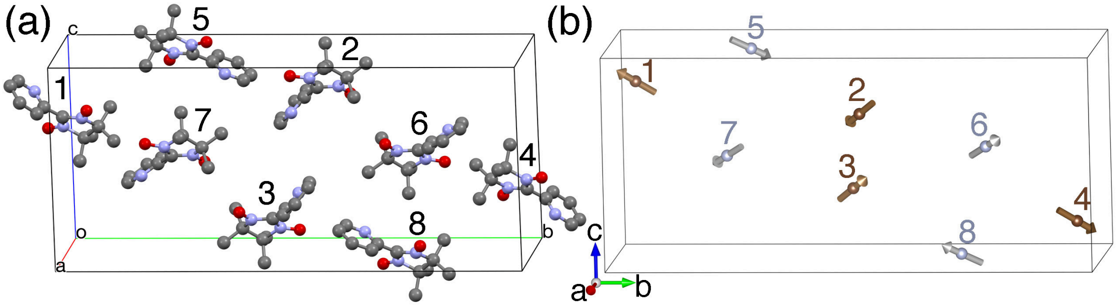

Figure 4.4 – (a) A NIT2Py single cell. The molecules are labeled 1 to 8. (b) Only the central C atoms of the ONCNO branch of each molecule is shown. The arrow represents the orientation of each molecule in the cell.

#	Symmetry Operator	Related Molecules
1	(x, y, z)	Identity
2	(-x, 1/2+y, 1/2-z)	1↔2, 3↔4, 5↔6, 7↔8
3	(-x, -y, -z)	1↔4, 2↔3, 5↔8, 6↔7
4	(x, 1/2-y, 1/2+z)	1↔3, 2↔4, 5↔7, 6↔8

Table 4.I – The four symmetry operators of the NIT2Py single cell. The last column represents the correlations between the eight molecules in the unit cell after applying each of the symmetry operators.

molecules 5, 6, 7 and 8. Therefore, the eight molecules in the NIT2Py unit cell can be categorized in two symmetry groups: group I includes molecules 1, 2, 3, and 4, and group II is composed of molecules 5, 6, 7, and 8.

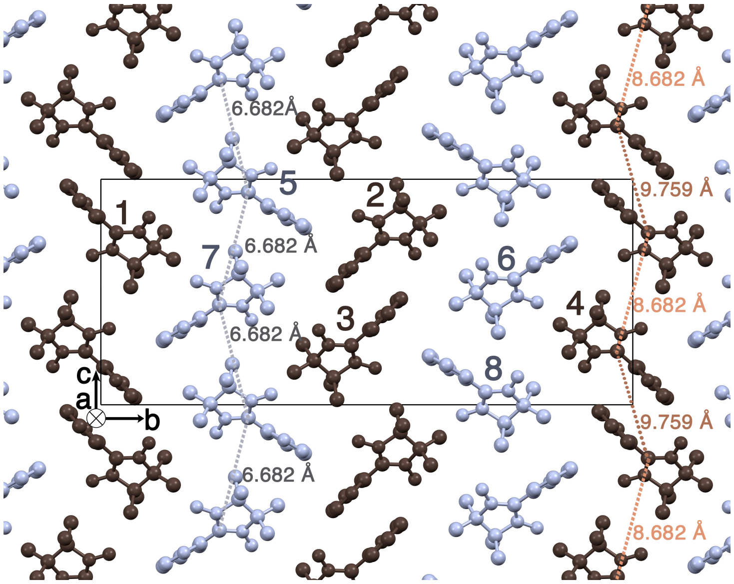

Figure 4.5 – The orientation of the molecules in an NIT2Py crystal unit cell along axis *a*. Molecules labeled as 1, 2, 3, and 4 are part of the symmetry group I. Molecules 5, 6, 7, and 8 belong to symmetry group II. The brown and gray colors indicate the molecules corresponding to symmetry groups I and II respectively. For the purpose of simplicity, the hydrogen atoms are omitted from this representation.

4.3 Spin Hamiltonian of NIT2Py in terms of the nearest-neighbor interactions

Because the spin-orbit coupling interactions are relatively negligible in most organic free radical molecules, the orbital contribution is quenched, and hence the states of the system can be determined as pure spin multiplets. So, when designing a spin Hamiltonian, only the spin angular momentum operators and the interactions between them are taken into account. Moreover, the spin Hamiltonian must properly express the symmetry of the molecules and the lattice, be invariant under all symmetry operations, and maintain the space group symmetry. Consequently, symmetry plays an important role in creating a valid model Hamiltonian.

The starting point is to consider a spin Hamiltonian given by

$$H=\sum_{i,j,k}\sum_{A>B}(J^{A,B}_{(0,0,0)}\boldsymbol{S}^{A}_{(i,j,k)}\cdot\boldsymbol{S}^{B}_{(i,j,k)}+J^{A,B}_{(1,0,0)}\boldsymbol{S}^{A}_{(i,j,k)}\cdot\boldsymbol{S}^{B}_{(i+1,j,k)}+J^{A,B}_{(0,1,0)}\boldsymbol{S}^{A}_{(i,j,k)}\cdot\boldsymbol{S}^{B}_{(i,j+1,k)}$$
$$+J^{A,B}_{(0,0,1)}\boldsymbol{S}^{A}_{(i,j,k)}\cdot\boldsymbol{S}^{B}_{(i,j,k+1)}), \tag{4.1}$$

where $J^{A,B}_{(n,m,l)}$ are the coefficients of interactions between the magnetic moments of molecules A and B at sites (i,j,k) with $\mathbf{S}^{A}_{(i,j,k)}$ and $\mathbf{S}^{B}_{(i,j,k)}$ spins, respectively. The Hamiltonian of Eq. (4.1) cannot be complete without taking into account all the possible interactions in different directions, but, for the purpose of our work, we only focused on the interactions in the $(0,0,0)$, $(1,0,0)$, $(0,1,0)$, and $(0,0,1)$ directions. Because the spin Hamiltonian must be invariant under the symmetry operations, there has to be symmetry between its different exchange interaction terms. So, the molecules in symmetry groups I and II are expected to have symmetric interactions. For instance, the interactions between molecules 1 and 4 as well as between molecules 2 and 3 in symmetry group I have the same symmetries as the interactions between molecules 5 and 7 as well as between molecules 6 and 8 in symmetry group II.

Different magnetic interactions between the eight molecules in the NIT2Py unit cell are categorized depending on their corresponding Js. All the magnetic interactions with an identical J are set into one term in the Hamiltonian. We use the symmetry operators in Table 4.I to identify the interactions with an indistinguishable J. First, the interactions between molecules of symmetry group II are examined. We verify if the interaction between molecules 5 and 7 at sites (i,j,k) in the unit cell is identical to the one between molecule 5 in the unit cell and molecule 7 in the nearest neighboring cell along the c axis. In other words, is interaction $(\boldsymbol{S}^{5}_{(i,j,k)}\cdot\boldsymbol{S}^{7}_{(i,j,k)})$ identical to interaction $(\boldsymbol{S}^{5}_{(i,j,k)}\cdot\boldsymbol{S}^{7}_{(i,j,k+1)})$? The same question arises for the interactions corresponding to the other two molecules of symmetry group II: is interaction $\boldsymbol{S}^{8}_{(i,j,k)}\cdot\boldsymbol{S}^{6}_{(i,j,k)}$ identical to interaction $\boldsymbol{S}^{8}_{(i,j,k)}\cdot\boldsymbol{S}^{6}_{(i,j,k+1)}$? To answer those questions, the corresponding symmetry operators can be used and the distances between the interacting molecules can be compared.

As shown in Fig. 4.5, the distance between molecules 5 and 7 in the same cell is the same as the distance between molecule 5 in one cell and molecule 7 in the nearest neighboring cell along the c axis. The result can be repeated for molecules 6 and 8. The corresponding interactions have the same exchange coupling constant, J_{III}, and are hence placed in the same term as

$$J_{\mathrm{III}}\left(\boldsymbol{S}^{5}_{(i,j,k)}\cdot\boldsymbol{S}^{7}_{(i,j,k)}+\boldsymbol{S}^{5}_{(i,j,k)}\cdot\boldsymbol{S}^{7}_{(i,j,k+1)}+\boldsymbol{S}^{8}_{(i,j,k)}\cdot\boldsymbol{S}^{6}_{(i,j,k)}+\boldsymbol{S}^{8}_{(i,j,k)}\cdot\boldsymbol{S}^{6}_{(i,j,k+1)}\right), \qquad (4.2)$$

which will then be integrated into the Hamiltonian.

We applied the same logic to the interactions between all of the molecules in symmetry group I. The interactions between molecules 1 and 4 as well as between molecules 2 and 3 in the same cell are compared to the interactions in which one molecule is in a cell, and the other is in its nearest neighboring cell along the c axis.

As shown in Fig. 4.5, the distance between molecules 1 and 4 in the unit cell is not the same as the distance between molecule 1 in the cell and molecule 4 in the nearest neighboring cell along the c axis. So, the corresponding interactions, $\boldsymbol{S}^{1}_{(i,j,k)}\cdot\boldsymbol{S}^{4}_{(i,j,k)}$ and $\boldsymbol{S}^{1}_{i,j,k}\cdot\boldsymbol{S}^{4}_{i,j,k+1}$, have different exchange coupling constants. The same result is obtained for interactions $\boldsymbol{S}^{2}_{(i,j,k)}\cdot\boldsymbol{S}^{3}_{(i,j,k)}$ and $\boldsymbol{S}^{2}_{i,j,k}\cdot\boldsymbol{S}^{3}_{i,j,k+1}$.

In the same way, the nearest neighboring interactions between the molecules of the same symmetry group, and among the molecules interacting between the two symmetry groups are examined, and the ones with an identical exchange coupling constant are categorized in the same term. Those terms are given in the spin Hamiltonian of Eq. (4.3). The first term in the Hamiltonian of Eq. (4.3), J_{I}, includes the interactions between each molecule in symmetry group I with its identical molecule in the nearest neighboring cell along the a axis, as shown in Fig. 4.6(a). In Eq. (4.3), the second term, J_{II}, corresponding to the molecules in symmetry group II and their twins in the neighboring cell along axis a, are illustrated in Fig. 4.6(b). The third term, J_{III}, was discussed in Eq.4.2 above and is shown in Fig. 4.6(c). The fourth term with J_{IV} consists of the nearest neighboring interactions occurring between the molecules of symmetry group I. In the fourth term, the distance between molecules 1 at (i,j,k) and 4 at $(i+1,j-1,k)$ is the same as the distance between molecules 2 at (i,j,k) and 3 at $(i-1,j,k+1)$, as shown in Fig. 4.6(d). The fifth and sixth terms are associated with the nearest neighboring interactions between the molecules of symmetry group I and those in symmetry group II. Those different groups of interactions are given in two distinct terms based on their exchange coupling constants J_{V} and J_{VII}, and are shown in Fig. 4.6(e) and (f) respectively. Finally, the sum of all the

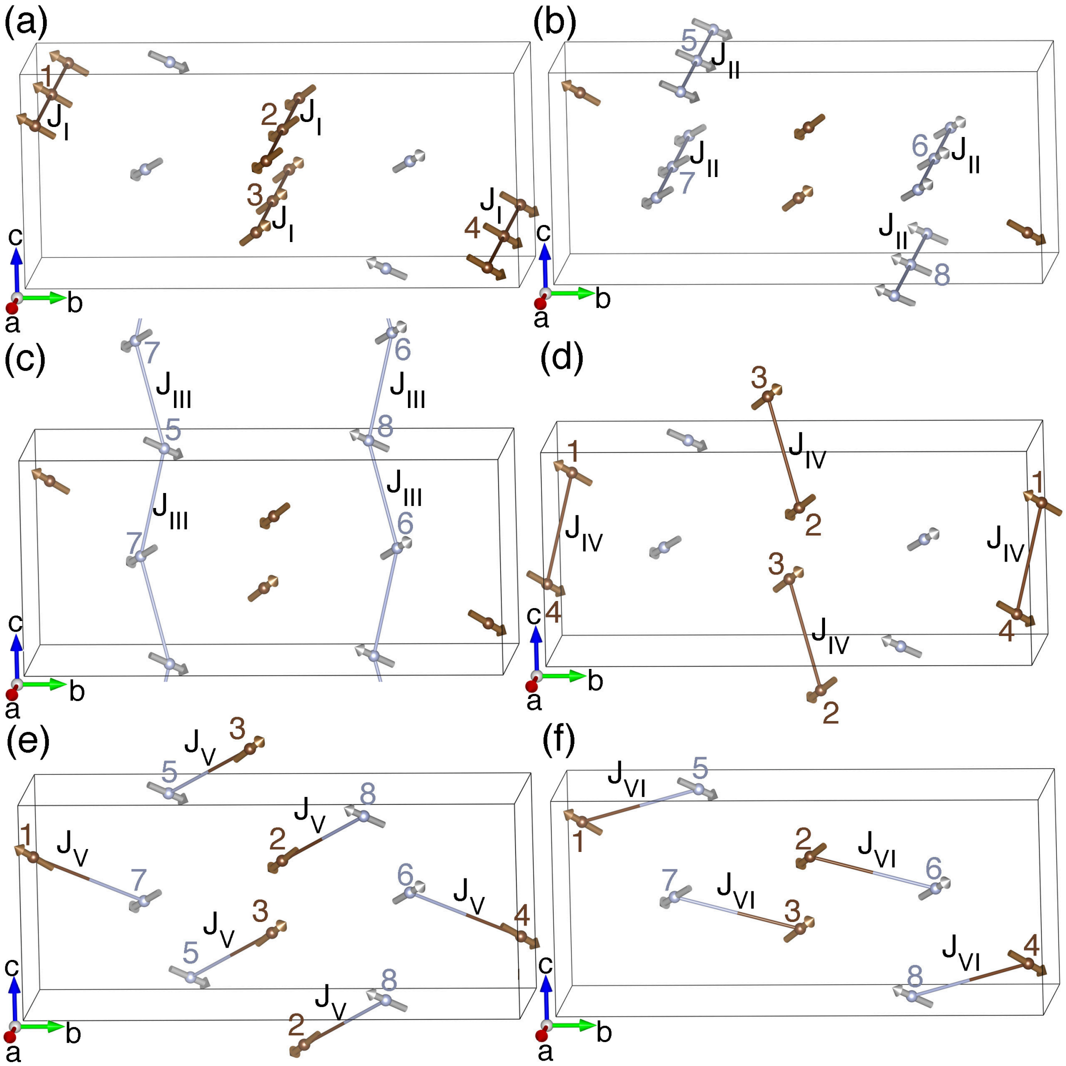

Figure 4.6 – Representation of the exchange interactions given in the spin Hamiltonian of Eq. (4.3).

exchange interaction terms related to the nearest neighboring interactions are given as the following spin Hamiltonian:

$$\begin{aligned}
H = \sum_{i,j,k} & J_{\mathrm{I}}(\mathbf{S}^1_{i,j,k}\cdot\mathbf{S}^1_{i+1,j,k}+\mathbf{S}^2_{i,j,k}\cdot\mathbf{S}^2_{i+1,j,k}+\mathbf{S}^3_{i,j,k}\cdot\mathbf{S}^3_{i+1,j,k}+\mathbf{S}^4_{i,j,k}\cdot\mathbf{S}^4_{i+1,j,k}) \\
& +J_{\mathrm{II}}(\mathbf{S}^5_{i,j,k}\cdot\mathbf{S}^5_{i+1,j,k}+\mathbf{S}^6_{i,j,k}\cdot\mathbf{S}^6_{i+1,j,k}+\mathbf{S}^7_{i,j,k}\cdot\mathbf{S}^7_{i+1,j,k}+\mathbf{S}^8_{i,j,k}\cdot\mathbf{S}^8_{i+1,j,k}) \\
& +J_{\mathrm{III}}(\mathbf{S}^5_{i,j,k}\cdot\mathbf{S}^7_{i,j,k}+\mathbf{S}^5_{i,j,k}\cdot\mathbf{S}^7_{i,j,k+1}+\mathbf{S}^8_{i,j,k}\cdot\mathbf{S}^6_{i,j,k}+\mathbf{S}^8_{i,j,k}\cdot\mathbf{S}^6_{i,j,k+1}) \\
& +J_{\mathrm{IV}}(\mathbf{S}^1_{i,j,k}\cdot\mathbf{S}^4_{i+1,j-1,k}+\mathbf{S}^2_{i,j,k}\cdot\mathbf{S}^3_{i-1,j,k+1}) \\
& +J_{\mathrm{V}}(\mathbf{S}^1_{i,j,k}\cdot\mathbf{S}^7_{i,j,k}+\mathbf{S}^5_{i,j,k}\cdot\mathbf{S}^3_{i,j,k+1}+\mathbf{S}^2_{i,j,k}\cdot\mathbf{S}^8_{i,j,k+1}+\mathbf{S}^6_{i,j,k}\cdot\mathbf{S}^4_{i,j,k}) \\
& +J_{\mathrm{VI}}(\mathbf{S}^1_{i,j,k}\cdot\mathbf{S}^5_{i+1,j,k}+\mathbf{S}^2_{i,j,k}\cdot\mathbf{S}^6_{i-1,j,k}+\mathbf{S}^8_{i,j,k}\cdot\mathbf{S}^4_{i+1,j,k}+\mathbf{S}^7_{i,j,k}\cdot\mathbf{S}^3_{i-1,j,k}).
\end{aligned} \tag{4.3}$$

Because this Hamiltonian only includes the interactions between the nearest neighboring cells, it does not fully describe all the magnetic interactions in the NIT2Py system. To obtain a general Hamiltonian that expresses the full energy spectrum of this magnetic system, we need to take into account all the possible inequivalent interactions. In following sections, we use a more systematic approach that both considers all the possible interactions and uses the corresponding symmetry operations to decrease the quantity of interactions in the system to create the Hamiltonians for a single cell and a supercell.

4.4 General Hamiltonian of a single cell of NIT2Py

A general spin Hamiltonian for the NIT2Py $1\times1\times1$ single cell is produced by looking at all the possible two-body interactions, $\boldsymbol{S}_i\cdot\boldsymbol{S}_j$. Here, i and j can take any form from 1 to 8 because of the eight molecules in the single cell. Each molecule has one free electron that gives rise to 28 total magnetic interactions ($8!/6!2!$) provided that no double counting occurs. Among those 28 interactions, some possess the same exchange coupling constant. In order to find the equivalent interactions for any of the $\boldsymbol{S}_i\cdot\boldsymbol{S}_j$ interactions in the third column of Table 4.II, each of the symmetry operators in Table 4.I are applied. Depending on which symmetry operator is being applied, the spin of the related molecule is substituted for each of the $\boldsymbol{S}_i$ and $\boldsymbol{S}_j$ spins in the initial interaction. The interactions that are equivalent to the initial interaction in column 3 are given in columns 4 to 7 of Table 4.II. For instance, the initial interaction corresponding to J_{10} in Table 4.II is $\boldsymbol{S}_2 \cdot \boldsymbol{S}_5$. To find its equivalent interaction by applying symmetry operator 1, the identical interaction is resulted because each molecule is related to itself. Then, by applying symmetry operator 2, as molecule 2 relates to molecule 1, and molecule 5 to molecule 6, we get $\boldsymbol{S}_1 \cdot \boldsymbol{S}_6$. The same way, $\boldsymbol{S}_3 \cdot \boldsymbol{S}_8$ and $\boldsymbol{S}_4 \cdot \boldsymbol{S}_7$ are found by applying symmetry operator 3 and 4, respectively. Because the resulting interactions for J_{10} are also obtained for J_5, one concludes that $J_{10} = J_5$. Therefore, only one of those exchange coupling constants must be incorporated into the general Hamiltonian of the system. As a result, a total of 10 inequivalent Js are obtained in the NIT2Py $1 \times 1 \times 1$ single cell. Consequently, by summing up all the different interactions along with their corresponding exchange interaction constants, the general Hamiltonian for the single cell is written as

$$\begin{aligned}
H = {} & J_1(\mathbf{S}_1 \cdot \mathbf{S}_2 + \mathbf{S}_3 \cdot \mathbf{S}_4) + J_2(\mathbf{S}_1 \cdot \mathbf{S}_3 + \mathbf{S}_2 \cdot \mathbf{S}_4) + J_3(\mathbf{S}_1 \cdot \mathbf{S}_4 + \mathbf{S}_2 \cdot \mathbf{S}_3) \\
& + J_4(\mathbf{S}_1 \cdot \mathbf{S}_5 + \mathbf{S}_2 \cdot \mathbf{S}_6 + \mathbf{S}_3 \cdot \mathbf{S}_7 + \mathbf{S}_4 \cdot \mathbf{S}_8) + J_5(\mathbf{S}_1 \cdot \mathbf{S}_6 + \mathbf{S}_2 \cdot \mathbf{S}_5 + \mathbf{S}_3 \cdot \mathbf{S}_8 + \mathbf{S}_4 \cdot \mathbf{S}_7) \\
& + J_6(\mathbf{S}_1 \cdot \mathbf{S}_7 + \mathbf{S}_2 \cdot \mathbf{S}_8 + \mathbf{S}_3 \cdot \mathbf{S}_5 + \mathbf{S}_4 \cdot \mathbf{S}_6) + J_7(\mathbf{S}_1 \cdot \mathbf{S}_8 + \mathbf{S}_2 \cdot \mathbf{S}_7 + \mathbf{S}_3 \cdot \mathbf{S}_6 + \mathbf{S}_4 \cdot \mathbf{S}_5) \\
& + J_{23}(\mathbf{S}_5 \cdot \mathbf{S}_6 + \mathbf{S}_7 \cdot \mathbf{S}_8) + J_{24}(\mathbf{S}_5 \cdot \mathbf{S}_7 + \mathbf{S}_6 \cdot \mathbf{S}_8) + J_{25}(\mathbf{S}_5 \cdot \mathbf{S}_8 + \mathbf{S}_6 \cdot \mathbf{S}_7). \qquad (4.4)
\end{aligned}$$

The coefficient of each J_k in the Hamiltonian of Eq. (4.5) is calculated depending of the spins in the configuration (α) under study. The resulting coefficient of each J_k for that configuration replaces coefficient $a_{\alpha,k}$ of the same J_k in the Ising energy of Eq. (3.41). For instance, the coefficient of J_1 in the Ising energy of Eq. (4.5), based on the Hamiltonian of Eq. (4.5), is given as $a_{\alpha,1} = (\mathbf{S}_1 \cdot \mathbf{S}_2 + \mathbf{S}_3 \cdot \mathbf{S}_4)$. By taking into account configuration 1 ($\alpha = 1$) in Table 6.I, with $S_1 = -1/2$, $S_2 = -1/2$, $S_3 = -1/2$, and $S_4 = -1/2$, coefficient $a_{1,1}$ is calculated as 1/2.

The Ising energy of the $1 \times 1 \times 1$ single cell is given based on Eq. (3.41) as

$$\begin{aligned}
\varepsilon_{\alpha}^{1\times1\times1}(\text{Ising}) = {} & \frac{1}{4}(a_{\alpha,1}J_1 + a_{\alpha,2}J_2 + a_{\alpha,3}J_3 + a_{\alpha,4}J_4 + a_{\alpha,5}J_5 + a_{\alpha,6}J_6 + a_{\alpha,7}J_7 \\
& + a_{\alpha,23}J_{23} + a_{\alpha,24}J_{24} + a_{\alpha,25}J_{25}). \qquad (4.5)
\end{aligned}$$

Table 4.II – The 28 exchange coupling constants corresponding to all the possible magnetic interactions between the eight molecules in the NIT2Py single cell. The $\boldsymbol{S}_i \cdot \boldsymbol{S}_j$ interactions, in which i and j can be a value from 1 to 8, are given. The double-counting of interactions is avoided. The effect of each of the four symmetry operators of the single cell on every possible interaction is shown. As a result, the equivalent Js for the exchange coupling constants are provided in the second column.

J	Symmetry equivalent J	$\boldsymbol{S}_i \cdot \boldsymbol{S}_j$	Symmetry operator 1	Symmetry operator 2	Symmetry operator 3	Symmetry operator 4
J_1	-	$\boldsymbol{S}_1 \cdot \boldsymbol{S}_2$	$\boldsymbol{S}_1 \cdot \boldsymbol{S}_2$	$\boldsymbol{S}_2 \cdot \boldsymbol{S}_1$	$\boldsymbol{S}_4 \cdot \boldsymbol{S}_3$	$\boldsymbol{S}_3 \cdot \boldsymbol{S}_4$
J_2	-	$\boldsymbol{S}_1 \cdot \boldsymbol{S}_3$	$\boldsymbol{S}_1 \cdot \boldsymbol{S}_3$	$\boldsymbol{S}_2 \cdot \boldsymbol{S}_4$	$\boldsymbol{S}_4 \cdot \boldsymbol{S}_2$	$\boldsymbol{S}_3 \cdot \boldsymbol{S}_1$
J_3	-	$\boldsymbol{S}_1 \cdot \boldsymbol{S}_4$	$\boldsymbol{S}_1 \cdot \boldsymbol{S}_4$	$\boldsymbol{S}_2 \cdot \boldsymbol{S}_3$	$\boldsymbol{S}_4 \cdot \boldsymbol{S}_1$	$\boldsymbol{S}_3 \cdot \boldsymbol{S}_2$
J_4	-	$\boldsymbol{S}_1 \cdot \boldsymbol{S}_5$	$\boldsymbol{S}_1 \cdot \boldsymbol{S}_5$	$\boldsymbol{S}_2 \cdot \boldsymbol{S}_6$	$\boldsymbol{S}_4 \cdot \boldsymbol{S}_8$	$\boldsymbol{S}_3 \cdot \boldsymbol{S}_7$
J_5	-	$\boldsymbol{S}_1 \cdot \boldsymbol{S}_6$	$\boldsymbol{S}_1 \cdot \boldsymbol{S}_6$	$\boldsymbol{S}_2 \cdot \boldsymbol{S}_5$	$\boldsymbol{S}_4 \cdot \boldsymbol{S}_7$	$\boldsymbol{S}_3 \cdot \boldsymbol{S}_8$
J_6	-	$\boldsymbol{S}_1 \cdot \boldsymbol{S}_7$	$\boldsymbol{S}_1 \cdot \boldsymbol{S}_7$	$\boldsymbol{S}_2 \cdot \boldsymbol{S}_8$	$\boldsymbol{S}_4 \cdot \boldsymbol{S}_6$	$\boldsymbol{S}_3 \cdot \boldsymbol{S}_5$
J_7	-	$\boldsymbol{S}_1 \cdot \boldsymbol{S}_8$	$\boldsymbol{S}_1 \cdot \boldsymbol{S}_8$	$\boldsymbol{S}_2 \cdot \boldsymbol{S}_7$	$\boldsymbol{S}_4 \cdot \boldsymbol{S}_5$	$\boldsymbol{S}_3 \cdot \boldsymbol{S}_6$
J_8	J_3	$\boldsymbol{S}_2 \cdot \boldsymbol{S}_3$	$\boldsymbol{S}_2 \cdot \boldsymbol{S}_3$	$\boldsymbol{S}_1 \cdot \boldsymbol{S}_4$	$\boldsymbol{S}_3 \cdot \boldsymbol{S}_2$	$\boldsymbol{S}_4 \cdot \boldsymbol{S}_1$
J_9	J_2	$\boldsymbol{S}_2 \cdot \boldsymbol{S}_4$	$\boldsymbol{S}_2 \cdot \boldsymbol{S}_4$	$\boldsymbol{S}_1 \cdot \boldsymbol{S}_3$	$\boldsymbol{S}_3 \cdot \boldsymbol{S}_1$	$\boldsymbol{S}_4 \cdot \boldsymbol{S}_2$
J_{10}	J_5	$\boldsymbol{S}_2 \cdot \boldsymbol{S}_5$	$\boldsymbol{S}_2 \cdot \boldsymbol{S}_5$	$\boldsymbol{S}_1 \cdot \boldsymbol{S}_6$	$\boldsymbol{S}_3 \cdot \boldsymbol{S}_8$	$\boldsymbol{S}_4 \cdot \boldsymbol{S}_7$
J_{11}	J_4	$\boldsymbol{S}_2 \cdot \boldsymbol{S}_6$	$\boldsymbol{S}_2 \cdot \boldsymbol{S}_6$	$\boldsymbol{S}_1 \cdot \boldsymbol{S}_5$	$\boldsymbol{S}_3 \cdot \boldsymbol{S}_7$	$\boldsymbol{S}_4 \cdot \boldsymbol{S}_8$
J_{12}	J_7	$\boldsymbol{S}_2 \cdot \boldsymbol{S}_7$	$\boldsymbol{S}_2 \cdot \boldsymbol{S}_7$	$\boldsymbol{S}_1 \cdot \boldsymbol{S}_8$	$\boldsymbol{S}_3 \cdot \boldsymbol{S}_6$	$\boldsymbol{S}_4 \cdot \boldsymbol{S}_5$
J_{13}	J_6	$\boldsymbol{S}_2 \cdot \boldsymbol{S}_8$	$\boldsymbol{S}_2 \cdot \boldsymbol{S}_8$	$\boldsymbol{S}_1 \cdot \boldsymbol{S}_7$	$\boldsymbol{S}_3 \cdot \boldsymbol{S}_5$	$\boldsymbol{S}_4 \cdot \boldsymbol{S}_6$
J_{14}	J_1	$\boldsymbol{S}_3 \cdot \boldsymbol{S}_4$	$\boldsymbol{S}_3 \cdot \boldsymbol{S}_4$	$\boldsymbol{S}_4 \cdot \boldsymbol{S}_3$	$\boldsymbol{S}_2 \cdot \boldsymbol{S}_1$	$\boldsymbol{S}_1 \cdot \boldsymbol{S}_2$
J_{15}	J_6	$\boldsymbol{S}_3 \cdot \boldsymbol{S}_5$	$\boldsymbol{S}_3 \cdot \boldsymbol{S}_5$	$\boldsymbol{S}_4 \cdot \boldsymbol{S}_6$	$\boldsymbol{S}_2 \cdot \boldsymbol{S}_8$	$\boldsymbol{S}_1 \cdot \boldsymbol{S}_7$
J_{16}	J_7	$\boldsymbol{S}_3 \cdot \boldsymbol{S}_6$	$\boldsymbol{S}_3 \cdot \boldsymbol{S}_6$	$\boldsymbol{S}_4 \cdot \boldsymbol{S}_5$	$\boldsymbol{S}_2 \cdot \boldsymbol{S}_7$	$\boldsymbol{S}_1 \cdot \boldsymbol{S}_8$
J_{17}	J_4	$\boldsymbol{S}_3 \cdot \boldsymbol{S}_7$	$\boldsymbol{S}_3 \cdot \boldsymbol{S}_7$	$\boldsymbol{S}_4 \cdot \boldsymbol{S}_8$	$\boldsymbol{S}_2 \cdot \boldsymbol{S}_6$	$\boldsymbol{S}_1 \cdot \boldsymbol{S}_5$
J_{18}	J_5	$\boldsymbol{S}_3 \cdot \boldsymbol{S}_8$	$\boldsymbol{S}_3 \cdot \boldsymbol{S}_8$	$\boldsymbol{S}_4 \cdot \boldsymbol{S}_7$	$\boldsymbol{S}_2 \cdot \boldsymbol{S}_5$	$\boldsymbol{S}_1 \cdot \boldsymbol{S}_6$
J_{19}	J_7	$\boldsymbol{S}_4 \cdot \boldsymbol{S}_5$	$\boldsymbol{S}_4 \cdot \boldsymbol{S}_5$	$\boldsymbol{S}_3 \cdot \boldsymbol{S}_6$	$\boldsymbol{S}_1 \cdot \boldsymbol{S}_8$	$\boldsymbol{S}_2 \cdot \boldsymbol{S}_7$
J_{20}	J_6	$\boldsymbol{S}_4 \cdot \boldsymbol{S}_6$	$\boldsymbol{S}_4 \cdot \boldsymbol{S}_6$	$\boldsymbol{S}_3 \cdot \boldsymbol{S}_5$	$\boldsymbol{S}_1 \cdot \boldsymbol{S}_7$	$\boldsymbol{S}_2 \cdot \boldsymbol{S}_8$
J_{21}	J_5	$\boldsymbol{S}_4 \cdot \boldsymbol{S}_7$	$\boldsymbol{S}_4 \cdot \boldsymbol{S}_7$	$\boldsymbol{S}_3 \cdot \boldsymbol{S}_8$	$\boldsymbol{S}_1 \cdot \boldsymbol{S}_6$	$\boldsymbol{S}_2 \cdot \boldsymbol{S}_5$
J_{22}	J_4	$\boldsymbol{S}_4 \cdot \boldsymbol{S}_8$	$\boldsymbol{S}_4 \cdot \boldsymbol{S}_8$	$\boldsymbol{S}_3 \cdot \boldsymbol{S}_7$	$\boldsymbol{S}_1 \cdot \boldsymbol{S}_5$	$\boldsymbol{S}_2 \cdot \boldsymbol{S}_6$
J_{23}	-	$\boldsymbol{S}_5 \cdot \boldsymbol{S}_6$	$\boldsymbol{S}_5 \cdot \boldsymbol{S}_6$	$\boldsymbol{S}_6 \cdot \boldsymbol{S}_5$	$\boldsymbol{S}_8 \cdot \boldsymbol{S}_7$	$\boldsymbol{S}_7 \cdot \boldsymbol{S}_8$
J_{24}	-	$\boldsymbol{S}_5 \cdot \boldsymbol{S}_7$	$\boldsymbol{S}_5 \cdot \boldsymbol{S}_7$	$\boldsymbol{S}_6 \cdot \boldsymbol{S}_8$	$\boldsymbol{S}_8 \cdot \boldsymbol{S}_6$	$\boldsymbol{S}_7 \cdot \boldsymbol{S}_5$
J_{25}	-	$\boldsymbol{S}_5 \cdot \boldsymbol{S}_8$	$\boldsymbol{S}_5 \cdot \boldsymbol{S}_8$	$\boldsymbol{S}_6 \cdot \boldsymbol{S}_7$	$\boldsymbol{S}_8 \cdot \boldsymbol{S}_5$	$\boldsymbol{S}_7 \cdot \boldsymbol{S}_6$
J_{26}	J_{25}	$\boldsymbol{S}_6 \cdot \boldsymbol{S}_7$	$\boldsymbol{S}_6 \cdot \boldsymbol{S}_7$	$\boldsymbol{S}_5 \cdot \boldsymbol{S}_8$	$\boldsymbol{S}_7 \cdot \boldsymbol{S}_6$	$\boldsymbol{S}_8 \cdot \boldsymbol{S}_5$
J_{27}	J_{24}	$\boldsymbol{S}_6 \cdot \boldsymbol{S}_8$	$\boldsymbol{S}_6 \cdot \boldsymbol{S}_8$	$\boldsymbol{S}_5 \cdot \boldsymbol{S}_7$	$\boldsymbol{S}_7 \cdot \boldsymbol{S}_5$	$\boldsymbol{S}_8 \cdot \boldsymbol{S}_6$
J_{28}	J_{23}	$\boldsymbol{S}_7 \cdot \boldsymbol{S}_8$	$\boldsymbol{S}_7 \cdot \boldsymbol{S}_8$	$\boldsymbol{S}_8 \cdot \boldsymbol{S}_7$	$\boldsymbol{S}_6 \cdot \boldsymbol{S}_5$	$\boldsymbol{S}_5 \cdot \boldsymbol{S}_6$

The 10 inequivalent Js of the single cell given in the Hamiltonian of Eq. (4.4) and in the Ising energy of Eq. (4.5) are shown in Fig. 4.7. Note that J_1, J_2, J_{23}, and J_{24} must be doubled because two identical interactions are created from two identical molecules j placed within equal distances of molecule i. For instance, the interactions existing between molecule 1 and two different molecules 2 are both J_1 because they have the same distance, as can be seen in Fig. 4.7. The general Hamiltonian of Eq. (4.4) and the Ising energy of Eq. (4.5) will later be used in 6.5.5 to evaluate the magnitudes and signs of the Js of the single cell by using the total energy difference approach.

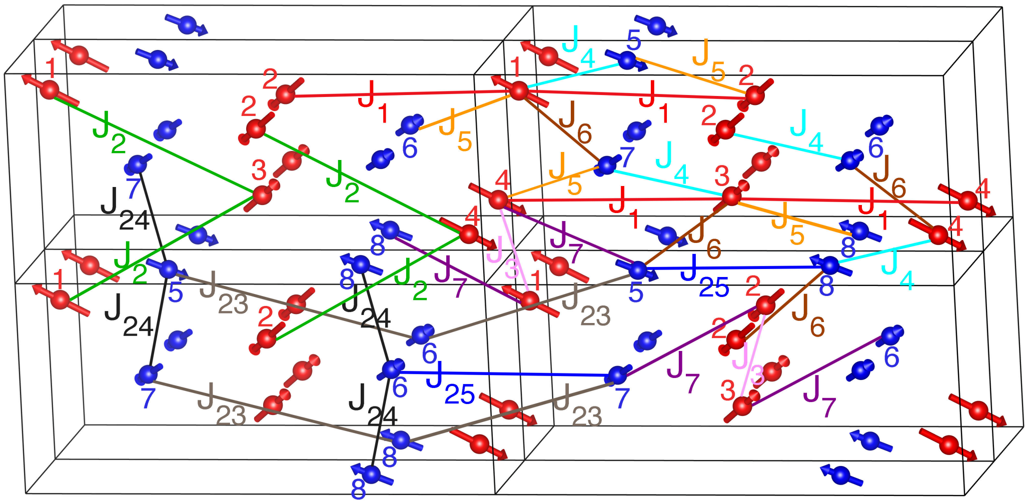

Figure 4.7 – The 10 inequivalent exchange coupling constants of a NIT2Py single cell. The carbon atom in the middle of the ONCNO branch of each molecule stands in for the whole molecule as an arrow showing the alignment.

4.5 General Hamiltonian of the $2 \times 1 \times 1$ supercell

To separate the exchange couplings in the single cell, larger cells, namely supercells, must be created.

The $2 \times 1 \times 1$ supercell is generated by doubling the single cell along the crystallographic a axis. It has 16 molecules, with molecules 1 to 8 having the same intermolecular distance as those that in the single cell, and molecules 9 to 16 as the respective replicates of the first eight molecules, as can be seen in Fig 4.8(a). For clarity, only the middle

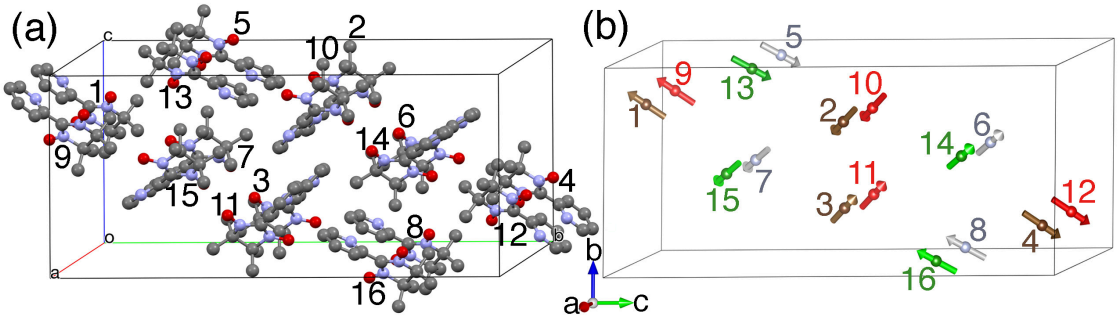

Figure 4.8 – (a) The 16 molecules of the NIT2Py 2 × 1 × 1 supercell labeled 1 to 16. (b) To represent each molecule, only the carbon atom of the ONCNO branch is shown by an arrow illustrating its orientation in the supercell.

carbon atom of the ONCNO branch of each molecule is featured in Fig. 4.8(b). As mentioned in Table 4.III, there are eight symmetry operators associated with the 2 × 1 × 1 supercell. The relationships between the 16 molecules after having applied each of those symmetry operators are given in the last column of Table 4.III.

The 16 molecules in the supercell offer 16 possibilities for i and j in the two-body interactions $\boldsymbol{S}_i \cdot \boldsymbol{S}_j$. If we disregard the double-counting of interactions, the total number of possible interactions for the 2 × 1 × 1 supercell amounts to 120 ($16!/14!\,2!$). So, there are 120 exchange coupling constants, J_1 to J_{120}, for all the interactions. By repeating the method seen for the single cell, we find the inequivalent Js in the supercell. We apply each of the symmetry operators of the 2 × 1 × 1 supercell to a given two-body interaction to find the identical ones having the same J. A list of all the 120 interactions along with their identical interaction identified by applying each of the eight symmetry operators can be seen in Annex V. Therefore, we can obtain the interactions that share the same exchange coupling constant and categorize them into one term with the corresponding J. Among the 120 Js in the 2 × 1 × 1 supercell, 22 independent Js were found. By taking into account all the two-body interactions related to those 22 independent Js, the general

#	Symmetry Operator	Related Molecules
1	(x, y, z)	Identity
2	(-x, 1/2+y, 1/2-z)	1↔2, 3↔4, 5↔6, 7↔8, 9↔10, 11↔12, 13↔14, 15↔16
3	(-x, -y, -z)	1↔4, 2↔3, 5↔8, 6↔7, 9↔12, 10↔11, 13↔16, 14↔15
4	(x, 1/2-y, 1/2+z)	1↔3, 2↔4, 5↔7, 6↔8, 9↔11, 10↔12, 13↔15, 14↔16
5	(1/2-x, -y, -z)	1↔12, 2↔11, 3↔10, 4↔9, 5↔16, 6↔15, 7↔14, 8↔13
6	(1/2-x, 1/2+y, 1/2-z)	1↔10, 2↔9, 3↔12, 4↔11, 5↔14, 6↔13, 7↔16, 8↔15
7	(1/2+x, y, z)	1↔9, 2↔10, 3↔11, 4↔12, 5↔13, 6↔14, 7↔15, 8↔16
8	(1/2+x, 1/2-y, 1/2+z)	1↔11, 2↔12, 3↔9, 4↔10, 5↔15, 6↔16, 7↔13, 8↔14

Table 4.III – The eight symmetry operators corresponding to the NIT2Py $2 \times 1 \times 1$ supercell. The relationship between the 16 molecules in the supercell as a result of applying each of the eight symmetry operators is given.

Hamiltonian for the NIT2Py $2 \times 1 \times 1$ supercell is written as

$$\begin{aligned}
H = {} & J_1(\mathbf{S}_1\cdot\mathbf{S}_2+\mathbf{S}_3\cdot\mathbf{S}_4+\mathbf{S}_9\cdot\mathbf{S}_{10}+\mathbf{S}_{11}\cdot\mathbf{S}_{12})+J_2(\mathbf{S}_1\cdot\mathbf{S}_3+\mathbf{S}_2\cdot\mathbf{S}_4+\mathbf{S}_9\cdot\mathbf{S}_{11}+\mathbf{S}_{10}\cdot\mathbf{S}_{12}) \\
& +J_3(\mathbf{S}_1\cdot\mathbf{S}_4+\mathbf{S}_2\cdot\mathbf{S}_3+\mathbf{S}_9\cdot\mathbf{S}_{12}+\mathbf{S}_{10}\cdot\mathbf{S}_{11}) \\
& +J_4(\mathbf{S}_1\cdot\mathbf{S}_5+\mathbf{S}_2\cdot\mathbf{S}_6+\mathbf{S}_3\cdot\mathbf{S}_7+\mathbf{S}_4\cdot\mathbf{S}_8+\mathbf{S}_9\cdot\mathbf{S}_{13}+\mathbf{S}_{10}\cdot\mathbf{S}_{14}+\mathbf{S}_{11}\cdot\mathbf{S}_{15}+\mathbf{S}_{12}\cdot\mathbf{S}_{16}) \\
& +J_5(\mathbf{S}_1\cdot\mathbf{S}_6+\mathbf{S}_2\cdot\mathbf{S}_5+\mathbf{S}_3\cdot\mathbf{S}_8+\mathbf{S}_4\cdot\mathbf{S}_7+\mathbf{S}_9\cdot\mathbf{S}_{14}+\mathbf{S}_{10}\cdot\mathbf{S}_{13}+\mathbf{S}_{11}\cdot\mathbf{S}_{16}+\mathbf{S}_{12}\cdot\mathbf{S}_{15}) \\
& +J_6(\mathbf{S}_1\cdot\mathbf{S}_7+\mathbf{S}_2\cdot\mathbf{S}_8+\mathbf{S}_3\cdot\mathbf{S}_5+\mathbf{S}_4\cdot\mathbf{S}_6+\mathbf{S}_9\cdot\mathbf{S}_{15}+\mathbf{S}_{10}\cdot\mathbf{S}_{16}+\mathbf{S}_{11}\cdot\mathbf{S}_{13}+\mathbf{S}_{12}\cdot\mathbf{S}_{14}) \\
& +J_7(\mathbf{S}_1\cdot\mathbf{S}_8+\mathbf{S}_2\cdot\mathbf{S}_7+\mathbf{S}_3\cdot\mathbf{S}_6+\mathbf{S}_4\cdot\mathbf{S}_5+\mathbf{S}_9\cdot\mathbf{S}_{16}+\mathbf{S}_{10}\cdot\mathbf{S}_{15}+\mathbf{S}_{11}\cdot\mathbf{S}_{14}+\mathbf{S}_{12}\cdot\mathbf{S}_{13}) \\
& +J_8(\mathbf{S}_1\cdot\mathbf{S}_9+\mathbf{S}_2\cdot\mathbf{S}_{10}+\mathbf{S}_3\cdot\mathbf{S}_{11}+\mathbf{S}_4\cdot\mathbf{S}_{12})+J_9(\mathbf{S}_1\cdot\mathbf{S}_{10}+\mathbf{S}_2\cdot\mathbf{S}_9+\mathbf{S}_3\cdot\mathbf{S}_{12}+\mathbf{S}_4\cdot\mathbf{S}_{11}) \\
& +J_{10}(\mathbf{S}_1\cdot\mathbf{S}_{11}+\mathbf{S}_2\cdot\mathbf{S}_{12}+\mathbf{S}_3\cdot\mathbf{S}_9+\mathbf{S}_4\cdot\mathbf{S}_{10})+J_{11}(\mathbf{S}_1\cdot\mathbf{S}_{12}+\mathbf{S}_2\cdot\mathbf{S}_{11}+\mathbf{S}_3\cdot\mathbf{S}_{10}+\mathbf{S}_4\cdot\mathbf{S}_9) \\
& +J_{12}(\mathbf{S}_1\cdot\mathbf{S}_{13}+\mathbf{S}_2\cdot\mathbf{S}_{14}+\mathbf{S}_3\cdot\mathbf{S}_{15}+\mathbf{S}_4\cdot\mathbf{S}_{16}+\mathbf{S}_5\cdot\mathbf{S}_9+\mathbf{S}_6\cdot\mathbf{S}_{10}+\mathbf{S}_7\cdot\mathbf{S}_{11}+\mathbf{S}_8\cdot\mathbf{S}_{12}) \\
& +J_{13}(\mathbf{S}_1\cdot\mathbf{S}_{14}+\mathbf{S}_2\cdot\mathbf{S}_{13}+\mathbf{S}_3\cdot\mathbf{S}_{16}+\mathbf{S}_4\cdot\mathbf{S}_{15}+\mathbf{S}_5\cdot\mathbf{S}_{10}+\mathbf{S}_6\cdot\mathbf{S}_9+\mathbf{S}_7\cdot\mathbf{S}_{12}+\mathbf{S}_8\cdot\mathbf{S}_{11}) \\
& +J_{14}(\mathbf{S}_1\cdot\mathbf{S}_{15}+\mathbf{S}_2\cdot\mathbf{S}_{16}+\mathbf{S}_3\cdot\mathbf{S}_{13}+\mathbf{S}_4\cdot\mathbf{S}_{14}+\mathbf{S}_5\cdot\mathbf{S}_{11}+\mathbf{S}_6\cdot\mathbf{S}_{12}+\mathbf{S}_7\cdot\mathbf{S}_9+\mathbf{S}_8\cdot\mathbf{S}_{10}) \\
& +J_{15}(\mathbf{S}_1\cdot\mathbf{S}_{16}+\mathbf{S}_2\cdot\mathbf{S}_{15}+\mathbf{S}_3\cdot\mathbf{S}_{14}+\mathbf{S}_4\cdot\mathbf{S}_{13}+\mathbf{S}_5\cdot\mathbf{S}_{12}+\mathbf{S}_6\cdot\mathbf{S}_{11}+\mathbf{S}_7\cdot\mathbf{S}_{10}+\mathbf{S}_8\cdot\mathbf{S}_9) \\
& +J_{55}(\mathbf{S}_5\cdot\mathbf{S}_6+\mathbf{S}_7\cdot\mathbf{S}_8+\mathbf{S}_{13}\cdot\mathbf{S}_{14}+\mathbf{S}_{15}\cdot\mathbf{S}_{16})+J_{56}(\mathbf{S}_5\cdot\mathbf{S}_7+\mathbf{S}_6\cdot\mathbf{S}_8+\mathbf{S}_{13}\cdot\mathbf{S}_{15}+\mathbf{S}_{14}\cdot\mathbf{S}_{16}) \\
& +J_{57}(\mathbf{S}_5\cdot\mathbf{S}_8+\mathbf{S}_6\cdot\mathbf{S}_7+\mathbf{S}_{13}\cdot\mathbf{S}_{16}+\mathbf{S}_{14}\cdot\mathbf{S}_{15})+J_{62}(\mathbf{S}_5\cdot\mathbf{S}_{13}+\mathbf{S}_6\cdot\mathbf{S}_{14}+\mathbf{S}_7\cdot\mathbf{S}_{15}+\mathbf{S}_8\cdot\mathbf{S}_{16}) \\
& +J_{63}(\mathbf{S}_5\cdot\mathbf{S}_{14}+\mathbf{S}_6\cdot\mathbf{S}_{13}+\mathbf{S}_7\cdot\mathbf{S}_{16}+\mathbf{S}_8\cdot\mathbf{S}_{15})+J_{64}(\mathbf{S}_5\cdot\mathbf{S}_{15}+\mathbf{S}_6\cdot\mathbf{S}_{16}+\mathbf{S}_7\cdot\mathbf{S}_{13}+\mathbf{S}_8\cdot\mathbf{S}_{14}) \\
& +J_{65}(\mathbf{S}_5\cdot\mathbf{S}_{16}+\mathbf{S}_6\cdot\mathbf{S}_{15}+\mathbf{S}_7\cdot\mathbf{S}_{14}+\mathbf{S}_8\cdot\mathbf{S}_{13}). \qquad (4.6)
\end{aligned}$$

The Ising energy of the $2 \times 1 \times 1$ supercell is obtained using Eq. (3.41), in which the coefficients $a_{\alpha k}$ depend on a given spin configuration α and are attained by the coefficients of J_ks in the Hamiltonian of Eq. (4.6).

$$\begin{aligned}\varepsilon_{\alpha}^{2\times1\times1}(\text{Ising}) = \frac{1}{4}(&a_{\alpha,1}J_1 + a_{\alpha,2}J_2 + a_{\alpha,3}J_3 + a_{\alpha,4}J_4 + a_{\alpha,5}J_5 + a_{\alpha,6}J_6 + a_{\alpha,7}J_7 \\ &+ a_{\alpha,8}J_8 + a_{\alpha,9}J_9 + a_{\alpha,10}J_{10} + a_{\alpha,11}J_{11} + a_{\alpha,12}J_{12} + a_{\alpha,13}J_{13} + a_{\alpha,14}J_{14} \\ &+ a_{\alpha,15}J_{15} + a_{\alpha,55}J_{55} + a_{\alpha,56}J_{56} + a_{\alpha,57}J_{57} + a_{\alpha,62}J_{62} + a_{\alpha,63}J_{63} \\ &+ a_{\alpha,64}J_{64} + a_{\alpha,65}J_{65}). \end{aligned} \tag{4.7}$$

Bear in mind that J_1, J_2, J_8, J_9, J_{10}, J_{55}, J_{56}, J_{62}, J_{63}, and J_{64} correspond to interactions that are repeated between a molecule i and two molecules j, each within the same distance of i. So, the coefficients of those Js must be doubled.

4.6 The equivalent interactions based on the general Hamiltonians of the $1 \times 1 \times 1$ cell and $2 \times 1 \times 1$ supercell

The 10 inequivalent Js of the $1 \times 1 \times 1$ single cell in Eq. (4.4) are compared to the 22 inequivalent Js of the $2 \times 1 \times 1$ supercell in Eq. (4.6) to determine which of Js are identical in both cells. To make this comparison, the molecule labeling in the supercell must be conform with that of the single cell.

However, when working with 3D visualization programs for electronic and structural analysis such as VESTA and Mercury, one has to be particularly careful to avoid labeling the supercell molecules based only on the way the molecules are positioned in the single cell. The reason for this is that those programs have the tendency to show only the molecules with positive coordinates that are confined within the frame of the unit cell. Thus, they do not necessarily show all the molecules with coordinates initially assigned in the input file, but instead show an image with positive coordinates of a molecule having negative ones. The solution to avoid making that mistake is to measure the distances between the molecules labeled from 1 to 8 in the single cell and labeling molecules 1 to 8 in the $2 \times 1 \times 1$ supercell correspondingly.

After having established a consistency in the labeling of the molecules in both the single cell and $2 \times 1 \times 1$ supercell, the equivalent Js are found based on the similar distances between the interacting molecules. The middle carbon atom in the ONCNO branch of the interacting molecules is set as the reference point to measure the distances. Based on a distance between two carbon atoms of a pair of molecules related to a given J in the single cell, the equivalent J in the supercell is found. Table 4.IV shows some common distances between the carbon atoms of the interacting pair of molecules in the single cell and $2 \times 1 \times 1$ supercell, and their equivalent Js in each cell. Note that interactions J_8 and J_{62} correspond to intercell interactions, of which the former is related to the interactions between the pairs of molecules in symmetry group I and the later to the ones in symmetry group II. Those two interactions cannot be obtained in the single cell.

d_{C-C}(Å)	J $1 \times 1 \times 1$ single cell	$M_i - M_j$ $1 \times 1 \times 1$ single cell	J $2 \times 1 \times 1$ supercell	$M_i - M_j$ $2 \times 1 \times 1$ supercell
15.034	J_1	(1-2), (1-2), (3-4), (3-4)	J_9	(1-10), (1-10), (2-9), (2-9)
16.182	J_1	(1-2), (1-2), (3-4), (3-4)	J_1	(1-2), (1-2), (3-4), (3-4), (9-10), (9-10), (11-12), (11-12)
14.782	J_2	(1-3), (1-3), (2-4), (2-4)	J_2	(1-3), (1-3), (2-4), (2-4), (9-11), (9-11), (10-12), (10-12)
15.559	J_2	(1-3), (1-3), (2-4), (2-4)	J_{10}	(1-11), (1-11), (2-12), (2-12), (3-9), (3-9), (4-10), (4-10)
6.435	J_3	(1-4), (2-3)	J_{11}	(1-12), (2-11), (3-10), (4-9)
6.991	J_3	(1-4), (2-3)	J_{11}	(1-12), (2-11), (3-10), (4-9)
7.940	J_3	(1-4), (2-3)	J_3	(1-4), (2-3), (9-12), (10-11)
8.626	J_3	(1-4), (2-3)	J_3	(1-4), (2-3), (9-12), (10-11)
7.861	J_4	(1-5), (2-6), (3-7), (4-8)	J_{12}	(1-13), (2-14), (3-15), (4-16), (5-9), (6-10), (7-11), (8-12)
9.406	J_4	(1-5), (2-6), (3-7), (4-8)	J_4	(1-5), (2-6), (3-7), (4-8), (9-13), (10-14), (11-15), (12-16)
8.083	J_5	(1-6), (2-5), (3-8), (4-7)	J_5	(1-6), (2-5), (3-8), (4-7), (9-14), (10-13), (11-16), (12-15)
9.490	J_5	(1-6), (2-5), (3-8), (4-7)	J_{13}	(1-14), (2-13), (3-16), (4-15), (5-10), (6-9), (7-12), (8-11)
7.397	J_6	(1-7), (2-8), (3-5), (4-6)	J_{14}	(1-15), (2-16), (3-13), (4-14), (5-11), (6-12), (7-9), (8-10)
8.197	J_6	(1-7), (2-8), (3-5), (4-6)	J_6	(1-7), (2-8), (3-5), (4-6), (9-15), (10-16), (11-13), (12-14)
10.181	J_7	(1-8), (2-7), (3-6), (4-5)	J_7	(1-8), (2-7), (3-6), (4-5), (9-16), (10-15), (11-14), (12-13)
10.685	J_7	(1-8), (2-7), (3-6), (4-5)	J_{15}	(1-16), (2-15), (3-14), (4-13), (5-12), (6-11), (7-10), (8-9)
15.942	J_{23}	(5-6), (5-6), (7-8), (7-8)	J_{63}	(5-14), (6-13), (7-16), (8-15)
16.363	J_{23}	(5-6), (5-6), (7-8), (7-8)	J_{55}	(5-6), (7-8), (13-14), (15-16)
6.682	J_{24}	(5-7), (5-7), (6-8), (6-8)	J_{56}	(5-7), (6-8), (13-15), (14-16)
8.260	J_{24}	(5-7), (5-7), (6-8), (6-8)	J_{64}	(5-15), (6-16), (7-13), (8-14)
13.808	J_{25}	(5-8), (6-7)	J_{57}	(5-8), (6-7), (14-15), (4-12)
13.829	J_{25}	(5-8), (6-7)	J_{65}	(5-16), (6-15), (7-14), (8-13)
6.147	-	-	J_8	(1-9), (1-9), (2-10), (2-10), (3-11), (3-11), (4-12), (4-12)
6.147	-	-	J_{62}	(5-13), (5-13), (6-14), (6-14), (7-15), (7-15), (8-16), (8-16)

Table 4.IV – Based on the distance between the central C atom in the ONCNO branch of the interacting molecules, the 10 inequivalent Js of the single cell are compared to the 22 Js in the $2 \times 1 \times 1$ supercell.

CHAPTER 5

EXPERIMENTAL RESULTS

In this chapter, we will first study the magnetization and magnetic susceptibility of the α and β phases of NIT2Py. We will compare the results of the specific heat of both the α and β phases at diferent applied magnetic field. Also, the specific heat measurement of both phases will be discussed. Because of the interesting results obtained for the α phase, we will study the magnetization of this phase at high magnetic fields using a pulsed magnet. Using the temperature dependence of magnetic specific heat and magnetocaloric measurements of the α phase, we will establish an (B,T) phase diagram. We will examine the critical exponents close to a critical field of the (B,T) phase diagram of the α phase on the power law.

5.1 Magnetization of NIT2Py

Magnetization and magnetic susceptibility are measured for crystals of NIT2Py using a magnetic property measurement system (MPMS). The MPMS machine is a sensitive magnetometer designed by Quantum Design that provides a new level of speed and sensitivity by combining the properties of the vibrating sample magnetometer (VSM) with the superconducting quantum interference device (SQUID) magnetometer. The operating range of temperature in this SQUID VSM system is between 1.8 K and 400 K. In addition, SQUID VSM uses a superconducting helium-cooled magnet that can reach a maximum magnetic field of 7 T. Furthermore, the magnetization measurement in the SQUID VSM can be performed with a sensitivity of $\leq 10^{-8}$. An adhesive material is needed to attach the NIT2Py samples to the quartz sample holder of the MPMS. The adhesive should not dissolve the organic sample, should be able to withstand cryogenic temperatures, and should not possess a large magnetic background. Apiezon N was selected due to its adhesive property, good thermal conductivity, and low temperature stability.

In Fig. 5.1(a) and (b), magnetization as a function of applied magnetic field at various temperatures is shown for the α and β phases of NIT2Py respectively. As discussed in 2.5, the magnetization reaches saturation at large magnetic fields and low temperatures. In Fig. 5.1, the magnetization of the β phase at 2 K reaches saturation after 7 T. However, the magnetization of the α phase does not reach saturation even at the highest field and lowest temperature available in the SQUID magnetometer, as seen in Fig. 5.1(a). To study the α phase, the magnetization of a polycrystalline sample is measured at 1.43 K in the Dresden High Magnetic Field Laboratory (Hochfeld-Magnetlabor Dresden, HLD) using high pulsed magnetic fields. The results are shown in Fig. 5.2. The Apiezon N grease is also used to mount the sample on a plastic sample holder, which was placed in a conventional ^{4}He cryostat in the middle of a coil. For the saturation magnetization to reach the value expected for an unpaired electron per molecule (i.e. 1 μ_B per molecule), a multiplication factor derived from the value of the slope at low applied fields is used to correct the 1.43 K curve. Moreover, a low-temperature magnetization measurement at 0.5 K is performed using an MPMS at Max Planck Institute in Dresden, and the results are shown in Fig. 5.2. At 0.5 K, a magnetization plateau is observed at about 0.5 μ_B per molecule. This magnetization plateau, located at half of the saturation value, is reproduced by the proposed mean-field model of interacting tetramers, given in section 7.4.2,

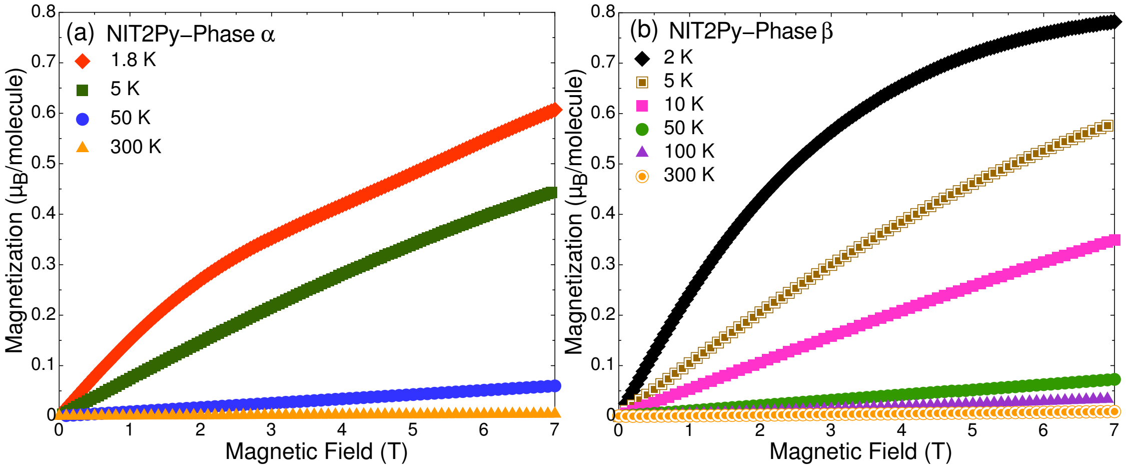

Figure 5.1 – The magnetization as a function of applied magnetic field measured at different temperatures for the (a) α and (b) β phases of NIT2Py.

and also by using the exact diagonalization of the Heisenberg Hamiltonian, discussed in section 7.5.

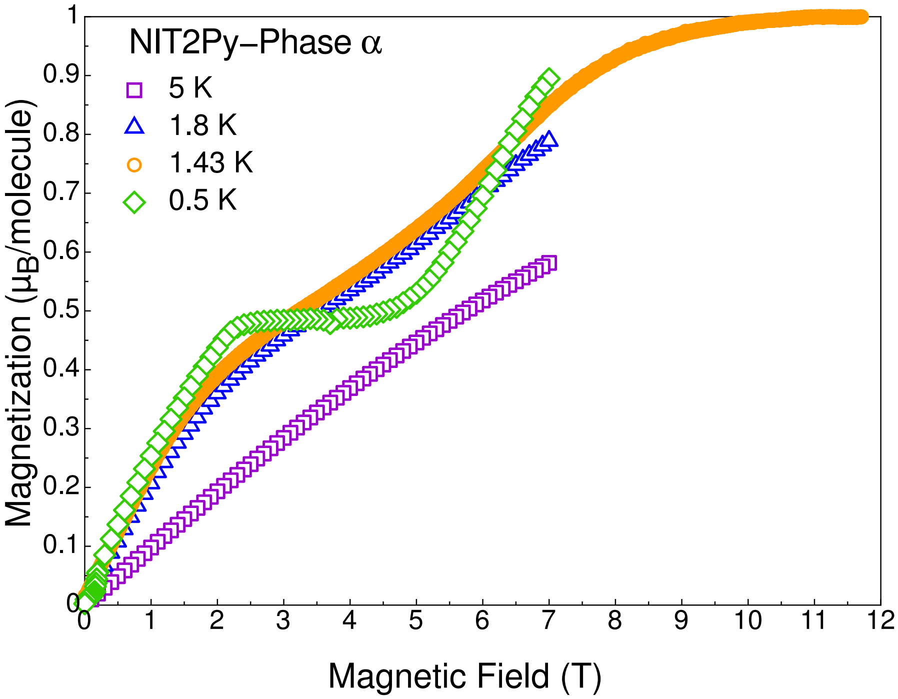

Figure 5.2 – Magnetization as a function of the applied magnetic field of a polycrystalline sample of the α phase of NIT2Py. The data related to the 1.43 K curve is obtained from the magnetization measurement using a pulsed magnet, and the remaining data associated to measurements by a MPMS.

5.2 Magnetic susceptibility of NIT2Py

The magnetic susceptibility at high temperatures in the α and β phases of NIT2Py are measured in applied fields of 1 T and 0.5 T, respectively. As discussed in 2.4, the total susceptibility consists of paramagnetic (χ_{Para}) and diamagnetic (χ_{Dia}) contributions. To find the contribution of the unpaired electron in the susceptibility, the χ_{Dia} must be subtracted from the measured susceptibility. Estimations of the χ_{Dia} values are obtained by considering the tabulated values of the diamagnetic correction factors, namely the Pascal constants, for different atoms, molecules, and bonds. Nevertheless, a large number of conflicts between documented values of the Pascal constants appear in various reference works [111]. Another way of obtaining a rough approximation of the diamagnetic contribution of a compound is by using $\chi_D \approx -1/2(\text{Molecular Weight}) \times 10^{-6}$ emu/mol, which yields -1.17×10^{-4} emu/mol for NIT2Py. However, in this work, a more precise correction value is obtained by minimizing the deviation of the inverse of the paramagnetic susceptibility ($1/\chi_{\text{Para}}$) in the high-temperature range from a straight line due to the Curie-Weiss law in Eq.(2.42).

So, to find the diamagnetic contribution of the measured susceptibility of the α phase, the χ in the high temperature range of 50 K up to 300 K must first be fitted to the Curie-Weiss law in Eq. (2.42), to which a constant is added, as shown in Fig. 5.3(a). Secondly, the obtained constant in the previous step is subtracted from χ, and subsequently $1/(\chi - \text{const})$ is plotted as a function of the temperature. Thirdly, $1/(\chi - \text{const})$ as a function of temperature is fitted to the inverse of the susceptibility in Eq. (2.42), and the obtained chi-squared value of the fit is recorded. By repeating the last step for various constants (χ_{Dia}), different chi-squared values are achieved, as displayed in Fig. 5.3(b). Lastly, by minimizing those chi-squared values obtained for different χ_{Dia} values, the diamagnetic contribution is found. The results are shown in Fig. 5.3(c). The χ_{Para} of the NIT2Py α phase is obtained by subtracting the resulting χ_{Dia} from the measured susceptibility. As shown in Fig. 5.3(d), the high temperature range of the $1/\chi_{\text{Para}}$ is fitted to the inverse of the susceptibility in Eq. (2.42). The negative Curie-Weiss temperature of -3.37 K shows that dominant AFM interactions exist between the NIT2Py molecules. The effective magnetic moment obtained from the Curie-Weiss fit for the α phase amounts to 1.49 μ_{B}.

The same steps of the process are executed to find the diamagnetic and paramagnetic contributions of the NIT2Py β phase. The results as well as the fitting the $1/\chi_{\text{Para}}$ by the Curie-Weiss law are shown in Fig. 5.4(a) to (d). A positive Curie-Weiss temperature of 1.81 K obtained for that phase indicates predominant FM interactions between the molecules. Also, the Curie-Weiss fit for that phase resulted in an effective magnetic moment of 1.47 μ_{B}. The obtained values of the effective moments are lower than the expected μ_{eff} of 1.73 μ_{B} for one unpaired electron per molecule based on Eq. (2.41).

Obtaining a lower value of effective moment can be explained by the error in calibrating the geometry of the sample by the SQUID magnetometer due to the small diameters of the samples, which leads to a reduction in the measured magnetic moment. Also, the lower value of effective moment can be explained by the existence of some impurities with no magnetic signals in the polycrystalline NIT2Py samples.

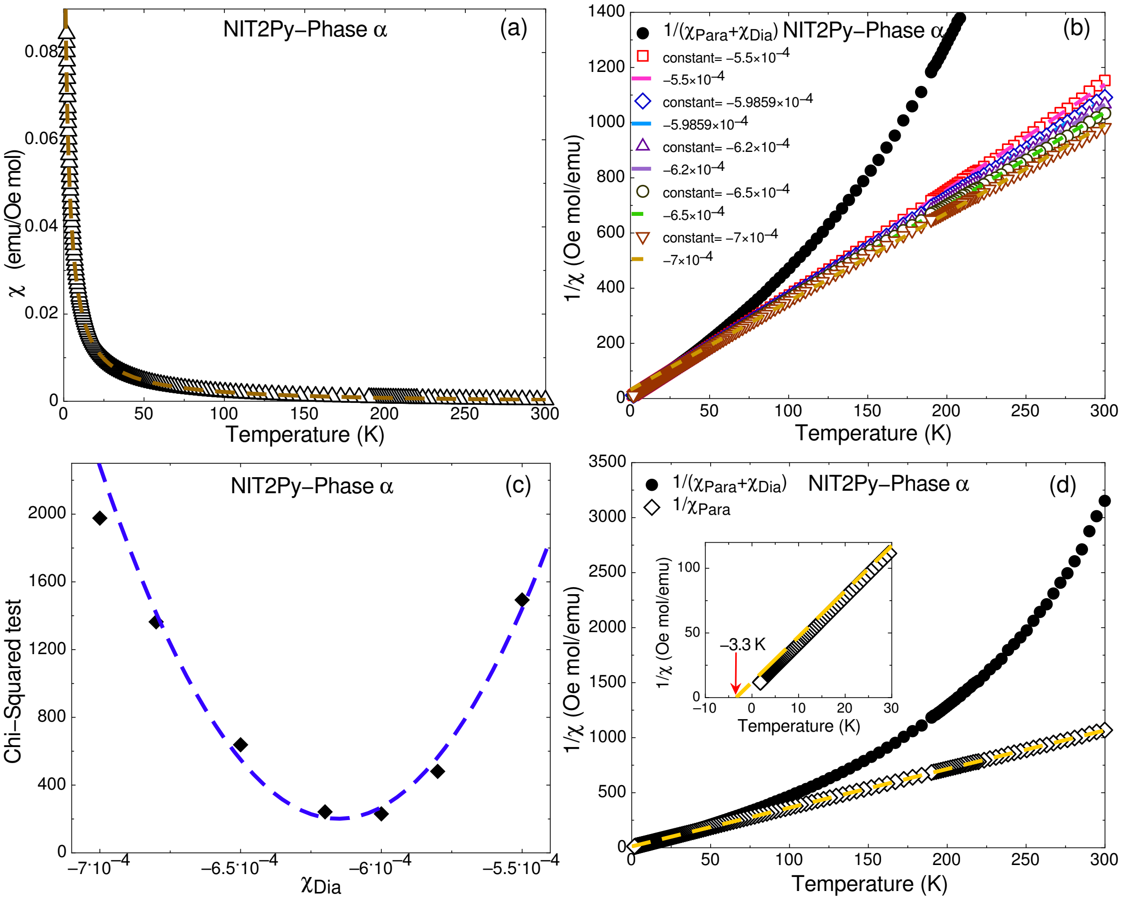

Figure 5.3 – (a) The temperature dependence of the susceptibility of the NIT2Py α phase in an applied field of 1 T. The dashed line is the fit in the high temperature range (50 K to 300 K) to Eq. (2.42) to which a constant is added, yielding constant -5.9859×10^{-4}. (b) The temperature dependence of the $1/(\chi - \text{constant})$ plotted for different constants. The dashed lines are the corresponding fits to the inverse of susceptibility in Eq. (2.42). (c) The chi-squared deviation from a straight line for various values of χ_{Dia}. The dashed line is a fit to $F(x) = a_2 + a_3(x - a_1)^2$, which results in finding the minimum point of the curve at $\chi_{\text{Dia}} = -6.182 \times 10^{-4}$ emu/mol. (d) The inverse of susceptibility as a function of temperature before (full circles) and after (empty diamonds) subtracting the diamagnetic contribution. The dashed yellow line is a fit to Eq. (2.42) in 50 K to 300 K, which leads to $\theta_{CW} = -3.37$ K.

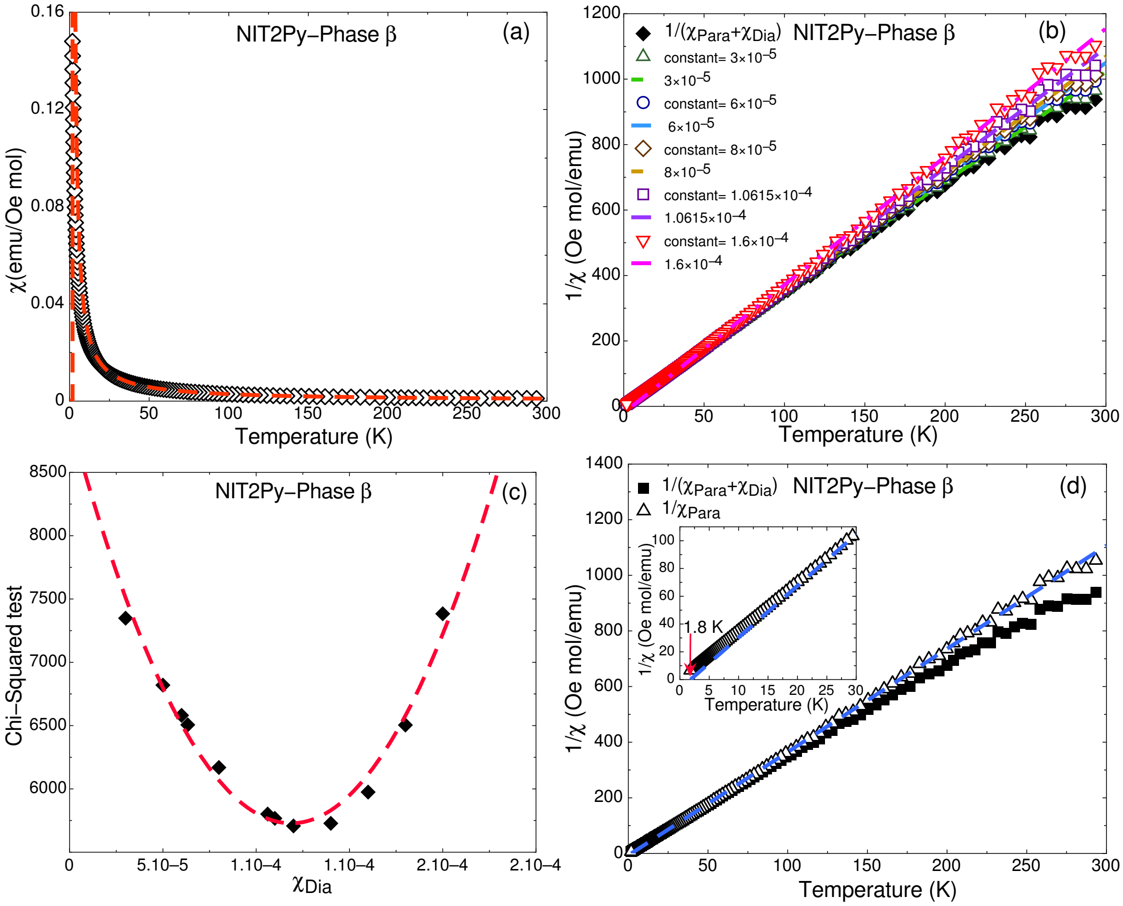

Figure 5.4 – (a) The temperature dependence of the susceptibility of the NIT2Py β phase in an applied field of 0.5 T. The dashed line represents the fit at a high temperature range (50 K to 300 K) to Eq. (2.42) and an added constant, resulting in a constant of 1.0615×10^{-4}. (b) $1/(\chi - \text{constant})$ as a function of temperature shown for various constant values. The dashed lines are the fits to the inverse of susceptibility in Eq. (2.42) for each illustrated curve. (c) The chi-squared deviation from a straight line for different values of χ_{Dia}. The dashed line is a fit to $F(x) = a_2 + a_3(x - a_1)^2$, which gives rise to obtaining the minimum point of the curve at $\chi_{\text{Dia}} = 1.17 \times 10^{-4}$ emu/mol. (d) The inverse of susceptibility as a function of temperature before (full squares) and after (empty triangles) subtracting the diamagnetic contribution. The dashed blue line is a fit to Eq. (2.42) in a 50 K to 300 K range, yielding $\theta_{CW} = 1.81$ K.

5.3 Specific heat of NIT2Py

A physical property measurement system (PPMS) from Quantum Design, equipped with a ^{3}He insert and a 9 T magnet is used to measure the specific heat of the NIT2Py

α and β phases. The PPMS uses the relaxation technique, which enables researchers to measure small samples of 1-500 mg with accuracy. PPMS can support a range of temperature between 1.9 K and 400 K, which can be decreased to 0.4 K by using the ^{3}He insert.

The specific heat contribution of the adhesive must be subtracted from the measured data because a thin layer of Apiezon N grease was used to mount the samples to the PPMS platform. The heat capacity of the Apiezon N grease is calculated based on the function in Eq. (5.1),

$$C = \exp \sum_i a_i (\ln T)^i, \tag{5.1}$$

where the values of the coefficients a_i are exploited based on the published values for different ranges of temperatures: $T > 0.1$ K and $T < 4.1$ K, $T \geq 4.1$ K and $T < 17.5$ K, and $T \geq 17.5$ K and $T < 187$ K [112]. As shown in the log-log plots in Fig. 5.5(a) and (b), the specific heat curves are compared by using different masses of the Apiezon N and applying Eq. (5.1) to those of the NIT2Py α and β phases measured at zero applied magnetic field. The specific heat of the Apiezon N related to each NIT2Py phase is calculated by multiplying the mass of the corresponding sample, 0.61 mg for α phase and 0.46 mg for β phase, to Eq. (5.1) and by using the coefficients of reference [112].

After subtracting the specific heat contribution of the Apiezon N grease, the magnetic specific heat of an insulating magnet such as NIT2Py can be found by subtracting the phonon contribution (C_{ph}): $C_{\text{mag}} = (C_{\text{sample}} - C_{\text{Ap}}) - C_{\text{ph}}$. To find the phonon contribution, $C_{\text{sample}} - C_{\text{Ap}}$ is fitted to the Debye model. Because of the small Debye temperatures reported for organic radicals with almost similar chemical structures, such as 88.7 K and 140 K, measured for the two different phases of the p-NPNN radical [38], the Debye-T^3 law of Eq. (2.45) is not sufficient to obtain the phonon specific heat of NIT2Py. Instead, the general Debye model in the integral of Eq. (2.44) is used to determine the C_{ph} of NIT2Py. The fitting is performed in the temperature range of 13 K to 33 K for the α phase, and 13 K to 20 K for the β phase.

As shown in Fig. 5.6(a) and (b), by plotting the resulting C_{mag} as a function of tem-

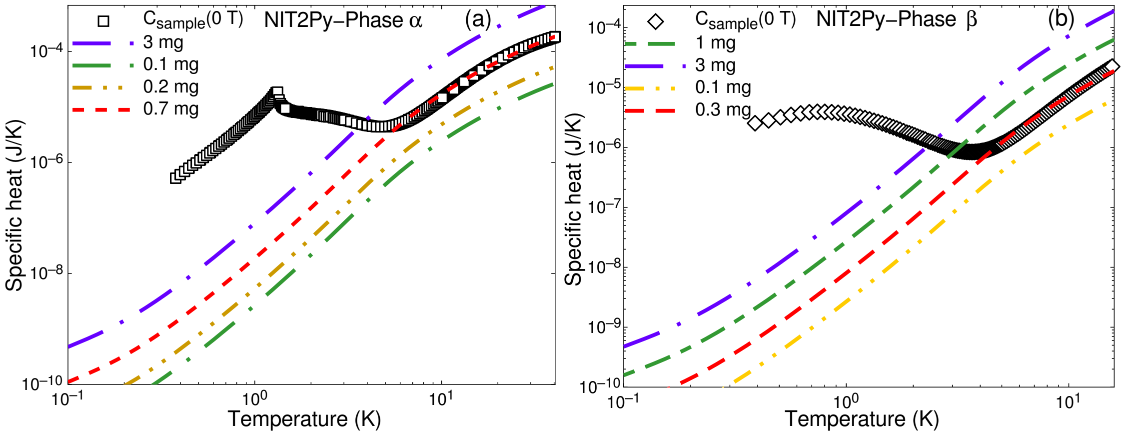

Figure 5.5 – The behavior of the specific heat of the Apiezon N grease based on Eq. (5.1) as a function of temperature by changing its mass. The results are compared to the specific heat of NIT2Py measured at zero applied field for the (a) α phase with a sample mass of 0.61 mg, and (b) the β phase with a sample mass of 0.46 mg.

perature, negative values associated with the magnetic specific heat of both NIT2Py phases are observed. Those negative values indicate an imprecision in the measurement of the masses of the Apiezon N grease in both phases, resulting in an overestimation of the C_{Ap}. Because measuring the exact mass of the Apiezon N grease in the specific heat measurement of NIT2Py is an arduous task, an effective mass for that grease is used.

The effective mass is obtained by comparing the behavior of different C_{mag} curves as a function of temperature evaluated for various Apiezon N masses for each of the phases. Before the comparison can be made, the corresponding C_{Ap} must first be assessed using Eq. (5.1) for each Apiezon N mass separately. The resulting C_{Ap} for each Apiezon N mass is subtracted from the measured specific heat individually. Subsequently, by using the above mentioned process, different magnetic specific heats are obtained for different Apiezon N masses, shown in Fig. 5.6. Therefore, the effective mass of the Apiezon N grease is obtained as 0.31 mg for the NIT2Py α phase, and 0.09 mg for the β phase, because both show positive values of C_{mag} versus T for the corresponding phase.

In Fig. 5.7(a), the Apiezon N specific heat of the α phase is plotted by using the effective mass obtained for that phase in Eq. (5.1). The resulting C_{Ap} is subtracted from the measured specific heat in zero applied field. In Fig. 5.7(b), the fit to the Debye

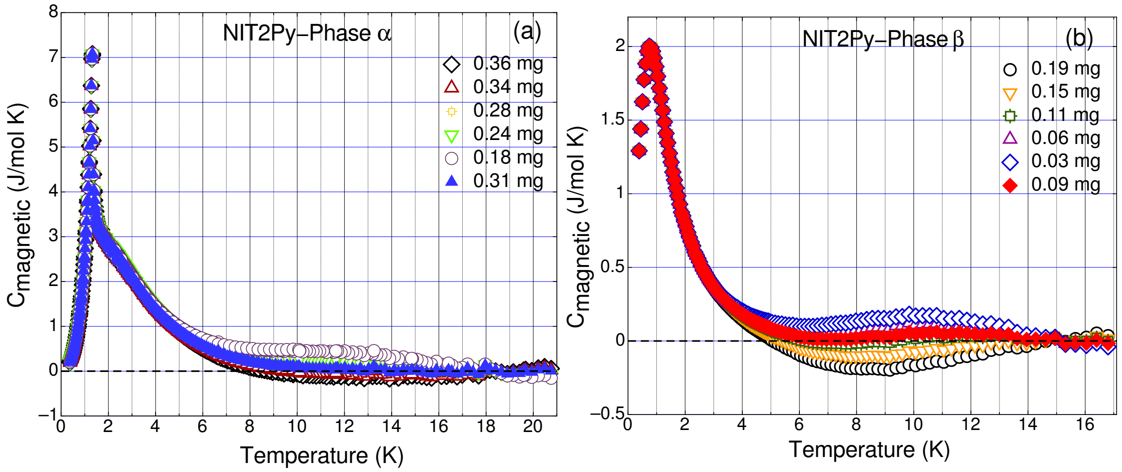

Figure 5.6 – Temperature dependence of magnetic specific heat after subtracting the Apiezon N grease and the phonon contributions from the measured specific heat. Different curves are related to different values of specific heat of the Apiezon N grease calculated by taking into account various masses for the grease in each of the phases. The effective mass of the α phase is determined as 0.31 mg and the one for the β phase as 0.09 mg.

model yields $\theta_D = 121.3\text{K}$ and N = 2.3. Finally, the magnetic specific heat is revealed. As shown in Fig. 5.8(a), the same process is repeated for the β phase using the effective mass obtained for that phase in Eq. (5.1). In Fig. 5.8(b), the fit to the Debye model gives rise to the $\theta_{\text{D}} = 116.8$ K and N = 2.1. Also, the magnetic specific heat for the zero field of the β phase is illustrated. We expect that each NIT2Py molecule acts as a vibration element and yields N=1.

5.4 Magnetic specific heat of NIT2Py in applied magnetic fields

In Fig. 5.9(a) and (b), the log-log plot of the specific heat after subtracting the heat capacity of the Apiezon N is shown at zero-field, as well as at applied magnetic fields of 3 T and 6 T for the NIT2Py α and β phases respectively. The Debye temperature is obtained as $\theta_D = 121.3\text{K}$ for the α phase, and as $\theta_{\text{D}} = 116.8\text{K}$ for the β phase. In Fig. 5.9(a) and (b), all the curves merge around the 10 K mark. Also, the phonon contribution of each phase is much smaller than the magnetic contribution, and hence the Debye model is a good approximation to estimate the size of the Debye temperature in

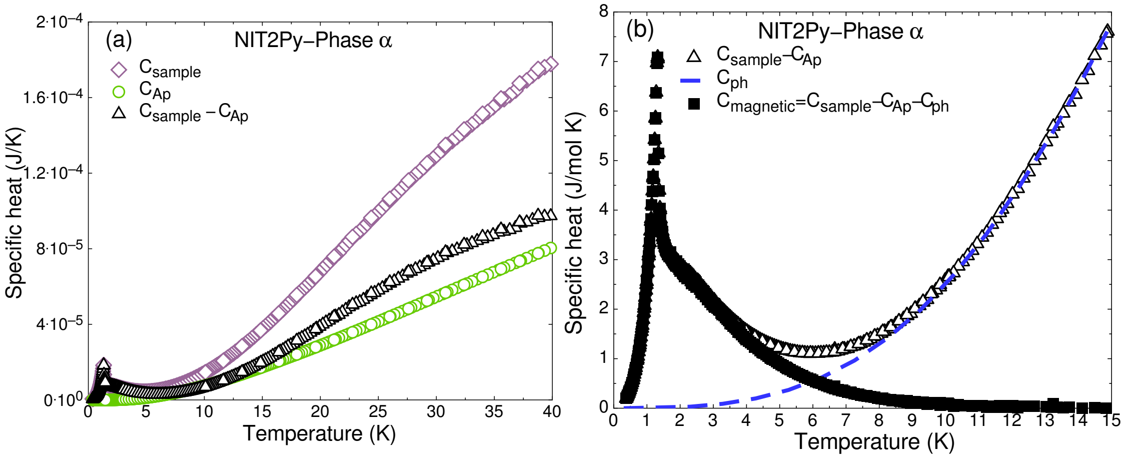

Figure 5.7 – (a) The temperature dependence of the zero-field specific heat of the NIT2Py α phase with a sample mass of 0.61 mg, seen before and after subtracting the Apiezon N contribution. The Apiezon N specific heat is plotted by using Eq. (5.1) and the effective mass of the Apiezon N grease is 0.31 mg. (b) The phonon contribution illustrated as a dashed line, obtained by fitting the $C_{\text{sample}} - C_{\text{Ap}}$ to the Debye model between 13 K and 33 K. Magnetic specific heat is shown by subtracting the phonon specific heat from the resulting specific heat, minus the contribution of the Apiezon N.

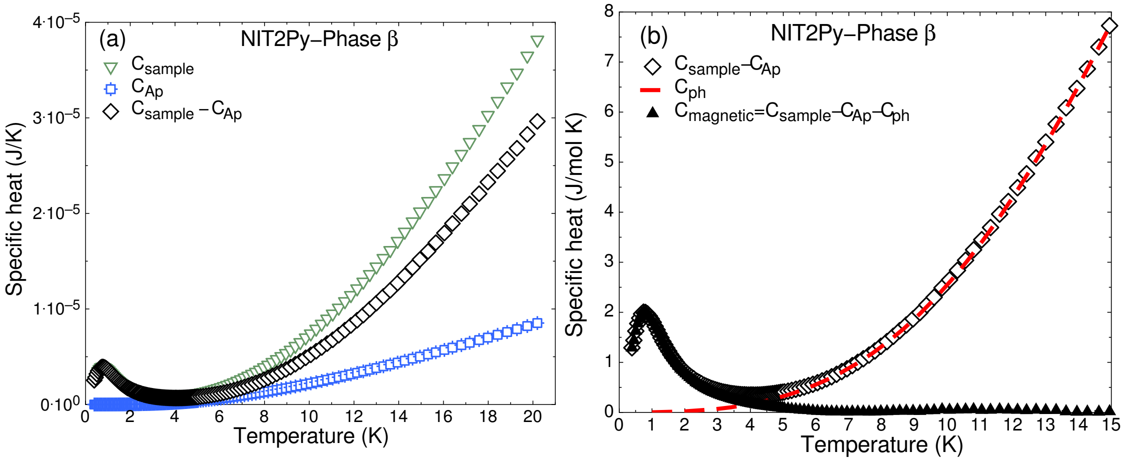

Figure 5.8 – (a) The zero-field specific heat of the NIT2Py β phase before and after subtracting the contribution of Apiezon N. The sample mass is 0.46 mg, and the effective mass of Apiezon N grease is 0.09 mg. (b) The dashed line showing the fit to the Debye model in the range of 13 K to 20 K. The magnetic specific heat is attained by excluding the phonon specific heat.

both phases.

Fig. 5.10 shows the magnetic specific field as a function of temperature in the NIT2Py

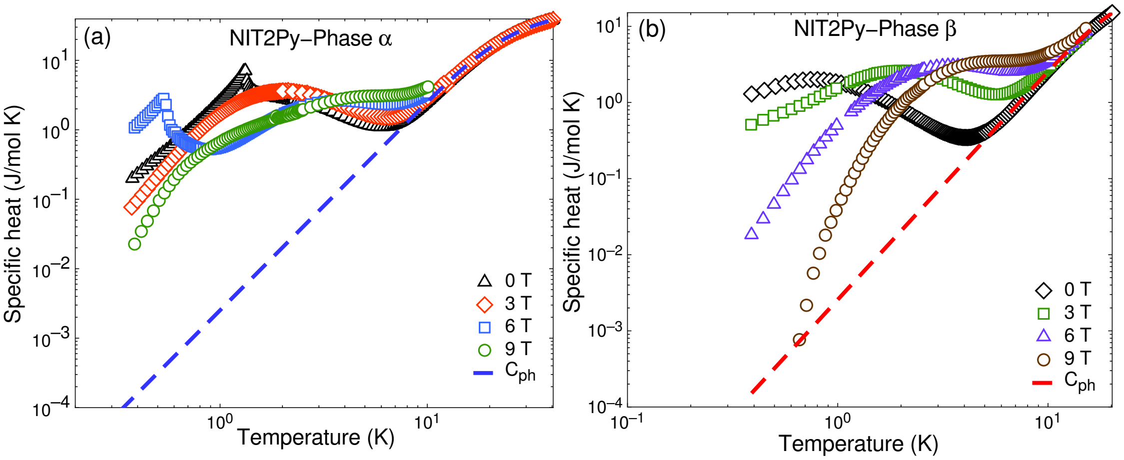

Figure 5.9 – The specific heat measured at 0 T, 3 T, 6 T, and 9 T after subtracting the C_{Ap} shown for (a) α and (b) β phases of NIT2Py. The dashed lines are the fit to the Debye model for each of the phases.

single crystal of the α phase at various applied magnetic fields from 0 T to 9 T. The sharp λ-peak in the magnetic specific heat at zero field indicates the onset of a 3D magnetically ordered state. That field-induced disorder-order transition occurs at the ordering transition of 1.32 K for the zero applied field. As shown in Fig. 5.10(b), by increasing the applied magnetic field, the λ-peak anomaly in the field dependence of the magnetic specific heat is gradually suppressed in its height, and its position is shifted to lower temperatures. At about 2.2 T, the sharp λ-peak totally disappears and no further signature of the transition reappears, even up to about 4.5 T. As shown in Fig. 5.10(c), at an applied field of 5.5 T, a new peak emerges at a transition temperature of 0.5 K. When the magnetic field is increased up to 6 T, the newly appeared peak shifts to higher temperatures and reaches a transition temperature of 0.53 K. Furthermore, when increasing the field up to about 7 T, the peak moves to lower temperatures.

As shown in Fig. 5.11, the temperature dependence of the magnetic specific heat of a single crystal of β phase is exhibited for various applied magnetic fields from 0 T to 9 T. A peak at zero applied field of the magnetic specific heat indicates a magnetic phase transition with a critical temperature of 0.74 K. By increasing the magnetic field, the peak broadens and shifts to higher temperatures. The behavior of the magnetic specific heat as a function of temperature of the NIT2Py β phase is comparable to that of the first

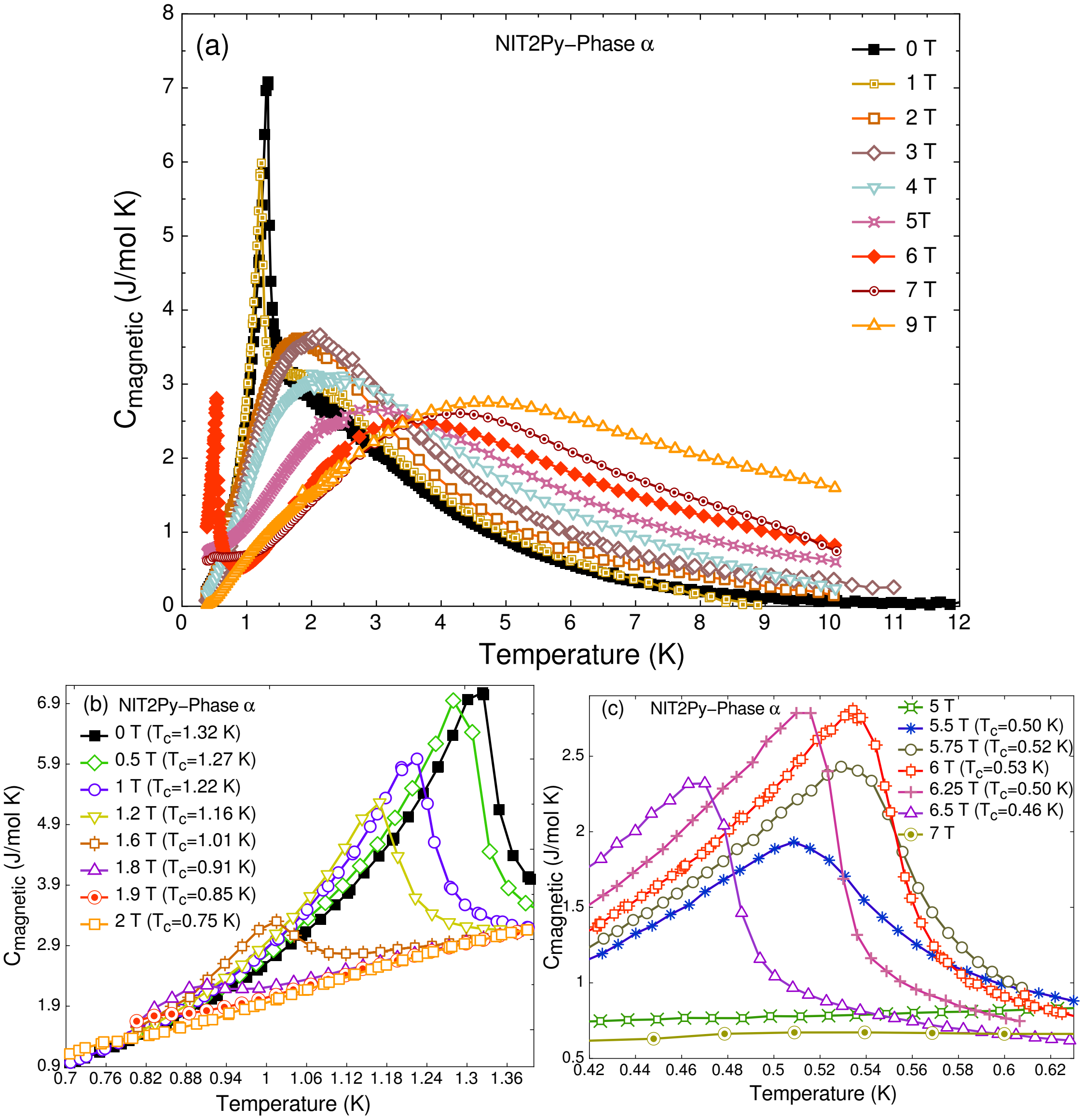

Figure 5.10 – (a) Temperature dependence of the magnetic specific heat of a single crystal of NIT2Py α phase in an applied magnetic field of 0 T to 9 T. The transition points correspond to magnetic specific heat curves measured between 0 T and 2 T shown in (a) and between 5 T and 7 T illustrated in (b).

purely organic free radical magnet, namely the β phase of p-NPNN [38].

The behaviors of the magnetic specific heat of both phases at different applied fields are compared in Fig. 5.12. At zero applied field in Fig. 5.12(a), the observed transition peak at 1.32 K in the α phase is associated with an ordered phase that is presumed to

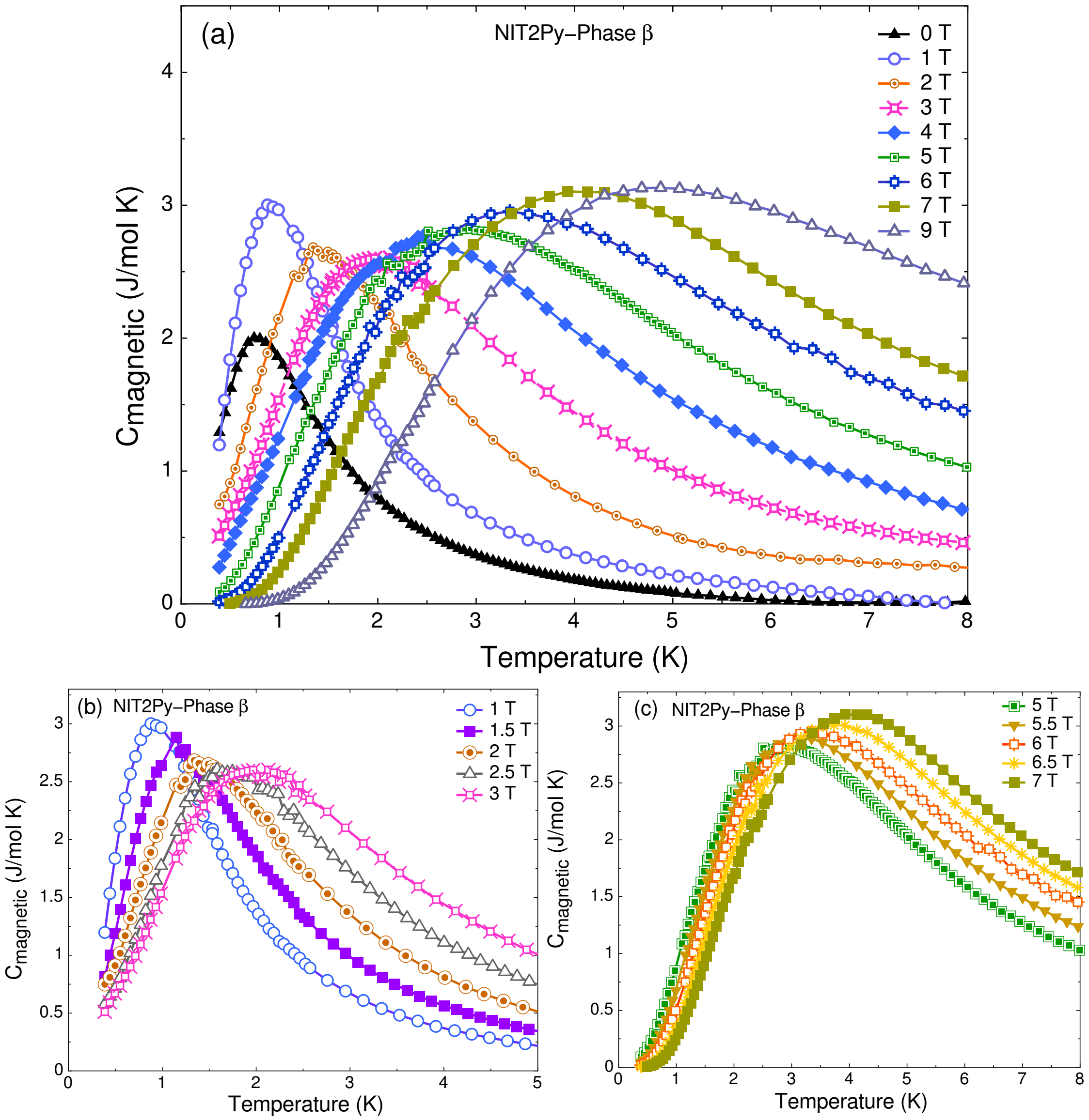

Figure 5.11 – (a) The magnetic specific heat of a single crystal of the NIT2Py β phase as a function of temperature with applied magnetic fields of 0 T to 9 T. The behavior of temperature dependence of the magnetic specific heat under the applied field in the range of (b) 1 T to 3 T and (c) 5 T to 7 T.

be an AFM order due to the negative Curie-Weiss temperature obtained in the magnetic susceptibility of that phase. Whereas, the transition peak at 0.74 K in the β phase is anticipated to be an FM order because of the positive value obtained for the corresponding Curie-Weiss temperature. In Fig. 5.12(b), the pick broadens at 3 T, and the Schottky anomaly is observed in both phases. However, the magnetic field dependence of the specific heats at 5.5 T, 6 T, and 6.5 T for the α and β phases are rather different, as demonstrated in Fig. 5.12(c), (d), and (e). For the α phase, a new peak exists between 5.5 T to about 7 T but never emerges in the β phase.

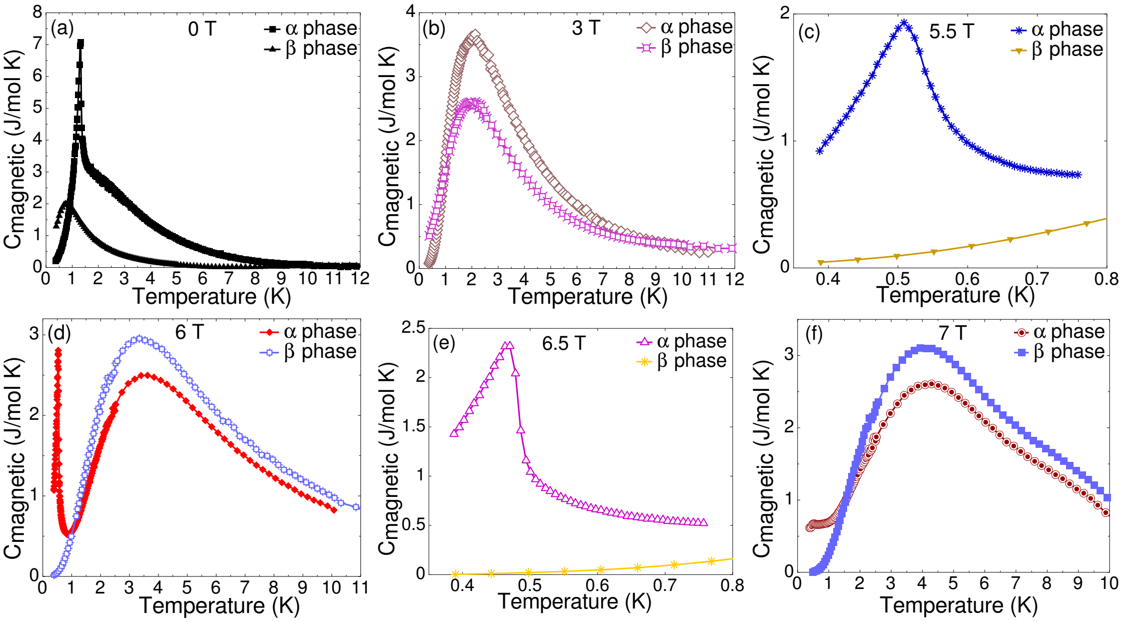

Figure 5.12 – The temperature dependence of the magnetic specific heat of the α and β phases are compared at (a) zero applied magnetic field, (b) 3 T, (c) 5.5 T, (d) 6 T, (e) 6.5 T, and (f) 7 T.

The temperature-magnetic-field (B, T) phase diagram of the α phase is shown in Fig. 5.13. Each point in the (B, T) phase diagram in Fig. 5.13 represents the transition temperature of each peak in Fig. 5.10(b) and (c), that is plotted as a function of the corresponding applied magnetic field. Additionally, the two different regions observed in the phase diagram are illustrated by colored regions. The first dome-shaped region appears at low applied magnetic fields up to about 2.2 T, and the second dome-shaped region occurs between about 5 T and 7 T. In addition to the dome-shaped regions in Fig. 5.13, we have superimposed the magnetization as a function of applied magnetic field measured at 0.5 K (green line) and 1.43 K (brown line). Interestingly, the 1/2 μ_B plateau corresponding to the magnetization curve of 0.5 K is located in the exact area between two phase regions of the phase diagram, where there is no magnetic order.

Notable characteristics observed for the NIT2Py α phase include a magnetic order at low applied fields, an exotic magnetic phase as a consequence of a newly emerged peak in the specific heat at applied fields between 5 T and 7 T, and an uncommon plateau at half value of the saturation magnetization. Those characteristics have motivated us to focus our research on the α phase in order to comprehend the nature of the dome-shaped regions in the phase diagram and the plateau at half saturation magnetization. The study of the magnetic system through DFT will be discussed in 7.

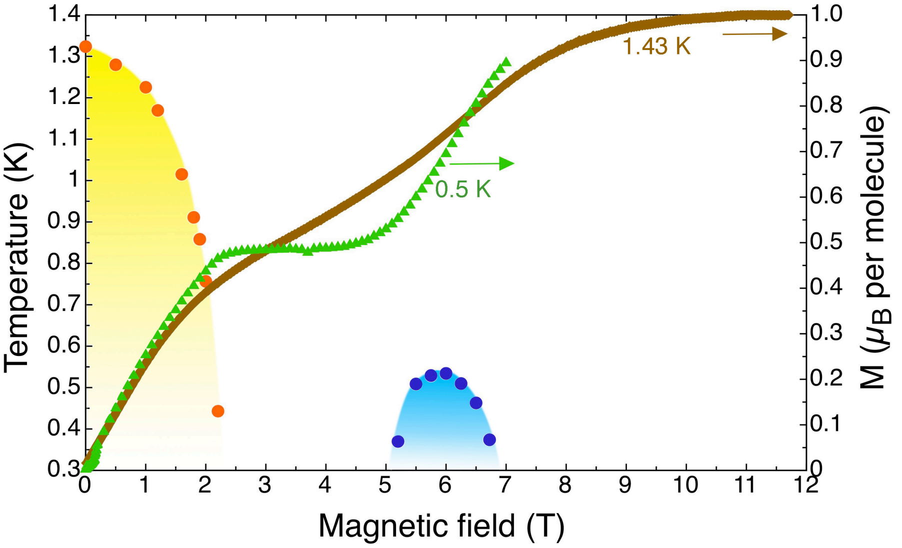

Figure 5.13 – The temperature-magnetic-field phase diagram of NIT2Py elaborated from the transition peaks in the magnetic specific heat at different applied magnetic fields in Fig. 5.10. The (B, T) phase diagram shows two regions, one occurring at low fields up to about 2.2 T, and the other between more or less 5 T and 7 T. Magnetization versus magnetic field $M(B)$ measured at 0.5 K and 1.43 K are overlaid on the phase diagram. The $M(B)$ curve at 0.5 K shows a plateau at half value of magnetization saturation.

Magnetocaloric effect (MCE) measurements are carried out to trace the field dependence of the transition temperatures near the critical fields of the second field-induced ordered phase in the (B, T) phase diagram, and hence to identify the corresponding phase boundaries. The transitions in the (B, T) phase diagram by the MCE measurements are determined from the peaks of the curves of several temperatures in $\mathrm{d}T/\mathrm{d}B$ versus applied field. As shown in Fig. 5.14(a) and (b), the phase boundaries of the second field-induced ordered phase in the (B, T) phase diagram obtained by the MCE measurements are consistent with the ones from the specific heat measurements. The second field-induced disorder-order transition occurs upon applying magnetic fields of about 4.5 T, and this ordered phase exists up to about 7.3 T.

The transition temperatures, obtained from specific heat measurements while applying a pressure of 10 kbar, are shown in Fig. 5.14(a). At 0 kbar, the zero-field specific heat has a transition temperature of 1.32 K. However, upon applying a pressure of 10 kbar, that transition temperature spikes up slightly to reach 1.65 K. Additionally, by applying a pressure of 10 kbar, the transition temperatures of the specific heat measurements related to the second field-induced phase appear at larger applied fields and keep approximately the same transition temperatures as compared to the ones measured at 0 kbar.

To interpret the phase transition below a certain critical field as a BEC of magnon, the gap must close at that critical field. In a system with small dispersion along a given crystallographic direction, the magnon dispersion is small along that direction, and one can treat the system with a 2D quadratic magnon dispersion relation. If we consider a 2D character for the magnon dispersion and that $T < \Delta$, then the main contribution to the magnetic specific heat as a function of temperature is given by $C_{mag} \simeq \exp(-\Delta/T)/T$. So, the slope of the plot of C_{mag}/T versus $1/T$ of the NIT2Py experimental data resulted in the value of the gap, Δ_{2D}. Also, treating a system with a 3D dispersion relation results in the leading term in the magnetic specific heat being $C_{mag} \simeq \exp(-\Delta/T)/\sqrt{T}$. In that case, the value of the gap, Δ_{3D}, can be calculated by the slope of the plot of $C_{mag}/\sqrt{T}$ versus $1/T$ [87]. As shown in Fig. 5.14(a), the values evaluated for Δ_{2D} and Δ_{3D} are relatively the same.

An explicit indication for a BEC characterization of a field-induced phase transition could occur through the establishment of the critical exponent $\phi = d/z$ in the field dependence of the critical temperature. Based on the power law $B_c(T) - B \propto T_c^{\phi}$, the critical exponent ϕ can be evaluated close to the critical field B_c [87]. The critical exponent is highly sensitive to the value selected for the critical field [79]. As shown in Fig. 5.14(c), the field dependence of the critical temperature close to the upper critical field of the second dome is well delineated by the power law. We found that when critical temperature, T_N, approaches zero, the upper critical field corresponding to all ϕs converges to a value of 7.345(3) T. The critical exponent is calculated as ϕ=1.47(9) by using the critical field of 7.345(3) T, as shown in Fig.5.14(d).

Additionally, as shown in Fig. 5.14(a), above the upper critical field of 7.345 T, the gap (Δ) opens in the spin excitation spectrum, and a fully spin-polarized FM state is observed.

Briefly, obtaining a critical exponent of ϕ=1.47(9) close to the theoretically predicted value of ϕ_{BEC}=3/2 for a 3D quadratic dispersion of a low-energy magnon [113, 114], along with the fact that a spin gap is opened above the upper critical field of the second field-induced ordered phase confirm the idea of BEC in the NIT2Py.

As discussed in 2.6.1, a Schottky anomaly appears as a broad maximum in the magnetic specific heat where the value of thermal energy ($k_\mathrm{B}T$) is close to that of the energy difference between two levels ($k_\mathrm{B}\Delta_\varepsilon$). Note that the value of Δ_ε is directly related to the position of the peak in the magnetic specific heat curve. When fitting the magnetic specific heat curves of the α phase at different applied fields to the Schottky anomaly given in Eq. (2.46), the value of the Δ_ε parameter of each curve is obtained. As shown in Fig. 5.15(a), (b), and (c), the magnetic specific heat at 3 T, 8 T, and 9 T are fitted once to a function consisting of only one Schottky anomaly in Eq. (2.46), and once to a function composed of a sum of two Schottky anomalies with $\Delta_{\varepsilon 1}$ and $\Delta_{\varepsilon 2}$. As shown in Fig. 5.15 (a), the fit of 3 T with one Schottky anomaly is satisfactory. However, at larger applied magnetic fields, the fit needs to be optimized by adding another Schottky anomaly to the Eq. (2.46), as shown in Fig. 5.15(b) and (c).

In Fig. 5.15 (d), the $\Delta_{\varepsilon 1}$ and $\Delta_{\varepsilon 2}$ values, resulting from each of the magnetic specific heat curves between 0 T to 9 T being fitted to a function including the sum of two Schottky anomalies, are plotted as a function of the applied field. The $\Delta_{\varepsilon 1}$ values increase more or less linearly when augmenting the applied magnetic field due to the Zeeman splitting of the levels. That increasing of the $\Delta_{\varepsilon 1}$ values at large magnetic fields is well fitted by $g\mu_B B/k_B$, which is shown as a dashed line in Fig. 5.15(d). The minimum point of all the $\Delta_{\varepsilon 2}$ points, occurring at about 6 T, is where the energy levels cross. One notices that the applied magnetic field of 6 T is also where the second dome-shaped region in the phase diagram of Fig. 5.13 appears.

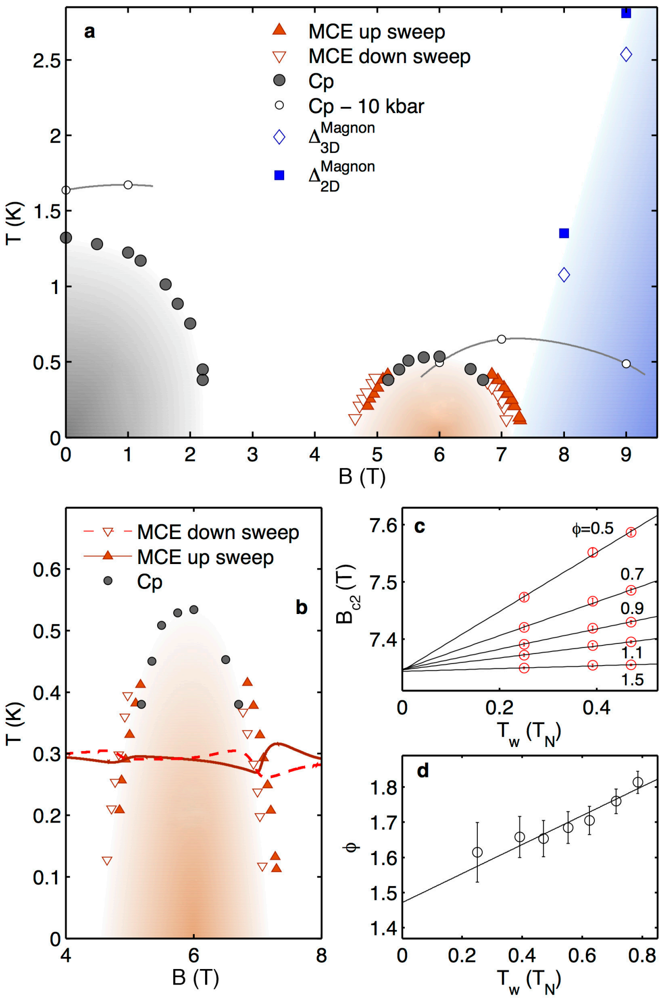

Figure 5.14 – (a) The temperature-magnetic-field phase diagram of NIT2Py obtained by the specific heat and MCE measurements. The temperature dependence of specific heat measured under pressures of 10 kbar is shown as empty circles. The values of Δ_{2D} and Δ_{3D} shown respectively as solid squares and empty diamonds are obtained by finding the slope of the plot of the C_{mag}/T and $C_{mag}/\sqrt{T}$ vs $1/T$ above the critical field of 7.345 T. (b) Comparison of the boundaries of the second dome-shaped phase based on MCE and specific heat measurements. The effect of increasing and decreasing the applied field is shown in the MCE measurement. (c) The field dependence of the critical temperature close to the upper critical field of the second dome-shaped phase. Different critical exponents are calculated for various values of upper critical field. (d) When T_N approaches zero, the critical value ϕ converges to 1.47(9).

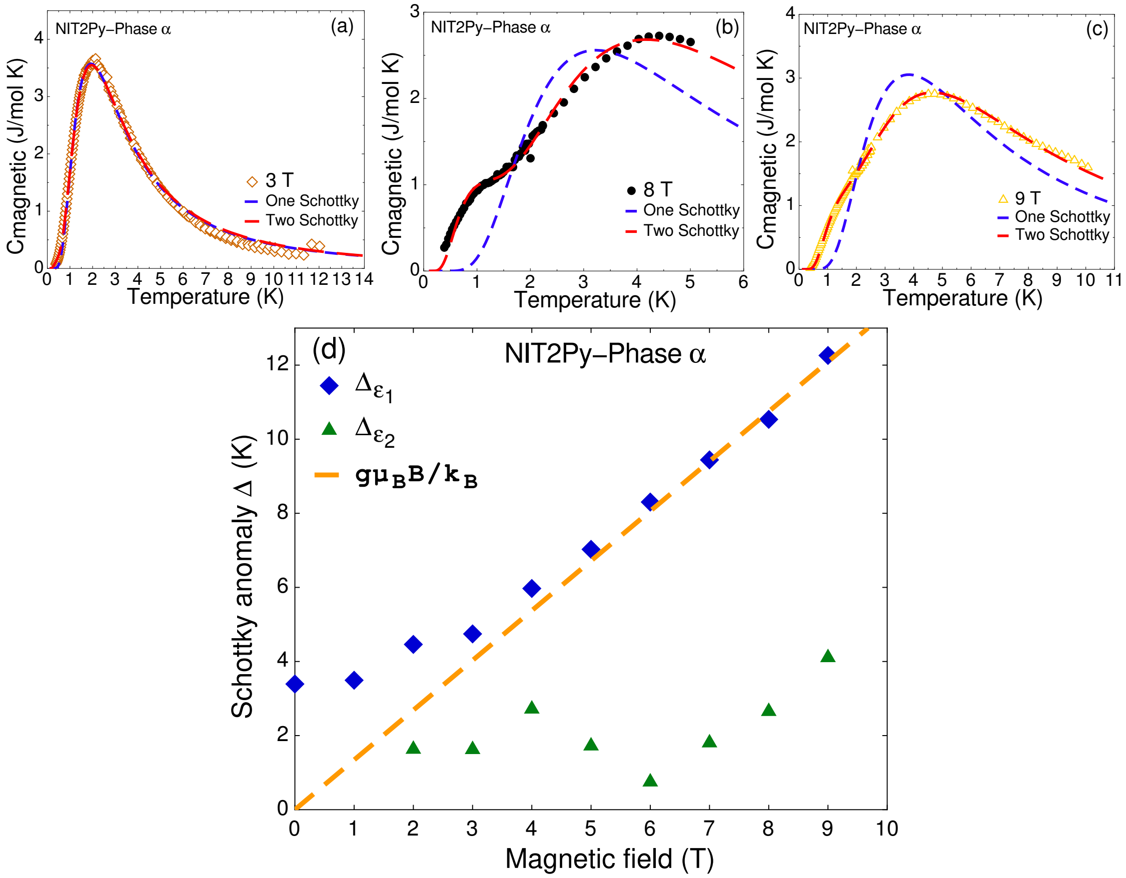

Figure 5.15 – The magnetic specific heat curves of the α phase at (a) 3 T, (b) 8 T, and (c) 9 T. The blue dashed line shows the fit to one Schottky function in Eq. (2.46). The red dashed line is a fit to a sum of two Schottky functions consisting of fitting parameters $\Delta_{\varepsilon 1}$ and $\Delta_{\varepsilon 2}$. (d) The resulting $\Delta_{\varepsilon 1}$ and $\Delta_{\varepsilon 2}$ obtained from fitting the magnetic specific heat curves related to different applied fields to a function including a sum of two Schottky anomalies are shown respectively as blue diamonds and green triangles. The dashed line in (d) shows a fit to $g\mu_B B/k_B$.

5.5 Magnetic entropy

The magnetic entropy (S_{mag}) is calculated based on Eq. (2.47) and by using the values of the magnetic specific heat obtained in the previous section. Due to the lack of experimental data for very low temperatures, a number of data points are added between 0 K to 0.4 K. To find those data points, a point is first added to the C_{mag}/T curve at 0 K. Then, as shown in Fig. 5.16(a), the C_{mag}/T curve is fitted to a power law, $C_{\text{mag}} \propto T3$, which is expected for antiferromagnons in 3D at temperatures well below T_{AFM}. In Fig. 5.16(b), the magnetic entropy is calculated at different applied magnetic fields by analysing the integral of Eq. (2.47) as well as by taking into account the experimental values of C_{mag} and the extra added points.

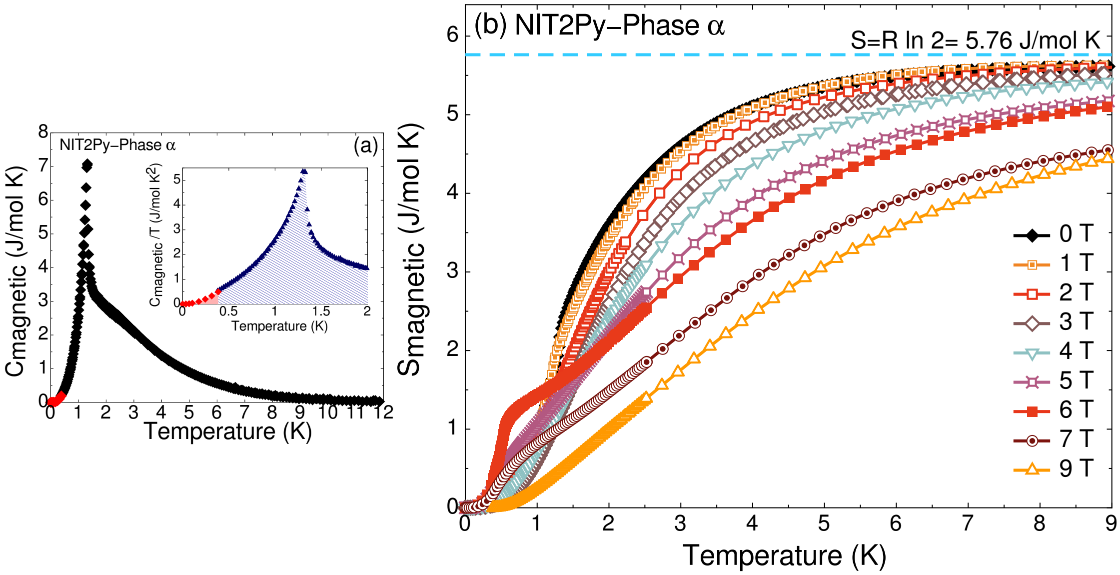

Figure 5.16 – (a) The temperature dependence of the magnetic specific heat of the NIT2Py α phase shown at zero applied field. The added red data points between 0 K to 0.4 K are based on the fitting procedure shown in the inset, in which the temperature dependence of the C_{mag}/T curve was fitted to a power law, $C_{\mathrm{mag}} \propto T3$. (b) The magnetic entropy as a function of temperature represented for various applied magnetic fields between 0 T and 9 T. The solid line at 5.76 J/mol K is the maximum value expected for the magnetic entropy of a S=1/2 spin system at very high temperatures.

As seen in Fig. 5.16(b), the magnetic entropy reaches a value of 5.76 J/mol K at very high temperatures, which is the expected value for the entropy of a spin-1/2 system as given by $R\ln(2S+1)$, where $\mathrm{R} = 8.314$ J/mol K. There is a small lack of entropy in the magnetic entropy curves of 5 T to 7 T at temperatures smaller than 0.4 K as compared to the other curves. That is an indication of the presence of transition peaks in the magnetic specific heat of those curves at temperatures below 0.4 K. Unfortunately, the limits of our MPMS to measure the specific heat at temperatures below 0.4 K do not allow us to observe those transition peaks.

5.6 Contributions

Synthesization of the NIT2Py compound (see Annex I) was carried out by a group of collaborating chemists: Professor Christian Reber of University of Montreal, Professor Dominique Juneau and his PhD student Anthony Lannes of the University Claude Bernard Lyon 1. While carrying out the synthesization process to make more of the NIT2Py compound, Anthony Lannes generously showed me the step by step process of how it is done. The crystal structure of the two NIT2Py phases were obtained by Thierry Maris and Nicolas Gauthier at the X-ray diffraction laboratory in University of Montreal's chemistry department. We used the VSM SQUID Quantum Design in Dr. Andrea Bianchi's physics laboratory at University of Montreal to measure the magnetizations and magnetic susceptibilities of the two NIT2Py phases at a temperature range of 1.8 K to 300 K and at fields of up to 7 T. The specific heat measurements were done by Nicolas Gauthier and by myself using the PPMS Quantum Design in Dr. Andrea Bianchi's laboratory. The magnetization curve of the α phase at 1.43 K was measured by Dr. Joseph Law and Nicolas Gauthier using high pulsed magnetic fields in the Dresden High Magnetic Field Laboratory (Hochfeld-Magnetlabor Dresden, HLD). The magnetization measurement of the α phase were redone by Michael Nicklas and Nicolas Gauthier using an MPMS at Max Planck Institute in Dresden, which provided us with the result for the magnetization curve at 0.5 K. In Fig. 5.2, the curves were rescaled by Nicolas Gauthier with respect to the 1.43 K curve to reach the saturation value of 1 μ_B per molecule. He also undertook the analysis in Fig. 5.14.

CHAPTER 6

THE RESULTS OF ELECTRONIC STRUCTURE CALCULATIONS

To perform electronic structure calculations for NIT2Py as a system of electrons and nuclei, an open-source package of programs called ABINIT was used. ABINIT applies density functional theory by solving the Kohn-Sham (K-S) equations of electrons, using a planewave basis set and pseudopotentials. For more general information regarding the ABINIT package, one may visit the ABINIT homepage [115], or read the review article [52]. We took advantage of ABINIT to optimize the atomic coordinates, to study the electronic structure of the ground state, to calculate the total energy of the spin polarized and unpolarized, and to evaluate the magnetic moment of the system. Additionally, the total energies of a variety of supercells corresponding to different spin configurations are calculated to obtain magnetic exchange interactions in NIT2Py through the total energy difference mapping approach.

Different exchange-correlation choices are available in ABINIT [115]. The Perdew-Burke-Ernzerhof (PBE) Generalized Gradient Approximation (GGA) functional is employed throughout the calculations in this research[102]. Different GGA (PBE) pseudopotentials, such as the PAW pseudopotential [103] and the norm-conserving (NC) pseudopotential [107], are examined. For the NC pseudopotential, we use the one provided by Fritz-Haber-Institute (FHI). However, the PAW pseudopotential available by the ABINIT website [108] is mainly used in the study presented in this thesis.

6.1 A single NITR molecule in a box

A NITR molecule $(H_{12}C_8N_3O_2)$ is originally placed in a cubic unit cell with lattice parameters $a = b = c = 14$ Å and $\alpha = \beta = \gamma = 90^\circ$, as shown in Fig. 6.1(a). Then, by displacing the coordinates of the carbon atom in the ONCNO branch of this molecule in the origin (0, 0, 0) as shown in Fig. 6.1 (b), the coordinates of other atoms are shifted correspondingly. Finally, by applying a rotation matrix on the x, y, and y coordinates of all the atoms, the NITR molecule is rotated 45° on the z axis, as illustrated in Fig. 6.1(c). The cartesian coordinates of atoms within a unit cell in Angstrom are defined. Also, 42 states are considered for the NITR molecule.

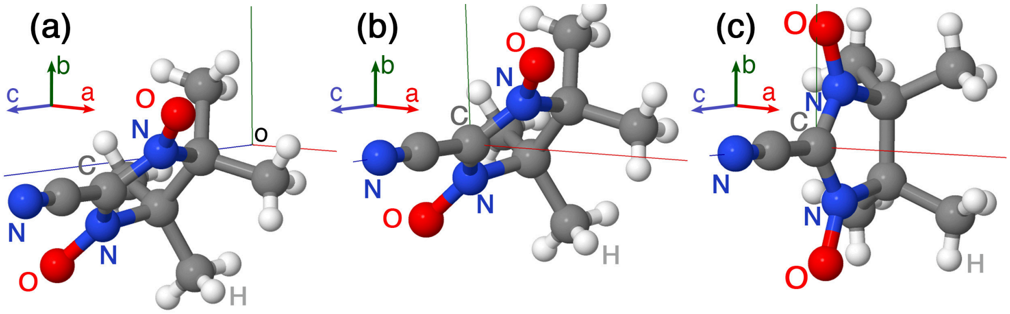

Figure 6.1 – (a) A NITR molecule in a box. (b) All the atoms are shifted according to the displacement of the carbon atom in the ONCNO branch to the origin of the axes (c) The molecule is rotated 45° on the c axis.

Furthermore, one k-point, the Γ point, is used to perform the total energy calculations of a single molecule in a box. Because in these calculations, the molecules are far enough and there is no dispersion.

To study this magnetized system, we set a scalar magnetization and arbitrarily choose the spin component along the z direction. We consider a diagonalized density matrix comprised of distinct magnitudes for the spin up and down. Also, we establish a scalar wavefunction and a collinear magnetization for a spin-polarized calculation with different wavefunctions for the spin up and down corresponding to each k-point. We assign the direction of the spin arbitrarily, and then we let the charge relax. Note that the initial non-zero magnitudes of the spin are only set for the two O atoms in the ONCNO branch of the NITR molecule and the spin of the remaining atoms is set to zero. Additionally, a spin-unpolarized calculation is done by setting a diagonal density matrix with identical values of spin up and down that leads to zero magnetization. The total energy of the spin-polarized system of the NITR molecule in a box is obtained as 0.28457 eV lower than the spin-unpolarized one, which indicates that the energy of the magnetized system is favored.

The structural optimization of the single NITR molecule in a box is performed by using the Broyden-Fletcher-Goldfarb-Shanno (BFGS) minimization. So, the atoms are moved to relax their coordinates until the structure is stabilized to its lowest energy configuration. Also, in coordinates optimization, the difference of forces is set as a tolerance, which, upon reaching for a second time that tolerance by a larger value, ends the SCF cycle.

We consider the differences between the energies computed for the spin-polarized and for the spin-unpolarized calculations in each of the PAW and NC approaches, which are given by $\Delta E(NC) = E_{unp}(NC) - E_p(NC)$ and $\Delta E(paw) = E_{unp}(paw) - E_p(paw)$, respectively. The difference between the two approaches ($\Delta E(NC) - \Delta E(paw)$) is of about 20 meV, which has an error of less than 10 % as compared to the energy differences between the spin-polarized and unpolarized in each approach. So, based on which pseudopotential is taken into consideration, we can expect an accuracy of less than 10 % in total energy differences.

6.2 A single NIT2Py molecule in a box

As discussed in chapter 1.2, the NIT2Py molecule $C_{12}H_{16}N_3O_2$ is obtained by using the NITR molecule and substituting the N atom in the -R position with a 2-pyridyl ring C_5H_4N. To achieve the atomic coordinates of a single NIT2Py molecule, the coordinates of a 2-pyridyl ring are added to the atomic coordinates of a single NITR molecule in the origin, as shown in Fig. 6.2(a) and (b). Additionally, by using a rotation matrix, the coordinates of the atoms in the 2-pyridyl ring are rotated with respect to the nitonyl nitroxide plane with c as the axis of rotation, as represented in Fig. 6.2(c). The chosen unit cell parameters are $a = b = 14$ Å, $c = 20$ Å, and $\alpha = \beta = \gamma = 90°$. Because of the extra 2-pyridyl ring in the NIT2Py molecule as compared to the NITR molecule, a larger value is set for the lattice constant c to avoid overlapping the spheres around each atom along the c axis.

A structural optimization is performed on the atomic coordinates of the single NIT2Py molecule by utilizing the BFGS minimization. The spin-polarized and spin-unpolarized calculations are executed, once with each pseudopotential, NC and PAW, and 52 states

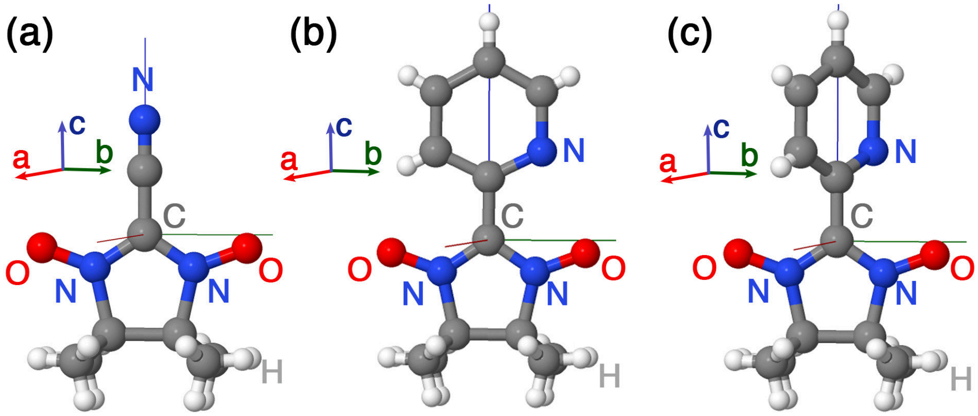

Figure 6.2 – A 2-pyridyl ring substituted by the nitrogen atom in the -R position of a NITR molecule shown in (a) to recreate a NIT2Py molecule exhibited in (b). Also, the 2-pyridyl ring is rotated around the *c* axis at 51° compared to the NN plane, as illustrated in (c).

are considered for the NIT2Py molecule. The difference between the total energies obtained by using NC and PAW approaches, $\Delta E(NC) - \Delta E(paw)$, is of about 44 meV. Then, we compare that difference to the energy difference between the spin-polarized and spin-unpolarized calculations. As a consequence, we can expect an accuracy of less than 20 % in the total energy differences depending on which pseudopotential is being used. This is significant because we will later use the differences in total energies of a number of spin configurations to evaluate the Js in the system.

6.3 Cutoff-energy convergence of a single molecule in a box

The cutoff-energy (E_{cut}) convergence is performed for NITR and NIT2Py by using spin-polarized and spin-unpolarized calculations, each with two different pseudopotentials, NC and PAW. The relaxed coordinates of the atoms achieved for the NITR and NIT2Py molecules in sections 6.1 and 6.2 respectively, are then utilized in the related E_{cut} convergence calculations. Note that, only one k-point, the Γ-point, is used in all those calculations.

The total d-c energy of a NITR molecule in a box is obtained for different values of E_{cut}s in a double-loop dataset, with an E_{cut} starting at 10 Ha and increasing up to 80 Ha by a 5 Ha interval in each set. In Fig. 6.3(a) and (b), the energy differences corresponding to various E_{cut}s are shown for the PAW and NC approaches and a spin-polarized and spin-unpolarized system, in which the energy obtained for an E_{cut} of 80 Ha is subtracted from all the energies. The energy difference related to the NC approach converges at an E_{cut} of about 30 Ha, but the one corresponding to PAW converges at an E_{cut} of about 15 Ha.

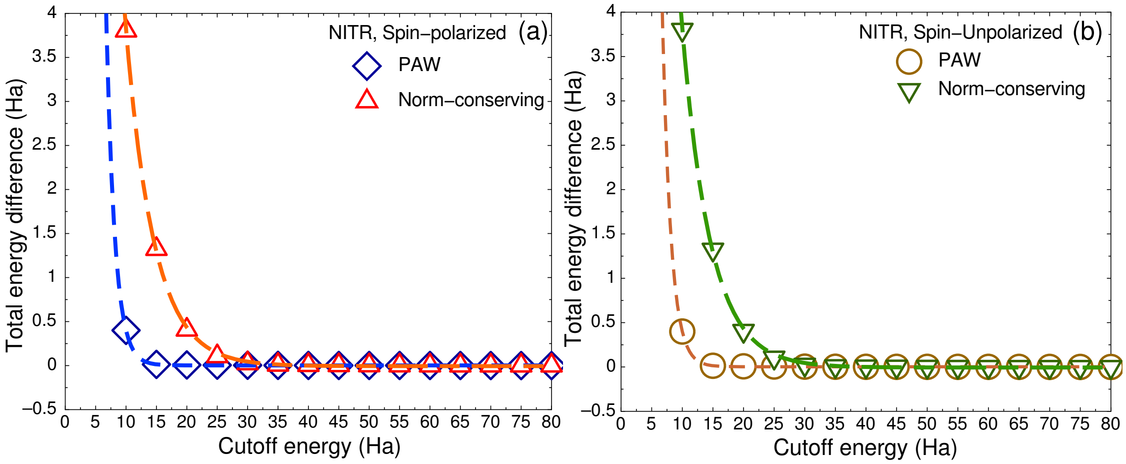

Figure 6.3 – The E_{cut} convergence of a NITR molecule in a box. The results are compared for two different calculations, spin-olarized and spin-unpolarized, and two different pseudopotentials, NC and PAW in each calculation. The difference of energy is computed by subtracting the measured energy from the one with an E_{cut}=80 Ha. Dashed lines are fits to a function of the form $f(x) = A\exp(-(x-x_0)/t_0)$.

The same calculations are performed for the NIT2Py molecule. Fig. 6.4 shows the energy difference between, on one hand, all the energies calculated for the various E_{cut}s, and one the other hand, the one for E_{cut}=80 Ha. We observe that the NC approach converges at an E_{cut} of about 30 Ha, but the one corresponding to PAW converges at an E_{cut} of about 15 Ha. Therefore, we conclude that using PAW pseudopotential gives rise to a faster convergence of the difference of energies.

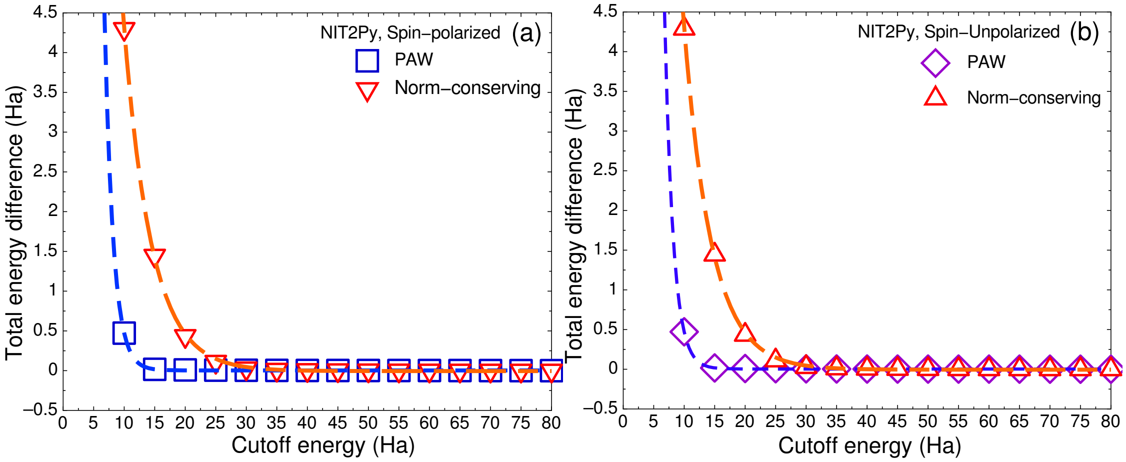

Figure 6.4 – The E_{cut} convergence with respect to the E_{cut} of a single NIT2Py molecule in a box. The spin-polarized and spin-unpolarized calculations were done using NC and PAW pseudopotentials. The difference in energy is calculated by subtracting the total energy computed for an E_{cut}=80 Ha from the energies obtained for the various E_{cut}s. Dashed lines are fits to a function of the form $f(x) = A\exp\left(-(x-x_0)/t_0\right)$.

6.4 Magnetization density of a single NIT2Py molecule

In ABINIT, the integral of the density inside the sphere around an atom can be evaluated for the spin up and down components. The difference between those integrated spin up and spin down densities gives an approximate value for the magnetic moment of an atom. In Fig. 6.5, the magnetization density for each atom of a single NIT2Py shows a unique delocalization of an unpaired electron on the two equivalent N and O atoms of the ONCNO branch of the molecule. In insets (a) and (b), a significant positive spin density shown by the yellow isosurface is distributed on the O1, O2, N2, and N3 atoms of the ONCNO branch. Also, a smaller negative value of the spin density is over the central carbon, C6, as represented by the blue isosurface.

6.5 $1\times1\times1$ NIT2Py single cell

6.5.1 Structural optimization of the single cell

The coordinates of the 264 atoms of the eight molecules in a unit cell of NIT2Py are optimized. The magnetic interactions in organic magnets are a direct consequence of

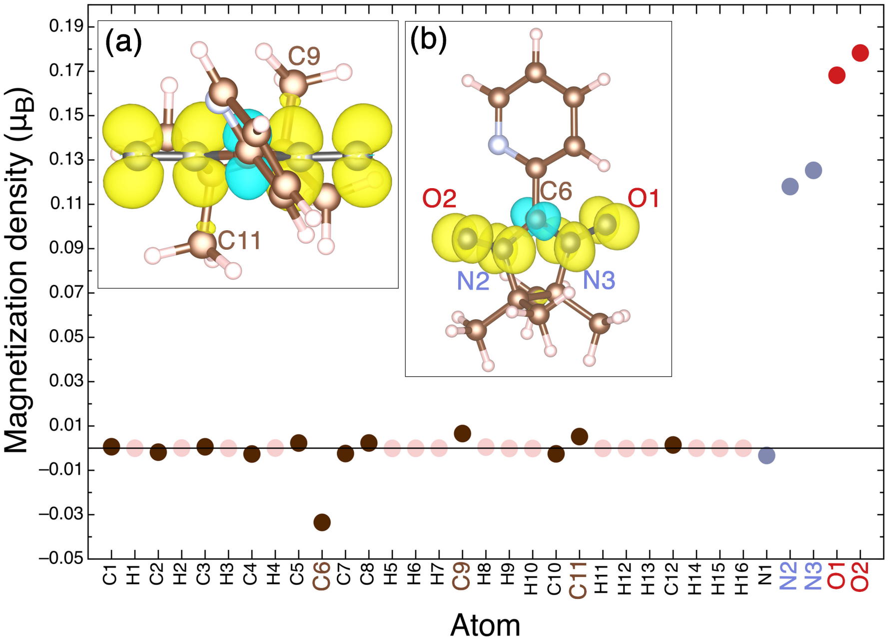

Figure 6.5 – The DFT results of the magnetization density in Bohr magneton units as a rough approximation of the magnetic moment of atoms in a single molecule of NIT2Py. Insets (a) and (b) show, respectively, the top and front view of a single NIT2Py molecule and the distribution of the unpaired electron over the equal N and O part of the ONCNO branch of each NIT2Py molecule. The positive magnetization density is represented by yellow isosurfaces and the negative by blue ones. For the purpose of clarity, only the atoms with the largest values of magnetization densities are labeled in the insets.

the overlapping of the p-orbitals of the interacting molecules and hence depend on the distances between the interacting molecules. So, the optimization of the cell shape and dimensions is ignored. As a consequence, the lattice parameters are fixed to the experimental values obtained in the X-ray diffraction measurement of NIT2Py. The lattice parameters of the $1 \times 1 \times 1$ NIT2Py single cell are set as a_1=6.1471 Å, a_2=30.0605 Å, and a_3=12.9583 Å, and by considering the angles between the lattice constants as α=90°, β=100.269°, and γ=90°. The optimized coordinates of atoms, used in the total energy calculations of the present research, are obtained by relaxing the atom positions in the NIT2Py unit cell in a non-magnetic calculation.

The ordering of atoms is established based on the ordering of their molecules, as labeled from 1 to 8 in Fig. 4.4. Furthermore, one k-point is considered in each of the three dimensions of the k-point grid, along with one shift with 0.5 as the shifting value in each dimension.

6.5.2 Density of states of NIT2Py

The density of states (DOS) in NIT2Py is calculated in GGA for the ground state AFM order (i.e. configuration 3 in table 6.I), of the single cell. A 412 k-point set, a PAW pseudopotential, and an E_{cut} of 15 Ha are used. As shown in Fig. 6.6, a gap in the energy spectrum of this compound indicates the insulating characteristics of this organic magnet.

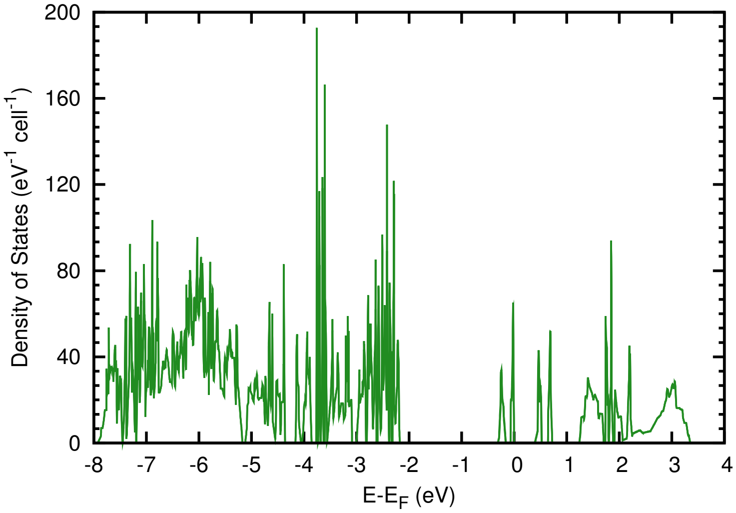

Figure 6.6 – DOS calculated in GGA (PBE) for the ground-state AFM order of the NIT2Py single cell.

6.5.3 Independent spin configurations of the single cell

As discussed in section 3.5.1, to evaluate the Js in a magnetic material in the DFT framework and by using the BS approach, different collinear arrangements of spins in a cell must be taken into consideration. Since each magnetic center can take S=1/2 spin up or down, shown by + and − respectively, the total number of spin configurations is 2^N, where N is the total number of magnetic units. In the case of a NIT2Py single cell with eight molecules, there is a total of $2^8 = 256$ configurations. Among those configurations, two have the same spin signs for all the molecules, $+$ or $-$, which yields S_z=4 or S_z=-4 respectively, 16 have one molecule with a different spin sign than the remaining molecules (S_z=3 or S_z=-3), 56 have two distinct spin signs (S_z=2 or S_z=-2), 112 have three different spin signs (S_z=1 or S_z=-1), and 70 have four molecules with various spin signs than the remaining molecules (S_z=0).

By considering the crystalline and the spin reversal symmetries, spin configurations with the same total energy, namely degenerate configurations, are attained.

In crystalline symmetry, each of the symmetry operators in Table 4.I and their corresponding molecule pairings are employed to determine the degenerate configurations for a given configuration. To do so, the spin of each of the molecule pairs needs to be inverted. For instance, in a given configuration $(-,+,-,-,+,+,+,-)$ in which only the sign of the S=1/2 spins of molecules 1 to 8 are respectively shown, the second symmetry operator, $(-x, 1/2+y, 1/2-z)$ is applied. By interchanging the spin of the paired molecules as $1 \leftrightarrow 2$, $3 \leftrightarrow 4$, $5 \leftrightarrow 6$, $7 \leftrightarrow 8$, the resulting configuration $(+,-,-,-,+,+,-,+)$ is degenerate to the initial configuration. In the same way, three more degenerate configurations are found with the three remaining symmetry operators.

Consequently, to find other degenerate configurations, spin reversal symmetry is used in which the spin sign of the degenerate configurations obtained by the crystalline symmetry are reversed. In the aforementioned example, the degenerate configuration of the given example is $(-,+,+,+,-,-,+,-)$. The same way, three more degenerate configurations are found. Thereby, in total, eight degenerate spin configurations are obtained for the configuration in the example.

By subtracting the number of degenerate spin configurations from the total number of the spin configurations, we obtain 44 independent spin configurations in the NIT2Py single cell. In the next section, we will calculate the total energy of 17 of those 44 independent spin configurations, in which four molecules have distinct spin signs and the total spin in the z direction is S_z=0 (see Annex III).

6.5.4 Total energies of the independent spin configurations of the single cell

As shown in section 6.4, the unpaired spin is mostly distributed on the two N and two O atoms of the ONCNO branch of each NIT2Py molecule. So, the spin is only assigned to those four atoms when calculating the total energy of a given spin configuration. For a scalar magnetization in ABINIT, an initial spin-magnetization can be assigned for each atom. The sign and magnitude of the spins of the atoms in the outcome of a total energy calculation of each configuration must be verified. To perform that verification, the magnetization densities of those atoms, which are obtained in the output by the difference between the integrated spin up and down densities, are compared to the spins of the same atoms considered in the input file.

In calculating the total energies of some of the independent configurations of the single cell, discrepancies between the sign and magnitude of spins of the atoms in the input and output are found. In those spin configurations, the resulting configuration chooses an AFM ground state in the system that differs from the initially selected spin configuration. Several tests are performed to keep the signs and magnitudes of spins of a certain configuration within desired signs and magnitudes.

First, we examine the effect of the various values of the E_{cut}. Then, different values of the dielectric macroscopic constant are tested to find the best value to accelerate the convergence of an SCF iteration. Additionally, the influence of assigning a preconditioner to the magnetization on the SCF procedure are studied. By putting a Lagrangian constraint on the direction of the magnetization, and by varying the amplitude of that constraint (from 0.001 to 100), the changes in the signs and magnitudes of the spins are explored.

Also, as discussed before, a rough approximation of the magnetic moment of an atom can be calculated from the difference of the integrated spin up and down densities inside of a sphere around that atom. By decreasing the sphere radius to a value equal or lower than half of the bound length between the atoms, one can avoid the overlapping of spheres in the NIT2Py molecule. The effect of different values of the radius on the resulting signs and values of the spins are examined.

Finally, by examining different pseudopotentials, we were able to obtain the desired spin signs and magnitudes in some configurations by using PAW pseudopotentials. So, out of the 44 independent configurations in a single cell, the spin signs and magnitudes of 17 configurations are kept invariant during calculations. In the 17 configurations, the spin signs of half of the molecules are different than the other half (S_z=0). The spin signs of the eight molecules in a single cell of NIT2Py associated to those 17 configurations are shown in Table 6.I. The initial spin values are chosen for the two O atoms of the ONCNO branch of each NIT2Py molecule, and the remaining atoms of that molecule are set to zero. The obtained magnetic moments for the molecules show that the spin of each molecule is mostly distributed on the two N and two O atoms of the ONCNO branch.

The difference between the energies calculated in direct and d-c decompositions of the total energies of 17 configurations in the single cell are in the range of 0.1 meV. Because the exchange coupling constants in the NIT2Py system are of the order of 10 K (1 meV), the difference between the direct and d-c decompositions of energies is larger than required. By comparing the direct energy to the d-c energy obtained for several configurations, we realized that the d-c energies are closer to the energies in the last SCF iteration of the energy convergence. Therefore, the total d-c energy is used in the evaluation of the Js.

For the sake of comparing, two different E_{cut}s are used: the first E_{cut} is 15 Ha, and the second E_{cut} is 30 Ha. For each calculation, a PAW cutoff for the double grid is taken into account with a value twice as much as the corresponding E_{cut}, 30 Ha and 60 Ha respectively.

6.5.5 Evaluation of exchange couplings in the $1 \times 1 \times 1$ NIT2Py single cell

Based on the general Heisenberg Hamiltonian in Eq. (4.4), 10 inequivalent Js are represented for the $1 \times 1 \times 1$ NIT2Py single cell. The least-squares fitting analysis discussed in 3.5.1 is used to evaluate the Js. The calculated DFT energy, $\varepsilon_{\alpha}^{1\times1\times1}(\text{DFT})$, for

config.	M_1	M_2	M_3	M_4	M_5	M_6	M_7	M_8	J_1	J_2	J_3	J_4	J_5	J_6	J_7	J_{23}	J_{24}	J_{25}	Deg.	Total d-c energy (eV) Ecut= 15 Ha k-point set=1×1×1	Total d-c energy (eV) Ecut= 30 Ha k-point set=1×1×1
1	-	-	-	-	+	+	+	+	0.5	0.5	0.5	-1	-1	-1	-1	0.5	0.5	0.5	2	-30569.77527	-30572.33892
2	+	-	+	-	+	-	+	-	-0.5	0.5	-0.5	1	-1	1	-1	-0.5	0.5	-0.5	2	-30569.77543	-30572.33906
3	-	+	-	+	+	-	+	-	-0.5	0.5	-0.5	-1	1	-1	1	-0.5	0.5	-0.5	2	-30569.77736	-30572.34098
4	-	+	+	-	-	+	+	-	-0.5	-0.5	0.5	1	-1	-1	1	-0.5	-0.5	0.5	2	-30569.77480	-30572.33845
5	-	-	+	+	+	+	-	-	0.5	-0.5	-0.5	-1	-1	1	1	0.5	-0.5	-0.5	2	-30569.77536	-30572.33899
6	-	+	-	-	+	+	+	-	0	0	0	0	0	-1	0	0	0	0	8	-30569.77608	-30572.33972
7	-	-	-	+	+	+	-	+	0	0	0	0	-1	0	0	0	0	0	8	-30569.77522	-30572.33886
8	-	+	-	+	+	+	-	-	-0.5	0.5	-0.5	0	0	0	0	0.5	-0.5	-0.5	4	-30569.77613	-30572.33975
9	-	+	-	+	+	-	-	+	-0.5	0.5	-0.5	0	0	0	0	-0.5	-0.5	0.5	4	-30569.77613	-30572.33975
10	-	-	+	+	+	-	-	+	0.5	-0.5	-0.5	0	0	0	0	-0.5	-0.5	0.5	4	-30569.77613	-30572.33975
11	-	-	-	+	-	+	+	+	0	0	0	0	0	0	-1	0	0	0	8	-30569.77524	-30572.33888
12	-	-	-	+	+	+	+	-	0	0	0	-1	0	0	0	0	0	0	8	-30569.77534	-30572.33898
13	-	-	+	+	-	-	+	+	0.5	-0.5	-0.5	1	1	-1	-1	0.5	-0.5	-0.5	2	-30569.77690	-30572.34051
14	-	-	+	+	-	+	-	+	0.5	-0.5	-0.5	0	0	0	0	-0.5	0.5	-0.5	4	-30569.77640	-30572.34002
15	-	+	+	-	-	-	+	+	-0.5	-0.5	0.5	0	0	0	0	0.5	-0.5	-0.5	4	-30569.77408	-30572.33774
16	-	+	+	-	-	+	-	+	-0.5	-0.5	0.5	0	0	0	0	-0.5	0.5	-0.5	4	-30569.77435	-30572.33801
17	-	+	+	-	+	-	-	+	-0.5	-0.5	0.5	-1	1	1	-1	-0.5	-0.5	0.5	2	-30569.77336	-30572.33703

Table 6.I – 17 inequivalent spin configurations of the $1 \times 1 \times 1$ NIT2Py single cell. In each configuration, the S=1/2 spin up or down of molecules 1 to 8 are represented in columns M1 to M8 with $+$ or $-$ respectively. For each of the configurations, the coefficients of the 10 inequivalent J_k ($a_{\alpha,k}$ given in Eq. (4.5)) are shown. The number of degenerate configurations is given in column Deg. The d-c total energies of each spin configuration calculated by using a 1 1 1 k-point set and for two different E_{cut}s, 15 Ha and 30 Ha, are shown in the last two columns.

each configuration α, of the single cell is given by

$$\varepsilon_{\alpha}^{1\times1\times1}(\mathrm{DFT}) = \varepsilon_{0}^{1\times1\times1} + \varepsilon_{\alpha}^{1\times1\times1}(\mathrm{Ising}), \tag{6.1}$$

where ε_0 is the spin-independent part of the total energy, which is considered to be a weighted average of the DFT computed energies of all the inequivalent configurations. In the case of the single cell of NIT2Py with 8 molecules, N=8, and 44 inequivalent spin configurations, $\alpha = 1, \cdots, 44$, ε_0 is obtained based on Eq. (3.44) as

$$\varepsilon_{0}^{1\times1\times1} = \frac{1}{2^8} \sum_{\alpha=1}^{44} g_{\alpha} \varepsilon_{\alpha}^{1\times1\times1}. \tag{6.2}$$

However, as only the energies of 17 inequivalent configurations out of 44 are calculated for the single cell, $\varepsilon_{0}^{1\times1\times1}$ is set as one of the fitting parameters in the least-squares procedure. To improve the fitting procedure, an initial value for $\varepsilon_{0}^{1\times1\times1}$ can be set, which is given as an average value of the energies of all the 17 configurations.

Also, the Ising energy in Eq. (6.3), $\varepsilon_{\alpha}^{1\times1\times1}(\mathrm{Ising})$, for each configuration α is calculated based on Eq. (4.5). In order to calculate a coefficient $a_{\alpha,k}$, it is substituted for the coefficient of the corresponding J_k comprised of a combination of pairwise $\boldsymbol{S}_i \cdot \boldsymbol{S}_j$ interactions (i and j =1 to 8), as seen in the general Hamiltonian of Eq. (4.4). In turn, to calculate the sum of the pairwise $S_i \cdot S_j$ interactions, the spin of S_i and S_j are substituted from the spin of each of the 8 molecules given in a certain configuration. The resulting coefficients for all the Js for a configuration are provided in columns 10 to 19 in Table 6.I. Note that, due to a factor of 1/4 in the Ising energy in Eq. (4.5), the coefficients $a_{\alpha,k}$ need to be multiplied by a factor of 4. Also, as mentioned in 4.4, interactions J_1, J_2, J_{23}, and J_{24} are repeated twice, and hence their corresponding coefficients $a_{\alpha,k}$ in Table 6.I need to be multiplied by a factor of 2 as well.

To obtain the Js, several steps need to be followed. First, by subtracting $\varepsilon_0(\mathrm{DFT})$ from the computed DFT energy for a certain configuration α, $\varepsilon_{\alpha}^{1\times1\times1}(\mathrm{DFT})$, a corresponding DFT relative energy for that configuration, $\Delta\varepsilon_{\alpha}^{1\times1\times1}(\mathrm{DFT})$, is calculated as

$$\Delta\varepsilon_{\alpha}^{1\times1\times1}(\mathrm{DFT}) = \varepsilon_{\alpha}^{1\times1\times1}(\mathrm{DFT}) - \varepsilon_{0}^{1\times1\times1}. \tag{6.3}$$

Second, the DFT related energy for a certain configuration α in Eq. (6.3) must be equivalent to the corresponding Ising energy in Eq. (4.5): $\Delta\varepsilon_{\alpha}^{1\times1\times1}(\mathrm{DFT}) = \varepsilon_{\alpha}^{1\times1\times1}(\mathrm{Ising})$. So, an error function, which is the deviation of the DFT relative energy from the corresponding Ising energy, is calculated for each configuration as

$$F_{\alpha}^{1\times1\times1} = \left[\Delta\varepsilon_{\alpha}^{1\times1\times1}(\mathrm{DFT}) - \varepsilon_{\alpha}^{1\times1\times1}(\mathrm{Ising})\right]^{2}. \tag{6.4}$$

The total error function, which is the sum over the error function of each configuration multiplied by the degeneracy of that configuration for the single cell is given by

$$F_{tot}^{1\times1\times1} = \sum_{\alpha=1}^{17} g_{\alpha}^{1\times1\times1} F_{\alpha}^{1\times1\times1}, \tag{6.5}$$

where $g_{\alpha}^{1\times1\times1}$ is the degeneracy of a certain configuration of the single cell as given in column 20 of Table 6.I.

Finally, the Js are obtained by minimizing the total error function in Eq. (6.5) as the total deviation of the DFT average energies and Ising energies for 17 inequivalent configurations. The least-squares fitting of total energies of the 17 inequivalent configurations of a single cell of NIT2Py in Table 6.I are performed once for energies computed with an E_{cut} of 15 Ha, and once for 30 Ha, as shown in Fig. 6.7. In Fig. 6.7(a), the DFT relative energy of each spin configuration is shown as a function of the corresponding Ising model energy for each E_{cut}. The resulting Js are represented in Fig. 6.7(b), where a positive value indicates an AFM interaction. An E_{cut} of 15 Ha is sufficient to calculate by DFT the total energies of different configurations of a single cell of NIT2Py.

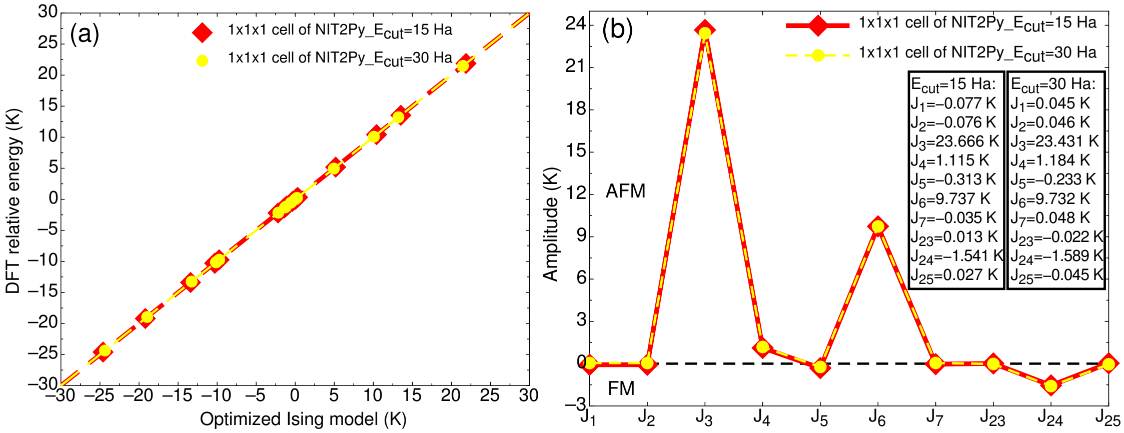

Figure 6.7 – (a) The DFT energy of each of the 17 inequivalent configurations of the NIT2Py single cell shown as a function of the corresponding Ising energy. The results obtained by using the least-squares fitting of total energies calculated by employing E_{cut}s of 15 Ha and 30 Ha are compared. The dashed lines represent the fits to a linear function ($f(x) = ax$), where slope a=1 is obtained. (b) The resulting Js are represented. Based on Eq. (3.36), $J > 0$ represents an AFM coupling and $J < 0$ an FM one.

6.6 NIT2Py $2 \times 1 \times 1$ supercell

As mentioned in 4.5, the first supercell is defined as $2 \times 1 \times 1$, and consists of 16 molecules and a total of 528 atoms (Fig. 4.8). The lattice constants of the $2 \times 1 \times 1$ supercell are obtained by doubling the length of the first component of the lattice constants of the single cell, which are given as $a'_1 = 2a_1$=12.2942 Å, $a'_2 = a_2$=30.0605 Å, and $a'_3 = a_3$=12.9583 Å. The angles between the lattice constants are set the same as the ones in the single cell, as α=90°, β=100.269°, and γ=90°. The reduced coordinates of the 528 atoms in the $2 \times 1 \times 1$ supercell are obtained by using the relaxed atomic coordinates of the 8 molecules in the single cell. So, the supercell coordinates for molecules 1 to 8 are obtained as $(\tau'_1 = \tau_1/2, \tau'_2 = \tau_2, \tau'_3 = \tau_3)$, where (τ_1, τ_2, τ_3) are the reduced coordinates of the 256 atoms in the single cell. The coordinates of molecules 9 to 16 in the supercell are $(\tau''_1 = \tau_1/2 + 1/2, \tau''_2 = \tau_2, \tau''_3 = \tau_3)$. The 16 molecules in the supercell are labeled as M_1 to M_{16}, as given in Fig. 4.8. In defining a supercell, it is necessary to prevent the code from considering a supercell as a non-primitive cell, which would stop the code.

6.6.1 Independent spin configurations of the $2 \times 1 \times 1$ supercell

The 32 inequivalent configurations used to evaluate the *J*s of a NIT2Py $2 \times 1 \times 1$ supercell are shown in Table 6.II. The *S*=1/2 spin up and down corresponding to each of the 16 molecules of each of the configurations are shown respectively by $+$ and $-$ in columns M1 to M16. Note that in 17 of the 32 configurations, the spins of M_1 to M_8 are identical to those demonstrated in the same molecules in the single cell (6.5.4), and the spins of M_9 to M_{16} are a repeat of the spins in M_1 to M_8 respectively. Those 17 configurations are called parallel configurations. In the 15 remaining configurations, the spins from M_1 to M_8 are identical to the spins of M_1 to M_8 in the single cell. However, the spins from M_9 to M_{16} have opposite signs to those in M_1 to M_8, respectively. For instance, M_1 has an up spin ($+$) and, correspondingly, M_9 has a down spin ($-$), M_2 has an opposite spin sign than that of M_{10}, the spin of M_3 is opposite to that of M_{11}, and so forth. We call those 15 configurations antiparallel configurations. A list of all the 32 inequivalent configurations of the $2 \times 1 \times 1$ supercell, along with the corresponding equivalent configurations due to crystalline and spin reversal symmetries, and the total number of degenerate configurations can be found in Annex IV.

In all of the supercell calculations, the initial spins values are assigned as $(0\ 0\ 0.12)$, $(0\ 0\ 0.12)$, $(0\ 0\ 0.16)$, and $(0\ 0\ 0.17)$ respectively for the N, N, O, and O atoms of the ONCNO branch of each of the 16 molecules, and are set to zero for the remaining atoms. The z-component values, m, of the spin of each atom $(0\ 0\ m)$, for the same four atoms are taken from the difference between the integrated spin up and down densities, $m = n(\uparrow) - n(\downarrow)$, for those atoms in total energy calculations of the single cell.

Different tests are effectuated to keep the sign and magnitude of spins unchanged in each of the configurations in the supercell. One consists of putting a constraint on the direction of magnetization along with verifying various amplitudes for it. However, none of those tests resulted in the desired spin magnitudes and signs for the selected atoms. In another test, the spin configurations are examined by imposing two different systems: an AFM system, and a spin-polarized system with various wavefunctions for the spin up and down for each k-point and band. Note that in both systems, we set a scalar wavefunction. Also, we set a scalar magnetization along the z axis with the diagonal density matrix and different magnitudes of spin up and down. With those two systems, we can fix each of the spin configurations in the supercell to the wanted configuration. We check the consistency of the resulting total d-c energies of the configurations in the supercell in which either of the two aforementioned systems is applied. We conclude that the difference between the energies is negligible. Therefore, both the AFM and collinear magnetization systems result in similar total d-c energies for different configurations. However, for some configurations, the application of either of those systems was insufficient to fix the spin configuration. So, we found the best value for the dielectric macroscopic constant to speed-up the SCF cycle and obtain the converged energies along with the chosen spin magnitudes and signs.

6.6.2 Total energies of the independent configurations of the $2 \times 1 \times 1$ supercell

The total energy DFT calculations of different independent configurations in the supercell are executed by using a PAW pseudopotential, an E_{cut} of 15 Ha, a double-grid cutoff of 30 Ha, and a 111 k-point set. We expected that the total d-c energy of each of the 17 parallel configurations in the $2 \times 1 \times 1$ supercell, $\varepsilon_{\alpha}^{2\times1\times1}(\mathrm{DFT})$, is twice the energy value of those identical configurations in the single cell, $\varepsilon_{\alpha}^{1\times1\times1}(\mathrm{DFT})$. So, the values of $\varepsilon_{\alpha}^{2\times1\times1}(\mathrm{DFT}) - 2\varepsilon_{\alpha}^{1\times1\times1}(\mathrm{DFT})$ are examined for the identical parallel configurations in the supercell and the single cell. For example, by comparing the energy difference of configuration $(-,+,-,+,+,-,+,-,-,+,-,+,+,-,+,-)$ in the supercell that has twice the value of its equivalent configuration in the single cell, $(-,+,-,+,+,-,+,-)$, a value of 4.38948 eV is obtained.

To find the cause of the differences between the total energies of the supercell and the single cell, we must first make sure that the coefficients of the Js are consistent between each of the configurations in the single cell and the corresponding parallel configurations in the supercell. Then, we verify the correctness of the atomic coordinates by looking at the Ewald energy. Because the Ewald energy per unit cell only depends on the coordinates of atoms and because those coordinates have not changed in different configurations, the Ewald energy remains the same even when changing the alignment of spins. So, by comparing the Ewald energy of each of the 17 parallel configurations of the supercell and twice the value of the Ewald energy of the corresponding configurations in the single cell, $\Delta\varepsilon_\alpha(\text{Ewald}) = \varepsilon_\alpha^{2\times1\times1}(\text{Ewald}) - 2\varepsilon_\alpha^{1\times1\times1}(\text{Ewald})$, negligible values are achieved for $\Delta\varepsilon_\alpha(\text{Ewald})$ which indicate the accuracy of the atomic coordinates. Furthermore, the agreement between the spin signs and magnitudes of the molecules in the supercell and the single cell obtained in the outcome of the 17 corresponding configurations are compared to the ones initially determined. Finally, the accuracy of calculating the energies of different configurations in the single cell and in the supercell will need to be examined. As will later be discussed, the energy differences of various configurations show that the precision of the total energy calculation of the single cell is not in accord with the ones in the supercell. In conclusion, the energies of the parallel configurations in the supercell cannot be calculated by doubling the energies of their identical configurations in the single cell. Table 6.II shows the calculated total d-c energies of the 17 parallel and 15 antiparallel configurations of the $2 \times 1 \times 1$ supercell of NIT2Py.

6.6.3 Evaluation of exchange couplings in the $2 \times 1 \times 1$ supercell

To evaluate the 22 Js of the general Heisenberg Hamiltonian of the $2 \times 1 \times 1$ supercell of NIT2Py, the same procedure that was done for the single cell is repeated. For each configuration α, the computed DFT energy is

$$\varepsilon_\alpha^{2\times1\times1}(\text{DFT}) = \varepsilon_0^{2\times1\times1} + \varepsilon_\alpha^{2\times1\times1}(\text{Ising}). \tag{6.6}$$

The spin-independent part of the total energy, ε_0, is given as a weighted average of the DFT computed energies of the 32 independent configurations of the supercell with N=16 molecules as

$$\varepsilon_0^{2\times1\times1} = \frac{1}{2^{16}} \sum_{\alpha=1}^{32} g_\alpha \varepsilon_\alpha^{2\times1\times1}. \tag{6.7}$$

ε_0 is considered as a fitting parameter in the least-squares fitting procedure, and an average value of the energies of the 32 configurations is set as an initial value for that

Config.	M_1	M_2	M_3	M_4	M_5	M_6	M_7	M_8	M_9	M_{10}	M_{11}	M_{12}	M_{13}	M_{14}	M_{15}	M_{16}	J_1	J_2	J_3	J_4	J_5	J_6	J_7	J_8	J_9	J_{10}	J_{11}	J_{12}	J_{13}	J_{14}	J_{15}	J_{55}	J_{56}	J_{57}	J_{62}	J_{63}	J_{64}	J_{65}	Deg.	Total d-c energy (eV) Ecut= 15 Ha k-point set=1×1×1
1	-	-	-	-	+	+	+	+	+	+	+	+	-	-	-	-	1	1	1	-2	-2	-2	-2	-1	-1	-1	-1	2	2	2	2	1	1	1	-1	-1	-1	-1	2	-61135.16023
2	-	-	-	-	+	+	+	+	-	-	-	-	+	+	+	+	1	1	1	-2	-2	-2	-2	1	1	1	1	-2	-2	-2	-2	1	1	1	1	1	1	1	2	-61135.16268
3	+	-	+	-	+	-	+	-	-	+	-	+	-	+	-	+	-1	1	-1	2	-2	2	-2	-1	1	-1	1	-2	2	-2	2	-1	1	-1	-1	1	-1	1	2	-61135.15677
4	+	-	+	-	+	-	+	-	+	-	+	-	+	-	+	-	-1	1	-1	2	-2	2	-2	1	-1	1	-1	2	-2	2	-2	-1	1	-1	1	-1	1	-1	2	-61135.15879
5	-	+	-	+	+	-	+	-	+	-	+	-	-	+	-	+	-1	1	-1	-2	2	-2	2	-1	1	-1	1	2	-2	2	-2	-1	1	-1	-1	1	-1	1	2	-61135.15828
6	-	+	-	+	+	-	+	-	-	+	-	+	+	-	+	-	-1	1	-1	-2	2	-2	2	1	-1	1	-1	-2	2	-2	2	-1	1	-1	1	-1	1	-1	2	-61135.16525
7	-	+	+	-	-	+	+	-	+	-	-	+	+	-	-	+	-1	-1	1	2	-2	-2	2	-1	1	1	-1	-2	2	2	-2	-1	-1	1	-1	1	1	-1	2	-61135.16129
8	-	+	+	-	-	+	+	-	-	+	+	-	-	+	+	-	-1	-1	1	2	-2	-2	2	1	-1	-1	1	2	-2	-2	2	-1	-1	1	1	-1	-1	1	2	-61135.15833
9	-	-	+	+	+	+	-	-	+	+	-	-	-	-	+	+	1	-1	-1	-2	-2	2	2	-1	-1	1	1	2	2	-2	-2	1	-1	-1	-1	-1	1	1	2	-61135.15480
10	-	-	+	+	+	+	-	-	-	-	+	+	+	+	-	-	1	-1	-1	-2	-2	2	2	1	1	-1	-1	-2	-2	2	2	1	-1	-1	1	1	-1	-1	2	-61135.16211
11	-	+	-	-	+	+	+	-	+	-	+	+	-	-	-	+	0	0	0	0	0	-2	0	-1	0	0	0	0	0	2	0	0	0	0	-1	0	0	0	8	-61135.15979
12	-	+	-	-	+	+	+	-	-	+	-	-	+	+	+	-	0	0	0	0	0	-2	0	1	0	0	0	0	0	-2	0	0	0	0	1	0	0	0	8	-61135.16179
13	-	-	-	+	+	+	-	+	+	+	+	-	-	-	+	-	0	0	0	0	-2	0	0	-1	0	0	0	0	2	0	0	0	0	0	-1	0	0	0	8	-61135.15827
14	-	-	-	+	+	+	-	+	-	-	-	+	+	+	-	+	0	0	0	0	-2	0	0	1	0	0	0	0	-2	0	0	0	0	0	1	0	0	0	8	-61135.16048
15	-	+	-	+	+	+	-	-	+	-	+	-	-	-	+	+	-1	1	-1	0	0	0	0	-1	1	-1	1	0	0	0	0	1	-1	-1	-1	-1	1	1	4	-61135.15707
16	-	+	-	+	+	+	-	-	-	+	-	+	+	+	-	-	-1	1	-1	0	0	0	0	1	-1	1	-1	0	0	0	0	1	-1	-1	1	1	-1	-1	4	-61135.16151
17	-	+	-	+	+	-	-	+	-	+	-	+	+	-	-	+	-1	1	-1	0	0	0	0	1	-1	1	-1	0	0	0	0	-1	-1	1	1	-1	-1	1	4	-61135.16151
18	-	-	+	+	+	-	-	+	+	+	-	-	-	+	+	-	1	-1	-1	0	0	0	0	-1	-1	1	1	0	0	0	0	-1	-1	1	-1	1	1	-1	4	-61135.15707
19	-	-	+	+	+	-	-	+	-	-	+	+	+	-	-	+	1	-1	-1	0	0	0	0	1	1	-1	-1	0	0	0	0	-1	-1	1	1	-1	-1	1	4	-61135.16151
20	-	-	-	+	-	+	+	+	-	-	-	+	-	+	+	+	0	0	0	0	0	0	-2	1	0	0	0	0	0	0	-2	0	0	0	1	0	0	0	8	-61135.16052
21	-	-	-	+	+	+	+	-	+	+	+	-	-	-	-	+	0	0	0	-2	0	0	0	-1	0	0	0	2	0	0	0	0	0	0	-1	0	0	0	8	-61135.15756
22	-	-	-	+	+	+	+	-	-	-	-	+	+	+	+	-	0	0	0	-2	0	0	0	1	0	0	0	-2	0	0	0	0	0	0	1	0	0	0	8	-61135.16244
23	-	-	+	+	-	-	+	+	+	+	-	-	+	+	-	-	1	-1	-1	2	2	-2	-2	-1	-1	1	1	-2	-2	2	2	1	-1	-1	-1	-1	1	1	2	-61135.15934
24	-	-	+	+	-	-	+	+	-	-	+	+	-	-	+	+	1	-1	-1	2	2	-2	-2	1	1	-1	-1	2	2	-2	-2	1	-1	-1	1	1	-1	-1	2	-61135.16091
25	-	-	+	+	-	+	-	+	+	+	-	-	+	-	+	-	1	-1	-1	0	0	0	0	-1	-1	1	1	0	0	0	0	-1	1	-1	-1	1	-1	1	4	-61135.15752
26	-	-	+	+	-	+	-	+	-	-	+	+	-	+	-	+	1	-1	-1	0	0	0	0	1	1	-1	-1	0	0	0	0	-1	1	-1	1	-1	1	-1	4	-61135.16203
27	-	+	+	-	-	-	+	+	+	-	-	+	+	+	-	-	-1	-1	1	0	0	0	0	-1	1	1	-1	0	0	0	0	1	-1	-1	-1	-1	1	1	4	-61135.15911
28	-	+	+	-	-	-	+	+	-	+	+	-	-	-	+	+	-1	-1	1	0	0	0	0	1	-1	-1	1	0	0	0	0	1	-1	-1	1	1	-1	-1	4	-61135.15902
29	-	+	+	-	-	+	-	+	+	-	-	+	+	-	+	-	-1	-1	1	0	0	0	0	-1	1	1	-1	0	0	0	0	-1	1	-1	-1	1	-1	1	4	-61135.15957
30	-	+	+	-	-	+	-	+	-	+	+	-	-	+	-	+	-1	-1	1	0	0	0	0	1	-1	-1	1	0	0	0	0	-1	1	-1	1	-1	1	-1	4	-61135.15954
31	-	+	+	-	+	-	-	+	+	-	-	+	-	+	+	-	-1	-1	1	-2	2	2	-2	-1	1	1	-1	2	-2	-2	2	-1	-1	1	-1	1	1	-1	2	-61135.15693
32	-	+	+	-	+	-	-	+	-	+	+	-	+	-	-	+	-1	-1	1	-2	2	2	-2	1	-1	-1	1	-2	2	2	-2	-1	-1	1	1	-1	-1	1	2	-61135.15971

Table 6.II – 32 inequivalent spin configurations of a supercell 2 × 1 × 1 of NIT2Py. The S=1/2 spin up or down of molecules 1 to 16 are represented in columns M1 to M16 by $+$ and $-$, respectively. The coefficients of the exchange couplings, $a_{\alpha,k}$ in Eq. (4.7), are given for each configuration. The number of degeneracy for each configuration is given in column Deg. The DFT total d-c energy of each spin configuration is calculated by setting E_{cut}=15 Ha and a k-point set of $1 \times 1 \times 1$.

parameter.

Subsequently, the Ising energy for each configuration of the supercell with k=22 is obtained through Eq. (4.7). To acquire the coefficients $a_{\alpha,k}$ in Eq. (4.7) for a given configuration, the coefficients of the corresponding J_k in the general Heisenberg Hamiltonian of the supercell in Eq. (4.6) are used. The coefficient of each J in the general Hamiltonian consists of a sum of pairwise $\boldsymbol{S}_i \cdot \boldsymbol{S}_j$ interactions, where i and j can take a value between 1 to 16. In each pairwise interaction, the values of S_i and S_j are taken from the spin of the corresponding molecule as given in columns M_1 to M_{16} in Table 6.II. Consequently, those coefficients are given in columns 18 to 39 in Table 6.II. Note that based on the Ising energy in Eq. (4.7), the coefficients of the Js in columns M_1 to M_{16} in Table 6.II have to be multiplied by a factor of 4. Additionally, the coefficients of J_1, J_2, J_8, J_9, J_{10}, J_{55}, J_{56}, J_{62}, J_{63}, and J_{64} have to be doubled due to occurring twice. So, the coefficients $a_{\alpha,k}$ related to these Js in the Table 6.II need to be multiplied by factor 2 as well.

The Js of the supercell are obtained through the least-squares fitting procedure of the minimization of the total error function, which is the sum of the error function of each configuration multiplied by the corresponding degeneracy. The error function of each configuration in the supercell is obtained as

$$F_{\alpha}^{2\times1\times1} = \left[\Delta\varepsilon_{\alpha}^{2\times1\times1}(\mathrm{DFT}) - \varepsilon_{\alpha}^{2\times1\times1}(\mathrm{Ising})\right]^2, \tag{6.8}$$

where the DFT relative energy of each configuration in the supercell is given by

$$\Delta\varepsilon_{\alpha}^{2\times1\times1}(\mathrm{DFT}) = \varepsilon_{\alpha}^{2\times1\times1}(\mathrm{DFT}) - \varepsilon_{0}^{2\times1\times1}. \tag{6.9}$$

and the Ising energy of each configuration is obtained based on Eq. (4.7).

Finally, by minimizing the total error function of the 32 different configurations of the supercell as

$$F_{tot}^{2\times1\times1} = \sum_{\alpha=1}^{32} g_{\alpha}^{2\times1\times1} F_{\alpha}^{2\times1\times1}, \tag{6.10}$$

the 22 independent Js are evaluated. Note that the degeneracy of each configuration in the supercell, $g_{\alpha}^{2\times1\times1}$, is given in column 40 of Table 6.II. Fig.6.8(a) illustrates the DFT relative energy for each spin configuration in the supercell in Eq. (6.9) with respect to the corresponding Ising energy. Fig. 6.8(b) shows the resulting Js of the supercell.

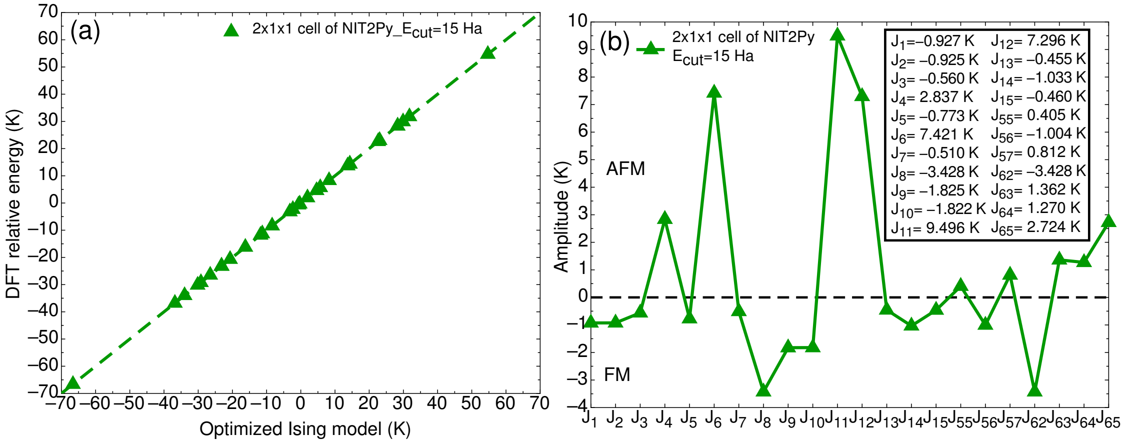

Figure 6.8 – The results obtained by the least-squares fitting procedure of the total d-c energies of the 32 different configurations of the NIT2Py $2\times1\times1$ supercell. In (a), the DFT relative energies of each of the 32 configurations are plotted as a function of the corresponding Ising energy. The dashed line is a fit to a linear function ($f(x) = ax$), where slope a=1 is obtained. In (b), the resulting 22 different Js are shown. According to Eq. (3.36), $J > 0$ represents an AFM coupling and $J < 0$ an FM one.

To verify the consistency of our results in the single cell and supercell, we must compare the resulting exchange coupling constants obtained for the $1\times1\times1$ single cell with their corresponding Js in the $2\times1\times1$ supercell.

6.7 Comparing the exchange couplings in the $1\times1\times1$ single cell and $2\times1\times1$ supercell

To compare a resulting exchange coupling from the $1\times1\times1$ single cell with its corresponding J in the $2\times1\times1$ supercell, identical magnetic interactions must be found in both cells. Identical magnetic interactions occur in both the single cell and supercell between molecules with the same intermolecular distance. By studying the Js based on the distances between the interacting molecules, the magnetic interactions can be identified regardless of the way the molecules are labeled in a cell. That approach provides us with a more practical method, especially if one is dealing with larger numbers of molecules.

Moreover, by taking into account the dominant exchange couplings, and hence reducing the number of Js, the least-squares fit can be optimized. The dominant Js correspond to the exchange couplings between the closest molecules because they offer the largest magnetic interactions. Parameters are set to identify the dominant Js. Firstly, the central carbon of the ONCNO branch of each molecule is chosen as the reference point to measure the distances between the interacting molecules. Secondly, the maximum measurement taken into consideration is a distance of 9.406 Å because anything beyond that has a relatively negligible value of exchange coupling. Thus, out of all the exchange coupling constants in the system, only 13 are found to be dominant, as given in Table 6.III and shown in Fig. 6.9. In Fig. 6.9, for the sake of clarity, only the central carbon of the ONCNO branch of each molecule is shown as well as an arrow representing the alignment of each molecule. $J_1(\mathrm{d}_{\mathrm{C-C}} = 6.147$ Å) and $J_{1p}(\mathrm{d}_{\mathrm{C-C}} = 6.147$ Å) represent the intercellular interactions between the molecules in the crystallographic a direction. Although J_1 and J_{1p} both correspond to interactions arising within molecules having the same distance, the interacting molecules belong respectively to symmetry groups I and II. As shown in Fig. 6.9(a), $J_2(\mathrm{d}_{\mathrm{C-C}} = 6.435$ Å), $J_4(\mathrm{d}_{\mathrm{C-C}} = 6.991$ Å), $J_7(\mathrm{d}_{\mathrm{C-C}} = 7.940$ Å), and $J_{11}(\mathrm{d}_{\mathrm{C-C}} = 8.626$ Å) occur within the molecules of symmetry group I. Whereas, in Fig. 6.9(b), $J_3(\mathrm{d}_{\mathrm{C-C}} = 6.682$ Å) and $J_{10}(\mathrm{d}_{\mathrm{C-C}} = 8.260$ Å) correspond to the interactions between the molecules belonging to symmetry group II. The remaining Js in Fig. 6.9(a), $J_8(\mathrm{d}_{\mathrm{C-C}} = 8.083$ Å), and in Fig. 6.9(b), $J_5(\mathrm{d}_{\mathrm{C-C}} = 7.397$ Å), $J_9(\mathrm{d}_{\mathrm{C-C}} = 8.197$ Å) , $J_6(\mathrm{d}_{\mathrm{C-C}} = 7.861$ Å) and $J_{12}(\mathrm{d}_{\mathrm{C-C}} = 9.406$ Å), are associated to interactions between molecules in both symmetry groups.

When mapping the magnetic structure of the NIT2Py system by defining the Js related to the magnetic interactions between the nearest neighboring molecules, a question arises: how do we distinguish the different Js corresponding to interactions between pairs of molecules having different intermolecular distances, but where all the pairs are the same $M_i - M_j$? In Fig. 6.9 for instance, interactions J_2, J_4, J_7 and J_{11} are all considered to be distinct because each one occurs between different $M_1 - M_4$ pairs (or different

$d_{C\text{-}C}$ (Å)	**J** 1x1x1 cell	**M_i-M_j** 1x1x1 cell	**J** 2x1x1 cell	**M_i-M_j** 2x1x1 cell	**Same J** (1x1x1 and 2x1x1 cells)
6.147	-	-	2×J_8	(M_1-M_9), (M_2-M_{10}), (M_3-M_{11}), (M_4-M_{12})	2×J_1
6.147	-	-	2×J_{62}	(M_5-M_{13}), (M_6-M_{14}), (M_7-M_{15}), (M_8-M_{16})	2×J_{1p}
6.435	J_3	(M_1-M_4), (M_2-M_3)	J_{11}	(M_1-M_{12}), (M_2-M_{11}), (M_3-M_{10}), (M_4-M_9)	J_2
6.682	2×J_{24}	(M_5-M_7), (M_5-M_7), (M_6-M_8), (M_6-M_8)	2×J_{56}	(M_5-M_7), (M_6-M_8), (M_{13}-M_{15}), (M_6-M_{13})	2×J_3
6.991	J_3	(M_1-M_4), (M_2-M_3)	J_{11}	(M_1-M_{12}), (M_2-M_{11}), (M_3-M_{10}), (M_4-M_9)	J_4
7.397	J_6	(M_1-M_7), (M_2-M_8), (M_3-M_5), (M_4-M_6)	J_{14}	(M_1-M_{15}), (M_2-M_{16}), (M_3-M_{13}), (M_4-M_{14}), (M_7-M_9), (M_8-M_{10}), (M_5-M_{11}), (M_6-M_{12})	J_5
7.861	J_4	(M_1-M_5), (M_2-M_6), (M_3-M_7), (M_4-M_8)	J_{12}	(M_1-M_{13}), (M_2-M_{14}), (M_3-M_{15}), (M_4-M_{16}), (M_5-M_9), (M_6-M_{10}), (M_7-M_{11}), (M_8-M_{12})	J_6
7.940	J_3	(M_1-M_4), (M_2-M_3)	J_3	(M_1-M_4), (M_2-M_3), (M_9-M_{12}), (M_{10}-M_{11})	J_7
8.083	J_5	(M_1-M_6), (M_2-M_5), (M_3-M_8), (M_4-M_7)	J_5	(M_1-M_6), (M_2-M_5), (M_3-M_8), (M_4-M_7), (M_9-M_{14}), (M_{10}-M_{13}), (M_{11}-M_{16}), (M_{12}-M_{15})	J_8
8.197	J_6	(M_1-M_7), (M_2-M_8), (M_3-M_5), (M_4-M_6)	J_6	(M_1-M_7), (M_2-M_8), (M_3-M_5), (M_4-M_6), (M_9-M_{15}), (M_{10}-M_{16}), (M_{11}-M_{13}), (M_{12}-M_{14})	J_9
8.260	2×J_{24}	(M_5-M_7), (M_5-M_7), (M_6-M_8), (M_6-M_8)	2×J_{64}	(M_5-M_{15}), (M_6-M_{16}), (M_7-M_{13}), (M_8-M_{14})	2×J_{10}
8.626	J_3	(M_1-M_4), (M_2-M_3)	J_3	(M_1-M_4), (M_2-M_3), (M_9-M_{12}), (M_{10}-M_{11})	J_{11}
9.406	J_4	(M_1-M_5), (M_2-M_6), (M_3-M_7), (M_4-M_8)	J_4	(M_1-M_5), (M_2-M_6), (M_3-M_7), (M_4-M_8), (M_9-M_{13}), (M_{10}-M_{14}), (M_{11}-M_{15}), (M_{12}-M_{16})	J_{12}

Table 6.III – The dominant Js in the $1 \times 1 \times 1$ single cell and the $2 \times 1 \times 1$ supercell categorized in terms of the closest intermolecular distances between the interacting molecules. The distance d_{C-C} between the middle carbon of the ONCNO branch of each molecule in a pairwise interaction is considered as the reference point to find the closest interacting molecules. $M_i - M_j$ represents the pairwise interaction between molecules M_i and M_j in each cell. The last column shows the relabeling of the dominant Js fitting in the same category, in other words sharing the same distance.

$M_2 - M_3$ pairs) and each one has a different intermolecular distance. However, they all take place between M_1 and M_4 (or between M_2 and M_3), which results in all those Js having the same coefficients $a_{\alpha,k}$. So, $a_{\alpha,2} = a_{\alpha,4} = a_{\alpha,7} = a_{\alpha,11}$. The same problem occurs for J_3 and J_{10}, leading to $a_{\alpha,3} = a_{\alpha,10}$, for J_5 and J_9, resulting in $a_{\alpha,5} = a_{\alpha,9}$, and for J_6 and J_{12} yielding $a_{\alpha,6} = a_{\alpha,12}$. The real problem arises when entering the parameters in the least-squares fitting procedure.

Indeed, the Js having identical coefficients are considered as equal parameters in the least-squares fitting procedure. To avoid that problem, the Js with the same coefficient must be separated by using a supercell approach, as will later be discussed. For now, as our immediate goal is to confirm the consistency between the $1 \times 1 \times 1$ single cell and $2 \times 1 \times 1$ supercell results, only one of the Js among the ones having the same coefficient is considered in the least-squares fit while the remaining Js are set to zero: $J_4 = J_7 = J_{11} = 0$, $J_{10} = 0$, $J_9 = 0$, and $J_{12} = 0$. Also, because J_1 and J_{1p} are intercellular interactions between the molecules along the a axis, and thus cannot be calculated in a single cell, they are also set to zero for the time being.

Finally, the least-squares fit procedure of the total energies is performed once for the 17 configurations of the single cell—results can be seen in Table 6.I—and once for the 17 corresponding, or parallel, configurations of the supercell. Results are illustrated in Table 6.II. As shown in Fig. 6.10, the resulting values of the Js associated with the single cell and supercell are not all consistent.

As the results of the corresponding Js in the single cell and supercell do not all match, the source of the discrepancy must be investigated. In 6.6.2, the accuracy of the coefficients $a_{\alpha,k}$ of different J_ks, the coordinates of the atoms, and the spin assigned to each molecule in each of the 17 configurations of the single cell and the corresponding 17 parallel configurations in the supercell were already verified. Having ruled out those potential sources of error, we then examine the precision in our total energy calculations for the various configurations of the single and supercell.

Because the energy differences between the independent configurations ($\Delta\varepsilon_\alpha$) are used to evaluate the Js, the energies must be calculated with a precision adequate for the NIT2Py system. As the magnitudes of the Js in NIT2Py are of the order of 10 K, the

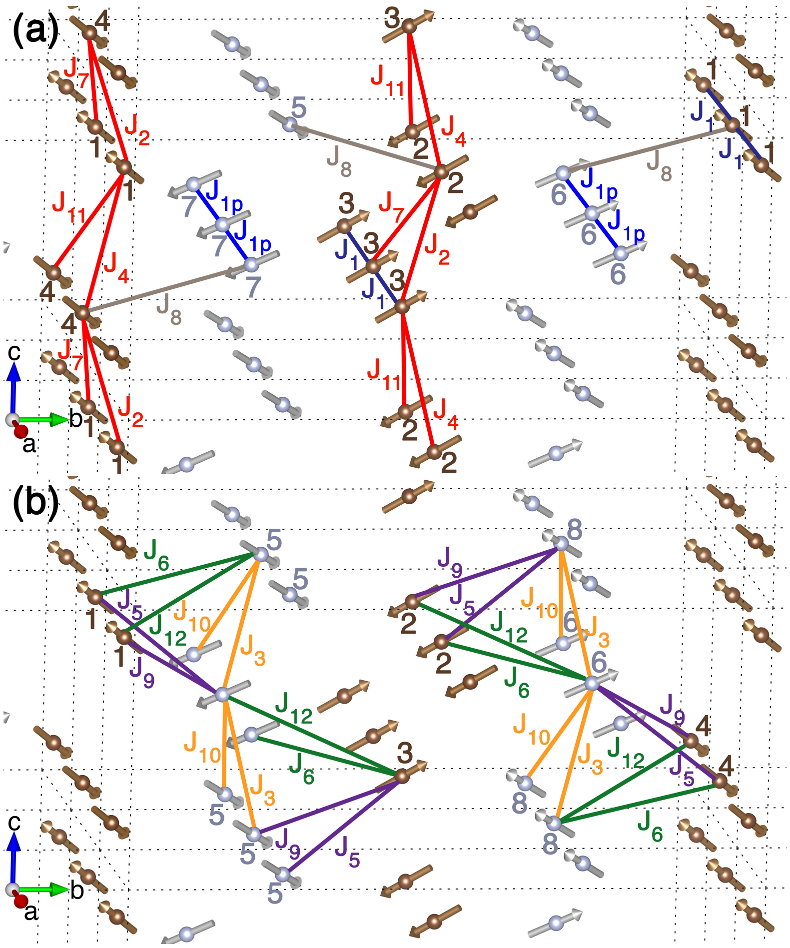

Figure 6.9 – The dominant Js between the interacting molecules having the closest distances between the two central carbons of their ONCNO branches (d_{C-C}). For clarity, those Js are shown in (a) and (b), which both show the repeat of the NIT2Py unit cell. (a) J_1, J_{1p}, J_2, J_4, J_7, J_8, and J_{11} are represented. (b) J_3, J_5, J_6, J_9, J_{10}, and J_{12} are shown. Note that the color of each J indicates interactions between the Js having identical coefficients albeit different distances.

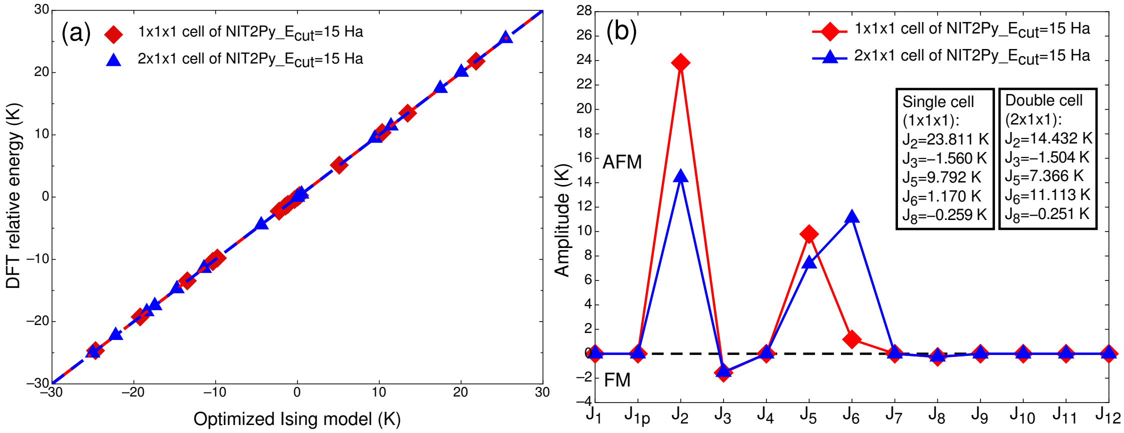

Figure 6.10 – Results obtained by the least-squares fitting procedure. (a) The DFT relative energy of each configuration as a function of the Ising energy for 17 configurations in the single cell and their identical configurations, 17 parallel configurations, in the supercell. (b) The best fit values obtained for the dominant Js in the single cell and supercell. Note that J_4, J_7, J_{11}, J_{10}, J_9, and J_{12} are set to zero.

required accuracy is in the order of 0.1 meV ($\sim$1 K). By subtracting the energy of a given configuration from the energies of other configurations, the error in energy differences is evaluated at more than 0.1 meV in the case of the $1 \times 1 \times 1$ single cell, and at about 0.001 eV ($\sim$10 K) in the case of the $2 \times 1 \times 1$ supercell. Therefore, the resulted errors in the energy differences of the various calculations are higher than the precision needed to calculate the Js in NIT2Py. That error may arise from a non-converged E_{cut} or non-converged number of k-points, hypotheses that will be examined in the next sections.

6.7.1 The convergence with respect to the cutoff energy

To find the converged value of the E_{cut} of the single cell, the total energies of some configurations among the 17 independent configurations in Table 6.I are calculated using E_{cut} values of 8 Ha, 15 Ha, and 30 Ha.

If the converged value of energies of configurations 1 and 2 are given respectively by $E_1 = E_1^{true} + C_1$ and $E_2 = E_2^{true} + C_2$, then the corresponding calculated energies E_1^{true} and E_2^{true} are each different from the converged values only by a constant, C_1 and C_2. Because equality between the two constants, $C_1 = C_2$, is improbable, the difference between the constant values of the two configurations must be less than the required

Config.	E_{I} (eV) (E_{cut}=8 Ha)	E_{II} (eV) (E_{cut} =15 Ha)	E_{III} (eV) (E_{cut} =30 Ha)	$\Delta E=(E_{I}-E_{II})$ (eV)	$\Delta E-\Delta E_{ave}$ (K)	$\Delta E'=(E_{II}-E_{III})$ (eV)	$\Delta E'-\Delta E'_{ave}$ (K)
1	-30202.32297	-30569.77527	-30572.33892	367.45230	-15.571	2.56365	0.219
2	-30202.32139	-30569.77543	-30572.33906	367.45404	4.626	2.56363	-0.041
3	-30202.32347	-30569.77736	-30572.34098	367.45388	2.832	2.56361	-0.242
4	-30202.31947	-30569.77480	-30572.33845	367.45532	19.505	2.56365	0.236
5	-30202.32364	-30569.77536	-30572.33899	367.45172	-22.237	2.56362	-0.092
6	-30202.32161	-30569.77608	-30572.33972	367.45447	9.596	2.56363	-0.002
7	-30202.32187	-30569.77522	-30572.33886	367.45335	-3.404	2.56364	0.084
8	-30202.32208	-30569.77613	-30572.33975	367.45404	4.652	2.56361	-0.161

Table 6.IV – The total d-c energies of 8 independent configurations in a single cell of NIT2Py are calculated using E_{cut}s of 8 Ha, 15 Ha, and 30 Ha. For each configuration, the energy difference calculated between E_{cut}s 8 Ha and 15 Ha, ΔE, is given in column 5. The average energy for all the energy differences between 8 Ha and 15 Ha of all 8 configurations is calculated as ΔE_{ave}= 367.45364 eV. Then, ΔE is subtracted from ΔE_{ave}, as presented in column 6. The same process is repeated to find the precision between E_{cut}s 15 Ha and 30 Ha of which the results are provided in the last column. The average energy in this case is $\Delta E'_{ave}$=2.56363 eV.

precision. In the case of the NIT2Py system, that difference must be $C_1 - C_2 < 1K$. To examine the precision of the differences $C_i - C_j$ of every two-body i and j configuration, one needs to calculate all the possible combinations. Instead, to find the precision of the energy differences by using two E_{cut}s, an average of energy differences, $\Delta E_{ave} = 1/\alpha(\Delta E_1 + \cdots + \Delta E_\alpha)$, is calculated, in which $\Delta E_\alpha = E_\alpha(E_{cut}1) - E_\alpha(E_{cut}2)$. Then, the difference of the ΔE_α from the average energy indicates the range of error in the calculated energy differences.

The difference between $\Delta E_\alpha = E_\alpha(E_{cut} = 8\ Ha) - E_\alpha(E_{cut} = 15\ Ha)$ and the corresponding average of all energy differences ranges from -22.23 K to 19.5 K in different configurations, as represented in Table 6.IV. That order of error is not acceptable for calculating the energy differences in the NIT2Py system. However, when we examine the difference between $\Delta E'_\alpha = E_\alpha(E_{cut} = 15\ Ha) - E_\alpha(E_{cut} = 30\ Ha)$ and the corresponding average energy, we notice that an acceptable precision ranging from -0.25 K to 0.23 K can be achieved. Therefore, an E_{cut} of 15 Ha is sufficient for calculating the energy differences of the configurations in a single cell of NIT2Py. A similar procedure was carried out to examine E_{cut}s of 15 Ha, 30 Ha, and 35 Ha in the $2 \times 1 \times 1$ supercell, which proves that 15 Ha is the appropriate E_{cut} for obtaining the energy differences with the desired precision in our system.

6.7.2 The convergence with respect to the k-point set

The convergence study regarding the k-points is carried out for the single cell and supercell of the NIT2Py system. A sufficient number of k-points in each of the three dimensions (*ngkpt*) must be found. In systems with a higher number of symmetries, more k-points are related to one another, and hence, a smaller number of k-points is needed to sample the Brillouin zone. Also, even though the different configurations of a given supercell share the same crystalline symmetries, their magnetic symmetries can be different. As a consequence, the number of symmetry operators is not necessarily identical in the different supercell configurations. So, even when the same number of k-points is set for different supercell configurations, the code chooses a different number of k-points to sample the Brillouin zone depending on the configuration under calculation.

In the single cell, the total energies of the 6 independent configurations of Table 6.I are calculated using a fixed E_{cut} of 15 Ha and the PAW cutoff for the double grid of 30 Ha, but a different number of k-points. For example, 111, 112, 211, 222, 411, 412, 422, 444, 611, and 811 k-point sets are represented in Table 6.V. The process of k-point sets convergence is carried out by finding the order of precision between each two different k-point sets, $(ngkpt)_i$ and $(ngkpt)_j$, when evaluating the energy differences between two independent configurations, α and α'. First, the energy differences between the configurations are evaluated once by using $(ngkpt)_i$ and once with $(ngkpt)_j$. In other words, $\Delta E_{\alpha,\alpha'}^{(ngkpt)_i} = E_{\alpha}^{(ngkpt)_i} - E_{\alpha'}^{(ngkpt)_i}$, and $\Delta E_{\alpha,\alpha'}^{(ngkpt)_j} = E_{\alpha}^{(ngkpt)_j} - E_{\alpha'}^{(ngkpt)_j}$ are calculated. Finally, the two obtained values are subtracted from each other as such: $\Delta E_{\alpha,\alpha'}^{(ngkpt)_i} - \Delta E_{\alpha,\alpha'}^{(ngkpt)_j}$.

The k-point sets convergence process is performed between different groups of k-point sets. In the first group, the number of k-point sets is increased in the first direction as 111, 211, 411, 611, and 811 k-point sets. For instance, the energy differences between configurations 3 and 5, $\Delta E_{3,5}^{211} - \Delta E_{3,5}^{411} = 2.006$ K, calculated by using the 211 and 411 k-point sets. Then, by comparing the 211 and 811 k-point sets for the same two

k-point set (ngkpt)	$\Delta E_{1,2}$ (eV)	$\Delta E_{2,3}$ (eV)	$\Delta E_{3,4}$ (eV)	$\Delta E_{4,5}$ (eV)	$\Delta E_{5,6}$ (eV)	$\Delta E_{1,3}$ (eV)	$\Delta E_{3,5}$ (eV)	$\Delta E_{1,5}$ (eV)
111	0.00016	0.00193	-0.00256	0.00056	0.00071	0.00209	-0.00200	0.00009
112	0.00002	0.00185	-0.00207	0.00028	0.00075	0.00188	-0.00179	0.00008
211	-0.00194	0.00322	-0.00346	0.00189	-0.00016	0.00128	-0.00157	-0.00028
222	-0.00180	0.00298	-0.00303	0.00167	-0.00015	0.00118	-0.00135	-0.00017
411	-0.00190	0.00320	-0.00328	0.00154	0.00009	0.00130	-0.00174	-0.00044
412	-0.00182	0.00302	-0.00287	0.00129	0.00014	0.00120	-0.00157	-0.00037
422	-0.00182	0.00302	-0.00354	0.00196	-0.00052	0.00120	-0.00157	-0.00037
444	-0.00183	0.00303	-0.00287	0.00129	-0.00104	0.00120	-0.00158	-0.00038
611	-0.00191	0.00321	-0.00329	0.00154	0.00009	0.00129	-0.00174	-0.00044
811	-0.00191	0.00321	-0.00329	0.00154	0.00010	0.00129	-0.00174	-0.00044

Table 6.V – The energy differences between independent configurations in a 1 × 1 × 1 NIT2Py single cell calculated by an E_{cut} of 15 Ha, a PAW energy cutoff for the double grid of 30 Ha, and different k-point sets.

configurations, 2.019 K is achieved. The k-point sets convergence procedure is applied to other configuration pairs. Consequently, the precision of calculating the total energy differences between the 211 and 411 k-point sets as well as between the 211 and 811 k-point sets, is of the order of 2 K, which is larger than the accepted precision in NIT2Py (less than 1 K$\sim$0.0001 eV). However, the accuracy between the 411 and 811 k-point sets for configurations 3 and 5 is of the order of 0.012 K. When considering the total energy differences of other configuration pairs, we conclude that the range of error is less than 1 K, which is sufficiently low in NIT2Py. Therefore, the number of k-points in the first dimension is set as 4.

In the second group, the number of k-points in the other two directions are increased while the one for the first direction is fixed to 4. For example, 411 and 412 k-point sets used in calculating the energy differences between configurations 3 and 5 yields -1.909 K, which is larger than the required precision in NIT2Py. However, the precision between the 412 and 422 k-point sets is of the order of 0.003 K, and between 412 and 444 k-point sets is of 0.019 K. Thus, 412 k-point set is sufficient to evaluate the *J*s in the NIT2Py system using the total energy difference mapping approaches.

For the k-point sets convergence process in the 2 × 1 × 1 supercell, the total energies of the parallel configurations in Table 6.II are calculated with a fixed E_{cut} of 15 Ha and a PAW cutoff for the double grid of 30 Ha, but different k-point sets such as 111, 211, 212, and 222. As shown in Table 6.VI, the differences between the total d-c energies of some of those configurations calculated for different k-point sets are compared. For example, by taking into account the 211 and 212 k-point sets, we have $\Delta E_{3,5}^{211} - \Delta E_{3,5}^{212}$=-4.381 K for configurations 3 and 5, and $\Delta E_{1,5}^{211} - \Delta E_{1,5}^{212}$=-5.933 K for configurations 1 and 5. So, the error between the 211 and 212 k-point sets is larger than the acceptable range for calculating the Js in NIT2Py. However, a reasonable error is obtained between the 212 and 222 k-point sets. For example, there is an error of 0.027 K for configurations 3 and 5, and 0.042 K for configurations 1 and 5. In conclusion, 212 is chosen as the k-point set in the total energy calculation of the $2 \times 1 \times 1$ supercell in NIT2Py.

However, an oddity arose for the single cell when using the 441, 481, 422, and 444 k-point sets: the convergence of energy differences in some configurations did not conform to the results of all the other configurations. So, the 17 configurations of the single cell given in Table 6.I are calculated using more k-point sets. Indeed, first, the k-points are increased in the first direction, such as 111, 211, 411, 611, and 811. Then, they are augmented in the second direction, like 411, 421, 441, and 481, in the third direction as 411, 412, 414, and 418, and, finally, in both the second and third directions as 411, 422, and 444. The resulting total energies are employed in the least-squares fitting procedure to obtain the dominant Js corresponding to each of the k-point sets in the single cell. To compare the resulting Js with those in the supercell, the total energies of the 17 parallel configurations in the supercell being identical to the 17 in the single cell, are calculated using a 212 k-point set.

The outcoming Js are compared in Table 6.IX, and shown in Fig.6.11(a). Excellent agreements are obtained between the Js in the $2 \times 1 \times 1$ supercell using 212 k-point set

k-point set (ngkpt)	$\Delta E_{1,2}$ (eV)	$\Delta E_{2,3}$ (eV)	$\Delta E_{3,4}$ (eV)	$\Delta E_{4,5}$ (eV)	$\Delta E_{1,3}$ (eV)	$\Delta E_{3,5}$ (eV)	$\Delta E_{1,5}$ (eV)
111	-0.00346	0.00150	0.00301	-0.00649	-0.00195	-0.00347	-0.00543
211	-0.00350	0.00160	0.00318	-0.00701	-0.00189	-0.00382	-0.00572
212	-0.00357	0.00181	0.00305	-0.00651	-0.00176	-0.00345	-0.00521
222	-0.00358	0.00181	0.00305	-0.00651	-0.00176	-0.00345	-0.00522

Table 6.VI – The energy differences between independent configurations in the $2 \times 1 \times 1$ supercell of NIT2Py. The energies in each configuration are calculated by an E_{cut} of 15 Ha, a PAW cutoff for the double grid of 30 Ha, and various k-point sets.

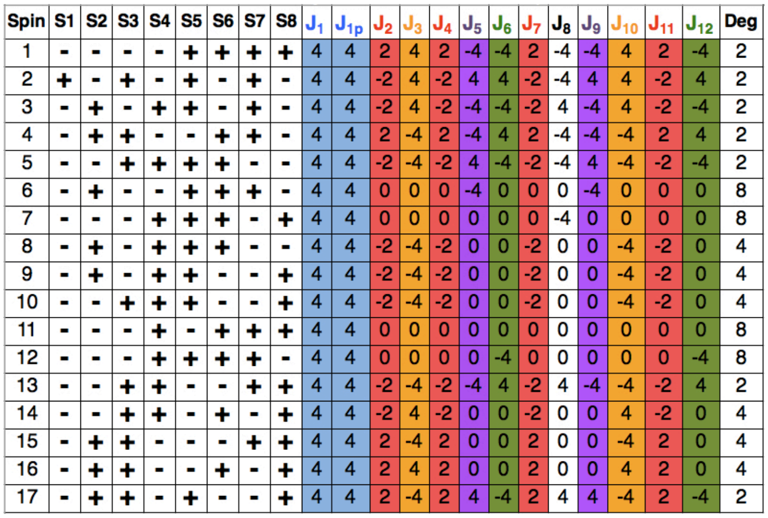

Spin	S1	S2	S3	S4	S5	S6	S7	S8	J_1	J_{1p}	J_2	J_3	J_4	J_5	J_6	J_7	J_8	J_9	J_{10}	J_{11}	J_{12}	Deg
1	-	-	-	-	+	+	+	+	4	4	2	4	2	-4	-4	2	-4	-4	4	2	-4	2
2	+	-	+	-	+	-	+	-	4	4	-2	4	-2	4	4	-2	-4	4	4	-2	4	2
3	-	+	-	+	+	-	+	-	4	4	-2	4	-2	-4	-4	-2	4	-4	4	-2	-4	2
4	-	+	+	-	-	+	+	-	4	4	2	-4	2	-4	4	2	-4	-4	-4	2	4	2
5	-	-	+	+	+	+	-	-	4	4	-2	-4	-2	4	-4	-2	-4	4	-4	-2	-4	2
6	-	+	-	-	+	+	+	-	4	4	0	0	0	-4	0	0	0	-4	0	0	0	8
7	-	-	-	+	+	+	-	+	4	4	0	0	0	0	0	0	-4	0	0	0	0	8
8	-	+	-	+	+	+	-	-	4	4	-2	-4	-2	0	0	-2	0	0	-4	-2	0	4
9	-	+	-	+	+	-	-	+	4	4	-2	-4	-2	0	0	-2	0	0	-4	-2	0	4
10	-	-	+	+	+	-	-	+	4	4	-2	-4	-2	0	0	-2	0	0	-4	-2	0	4
11	-	-	-	+	-	+	+	+	4	4	0	0	0	0	0	0	0	0	0	0	0	8
12	-	-	-	+	+	+	+	-	4	4	0	0	0	0	-4	0	0	0	0	0	-4	8
13	-	-	+	+	-	-	+	+	4	4	-2	-4	-2	-4	4	-2	4	-4	-4	-2	4	2
14	-	-	+	+	-	+	-	+	4	4	-2	4	-2	0	0	-2	0	0	4	-2	0	4
15	-	+	+	-	-	-	+	+	4	4	2	-4	2	0	0	2	0	0	-4	2	0	4
16	-	+	+	-	-	+	-	+	4	4	2	4	2	0	0	2	0	0	4	2	0	4
17	-	+	+	-	+	-	-	+	4	4	2	-4	2	4	-4	2	4	4	-4	2	-4	2

Table 6.VII – 17 inequivalent configurations of a 1 × 1 × 1 single cell. The *S*=1/2 spin up or down of molecules 1 to 8 are represented by $+$ and $-$ respectively. The columns with the same color correspond to the Js that have identical coefficients $a_{\alpha,k}$ in each configuration. The number of degeneracy for each configuration is given in the last column.

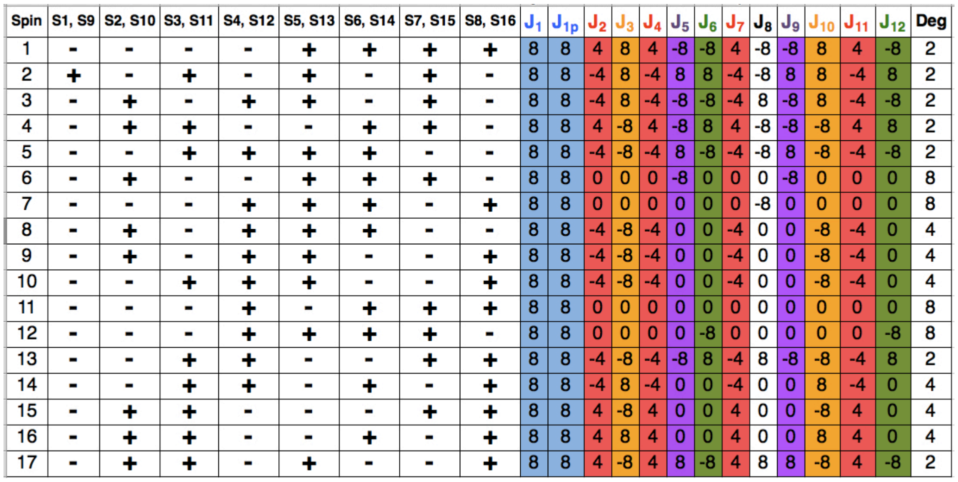

Spin	S1, S9	S2, S10	S3, S11	S4, S12	S5, S13	S6, S14	S7, S15	S8, S16	J_1	J_{1p}	J_2	J_3	J_4	J_5	J_6	J_7	J_8	J_9	J_{10}	J_{11}	J_{12}	Deg
1	-	-	-	-	+	+	+	+	8	8	4	8	4	-8	-8	4	-8	-8	8	4	-8	2
2	+	-	+	-	+	-	+	-	8	8	-4	8	-4	8	8	-4	-8	8	8	-4	8	2
3	-	+	-	+	+	-	+	-	8	8	-4	8	-4	-8	-8	-4	8	-8	8	-4	-8	2
4	-	+	+	-	-	+	+	-	8	8	4	-8	4	-8	8	4	-8	-8	-8	4	8	2
5	-	-	+	+	+	+	-	-	8	8	-4	-8	-4	8	-8	-4	-8	8	-8	-4	-8	2
6	-	+	-	-	+	+	+	-	8	8	0	0	0	-8	0	0	0	-8	0	0	0	8
7	-	-	-	+	+	+	-	+	8	8	0	0	0	0	0	0	-8	0	0	0	0	8
8	-	+	-	+	+	+	-	-	8	8	-4	-8	-4	0	0	-4	0	0	-8	-4	0	4
9	-	+	-	+	+	-	-	+	8	8	-4	-8	-4	0	0	-4	0	0	-8	-4	0	4
10	-	-	+	+	+	-	-	+	8	8	-4	-8	-4	0	0	-4	0	0	-8	-4	0	4
11	-	-	-	+	-	+	+	+	8	8	0	0	0	0	0	0	0	0	0	0	0	8
12	-	-	-	+	+	+	+	-	8	8	0	0	0	0	-8	0	0	0	0	0	-8	8
13	-	-	+	+	-	-	+	+	8	8	-4	-8	-4	-8	8	-4	8	-8	-8	-4	8	2
14	-	-	+	+	-	+	-	+	8	8	-4	8	-4	0	0	-4	0	0	8	-4	0	4
15	-	+	+	-	-	-	+	+	8	8	4	-8	4	0	0	4	0	0	-8	4	0	4
16	-	+	+	-	-	+	-	+	8	8	4	8	4	0	0	4	0	0	8	4	0	4
17	-	+	+	-	+	-	-	+	8	8	4	-8	4	8	-8	4	8	8	-8	4	-8	2

Table 6.VIII – 17 inequivalent parallel configurations of a 2 × 1 × 1 supercell. The $+$ and $-$ signs indicate the *S*=1/2 spin up or down of molecules 1 to 16. The columns with the same color correspond to the Js that have identical coefficients $a_{\alpha,k}$ in each configuration. Column Deg gives the number of degeneracy for each configuration.

Cell	k-point set	J_2(K)	J_3(K)	J_5(K)	J_6(K)	J_8(K)
1x1x1 cell	111	23.811	-1.560	9.792	1.170	-0.259
	412	13.424	-0.643	8.260	9.053	-0.270
	414	13.421	-0.641	8.271	9.066	-0.270
	418	13.428	-0.643	8.269	9.059	-0.269
	421	14.577	-1.520	8.331	10.028	-0.251
	441	16.959	-2.278	8.758	10.449	0.169
	481	14.576	-1.522	8.287	10.019	-4.850
	422	15.805	-1.397	8.684	9.483	0.163
	444	16.864	-2.363	8.266	11.357	2.024
2x1x1 supercell	111	14.432	-1.504	7.366	11.113	-0.251
	212	13.419	-0.644	8.257	9.049	-0.274

Table 6.IX – The resulting dominant Js by the least-squares fitting procedure of the total energies of the 17 configurations of the $1 \times 1 \times 1$ single cell and the 17 corresponding configurations of the $2 \times 1 \times 1$ supercell. The procedure is done for different k-point sets.

and the Js in $1 \times 1 \times 1$ single cell using 412 k-point sets, as shown in Fig. 6.11.

Therefore, based on the supercell total energy mapping approach, the result of least-squares fitting analysis of minimization of Eq. (3.45) for the total energies of 17 independent configurations in each of the $1 \times 1 \times 1$ cell and $2 \times 1 \times 1$ supercell for GGA-PBE functional are demonstrated in Fig. 6.12. In this figure, the DFT energies of different configurations and the associated Ising energies are well conformed, and the achieved Js in both the $1 \times 1 \times 1$ single cell and the $2 \times 1 \times 1$ supercell are in perfect agreement. In both cells, we have J_2=13.4 K, J_3=-0.6 K, J_5=8.2 K, J_6=9.0 K, and J_8=-0.2 K.

However, as mentioned in section 6.7, some Js must be separated. As shown in Fig. 6.13(a), J_2, J_4, J_7, and J_{11} are between the molecules with different intermolecular distances, but have the same molecule labels (1, 2, 3, and 4). Also, in Fig. 6.13(b), interactions J_3 and J_{10} are between the molecules with similar labels (5, 6, 7, and 8) but varying intermolecular distances. Furthermore, in Fig. 6.13(c), J_5 and J_9 are between similar molecules (1, 2, 3, 4, 5, 6, 7, and 8) but different intermolecular distances. Therefore, the coefficients $a_{\alpha,k}$ of those J_ks are identical, and hence those interactions are indistinguishable in the least-squares fitting procedure. So, the value obtained for J_2 is a combination of $J_2 + J_4 + J_7 + J_{11}$, for J_3 is the sum of $J_3 + J_{10}$, and for J_6 is the total of $J_6 + J_9$. To overcome this difficulty and separate those interactions, bigger supercells

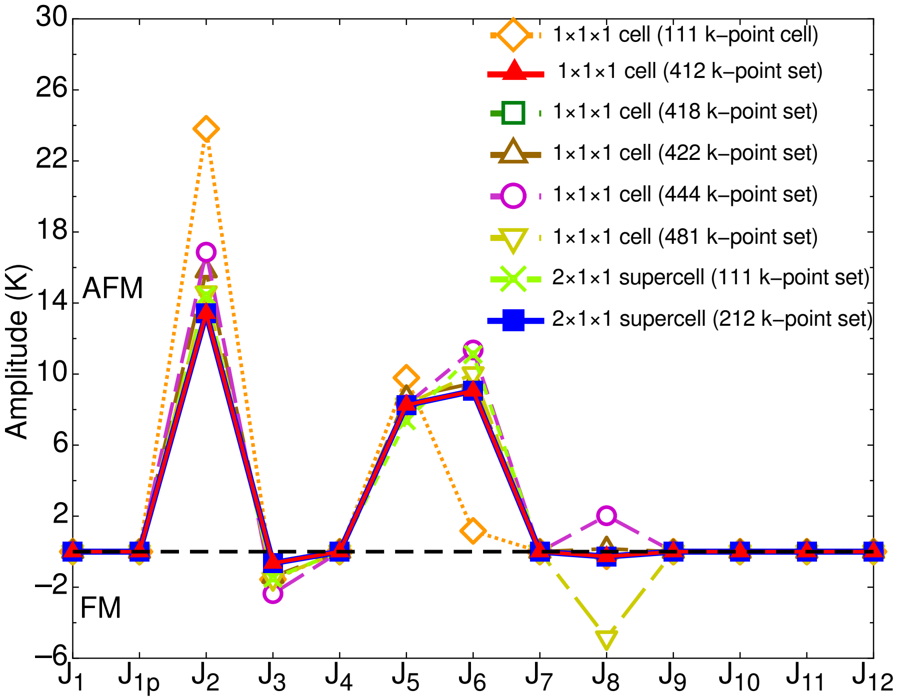

Figure 6.11 – By using different k-point sets, the dominant Js obtained from the least-squares fitting procedure of the total energies of the 17 configurations of the single cell. They are compared to the Js for the 17 parallel configurations of the $2 \times 1 \times 1$ supercell. Note that only J_2, J_3, J_5, J_6, and J_8 are considered in the fit, while the remaining ones are set to zero.

are needed, as will be introduced in the next section. Additionally, the four-state energy mapping approach discussed in section 3.5.2 will be used, which will allow us to distinguish a determined J by using the energies of only four different spin configurations.

6.8 Separate exchange couplings in NIT2Py using the four-state energy mapping approach

The four-state energy mapping approach is used to separate the Js. For instance, J_1 and J_{1p} can be separated using the $2 \times 1 \times 1$ supercell, as shown in the Fig. 6.14. J_1 can be evaluated by choosing any of the molecule pairs having that interaction between them. For instance, the interaction between molecule pair 1-9 is obtained as

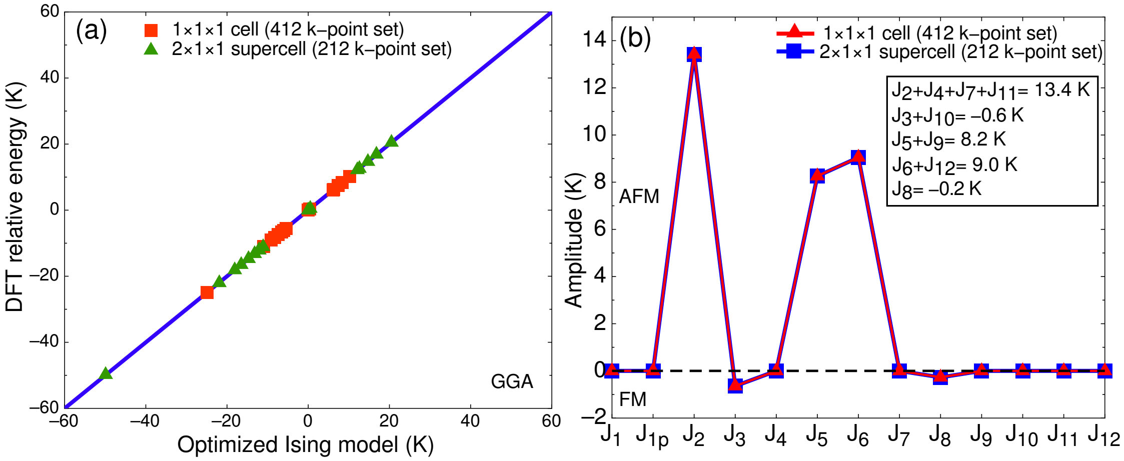

Figure 6.12 – The results of numerical evaluation of the Js obtained by using the least-squares fitting procedure of the total energy of the 17 independent spin configurations of the $1 \times 1 \times 1$ single cell and $2 \times 1 \times 1$ supercell of NIT2Py. In the single cell, a 412 k-point set, and in the supercell, a 212 k-point set was used. The E_{cut} is set to 15 Ha in calculations of both cells. (a) The DFT relative energy of each of those 17 independent configurations is plotted as a function of the optimized Ising energy. (b) The best fit values are represented. As stated by Eq. (3.36), $J > 0$ points to an AFM coupling and $J < 0$ an FM one.

$2 \times J_1^{eff} = 1/4(E_1 + E_4 - E_2 - E_3)$. Coefficient 2 takes into account the double interactions associated to each molecule. Energies E_1, E_2, E_3, and E_4 are related to four different configurations, in which collinear spin alignments are chosen for molecule pair 1-9 as ↑↑, ↑↓, ↓↑, and ↓↓. The same spin signs are set for the remaining molecules in the supercell, either all up or all down, as given in Eq. (6.11).

$$\begin{aligned}
E_1 &= E\left[S_1 :\uparrow, S_9 :\downarrow, \text{other spin sites} :\uparrow\right], \\
E_2 &= E\left[S_1 :\downarrow, S_9 :\uparrow, \text{other spin sites} :\uparrow\right], \\
E_3 &= E\left[S_1 :\uparrow, S_9 :\uparrow, \text{other spin sites} :\uparrow\right], \\
E_4 &= E\left[S_1 :\downarrow, S_9 :\downarrow, \text{other spin sites} :\uparrow\right]. \qquad (6.11)
\end{aligned}$$

To evaluate J_{1p}, we have $2 \times J_{1p}^{eff} = 1/4(E_1 + E_4 - E_2 - E_3)$, where the energies are related to four configurations with different collinear spin alignments for molecule pair 5-13. Yet, all the remaining molecules have the same spin alignment.

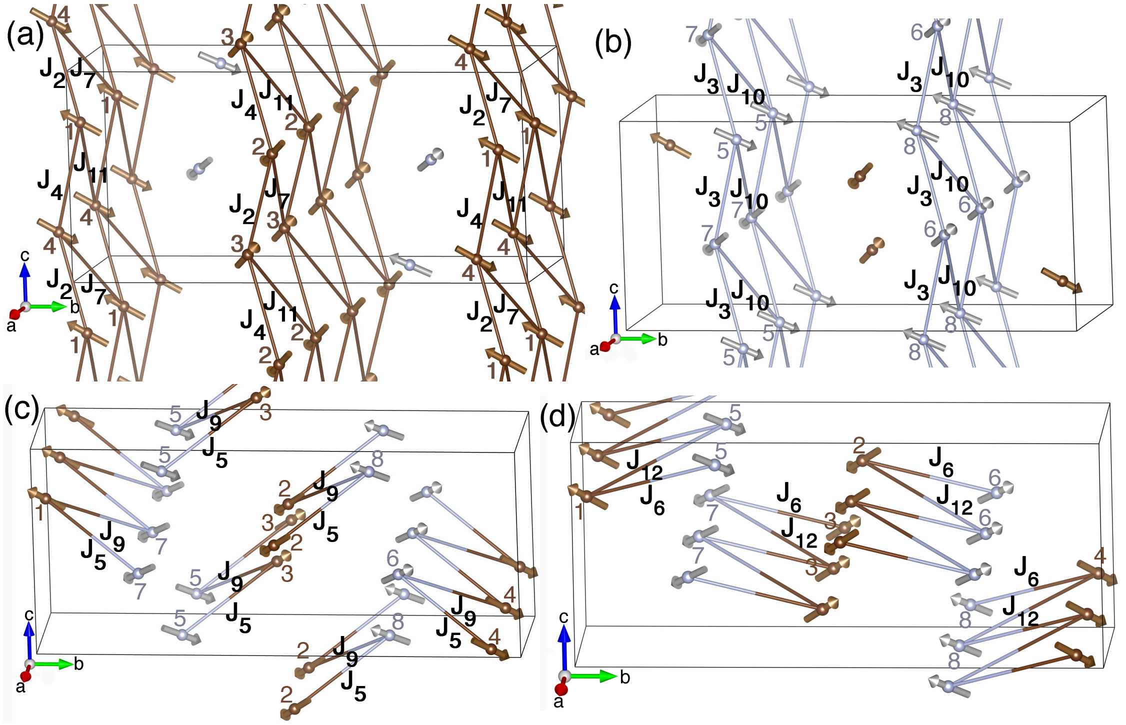

Figure 6.13 – A 1 × 1 × 1 NIT2Py single cell cannot separate (a) J_2, J_4, J_7, and J_{11} from each other, (b) J_3 from J_{10}, (c) J_5 from J_9, and (d) J_6 from J_{12}.

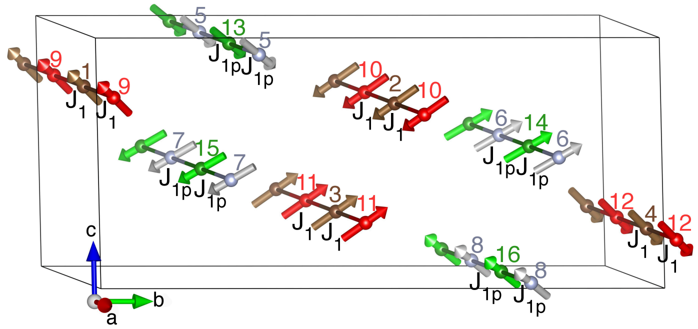

Figure 6.14 – J_1 and J_{1p} are separated by choosing different molecule pairs for each exchange coupling constant within a 2 × 1 × 1 supercell. J_1 is between pairs consisting of molecules in symmetry group I, and J_{1p} is between the ones in symmetry group II.

As shown in Fig. 6.15(b), $2 \times J_3$ and $2 \times J_{10}$ can be separated with the four-state energy approach within the 2 × 1 × 1 supercell. To do so, a different pair of interacting molecules, such as 5-7 for $2 \times J_3$ and 5-15 for $2 \times J_{10}$, are chosen. Note that to separate a given J, any other choice of molecule pair is possible provided that the pair possesses the corresponding J.

Also, as illustrated in Fig. 6.15(c), the remaining Js to be separated are: J_5, between molecule pair 1-15, to be separated from J_9, between molecule pair 1-7, as well as J_6, between pair molecules 1-13, to be separated from J_{12}, between molecule pair 1-5.

However, as shown in Fig. 6.15(a), the $2 \times 1 \times 1$ supercell does not permit a distinction between J_2 and J_4, nor between J_7 and J_{11} because it gives combinations $J_2 + J_4$ and $J_7 + J_{11}$. To separate those Js, we need a new supercell that can provide us with a different molecule pair for each J.

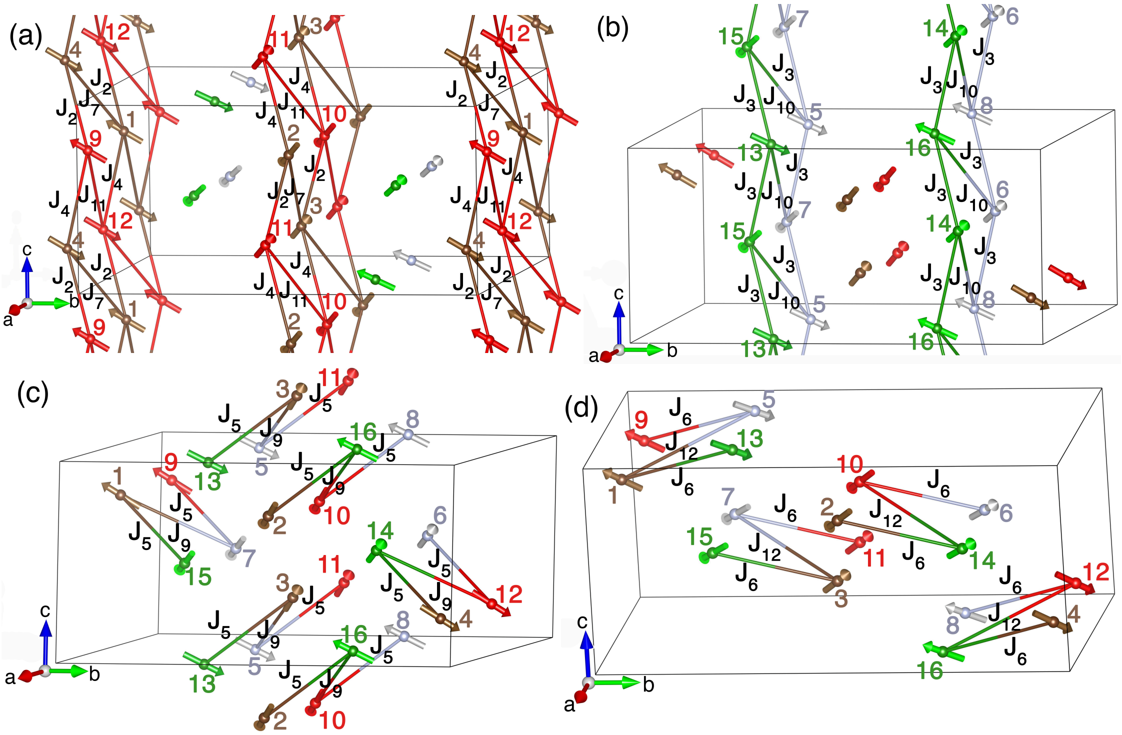

Figure 6.15 – A $2 \times 1 \times 1$ supercell is used to separate the exchange interaction constants (b) $2 \times J_3$ from $2 \times J_{10}$, (c) J_5 from J_9, and (d) J_6 from J_{12}. (a) J_2 and J_4 as well as J_7 and J_{11} cannot be separated using the $2 \times 1 \times 1$ supercell.

Note that all the calculations in the four-state energy mapping approach are executed in QUANTUM ESPRESSO (QE), which is an open-source computer code for electronic structure calculations based on DFT, plane waves, and pseudopotentials [53]. Contrarily to ABINIT, QE enables us to fix the desired spins in all the configurations, such as the ones with FM spin alignments. Also, the calculation time for the spin configurations is quicker as compared to ABINIT. For all the SCF calculations in QE, we use an ultrasoft pseudopotential with the PBE functional for four atom types [116]. Also, spin-polarized calculations with the magnetization along the z axis are employed. A starting spin polarization for self-consistency is set on two N and two O atoms of the ONCNO branch of each molecule with values of $0.12\ \hbar/2$ and $0.17\ \hbar/2$ respectively. Furthermore, we use the kinetic energy cutoff for wavefunctions of 80 Ry and a cutoff for a charge density and potential of 320 Ry. For a monoclinic P lattice, we define the crystallographic constants based on the X-ray results. Also, in each different supercell, we use a different k-point grid consisting of three parameters. In all the calculations, we define the displacement of the grid by half a grid step in each of the three directions.

6.8.1 The $1 \times 1 \times 2$ supercell of NIT2Py

The $1 \times 1 \times 2$ supercell is obtained by doubling the single cell along the c axis, as shown in Fig. 6.16(a). For the sake of simplicity, only the carbon atoms of the ONCNO branch of the 16 NIT2Py molecules are shown in Fig. 6.16(b), with an arrow representing the orientation of each molecule in the supercell. As shown in Fig. 6.17(a), it is not possible to separate J_2 from J_7 in the $1 \times 1 \times 2$ supercell of NIT2Py, as they both corre-

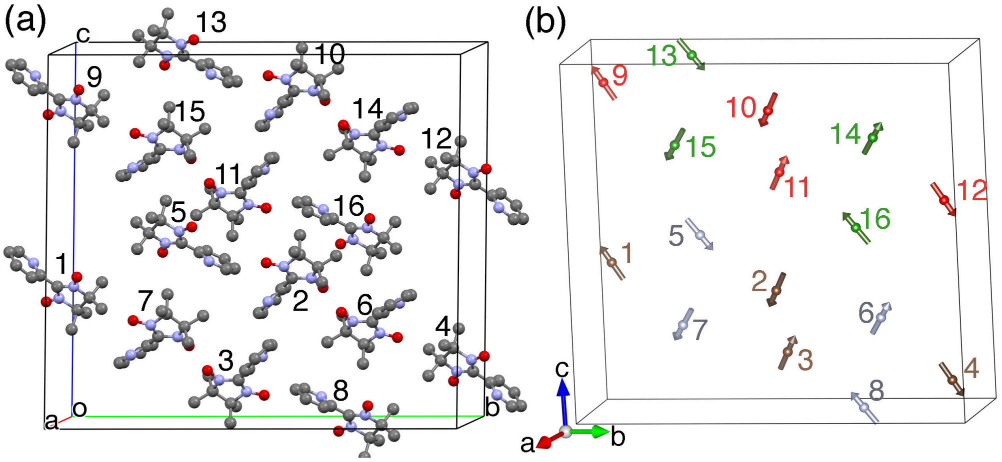

Figure 6.16 – (a) The $1 \times 1 \times 2$ supercell of NIT2Py including 16 molecules and 528 atoms. The hydrogen atoms are omitted for clarity. (b) The central carbon in the ONCNO branch of each molecule along with an arrow indicating the orientation of the corresponding molecule in the supercell.

spond to interactions between the same molecule pair, such as 1-12. Also, J_4 cannot be distinguished from J_{11}, as they both occur from interactions between a single molecule pair, like 9-12. Thus, the $1\times1\times2$ supercell does not allow us to separate those interactions. By employing the four-state energy mapping approach, the value of J_2+J_7 and J_4+J_{11} are calculated and given in Table 6.X. The calculations of the $1\times1\times2$ supercell are carried out with a 411 k-point set. To be able to evaluate those Js separately, a larger supercell is needed, which will be discussed in the next section.

As can be deduced from Fig. 6.17(b), (c), and (d), the $1\times1\times2$ supercell does not allow us to separate respectively J_3 from J_{10}, J_5 from J_9, and J_6 from J_{12}. For example, J_3 and J_{10} are both interactions between molecule pairs 5-15, J_5 and J_9 are interactions between molecule pairs 1-7, and J_6 and J_{12} are the interactions between molecule pairs 1-5.

6.8.2 The $2\times1\times2$ supercell of NIT2Py

The $2\times1\times2$ supercell of NIT2Py consisting of 32 molecules and 1056 atoms is created by multiplying by two the *a* and *c* axes of the single cell of NIT2Py. The 32 molecules of the $2\times1\times2$ supercell are exhibited in Fig. 6.18(a). For the sake of simplicity, the middle carbon in the ONCNO branch of each molecule is shown in Fig. 6.18(b) in which each molecule orientation in the supercell is represented by an arrow. The $2\times1\times2$ supercell permits the separation of interactions J_2, J_4, J_7, and J_{11}. As shown in Fig. 6.19, each of those interactions is now associated to a different molecule pair. For instance, J_2 can be evaluated by choosing a molecule pair such as molecules 1 and 28, which is separated from J_4 between molecules 1 and 20, from J_7 between molecules 1 and 12, and from J_{11} between molecules 1 and 4. Note that a 211 k-point set is chosen for the calculations of the $2\times1\times2$ supercell. Consequently, the values of those four exchange couplings are evaluated through the four-state energy mapping approach, as J_2=0.2 K, J_4=11.0 K, J_7=0.3 K, and J_{11}=0.8 K separately (see Table 6.X and Fig. 6.19).

As seen in Table 6.X, an excellent agreement is achieved between the Js, evaluated by using different supercells and also two different approaches. For example, the combination of $J_2+J_4+J_7+J_{11}$ using the $2\times1\times2$ supercell resulted in 12.4 K, which

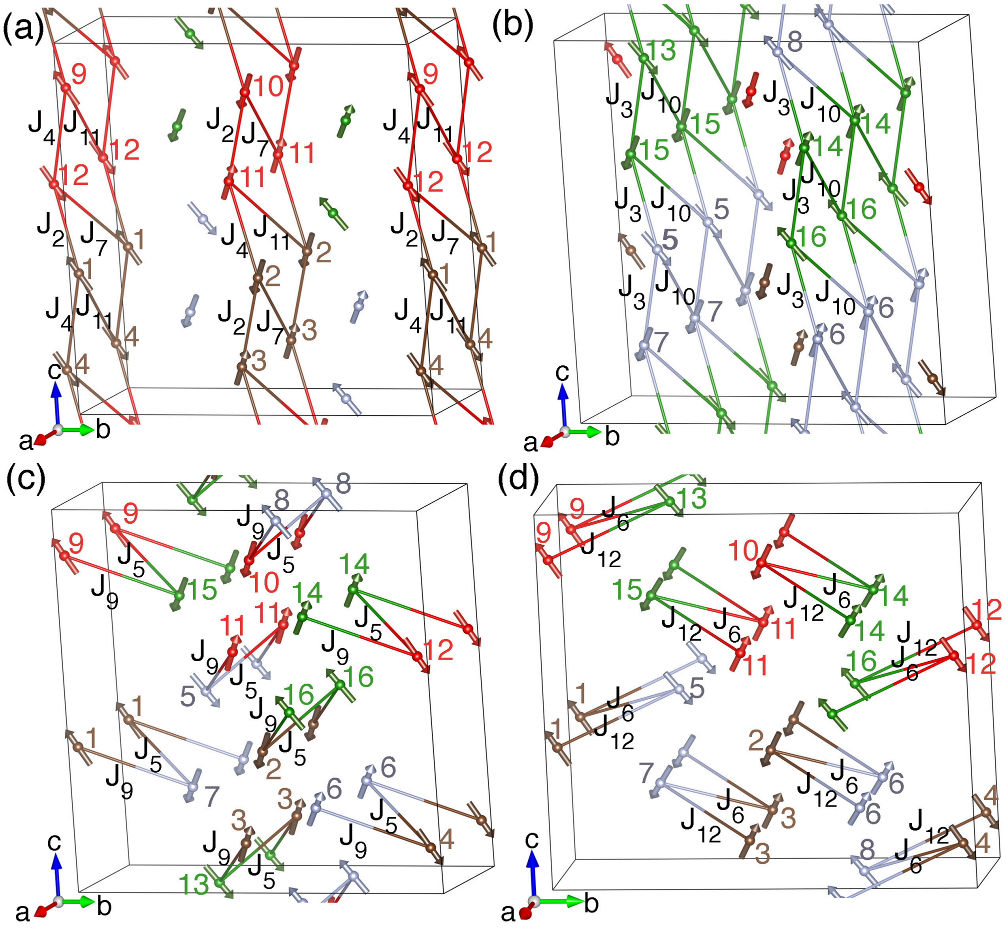

Figure 6.17 – The $1 \times 1 \times 2$ supercell of NIT2Py. (a) J_2 cannot be separated from J_7, and J_4 cannot be separated from J_{11}. Using that supercell, the separation of (b) J_3 from J_{10}, (c) J_5 from J_9, and (d) J_6 from J_{12} is not possible as well.

is equivalent to the sum of the same Js obtained by using $1 \times 1 \times 1$ single cell, and the $2 \times 1 \times 1$ and $1 \times 1 \times 2$ supercells. A summary of the resulting dominant magnetic exchange couplings in the NIT2Py system are shown in Fig. 6.20.

6.9 Contributions

Dr. Michel Côté provided precious help in understanding and using the powerful tools of electronic structure calculation and the ABINIT code. His expertise on ab initio calculation opened a new chapter in the study of the magnetic properties of the NIT2Py

J (K)	$d_{C\text{-}C}$ (Å)	A.I 1×1×1 single cell 412 k-point set	A.I 2×1×1 supercell 212 k-point set	A.II 1×1×1 single cell 412 k-point set	A.II 2×1×1 supercell 212 k-point set	A.II 1×1×2 supercell 411 k-point set	A.II 2×1×2 supercell 211 k-point set
J_1	6.147	-	-	-	-0.913	-	-
J_{1p}	6.147	-	-	-	-2.886	-	-
J_2	6.435	13.423-(J_4+J_7+J_{11})	13.419-(J_4+J_7+J_{11})	12.536-(J_4+J_7+J_{11})	J_4	0.539-(J_7)	0.221
J_3	6.682	-0.643-(J_{10})	-0.644-(J_{10})	-	-0.463	-	-
J_4	6.991	-	-	J_2	11.353-(J_2)	J_{11}	11.082
J_5	7.397	8.260-(J_9)	8.257-(J_9)	7.539-(J_9)	-0.484	-	-
J_6	7.861	9.053-(J_{12})	9.049-(J_{12})	8.573-(J_{12})	6.223	8.525-(J_{12})	-
J_7	7.940	-	-	J_2	1.185	J_2	0.320
J_8	8.083	-0.270	-0.274	-	-0.257	-	-
J_9	8.197	-	-	J_5	8.066	-	-
J_{10}	8.260	-	-	-	0.024	-	-
J_{11}	8.626	-	-	J_2	J_7	11.999-(J_4)	0.869
J_{12}	9.406	-	-	J_6	2.327	-	-

Table 6.X – A comparison of the evaluated numerical values for the dominant *J*s in NIT2Py by using the total energy mapping approach (A.I) and four-state energy mapping approach (A.II).

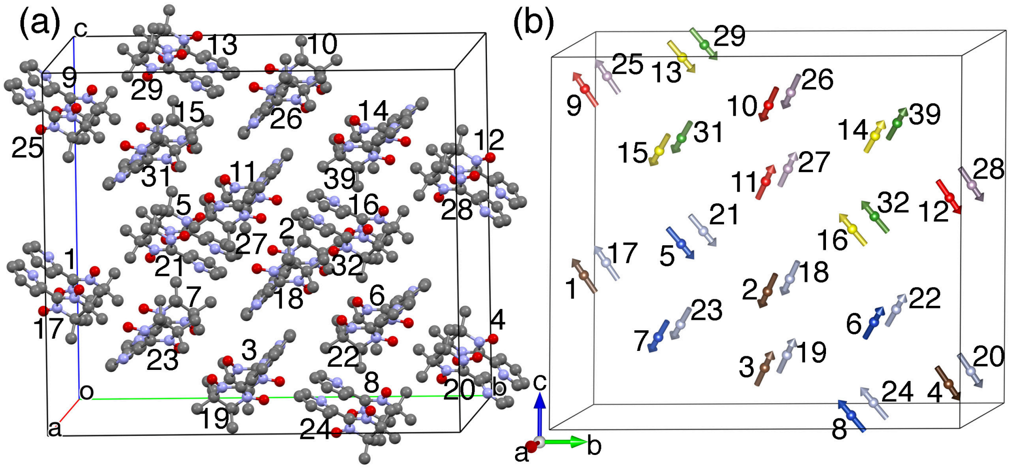

Figure 6.18 – (a) $2 \times 1 \times 2$ supercell of NIT2Py with 32 molecules and 1056 atoms. Note that the hydrogen atoms are omitted for the purpose of clarity. (b) The central carbon of the ONCNO branch of each molecule is shown by an arrow that stands in for the whole molecule and its corresponding orientation in that supercell.

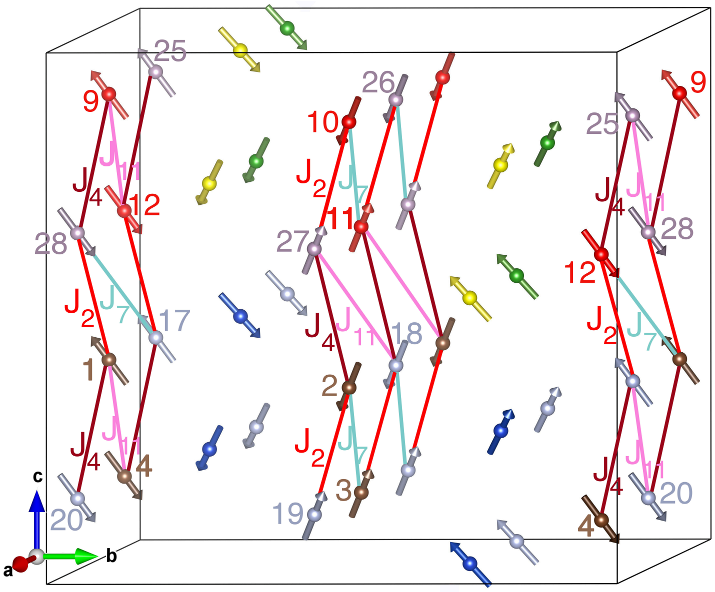

Figure 6.19 – The $2 \times 1 \times 2$ supercell of NIT2Py used to separate J_2, J_4, J_7, and J_{11}. The molecules are replaced by the middle C atom of their ONCNO branch, which are labeled 1 to 32. The arrows schematize the orientation of the molecules.

crystal.

Calculating the exchange interactions by using the total energy difference mapping approach was done with the help of Dr. Andres Saul who is an expert on electronic

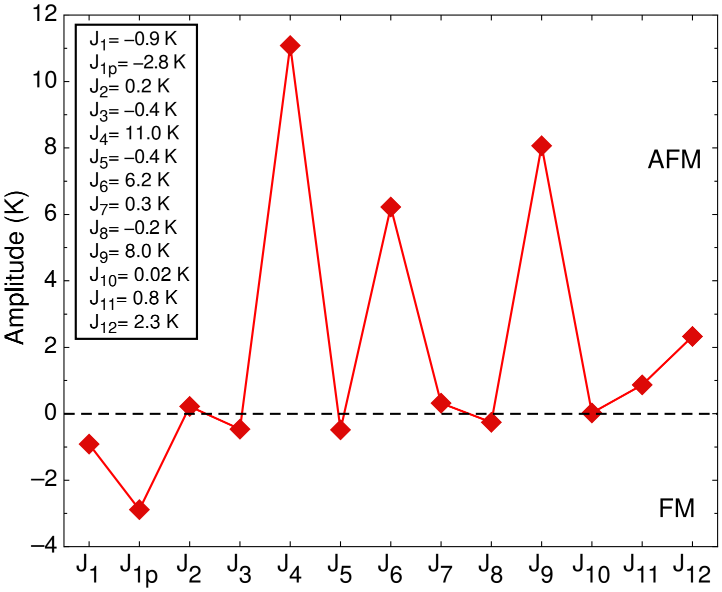

Figure 6.20 – Resulting dominant exchange couplings obtained for the NIT2Py system. Based on the convention used in Eq. (3.36), $J > 0$ represents an AFM coupling and $J < 0$ an FM one.

structure calculations, and computational and numerical methods in general. His extensive knowledge in evaluating magnetic properties by using DFT, broken-symmetry and energy-mapping approaches has allowed us to benefit from his experience for our system.

CHAPTER 7

RESULTS AND DISCUSSION

To describe the magnetic properties of the NIT2Py system, such as the 1/2 magnetization plateau and the exotic phases appearing as dome-shaped regions in the (H, T) phase diagram, we created a spin Hamiltonian for the NIT2Py magnetic system based on its distinguishable exchange interactions. We use the dominant exchange interactions evaluated with the help of first principle electronic structure calculations on the basis of energy-mapping approaches. Now, we need to establish a magnetic lattice for NIT2Py, which is a repeat pattern of the strongest exchange interactions determined by DFT, that can properly generate its observed magnetization characteristics. We will begin by examining a simple model in which half of the molecules in the NIT2Py unit cell form non-interacting dimers and the other half are considered as non-interacting spins. Then, we will employ the interacting dimer model by means of mean-field approximation. Subsequently, we will assess the non-interacting tetramer model. By involving the interactions between tetramers on the basis of MF approximation, we will study the magnetization of the system. Finally, the exact diagonalization of the Hamiltonian matrix associated with four interacting tetramers are performed, and the resulting magnetization of the system is compared to the experimental data.

7.1 Magnetic lattice of the NIT2Py system

If the magnetic lattice of a given magnetic system is constructed only on the basis of the geometrical pattern of arrangements of its molecules containing magnetic moments, there is the possibility of choosing an incorrect magnetic lattice, and in turn, of misinterpreting the magnetic properties of that system [117–119]. Because the magnetic energy levels of a magnetic system are determined by its electronic structure, the electronic structure calculation must be taken into consideration. Hence, to determine the correct magnetic lattice, it is indispensable that a selected magnetic lattice be consistent with the electronic structure of the magnetic system under study [62]. The magnetic lattice relevant to magnetic system of NIT2Py is defined based on a minimal set of exchange coupling constants that can correctly describe the magnetic properties of the system. The dominant exchange coupling constants were evaluated in terms of DFT calculation in chapter 6 and listed in Table 6.X. The numerical values for those Js resulting from the total energy mapping approach as compared to the four-states energy mapping approach are in very good agreement. The three strongest exchange interactions obtained in the NIT2Py system correspond to J_4, J_6 and J_9, as shown in Fig. 7.1(a). As illus-

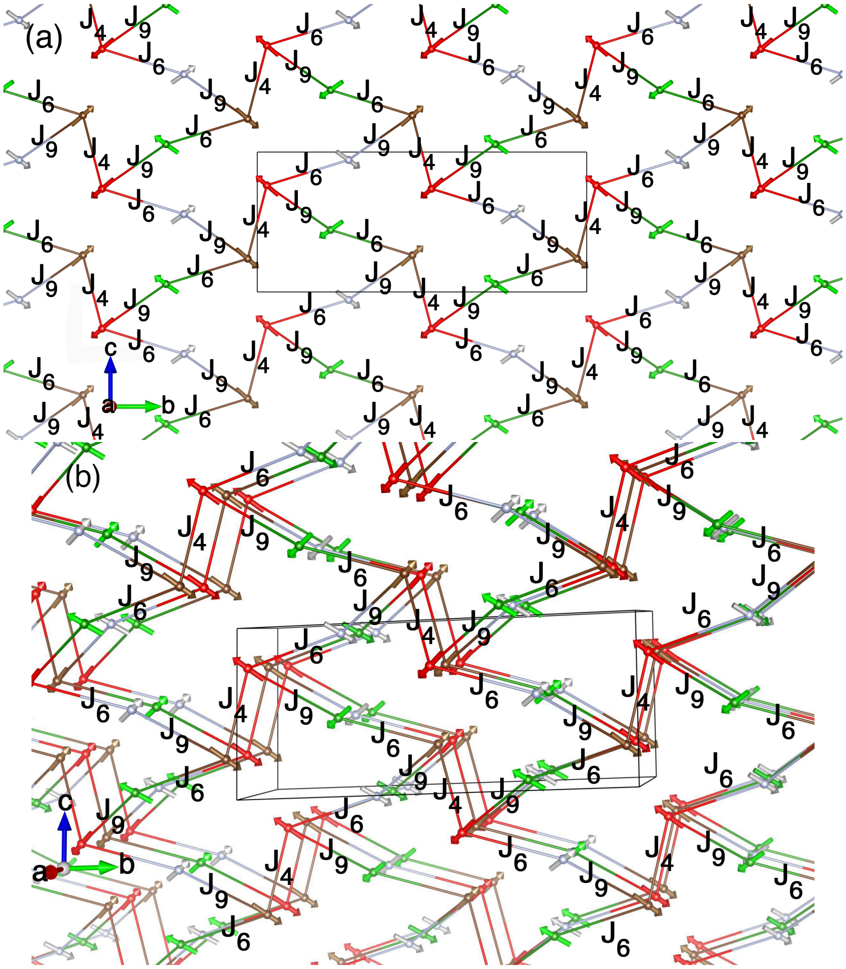

Figure 7.1 – The strongest exchange interactions in the NIT2Py system shown along the *bc* plane. (b) Magnetic interactions J_4, J_6 and J_9 shown in different *bc* planes parallel to one another, with no strong interaction between those planes.

trated in Fig. 7.1(b), the magnetic interactions corresponding to J_4, J_6 and J_9 are related to molecules that are interacting along a crystallographic *bc* plane. Because there is no strong interaction between the various *bc* planes along axis *a*, the exchange interactions in each of the planes can be considered as 2D interactions.

7.2 A simple model

Because the strongest exchange interaction among all interactions between the molecules is that of J_4, one can assume that every molecule pair having that interaction creates a dimer. If that is so, then half of the molecules in the unit cell, 4 out of 8 molecules, would form spin dimers while the other half would be independent S=1/2 spins, as shown in Fig. 7.2. In each of those spin dimers, two S=1/2 spins are coupled with an AFM coupling J_4 and hence form a singlet S=0 ground state and an S=1 excited triplet state.

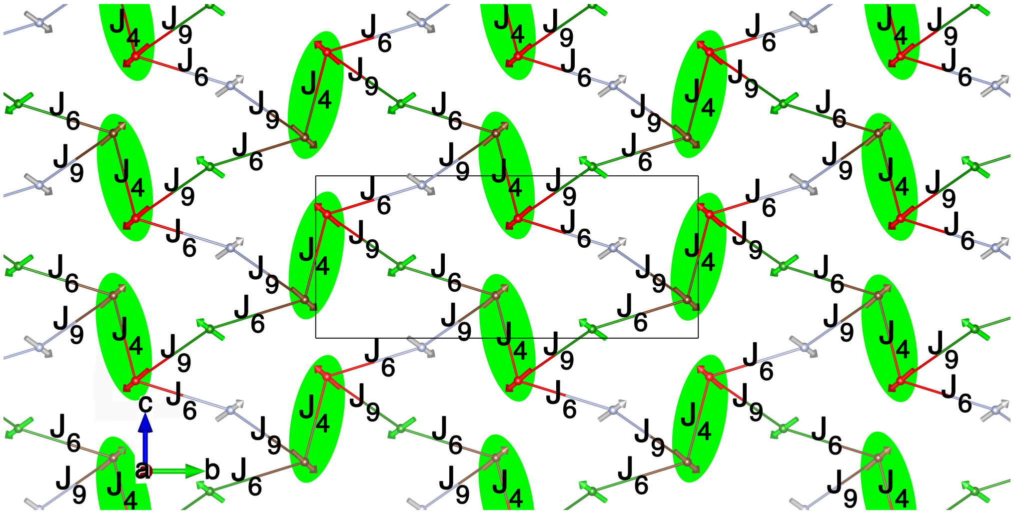

Figure 7.2 – The dimers with the intradimer exchange coupling J_4 formed by half of the molecules in the NIT2Py unit cell as highlighted by the green ellipsoid shapes. The other half of the molecules are free spins. The repeat of the dimers with strong intradimer exchange coupling J_4 is suggested as the magnetic lattice.

The magnetization of non-interacting magnetic moments is obtained based on Eq. 2.36, which is plotted as a function of applied magnetic field at 0.5 K, as shown in Fig. 7.3(a). Also, the magnetization of non-interacting dimers is plotted as a function of applied field at 0.5 K on the basis of Eq. (2.51), as shown in Fig. 7.3(b). Note that J in Eq. (2.51), which corresponds to the intradimer interaction J_4, is set to 8 K. In Fig. 7.3(c), the paramagnetic magnetization corresponding to non-interacting magnetic moments is combined with the magnetization of the other half of the molecules forming non-interacting dimers. The resulting magnetization is compared to the measured magnetization of the NIT2Py at 0.5 K. Additionally, in Fig. 7.4, the magnetization of the sum of the non-interacting spins and dimers at different temperatures is plotted as a function of applied field, and compared to the corresponding experimental data. The slope of the curves based on the simple model are not compatible with the ones from the experimental measurements. In the next model, the interactions among the spin dimers are included through the MF approach.

7.3 A model of interacting dimers

Until now, the dimers were not interacting with each other. However, with the help of MF approximation, the interactions between spin dimers can now be taken into account, as discussed in chapter 2.9.1. By solving numerically the transcendental equation for the magnetization ($M = f(M,B)$) for different temperatures of the interacting spin dimers in Eq. 2.78, the magnetization curves are plotted as a function of applied field in Fig. 7.5. The J in Eq. 2.78 is set at 6 K, representing an AFM intradimer coupling. Also, an AFM interdimer interactions of J'=2.6 K is considered in the theoretical magnetization curves.

As shown in Fig. 7.5, by comparing the model magnetization curve at 0.5 K and the corresponding experimental curve, one concludes that the model of interacting dimers cannot recreate the 1/2 magnetization plateau observed in our experiment. Similarly, the magnetization curves measured at other temperatures cannot be reproduced. In conclusion, this simple model is not in agreement with the experimental magnetization results and is therefore not relevant for the NIT2Py system. A more complicated model is needed to express the magnetic properties of the NIT2Py system.

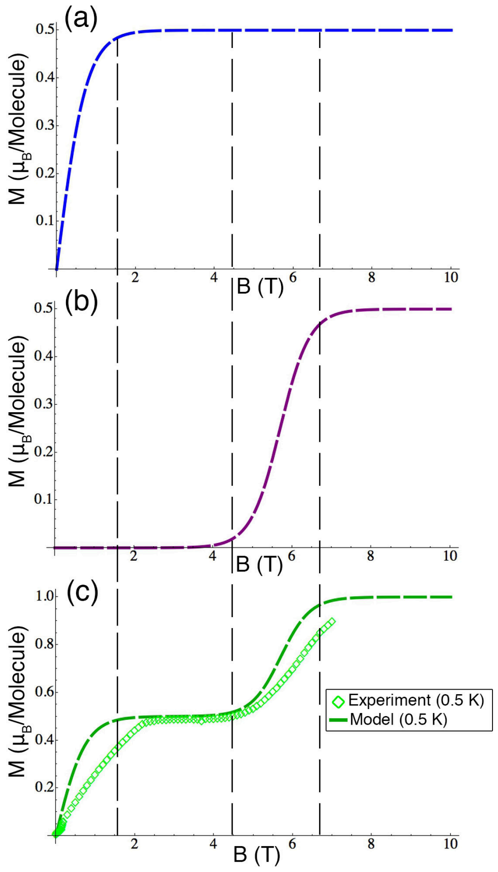

Figure 7.3 – Magnetization as a function of applied magnetic field at 0.5 K plotted for (a) non-interacting spins, (b) non-interacting dimers with an AFM intradimer exchange coupling constant of 8 K. (c) The experimental curve at 0.5 K is compared to the one from a simple model composed of the magnetization of half of the molecules in the NIT2Py unit cell acting as dimers and the other half as free spins.

7.4 A model of spin tetramers

A more appropriate magnetic lattice consists of the two strongest AFM exchange interactions, which leads to a larger magnetic superstructure called spin tetramer. In Fig. 7.1, we see a NIT2Py spin tetramer comprised of four interacting spins having two different exchange coupling constants, J_4 and J_9. A new magnetic lattice can be designed by repeating those spin tetramer units, as shown in Fig. 7.6. Next, the magnetization of a system of non-interacting tetramers discussed in chapter 2.8.2 will be used in our system. Then, the magnetization of interacting tetramers obtained in chapter 2.9.2 via

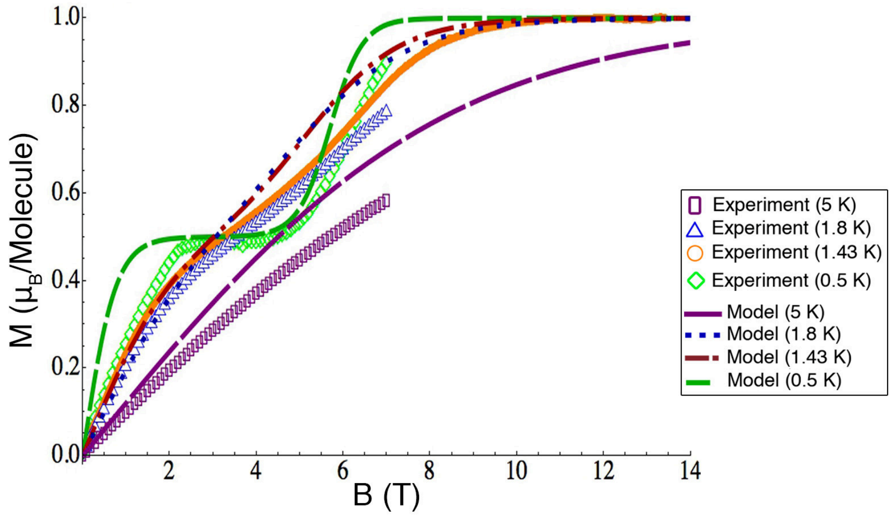

Figure 7.4 – Magnetization versus magnetic field measured at 5 K, 1.8 K, 1.43 K, and 0.5 K compared to those from a simple model consisting of a sum of the magnetization of non-interacting dimers (Eq. (2.51)) and magnetization of free spins (Eq. 2.36) shown respectively as long-dash, dot, dash-dot, and dash curves.

MF approximation will be utilized. The results of both magnetizations are compared to the experimental results at different temperatures.

7.4.1 A model of non-interacting spin tetramers

The magnetization of a system of non-interacting spin tetramers is given in Eq. 2.65, where coefficients A'_1, A'_2, and A'_3 are provided in Eq. 2.63. As shown in Fig. 7.7(a), the magnetization of a system of non-interacting tetramers is plotted as a function of the applied field at 0.5 K, with two AFM exchange couplings, J_9=2.8 K and J_4=6 K, being substituted respectively for J_1 and J_2 in the model magnetization of Eq. 2.65. By comparing the result of the model with the measured magnetization of NIT2Py at 0.5 K, the 1/2 magnetization plateau observed experimentally is well expressed by the tetramer model.

Also, the two ascending slopes of magnetization due to the applied field represented in Fig. 7.7(a) occurred at the two intersections of the lowest-energy levels of the tetramer system shown in Fig. 7.7(b). The first slope is placed where the $S_z = 1$ level of the lowest-

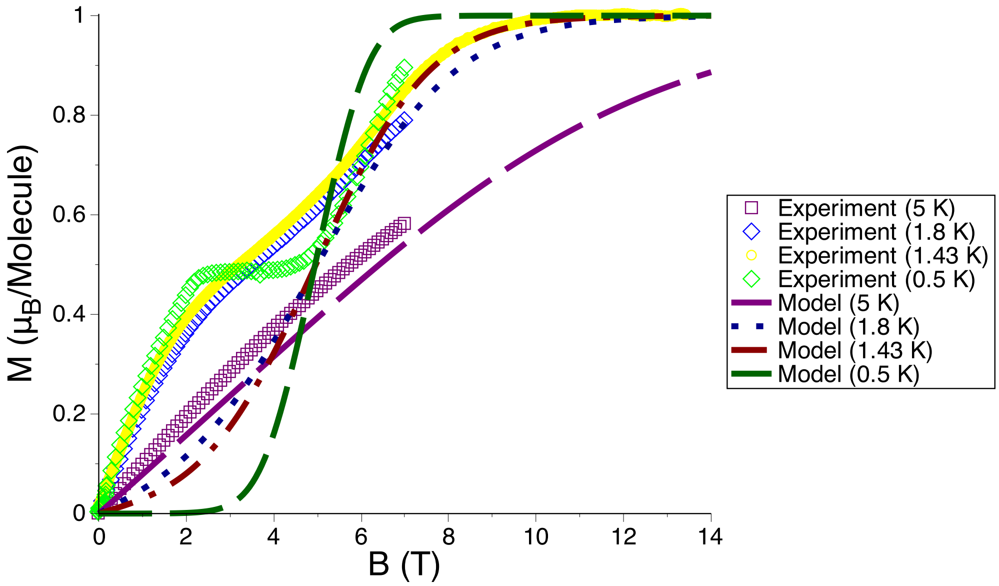

Figure 7.5 – Magnetization as a function of applied magnetic field at 5 K, 1.8 K, 1.43 K, and 0.5 K compared to the model of interacting dimers (Eq. (2.78)) with J=6 K, J'=2.6 K, and z'=1.

energy triplet state intersects with the singlet ground state. The second slope appears where the $S_z = 2$ level of the quintuplet state crosses the S_z level of the lowest-energy triplet state. The two regions of increasing M_z in the magnetization curve represent the regions with magnetic order in the NIT2Py system. As shown in Fig. 7.7(b), the slopes in those two regions are not fully reproduced by the model of non-interacting tetramers, which points to the fact that the magnetic interactions among the tetramers must be included.

Additionally, the magnetization as a function of applied field is calculated at different temperatures using Eq. (2.65) and the results are compared to the experimental curves, as shown in Fig. 7.8.

7.4.2 A model of interacting tetramers

If we take for granted that the intertetramer exchange interaction in the NIT2Py system is much smaller than the intratetramer exchange interaction, the mean-field approximation can be employed. As discussed in chapter 2.9.2, the interactions of a given

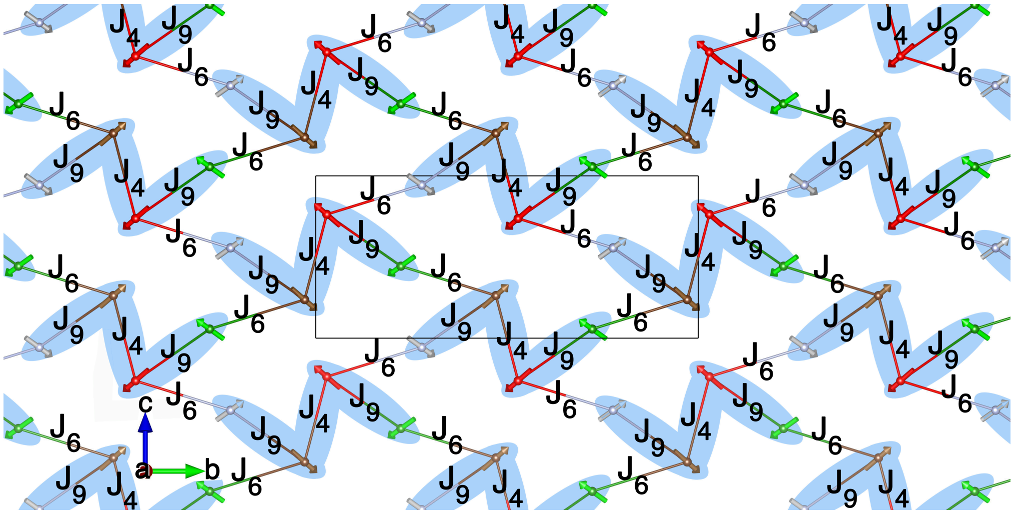

Figure 7.6 – A magnetic lattice constructed by a repeating pattern of spin tetramers shown by blue z-shaped areas. Each tetramer consists of four spins having two different exchange interactions, J_4 and J_9.

tetramer with its neighboring tetramers are replaced by an effective mean-field. The magnetization for a system of interacting tetramers is obtained in Eq. (2.85), where coefficients A_1', A_2', and A_3' are given in Eq. (2.63). To obtain the magnetization of interacting tetramers at various temperatures, the transcendental equation ($M = f(M,B)$) in Eq. (2.85) is solved numerically for different temperature values. Also, AFM exchange couplings of J_9=2.8 K and J_4=6 K are respectively substituted for the intratetramer couplings, J_1 and J_2 in Eq. (2.85). Also, an AFM intertetramer interaction is taken into account with a value of J'=1 K.

As shown in Fig. 7.9, the experimental magnetization isotherms of NIT2Py as a function of external magnetic field at different temperatures are compared to the model magnetization of interacting tetramers. Furthermore, as shown in Fig. 7.10, the magnetization as a function of temperature based on the model of interacting tetramers by MF are compared to the corresponding experimental curves measured at different applied magnetic field. Note that the values of J_4=6 K, J_9=2.8 K, J'=1 K are taken into account in the model.

Additionally, in section 5.4, the high temperature specific heat is studied in terms of Schottky anomaly. The Schottky anomaly appears in systems with discrete energy lev-

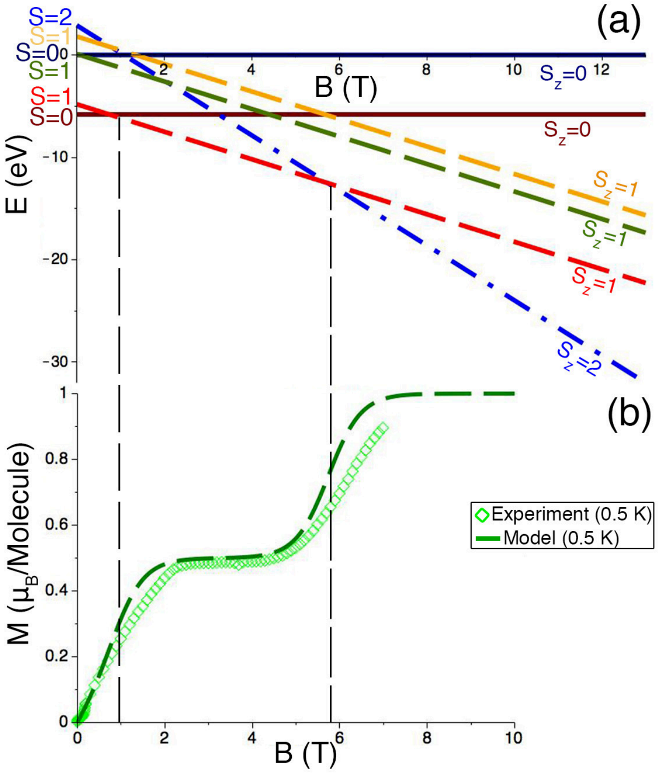

Figure 7.7 – (a) The energies of the two singlet states, the $S_z = 1$ levels of the three triplet states, and the $S_z = 2$ level of the quintuplet state of a system of non-interacting tetramers shown as a function of the applied magnetic field. The $S_z = 1$ of the lowest-energy triplet state crosses the single ground state, and then the $S_z = 2$ of the quintuplet state intersects with the $S_z = 1$ of the lowest-energy triplet state. (b) The magnetization of the model of non-interacting tetramers plotted as a function of applied field at 0.5 K, and the result compared to the corresponding experimental data.

els, and in the case of the NIT2Py system originates from different states in the tetramers. To gain deeper understanding of the Schottky anomaly, an antiferromagnetic MF decoupling of the Hamiltonian in Eq. (2.66) can be taken into account, which gives rise to a self-consistent equation for the staggered order parameter, $M_s = f(M_s, B, T)$. To determine the transition temperature T_{AFM}, the solution of that self-consistent equation needs to be found at B=0 when $M_s \to 0$. The scale of T_{AFM}, which is linked to J' ($T_{AFM} \sim J'$), should be considerably smaller compared to the scale of ordering within each tetramer, and should be of the order of the exchange integral J_1 and J_2. Consequently, along the temperature axis, it is possible that the NIT2Py system orders as follows: first, the

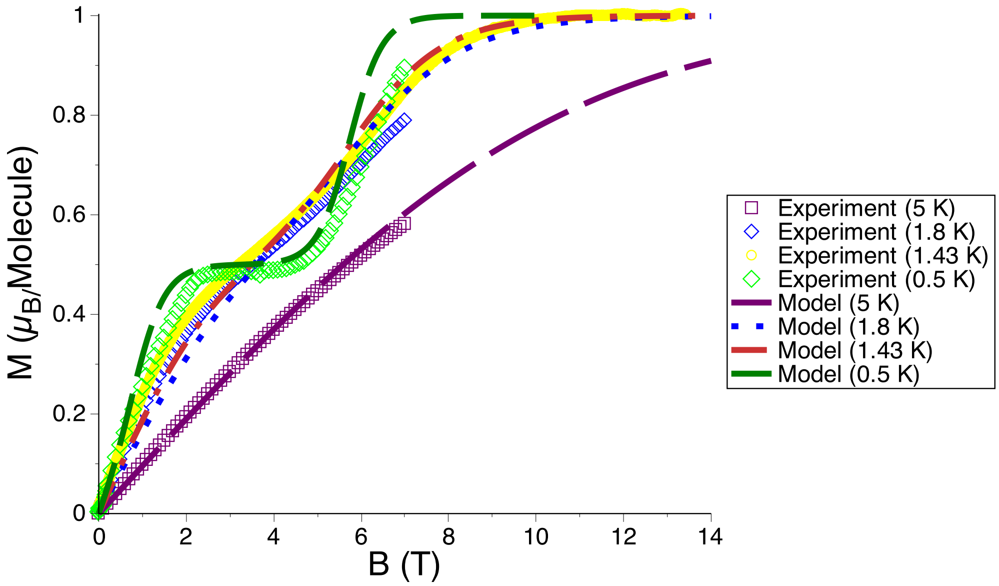

Figure 7.8 – Magnetization as a function of applied magnetic field at 5 K, 1.8 K, 1.43 K, and 0.5 K are compared to the model of non-interacting tetramers. The model curves are based on Eq. (2.65), with J_9=2.8 K and J_4=6 K represented respectively by J_1 and J_2.

system orders locally within the tetramers, with discrete, field-dependent energy levels, which results in Schottky like anomalies in the specific heat. Second, at low enough temperature, the system orders via J' at a true 3D phase transition. The appearance of those anomalies can be considered as an additional signature, which is thermodynamical, indicating the presence of tetramers as the elementary units of the NIT2Py system.

7.5 A model of exact diagonalization of the Heisenberg Hamiltonian

A 2D network of four interacting tetramers consisting of a total of 16 spin sites in the unit cell is constructed, as shown in Fig. 7.11. Each tetramer is composed of one J_4 and two J_9 interactions, and is interacting with two neighboring tetramers through two J_6 interactions. Consequently, the topology of the 2D network of four interacting tetramers is comprised of four J_4, eight J_9, and eight J_6 interactions. The corresponding spin sites for those interactions are given in Fig. 7.11. As discussed in chapter 2.10, by performing an exact diagonalization of the Hamiltonian matrix composed of four tetramers, N=16 spins, the eigenvalues and eigenvectors of this system are calculated.

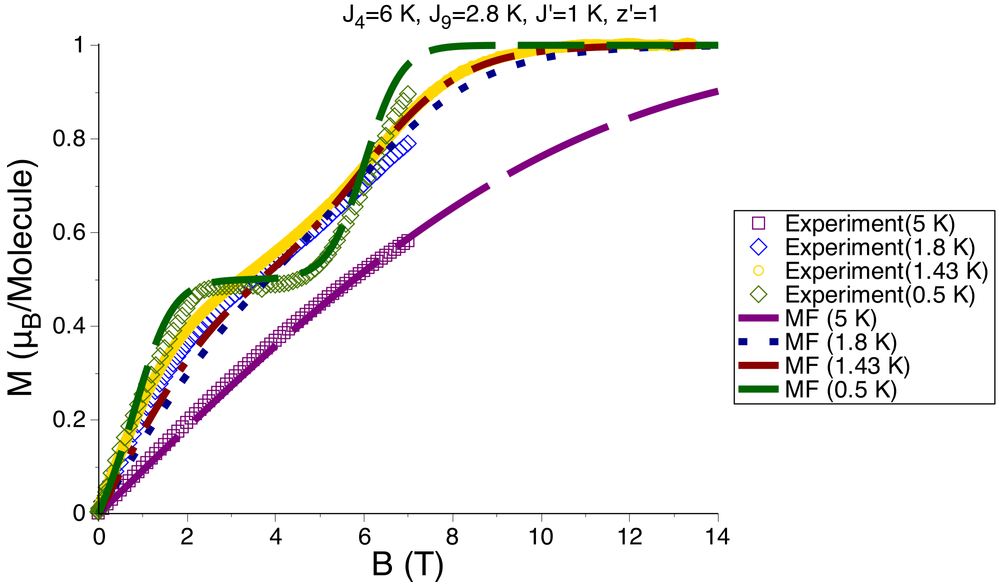

Figure 7.9 – Magnetization as a function of applied magnetic field at 5 K, 1.8 K, 1.43 K, and 0.5 K are compared to the model based on the mean-field (MF) approach of interacting tetramers exhibited respectively as long-dash, dot, dash-dot, and dash curves. The model curves are based on Eq. (2.85), with J_9=2.8 K, J_4=6 K, J'=1 K, and z'=1.

Consequently, the mean value of the magnetization of the system of four spin tetramers is evaluated by means of the resulting eigenvalues and eigenvectors of the Hamiltonian matrix. The magnetization of this system is plotted as a function of applied magnetic field for different temperatures. As shown in Fig. 7.12, the model is compared to the corresponding experimental curves. Additionally, magnetization model is plotted as a function of temperature for different applied fields. The model curves are compared to the experimental data, as shown in Fig. 7.13.

7.6 Comparison between mean-field and exact diagonalization approaches

We compare the magnetization obtained from the two different approaches: mean-field (MF) and exact diagonalization (ED) of the Hamiltonian of the system of four tetramers with 16 spin-1/2 in total. As shown in Fig. 7.14, the field dependence of the magnetization of a system of interacting tetramers resulted from the model based on the ED approach of the finite system is compatible with the model obtained from

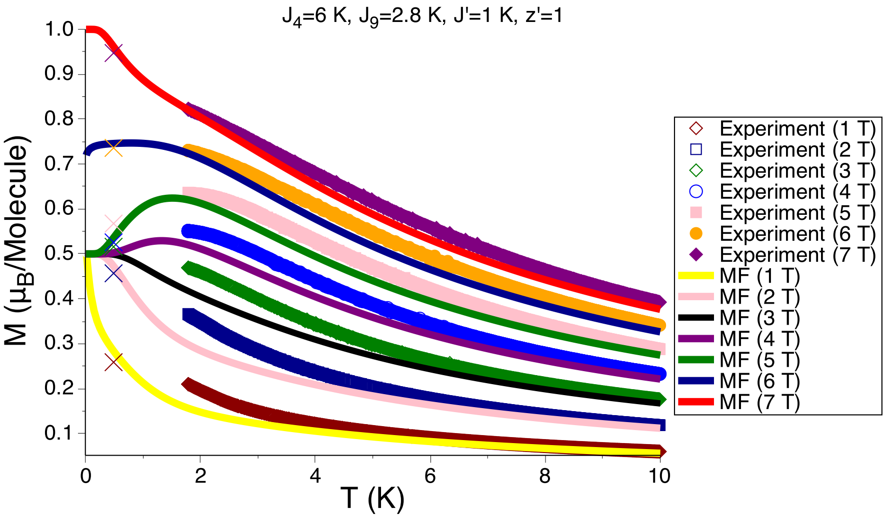

Figure 7.10 – The temperature dependence of magnetization at fields measured between 1 T to 7 T are compared to the model based on the mean-field (MF) approach of the interacting tetramers. The model curves are based on Eq. (2.85), with J_1=2.8 K, J_2=6 K, J'=1 K, and z'=1. The X symbols are associated with another set of experiments performed at 0.5 K.

the MF approach. As shown in Fig. 7.15(a), (b), (c), and (d), the magnetization as a function of applied field obtained based on the MF and ED approaches is compared to the experimental data measured at different temperatures. In Table 7.I, one can find a list of different models along with the corresponding exchange coupling constants used to reproduce the experimental data of the magnetization of the NIT2Py system. Note that in both models presented for interacting tetramers based on the MF and ED approaches, AFM intratetramer interactions with the values of J_4=6 K, and J_9=2.8 K are considered. Additionally, the model based on the MF approach takes into account an AFM of J'=1 K to include all the exchange interactions with the nearest neighbours. In the model based on the ED approach, J_6=1 K is chosen in order to include the intertetramer interactions. For the sake of comparison, the intertetramer interactions in both models are considered comparable with each other, $J' = J_6$=1 K.

The resulting strongest magnetic interactions by means of DFT calculations are J_4=11.0 K, J_9=8.0 K, and J_6=6.2 K. However, the values of J_4=6 K, J_9=2.8 K, and $J_6 = J'$=1 K are used in the two models based on the MF and ED approaches in order

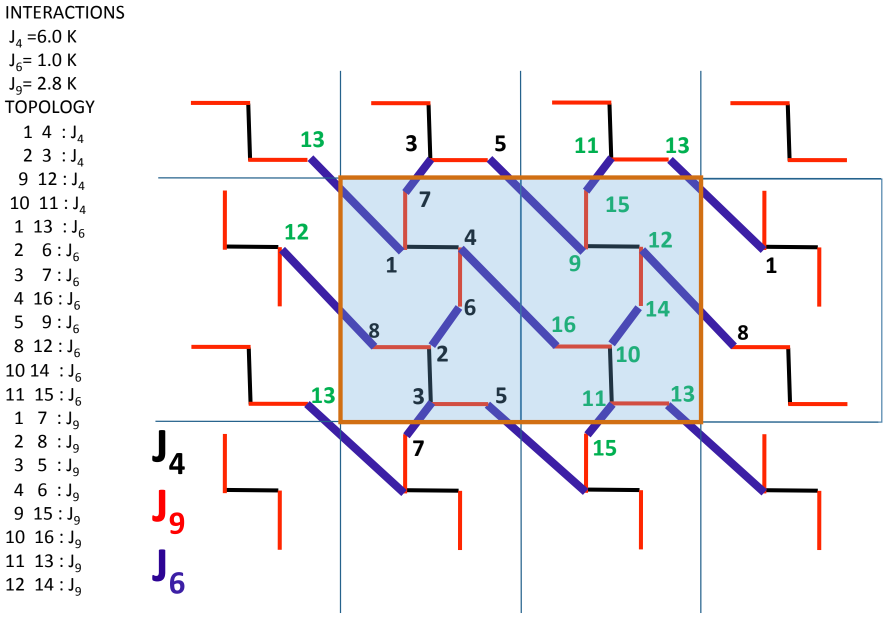

Figure 7.11 – 2D network of four interacting tetramers with intratetramer interactions J_4 and J_9 and intertetramer interaction J_6. Topology of the system consisting of all the interactions associated with the four tetramers. The two numbers given for each exchange coupling constant represent the corresponding interacting molecule pairs.

to reproduce the experimental results of the magnetization of NIT2Py. The difference between the values used in the models for the MF and ED approaches and those obtained by DFT calculations can arise, to some extent, from the fact that the ab-intio calculations are performed based on the X-ray data at T=150 K, whereas the magnetization isotherms are obtained at very low temperature. As opposed to inorganic solids, the thermal contraction is usually much more significant in organic solids. The effect of a decrease in intermolecular distances, which can be finite and anisotropic, on the amplitudes taken by the exchange integrals cannot be negligible. Additionally, the discrepancy between the input exchange parameters entering the MF and ED approaches and those predicted by DFT can be due to employing the conventional GGA-PBE functional in the DFT total energies calculations of the different configurations. It has been shown that GGA-PBE functional does not allow to correctly describe the van der Waals interactions [120]. As a consequence, GGA-PBE can lead to an overestimation of the magnitude of the exchange

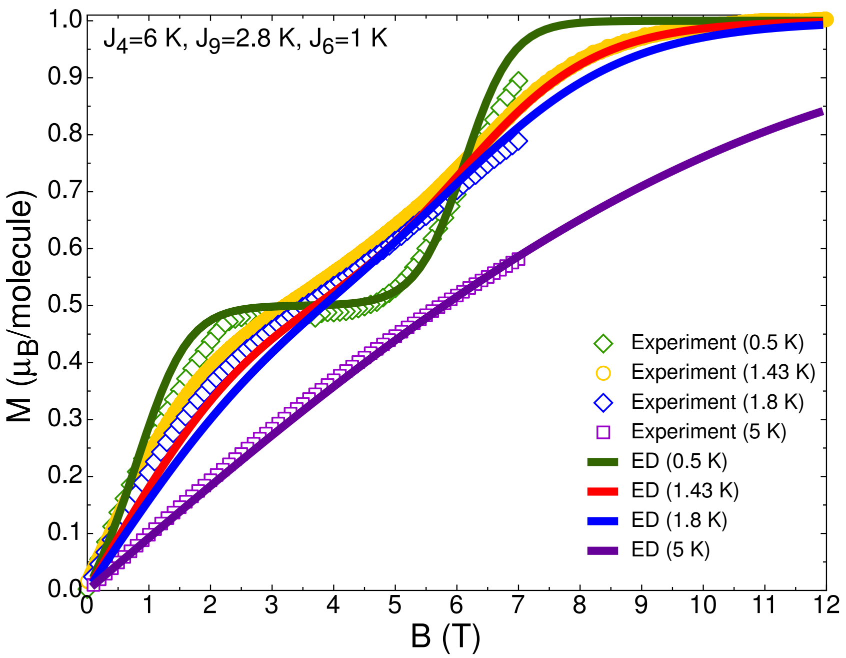

Figure 7.12 – Magnetization as a function of applied field of a model obtained by exact diagonalization of the Hamiltonian matrix of a system of four interacting tetramers, and plotted at 50 K, 5 K, 1.8 K, 1.43 K, and 0.5 K. Values of J_4=6 K, J_9=2.8 K, J_6=1 K are considered in the model. The model is compared to the experimental data.

couplings. This overestimation has been observed for some magnetic compounds such as for $Sr_3Cr_2O_8$, which is overestimated by an order of magnitude [91]. Also, for the βTeVO$_4$ and the CsV_2O_5 compounds, the values obtained using GGA-PBE are two times larger than those computed employing the PBE0 functional [48, 51].

With regards to the MF approach model, there is no substantial difference between exchange interactions J_6 and J_9. As a consequence, interaction J_9 is taken for the intratetramer interaction, and J_6 employed as the intertetramers interaction. In principle, in order for the mean-field approach to work better, we expect that the exchange interactions interconnecting the magnetic units in the magnetic lattice structures of a given system be weak enough as compared to the interactions between the spin constituents in those units [73]. However, based on the DFT result, those two interactions are obtained close in values, as J_9=8 K and J_6=6.2 K. As a consequence, the model based on the MF approach is questionable.

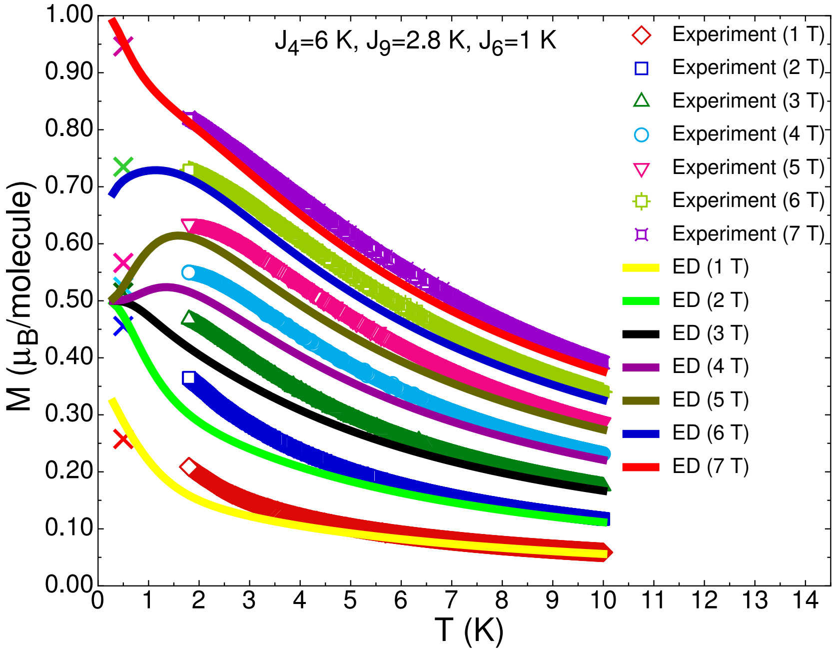

Figure 7.13 – The temperature dependence of magnetization for a model of exact diagonalization of the Hamiltonian consisting of four interacting tetramers is compared to the experimental data. The values of J_4=6 K, J_9=2.8 K, J_6=1 K are considered in the model. Note that the X symbols are related to another set of experiments carried out at 0.5 K.

As shown in Fig. 7.15(a), the 1/2 magnetization plateau is well reproduced by both models based on the MF and ED approaches. Also, both models can describe the field dependence of the magnetization corresponding to the two ordered phases. Because, in high temperatures with large thermal fluctuations, and also in very low temperatures where we have an ordered phase, the correlation effect decreases, the MF approach and the ED approach with a small number of spin sites, work well in those two regimes.

But, in the vicinity of a phase transition with a large correlation length, the MF approach and the ED approach on a finite cluster fail. However, as shown in Figs. 7.12 and 7.9, the behavior of magnetization close to the critical magnetic fields associated with the phase transitions is not well interpreted, neither by MF nor by the ED model. Additionally, the slopes of the field dependence magnetization curves at low-applied fields are constant at 0.5 K, 1.43 K, and 1.8 K. This characteristic is not observed in the magnetization models based on the ED approach with a finite number of spin sites or the

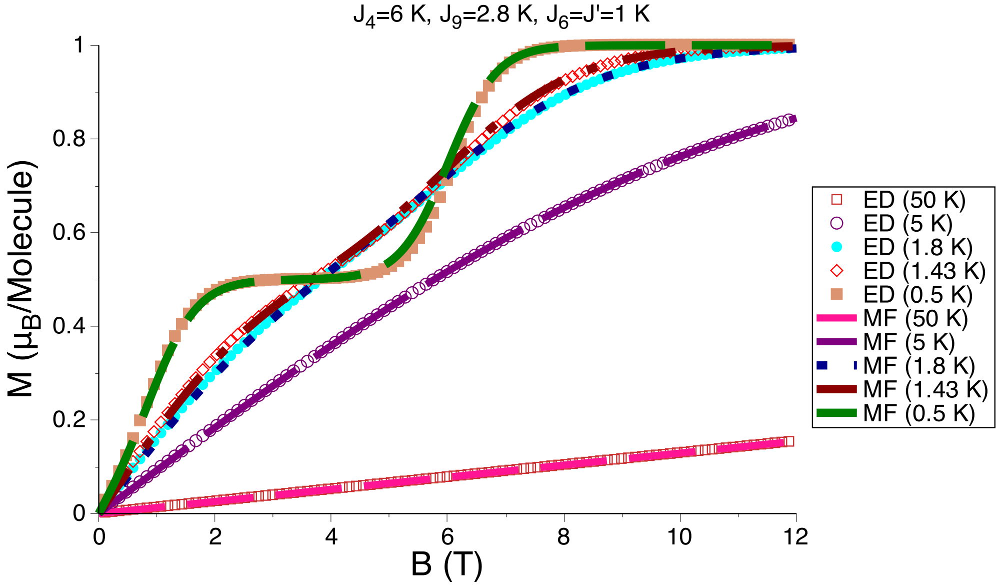

Figure 7.14 – Comparison between the magnetization as a function of temperature for two models obtained based on the mean-field (MF) approach and the exact diagonalization (ED) approach for the Hamiltonian of four interacting tetramers. In both models, the interactions are chosen as J_4=6 K, J_9=2.8 K, $J_6 = J'$=1 K.

MF approach.

To explain why the MF approach cannot capture the physics next to the phase transition, we can refer to section 2.9 where we defined the difference relative to the mean value of the spin as fluctuation, δS_i. The term $\delta S_i \delta S_j$ is considered to be negligible in the MF approach. However, near the phase transition, the fluctuations are sizable, and hence one cannot ignore the $\delta S_i \delta S_j$ term in the Hamiltonian of Eq. 2.70. Equivalently, upon approaching a phase transition, the correlation length enhances. A diverging correlation length adjacent to the transition line under field causes fluctuation effects, which in turn may result in deviations from the MF approach used in the calculations of magnetization as a function of magnetic field. However, M, the MF parameter used in section 2.9, alludes to uniform magnetization and not to the true order parameter related to the transition under field. In the case of an antiferromagnet, the order parameter is not the magnetization as the total, because the magnetization as a total is always zero. So, the true order parameter of the transition for AFM exchange between the tetramers is the

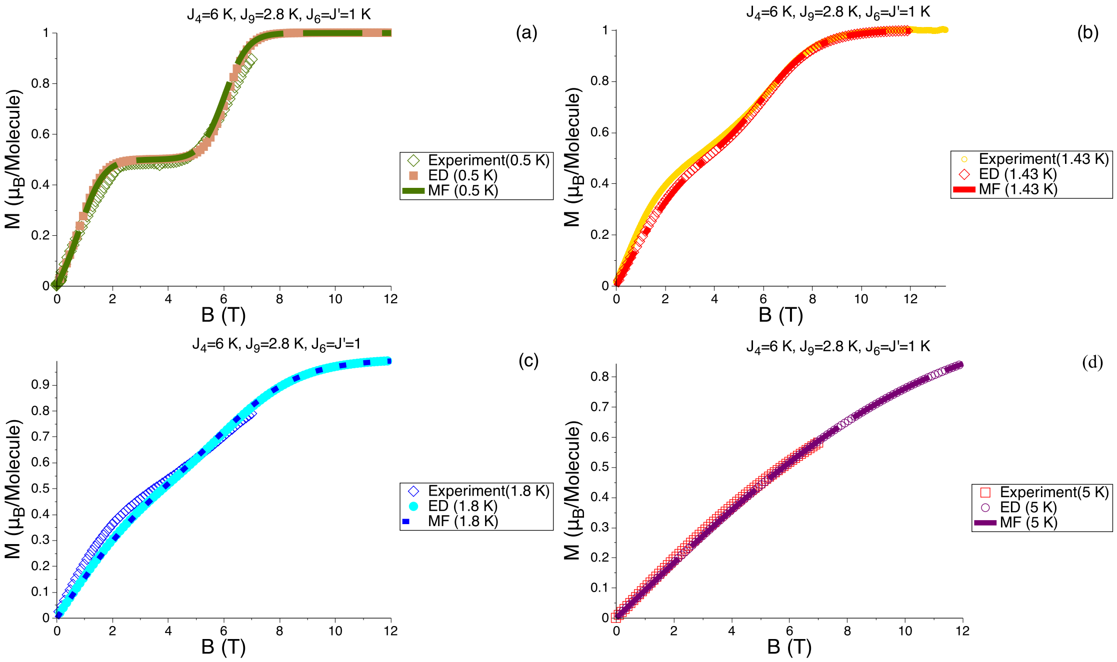

Figure 7.15 – Magnetization as a function of the applied field for two models based on ED of a Hamiltonian consisting of four interacting tetramers and MF approaches compared to the experimental data at (a) 0.5 K, (b) 1.43 K, (c) 1.8 K, and (d) 5 K.

magnetization of each sublattice, so-called staggered magnetization. Consequently, the fluctuation effects would be of an AFM character, and hence would not be given by the deviations δS_i that are tied to the uniform M.

Since, in the ED approach discussed here, we used a finite system composed of four spin tetramers, at some point the correlation length gets larger than the size of the defined ED system. In such a situation, the ED result is questionable. The ED approach can be improved by increasing the size of the cluster. However, as a result of the exponential growth of the Hamiltonian matrix size (i.e, Hilbert space), the exact diagonalization of systems with a larger number of spin sites is very challenging.

7.7 Contributions

The exact diagonalisation method presented in this thesis was carried out by our esteemed collaborator, Dr. Andres Saul. We thank him immensely for the results. The

Table 7.I – A list of exchange coupling constants used in different magnetization models to reproduce the observed experimental magnetization of the NIT2Py.

Model	J_4 (K)	J_9 (K)	J_6 (K)
DFT	11.0	8.0	6.2
Non-interacting dimers	8	-	-
Non-interacting tetramers	6	2.8	-
Interacting dimers by MF	6	-	J'=2.6
Interacting tetramers by MF	6	2.8	J'=1
Interacting tetramers by ED	6	2.8	1

Fig. 7.11 was provided by Dr. Andres Saul.

CHAPTER 8

CONCLUSION

The goal of this research was to aid in the development of a field of study that was once believed to be unattainable: that of organic magnetic materials. In this work, particular attention was dedicated to the study of the magnetic properties of a molecule-based magnet called NIT2Py, which is constructed from purely organic molecules that condense into a crystal with exceptional stability. The crystal structure of NIT2Py was shown by X-ray diffraction measurement as being a monoclinic structure with the space group $P2_1/c$.

Owing to a S=1/2 spin of an unpaired electron delocalized over a large part of NIT2Py molecule, each molecule bears a magnetic moment, which was shown by magnetization and susceptibility measurements. A temperature versus magnetic field phase diagram was established based on the magnetic specific heat and magnetocaloric effect measurements. The two magnetically ordered phases were observed as dome-shaped regions in the (B, T) phase diagram. Close to a quantum critical point at the upper critical field of the second dome-shaped region, the (B,T) phase boundary approaches a power law, $B_c(T) - B \propto T_c^{\phi}$, with a critical exponent of 1.47(9). The fact that the obtained critical exponent is close to the theoretically predicted universal value of 3/2 for a 3D BEC, and the observation of a spin gap opening above the upper critical field of the second dome-shaped ordered region justify the evidence for the realization of BEC in the NIT2Py. The field-induced dome-shaped ordered phases and spin levels intersecting have been reported for inorganic and organometallic compounds showing BEC properties, but now is observed for the first time in a spin-1/2 AFM purely organic quantum magnet.

Those interesting experimental results, such as exotic quantum phases in the (B,T) phase diagram, along with a 1/2 magnetization plateau, motivated us to study NIT2Py theoretically with the help of state-of-the-art electronic structure calculations.

To attain this goal, we needed to apply a model Hamiltonian based on the Heisenberg spin exchanges because the magnetic exchange interactions between the magnetic moments of the free radical molecules are weak and hence, the energy levels are closely packed. In chapter 4, we evaluated all the possible pairwise interactions between the magnetic moments of the molecules for both the single cell and the supercell. Next, to find the independent interactions among all the possible interactions, we utilized the appropriate symmetry operators of NIT2Py according to the cell under study. Then, we created a general model Hamiltonian based on the 10 independent Heisenberg spin exchange interactions of the single cell, and another on the 22 independent interactions of the supercell. The summation of all the resulting independent pairwise interactions in the model Hamiltonian produced the magnetic energy levels of the NIT2Py system.

The next step was to evaluate the sign and magnitude of the independent exchange couplings of the NIT2Py system. We performed electronic structure calculation through density functional theory and broken-symmetry formalism. Also, we employed the supercell total energy differences mapping approach, in which the total energies of independent spin configurations evaluated from DFT calculations were mapped into the Ising energies established by the model Hamiltonian. By using the crystalline and spin reversal symmetries of our system, the equivalent configurations of a given configuration were found. By identifying the equivalent configurations, we can in turn also identify the independent spin configurations in the single cell and supercell. We then calculated the total energy of some of the independent spin configurations for the single cell and supercell. We evaluated the exchange couplings by a least-squares minimization of the difference between DFT and Ising relative energies of all the independent configurations. However some exchange couplings could still not be separated.

In order to circumvent this problem, larger supercells were needed. We introduced a new energy mapping method, namely the four-states energy mapping, along with different supercells to evaluate the exchange couplings separately. The resulting exchange couplings of the single cell and supercells found by using both the total energy difference and four-states approaches were in perfect agreement. Having used DFT calculations, broken-symmetry formalism, and the energy-mapping approach yielded the strongest exchange interactions, J_4, J_6 and J_9.

However, to properly interpret the magnetic properties of the NIT2Py system, we needed to design a magnetic lattice based on the minimal set of strong spin exchanges. A simple model can be proposed in which the minimal set of strong spin exchanges is only comprised of spin dimers with antiferromagnetic intradimer interaction J_4. We formulated a magnetization equation for interacting dimers based on the mean-field theory. Nevertheless, we showed that even by taking into account the interactions between those spin dimers by means of mean-field theory, the magnetic properties of NIT2Py such as 1/2 plateau magnetization cannot be reproduced. We had to return to the drawing board to consider a more complex model.

We came up with a spin tetramer model which consists of four spins with two antiferromagnetic exchange couplings, J_4 and J_9. We established a more relevant magnetic lattice for NIT2Py on the basis of a repeat pattern of those spin tetramers. By diagonalizing a 16×16 matrix interaction obtained by applying the spin Hamiltonian of a tetramer on the 16 different spin configurations, we obtained the eigenvalues of the two singlet states ($S = 0$), three triplet states ($S = 1$), and one quintuplet ($S = 2$) state. Subsequently, we derived an equation for the magnetization of a system of spin tetramers, and showed that a 1/2 magnetization plateau can result from this new model. However, the regions of the field dependence of the magnetization isotherms, which represent the regions with magnetic ordering, need to be improved in the model.

To ameliorate the new model so as to tune it with the experimental results in the slope regions of the magnetization as a function of applied field, we included the interactions between the tetramers by using the mean-field approximation. We showed that the magnetization curve measured at 0.5 K can be well reproduced by our model of interacting spin tetramers.

We realized that the magnetization isotherms as a function of applied field measured at higher temperatures, such as 1.43 K and 5 K, all have the same slope at lower applied fields. This characteristic is not observed in the model of interacting tetramers by mean-field approach. Thus, considering all the interactions in the system only by an approximation of mean-field approach is not fully satisfactory and a more complete approach is necessary to express the measured magnetizations at all range of temperatures.

To obtained a more complete insight of this quantum system, we needed to construct a Hamiltonian matrix of interacting tetramers and diagonalized it numerically. We carried out the exact diagonalization process for up to four interacting tetramers, and 16 spin sites. We obtained the magnetization of the system of four interacting tetramers through the exact diagonalization method and compared the results with those of the experimental data. The experimental results are well reproduced by calculated magnetization. However, in order to improve the model, the exact diagonalization method for a larger number of tetramers and spin sites is needed.

So, the two approaches, MF and ED with a small number of spin tetramers, were used to interpret the magnetization characteristics observed in NIT2Py. The MF approach can give some physical intuitions about the behavior of the system. Larger systems can be tackled with the MF approach as it is less demanding numerically as compared to the ED approach. In the magnetically ordered region as well as the high temperature range, both the MF and ED approaches work well. But, as we approach the phase transitions, the correlation length increases, and both MF and ED with a small number of unit cells fail.

The outcome of this research will be published in two main articles. The first one is dedicated to the analysis of the experimental findings related to the magnetization, susceptibility, specific heat, the magnetocaloric effect, and the corresponding phase diagram. The model of interacting tetramers using mean-field approximation and the exact diagonalization of the spin Hamiltonian of four tetramers developed in the research of this thesis will be employed to reproduce the experimental results observed for NIT2Py such as the magnetization and specific heat. The second article will focus on evaluating the dominant spin exchanges of the NIT2Py system by electronic structure calculations through DFT using the broken-symmetry and energy-mapping approaches. The total energy differences associated with a number of supercells are used to separate the dominant exchange interactions and to identify the prominent ones in the system. Based on those electronic structure considerations and the obtained strongest exchange interactions, an appropriate magnetic lattice consisting of antiferromagnetically interacting tetramers is proposed.

The organic molecular crystals condensed from free radicals with a magnetic moment have the potential to initiate a new generation of electronic materials, namely plastic electronic materials. Those organic molecular crystals provide us with the possibility of working with molecules rather than atoms to produce novel technology, such as building blocks for magnets and organic semiconductors. For the time being, however, physicists are a lot more interested in studying molecular crystals by free radicals in which exotic quantum phases can be observed upon driving the system close to quantum critical points. In those materials, the overlap of the wavefunctions of the molecules can be tuned by either changing their molecular structure through synthetic chemistry methods or by utilization of hydrostatic pressure. Consequently, the magnetic interactions in those organic molecule-based magnets can be changed, which will open the door to the discovery of new interesting properties. Those characteristics can not be seen in inorganic magnets.

As a final thought, it is fairly unusual to do extensive work both theoretically and experimentally in a doctorate research project. That is why I feel privileged to have had the chance to touch on both during my studies. I went more in depth into theory than I was initially expecting. Working with two different professors with varying expertise enriched my understanding of the subject as well as my PhD research.

Future works

Concerning the future steps in the theoretical study of the magnetic properties of NIT2Py, we need to undertake the challenge of dealing with a system of a larger number of spin sites. We need to construct the required many-body Hamiltonian matrix by increasing the number of interacting tetramers, and to tackle the diagonalization problem numerically. However, the exponential augmentation of the matrix size with the number of spins (2^N) makes this task very challenging. For a larger quantum systems, more complex computational methods are required. Furthermore, other numerical studies of the magnetism can be executed by applying quantum Monte Carlo (QMC) simulations for a larger but still finite number of interacting tetramers. With QMC, we can directly sample the expectation value of a quantity without trying to calculate the ground state and the excited states of the system.

BIBLIOGRAPHY

[1] J. S. Miller, “Organometallic- and organic-based magnets: New chemistry and new materials for the new millennium,” *Inorganic Chemistry*, vol. 39, no. 20, pp. 4392–4408, 2000. [Online]. Available: http://dx.doi.org/10.1021/ic000540x

[2] J. Veciana and D. Arcon, *Pi Electron Magnetism: From Molecules to Magnetic Materials*, ser. Pi -electron magnetism: from molecules to magnetic materials. Springer, 2001. [Online]. Available: https://books.google.ca/books?id=S7xeUNdp0Z8C

[3] C. Train, L. Norel, and M. Baumgarten, “Organic radicals, a promising route towards original molecule-based magnetic materials,” *Coordination Chemistry Reviews*, vol. 253, no. 19-20, pp. 2342 – 2351, 2009, deutsche Forschungsgemeinschaft Molecular Magnetism Research Report. [Online]. Available: http://www.sciencedirect.com/science/article/pii/S001085450800180X

[4] J. S. Miller, “Magnetically ordered molecule-based materials,” *Chem. Soc. Rev.*, vol. 40, pp. 3266–3296, 2011. [Online]. Available: http://dx.doi.org/10.1039/C0CS00166J

[5] K. Mukai, H. Nishiguchi, and Y. Deguchi, “Anomaly in the χ-T curve of galvinoxyl radical,” *Journal of the Physical Society of Japan*, vol. 23, no. 1, pp. 125–125, 1967. [Online]. Available: http://dx.doi.org/10.1143/JPSJ.23.125

[6] M. S. Paul and C. Veyret, “Ferromagnetic ordering in an organic compound: Di-(2,2,6,6-tetramethyl-4 piperidinol-1 oxyl) (tanol suberate),” *Physics Letters A*, vol. 45, no. 5, pp. 362 – 364, 1973. [Online]. Available: http://www.sciencedirect.com/science/article/pii/0375960173902387

[7] G. Chouteau and C. Veyret-Jeandey, “Metamagnetism in tanol suberate,” *Journal de Physique*, vol. 42, no. 10, pp. 1441–1444, 1981. [Online]. Available: https://hal.archives-ouvertes.fr/jpa-00209335

[8] P.-M. Allemand, K. C. Khemani, A. Koch, F. Wudl, K. Holczer, S. Donovan, G. Grüner, and J. D. Thompson, "Organic molecular soft ferromagnetism in a fullerene C_{60}," *Science*, vol. 253, no. 5017, pp. 301–302, 1991. [Online]. Available: http://science.sciencemag.org/content/253/5017/301

[9] M. Takahashi, P. Turek, Y. Nakazawa, M. Tamura, K. Nozawa, D. Shiomi, M. Ishikawa, and M. Kinoshita, "Discovery of a quasi-1D organic ferromagnet, p-NPNN," *Phys. Rev. Lett.*, vol. 67, pp. 746–748, Aug 1991. [Online]. Available: http://link.aps.org/doi/10.1103/PhysRevLett.67.746

[10] M. Tamura, Y. Nakazawa, D. Shiomi, K. Nozawa, Y. Hosokoshi, M. Ishikawa, M. Takahashi, and M. Kinoshita, "Bulk ferromagnetism in the β-phase crystal of the *p*-nitrophenyl nitronyl nitroxide radical," *Chemical Physics Letters*, vol. 186, no. 4, pp. 401 – 404, 1991. [Online]. Available: http://www.sciencedirect.com/science/article/pii/000926149190198I

[11] O. Kahn, *Molecular magnetism.* VCH, 1993. [Online]. Available: https://books.google.ca/books?id=QwzwAAAAMAAJ

[12] J. S. Miller and A. J. Epstein, "Organic and organometallic molecular magnetic materials—designer magnets," *Angewandte Chemie International Edition in English*, vol. 33, no. 4, pp. 385–415, 1994. [Online]. Available: http://dx.doi.org/10.1002/anie.199403851

[13] I. Ratera and J. Veciana, "Playing with organic radicals as building blocks for functional molecular materials," *Chem. Soc. Rev.*, vol. 41, pp. 303–349, 2012. [Online]. Available: http://dx.doi.org/10.1039/C1CS15165G

[14] P. Coleman and A. J. Schofield, "Quantum criticality," *Nature*, vol. 433, pp. 226 – 229, 2005. [Online]. Available: http://dx.doi.org/10.1038/nature03279

[15] T. Makarova and F. Palacio, *Carbon Based Magnetism: An Overview of the Magnetism of Metal Free Carbon-based Compounds and Materials.*

Elsevier Science, 2006. [Online]. Available: https://books.google.ca/books?id=Qj9R7Tr45tUC

[16] M. Mas-Torrent, N. Crivillers, V. Mugnaini, I. Ratera, C. Rovira, and J. Veciana, “Organic radicals on surfaces: towards molecular spintronics,” *J. Mater. Chem.*, vol. 19, pp. 1691–1695, 2009. [Online]. Available: http://dx.doi.org/10.1039/B809875A

[17] L. Bogani and W. Wernsdorfer, “Molecular spintronics using single-molecule magnets,” *Nat Mater*, vol. 7, no. 3, pp. 179–186, 03 2008. [Online]. Available: http://dx.doi.org/10.1038/nmat2133

[18] J. Camarero and E. Coronado, “Molecular vs. inorganic spintronics: the role of molecular materials and single molecules,” *J. Mater. Chem.*, vol. 19, pp. 1678–1684, 2009. [Online]. Available: http://dx.doi.org/10.1039/B819594N

[19] L. Bogani, C. Danieli, E. Biavardi, N. Bendiab, A.-L. Barra, E. Dalcanale, W. Wernsdorfer, and A. Cornia, “Single-molecule-magnet carbon-nanotube hybrids,” *Angewandte Chemie International Edition*, vol. 48, no. 4, pp. 746–750, 2009. [Online]. Available: http://dx.doi.org/10.1002/anie.200804967

[20] C. Chappert, A. Fert, and F. N. Van Dau, “The emergence of spin electronics in data storage,” *Nat Mater*, vol. 6, no. 11, pp. 813–823, 11 2007. [Online]. Available: http://dx.doi.org/10.1038/nmat2024

[21] J. Lee, E. Lee, S. Kim, G. S. Bang, D. A. Shultz, R. D. Schmidt, M. D. E. Forbes, and H. Lee, “Nitronyl nitroxide radicals as organic memory elements with both n- and p-type properties,” *Angewandte Chemie*, vol. 123, no. 19, pp. 4506–4510, 2011. [Online]. Available: http://dx.doi.org/10.1002/ange.201004899

[22] A. K. Pal, S. Hansda, S. N. Datta, and F. Illas, “Theoretical investigation of stilbene as photochromic spin coupler,” *The Journal of Physical Chemistry A*, vol. 117, no. 8, pp. 1773–1783, 2013, pMID: 23418791. [Online]. Available: http://dx.doi.org/10.1021/jp306715y

[23] T. Ishiguro, K. Yamaji, and G. Saitō, *Organic superconductors*, ser. Springer series in solid-state sciences. Springer, 1998. [Online]. Available: https://books.google.ca/books?id=yOk9AQAAIAAJ

[24] S. Uji, H. Shinagawa, T. Terashima, T. Yakabe, Y. Terai, M. Tokumoto, A. Kobayashi, H. Tanaka, and H. Kobayashi, "Magnetic-field-induced superconductivity in a two-dimensional organic conductor," *Nature*, vol. 410, no. 6831, pp. 908–910, 04 2001. [Online]. Available: http://dx.doi.org/10.1038/35073531

[25] S. J. Blundell and F. L. Pratt, "Organic and molecular magnets," *Journal of Physics: Condensed Matter*, vol. 16, no. 24, p. R771, 2004. [Online]. Available: http://stacks.iop.org/0953-8984/16/i=24/a=R03

[26] K. Mukai, "Anomalous magnetic properties of stable crystalline phenoxyl radicals," *Bull. Chem. Soc. Jpn*, vol. 42, no. 1, pp. 40–46, 1969. [Online]. Available: http://ci.nii.ac.jp/naid/130001978675/en/

[27] K. Awaga, T. Sugano, and M. Kinoshita, "Ferromagnetic intermolecular interactions in a series of organic mixed crystals of galvinoxyl radical and its precursory closed shell compound," *The Journal of Chemical Physics*, vol. 85, no. 4, pp. 2211–2218, 1986. [Online]. Available: http://scitation.aip.org/content/aip/journal/jcp/85/4/10.1063/1.451115

[28] T. Brückel and F. J. I. für Festkörperforschung, *Neutron Scattering: Lectures of the JCNS Laboratory Course Held at Forschungszentrum Jülich and the Research Reactor FRM II of TU Munich*, ser. Schriften des Forschungszentrums Jülich / Materie und Material: Materie und Material. Forschungszentrum Jülich, Zentralbibliothek, 2007. [Online]. Available: https://books.google.ca/books?id=crbSV2i40x4C

[29] J. Veciana, J. Cirujeda, C. Rovira, and J. Vidal-Gancedo, "Ferromagnetic interactions in organic/molecular materials," *Advanced Materials*, vol. 7,

no. 2, pp. 221–225, 1995. [Online]. Available: http://dx.doi.org/10.1002/adma.19950070227

[30] S. o. m. Nakatsuji and H. Anzai, "Recent progress in the development of organomagnetic materials based on neutral nitroxide radicals and charge transfer complexes derived from nitroxide radicals," *J. Mater. Chem.*, vol. 7, pp. 2161–2174, 1997. [Online]. Available: http://dx.doi.org/10.1039/A702177A

[31] K. Inoue, T. Hayamizu, H. Iwamura, D. Hashizume, and Y. Ohashi, "Assemblage and alignment of the spins of the organic trinitroxide radical with a quartet ground state by means of complexation with magnetic metal ions. a molecule-based magnet with three-dimensional structure and high T_c of 46 k," *Journal of the American Chemical Society*, vol. 118, no. 7, pp. 1803–1804, 1996. [Online]. Available: http://pubs.acs.org/doi/abs/10.1021/ja952301s

[32] K. Takeda and K. Awaga, "Magnetic properties of $(m-\mathrm{MPYNN}^{+})\,[\mathrm{M}n_{12}\mathrm{O}_{12}(\mathrm{O}_2\mathrm{CP}h)_{16}(\mathrm{H}_2\mathrm{O})_4]^{-}$: Enhancement of magnetic relaxation in the mn_{12} cluster caused by the organic radical," *Phys. Rev. B*, vol. 56, pp. 14 560–14 565, Dec 1997. [Online]. Available: http://link.aps.org/doi/10.1103/PhysRevB.56.14560

[33] F. M. Romero, R. Ziessel, M. Bonnet, Y. Pontillon, E. Ressouche, J. Schweizer, B. Delley, A. Grand, and C. Paulsen, "Evidence for transmission of ferromagnetic interactions through hydrogen bonds in alkyne-substituted nitroxide radicals: Magnetostructural correlations and polarized neutron diffraction studies," *Journal of the American Chemical Society*, vol. 122, no. 7, pp. 1298–1309, 2000. [Online]. Available: http://pubs.acs.org/doi/abs/10.1021/ja992673r

[34] J. S. Miller and M. Drillon, Eds., *Magnetism: Molecules to Materials IV*. Wiley-VCH, 2002, vol. IV. [Online]. Available: http://onlinelibrary.wiley.com/book/10.1002/3527600698

[35] C. Hirel, D. Luneau, J. Pécaut, L. Öhrström, G. Bussière, and C. Reber, "The

cyano nitronyl nitroxide radical: Experimental and theoretical evidence for the fourth case of the McConnell-I mechanism," *Chemistry – A European Journal*, vol. 8, no. 14, pp. 3157–3161, 2002. [Online]. Available: http://dx.doi.org/10.1002/1521-3765(20020715)8:14<3157::AID-CHEM3157>3.0.CO;2-F

[36] F. L. de Panthou, D. Luneau, J. Laugier, and P. Rey, "Crystal structures and magnetic properties of a nitronyl nitroxide and of its imino analog. crystal packing and spin distribution dependence of ferromagnetic intermolecular interactions," *Journal of the American Chemical Society*, vol. 115, no. 20, pp. 9095–9100, 1993. [Online]. Available: http://dx.doi.org/10.1021/ja00073a027

[37] Y. Hosokoshi, K. Katoh, Y. Nakazawa, H. Nakano, and K. Inoue, "Approach to a single-component ferrimagnetism by organic radical crystals," *Journal of the American Chemical Society*, vol. 123, no. 32, pp. 7921–7922, 2001, pMID: 11493072. [Online]. Available: http://dx.doi.org/10.1021/ja015711r

[38] Y. Nakazawa, M. Tamura, N. Shirakawa, D. Shiomi, M. Takahashi, M. Kinoshita, and M. Ishikawa, "Low-temperature magnetic properties of the ferromagnetic organic radical, *p*-nitrophenyl nitronyl nitroxide," *Phys. Rev. B*, vol. 46, pp. 8906–8914, Oct 1992. [Online]. Available: http://link.aps.org/doi/10.1103/PhysRevB.46.8906

[39] S. Krämer, R. Stern, M. Horvatić, C. Berthier, T. Kimura, and I. R. Fisher, "Nuclear magnetic resonance evidence for a strong modulation of the bose-einstein condensate in $BaCuSi_2O_6$," *Phys. Rev. B*, vol. 76, p. 100406, Sep 2007. [Online]. Available: http://link.aps.org/doi/10.1103/PhysRevB.76.100406

[40] A. A. Aczel, Y. Kohama, C. Marcenat, F. Weickert, M. Jaime, O. E. Ayala-Valenzuela, R. D. McDonald, S. D. Selesnic, H. A. Dabkowska, and G. M. Luke, "Field-induced bose-einstein condensation of triplons up to 8 K in $Sr_3Cr_2O_8$," *Phys. Rev. Lett.*, vol. 103, p. 207203, Nov 2009. [Online]. Available: http://link.aps.org/doi/10.1103/PhysRevLett.103.207203

[41] T. Zenmoto, Y. Oshima, H. Nojiri, S. H. Lee, and M. Kofu, "High magnetic field micro-calorimeter and application for be-condensation of Cr5+ dimer system," *Journal of Low Temperature Physics*, vol. 159, no. 1, pp. 118–121, 2010. [Online]. Available: http://dx.doi.org/10.1007/s10909-009-0087-5

[42] S. A. Zvyagin, J. Wosnitza, C. D. Batista, M. Tsukamoto, N. Kawashima, J. Krzystek, V. S. Zapf, M. Jaime, N. F. Oliveira, and A. Paduan-Filho, "Magnetic excitations in the spin-1 anisotropic heisenberg antiferromagnetic chain system $\mathrm{NiCl_2-4SC(NH_2)_2}$," *Phys. Rev. Lett.*, vol. 98, p. 047205, Jan 2007. [Online]. Available: http://link.aps.org/doi/10.1103/PhysRevLett.98.047205

[43] L. Yin, J. S. Xia, V. S. Zapf, N. S. Sullivan, and A. Paduan-Filho, "Direct measurement of the bose-einstein condensation universality class in $\mathrm{NiCl_2-4SC(NH_2)_2}$ at ultralow temperatures," *Phys. Rev. Lett.*, vol. 101, p. 187205, Oct 2008. [Online]. Available: http://link.aps.org/doi/10.1103/PhysRevLett.101.187205

[44] V. N. Glazkov, T. S. Yankova, J. Sichelschmidt, D. Hüvonen, and A. Zheludev, "Electron spin resonance study of anisotropic interactions in a two-dimensional spin-gap magnet $\mathrm{(C_4H_{12}N_2)(Cu_2Cl_6)}$," *Phys. Rev. B*, vol. 85, p. 054415, Feb 2012. [Online]. Available: http://link.aps.org/doi/10.1103/PhysRevB.85.054415

[45] Y. Hosokoshi, Y. Nakazawa, K. Inoue, K. Takizawa, H. Nakano, M. Takahashi, and T. Goto, "Magnetic properties of low-dimensional quantum spin systems made of stable organic biradicals pnnno, $\mathrm{F_2PNNNO}$ and pimno," *Phys. Rev. B*, vol. 60, pp. 12 924–12 932, Nov 1999. [Online]. Available: http://link.aps.org/doi/10.1103/PhysRevB.60.12924

[46] I. Bostrem, V. Sinitsyn, A. Ovchinnikov, Y. Hosokoshi, and K. Inoue, "Bose-einstein condensation of semi-hard bosons in the S = 1 dimerized organic compound $\mathrm{F_2PNNNO}$," *Journal of Physics Condensed Matter*, vol. 22, no. 3, 2010. [Online]. Available: https://www.scopus.com/inward/record.uri?eid=2-s2.0-73849111924&partnerID=40&md5=901bf28dae95dd8d441952913ad7605d

[47] G. Radtke, C. Maunders, A. Saúl, S. Lazar, H. J. Whitfield, J. Etheridge, and G. A. Botton, “Electronic structure and stability of hexagonal $Ba_3Ti_2RuO_9$,” *Phys. Rev. B*, vol. 81, p. 085112, Feb 2010. [Online]. Available: http://link.aps.org/doi/10.1103/PhysRevB.81.085112

[48] A. Saúl and G. Radtke, “Magnetic couplings in CsV_2O_5: A new picture,” *Phys. Rev. Lett.*, vol. 106, p. 177203, Apr 2011. [Online]. Available: http://link.aps.org/doi/10.1103/PhysRevLett.106.177203

[49] A. Saúl, D. Vodenicarevic, and G. Radtke, “Theoretical study of the magnetic order in $\alpha - CoV_2O_6$,” *Phys. Rev. B*, vol. 87, p. 024403, Jan 2013. [Online]. Available: http://link.aps.org/doi/10.1103/PhysRevB.87.024403

[50] G. Radtke, A. Saúl, Y. Klein, and G. Rousse, “Magnetism of $Ba_4Ru_3O_{10}$ revealed by density functional calculations: Structural trimers behaving as coupled magnetic dimers,” *Phys. Rev. B*, vol. 87, p. 054436, Feb 2013. [Online]. Available: http://link.aps.org/doi/10.1103/PhysRevB.87.054436

[51] A. Saúl and G. Radtke, “Density functional approach for the magnetism of $\beta - TeVO_4$,” *Phys. Rev. B*, vol. 89, p. 104414, Mar 2014. [Online]. Available: http://link.aps.org/doi/10.1103/PhysRevB.89.104414

[52] X. Gonze, F. Jollet, F. A. Araujo, D. Adams, B. Amadon, T. Applencourt, C. Audouze, J.-M. Beuken, J. Bieder, A. Bokhanchuk, E. Bousquet, F. Bruneval, D. Caliste, M. Côté, F. Dahm, F. D. Pieve, M. Delaveau, M. D. Gennaro, B. Dorado, C. Espejo, G. Geneste, L. Genovese, A. Gerossier, M. Giantomassi, Y. Gillet, D. Hamann, L. He, G. Jomard, J. L. Janssen, S. L. Roux, A. Levitt, A. Lherbier, F. Liu, I. Lukačević, A. Martin, C. Martins, M. Oliveira, S. Poncé, Y. Pouillon, T. Rangel, G.-M. Rignanese, A. Romero, B. Rousseau, O. Rubel, A. Shukri, M. Stankovski, M. Torrent, M. V. Setten, B. V. Troeye, M. Verstraete, D. Waroquiers, J. Wiktor, B. Xu, A. Zhou, and J. Zwanziger, “Recent developments in the {ABINIT} software package,” *Computer Physics*

Communications, vol. 205, pp. 106 – 131, 2016. [Online]. Available: http://www.sciencedirect.com/science/article/pii/S0010465516300923

[53] P. Giannozzi, S. Baroni, N. Bonini, M. Calandra, R. Car, C. Cavazzoni, D. Ceresoli, G. L. Chiarotti, M. Cococcioni, I. Dabo, A. D. Corso, S. de Gironcoli, S. Fabris, G. Fratesi, R. Gebauer, U. Gerstmann, C. Gougoussis, A. Kokalj, M. Lazzeri, L. Martin-Samos, N. Marzari, F. Mauri, R. Mazzarello, S. Paolini, A. Pasquarello, L. Paulatto, C. Sbraccia, S. Scandolo, G. Sclauzero, A. P. Seitsonen, A. Smogunov, P. Umari, and R. M. Wentzcovitch, "Quantum espresso: a modular and open-source software project for quantum simulations of materials," *Journal of Physics: Condensed Matter*, vol. 21, no. 39, p. 395502, 2009. [Online]. Available: http://stacks.iop.org/0953-8984/21/i=39/a=395502

[54] J. C. Maxwell, "A dynamical theory of the electromagnetic field," *Philosophical Transactions of the Royal Society of London*, vol. 155, pp. 459–512, 01 1865. [Online]. Available: http://rstl.royalsocietypublishing.org/content/155/459.short

[55] N. Ashcroft and N. Mermin, *Solid state physics*, ser. Science: Physics. Saunders College, 1976. [Online]. Available: https://books.google.ca/books?id=FRZRAAAAMAAJ

[56] S. Blundell, *Magnetism in Condensed Matter (Oxford Master Series in Physics)*. Oxford University Press, USA, 12 2001.

[57] R. Skomski, *Simple Models of Magnetism*, ser. Oxford Graduate Texts. OUP Oxford, 2008. [Online]. Available: https://books.google.ca/books?id=O1EZg2Gd1LEC

[58] W. Heitler and F. London, ""wechselwirkung neutraler atome und homöopolare bindung nach der quantenmechanik," *Zeitschrift für Physik A*, vol. 44, pp. 455–472, 1927.

[59] W. Heisenberg, "Mehrkörperproblem und resonanz in der quantenmechanik,"

Zeitschrift für Physik, vol. 38, no. 6, pp. 411–426, 1926. [Online]. Available: http://dx.doi.org/10.1007/BF01397160

[60] P. A. M. Dirac, "On the theory of quantum mechanics," *Proceedings of the Royal Society of London A: Mathematical, Physical and Engineering Sciences*, vol. 112, no. 762, pp. 661–677, 1926. [Online]. Available: http://rspa.royalsocietypublishing.org/content/112/762/661

[61] J. Van Vleck, *The theory of electric and magnetic susceptibilities*, ser. International series of monographs on physics. Oxford University Press, 1952. [Online]. Available: https://books.google.ca/books?id=JL1UAAAAYAAJ

[62] H. Xiang, C. Lee, H.-J. Koo, X. Gong, and M.-H. Whangbo, "Magnetic properties and energy-mapping analysis," *Dalton Trans.*, vol. 42, pp. 823–853, 2013. [Online]. Available: http://dx.doi.org/10.1039/C2DT31662E

[63] C. Cohen-Tannoudji, B. Diu, F. Laloe, and B. Dui, *Quantum Mechanics (2 vol. set)*. Wiley-Interscience, Oct. 2006. [Online]. Available: http://www.amazon.com/exec/obidos/redirect?tag=citeulike07-20&path=ASIN/0471569526

[64] O. Kahn, *Molecular magnetism.* VCH, 1993. [Online]. Available: https://books.google.ca/books?id=QwzwAAAAMAAJ

[65] J. E. Greedan, "Geometrically frustrated magnetic materials," *J. Mater. Chem.*, vol. 11, pp. 37–53, 2001. [Online]. Available: http://dx.doi.org/10.1039/B003682J

[66] J. A. Hodges, P. Bonville, M. Rams, and K. Królas, "Low-temperature spin fluctuations in geometrically frustrated $Yb_3Ga_5O_{12}$," *Journal of Physics: Condensed Matter*, vol. 15, no. 26, p. 4631, 2003. [Online]. Available: http://stacks.iop.org/0953-8984/15/i=26/a=313

[67] P. Debye, "Zur theorie der spezifischen wärmen," *Annalen der Physik*, vol. 344, no. 14, pp. 789–839, 1912. [Online]. Available: http://dx.doi.org/10.1002/andp.19123441404

[68] M. Marder, *Condensed Matter Physics*. Wiley, 2010. [Online]. Available: https://books.google.ca/books?id=ijloadAt4BQC

[69] H. Kageyama, K. Yoshimura, R. Stern, N. V. Mushnikov, K. Onizuka, M. Kato, K. Kosuge, C. P. Slichter, T. Goto, and Y. Ueda, “Exact dimer ground state and quantized magnetization plateaus in the two-dimensional spin system $\mathrm{SrCu_2(BO_3)_2}$,” *Phys. Rev. Lett.*, vol. 82, pp. 3168–3171, Apr 1999. [Online]. Available: http://link.aps.org/doi/10.1103/PhysRevLett.82.3168

[70] K. Kodama, M. Takigawa, M. Horvatić, C. Berthier, H. Kageyama, Y. Ueda, S. Miyahara, F. Becca, and F. Mila, “Magnetic superstructure in the two-dimensional quantum antiferromagnet $\mathrm{SrCu_2(BO_3)_2}$,” *Science*, vol. 298, no. 5592, pp. 395–399, 2002. [Online]. Available: http://science.sciencemag.org/content/298/5592/395

[71] S. E. Sebastian, N. Harrison, P. Sengupta, C. D. Batista, S. Francoual, E. Palm, T. Murphy, N. Marcano, H. A. Dabkowska, and B. D. Gaulin, “Fractalization drives crystalline states in a frustrated spin system,” *Proceedings of the National Academy of Sciences*, vol. 105, no. 51, pp. 20 157–20 160, 2008. [Online]. Available: http://www.pnas.org/content/105/51/20157.abstract

[72] M. Sigrist, “Statistical physics,” ETH Zurich, lecturenotes 139, 2013. [Online]. Available: http://edu.itp.phys.ethz.ch/hs13/StatPhys/Lecture-Notes.pdf

[73] V. Zapf, M. Jaime, and C. D. Batista, “Bose-einstein condensation in quantum magnets,” *Rev. Mod. Phys.*, vol. 86, pp. 563–614, May 2014. [Online]. Available: http://link.aps.org/doi/10.1103/RevModPhys.86.563

[74] T. Giamarchi, C. Ruegg, and O. Tchernyshyov, “Bose-einstein condensation in magnetic insulators,” *Nat Phys*, vol. 4, no. 3, pp. 198–204, 03 2008. [Online]. Available: http://dx.doi.org/10.1038/nphys893

[75] H. Tanaka, A. Oosawa, T. Kato, H. Uekusa, Y. Ohashi, K. Kakurai, and A. Hoser, “Observation of field-induced transverse néel ordering in the spin gap system

$TlCuCl_3$," *Journal of the Physical Society of Japan*, vol. 70, no. 4, pp. 939–942, 2001. [Online]. Available: http://dx.doi.org/10.1143/JPSJ.70.939

[76] A. Oosawa, T. Kato, H. Tanaka, K. Kakurai, M. Müller, and H.-J. Mikeska, "Magnetic excitations in the spin-gap system $TlCuCl_3$," *Phys. Rev. B*, vol. 65, p. 094426, Feb 2002. [Online]. Available: http://link.aps.org/doi/10.1103/PhysRevB.65.094426

[77] F. Yamada, T. Ono, M. Fujisawa, H. Tanaka, and T. Sakakibara, "Magnetic-field induced quantum phase transition and critical behavior in a gapped spin system," *Journal of Magnetism and Magnetic Materials*, vol. 310, no. 2, Part 2, pp. 1352 – 1354, 2007, proceedings of the 17th International Conference on MagnetismThe International Conference on Magnetism. [Online]. Available: http://www.sciencedirect.com/science/article/pii/S0304885306015824

[78] M. Jaime, V. F. Correa, N. Harrison, C. D. Batista, N. Kawashima, Y. Kazuma, G. A. Jorge, R. Stern, I. Heinmaa, S. A. Zvyagin, Y. Sasago, and K. Uchinokura, "Magnetic-field-induced condensation of triplons in han purple pigment $BaCuSi_2O_6$," *Phys. Rev. Lett.*, vol. 93, p. 087203, Aug 2004. [Online]. Available: http://link.aps.org/doi/10.1103/PhysRevLett.93.087203

[79] S. E. Sebastian, P. A. Sharma, M. Jaime, N. Harrison, V. Correa, L. Balicas, N. Kawashima, C. D. Batista, and I. R. Fisher, "Characteristic bose-einstein condensation scaling close to a quantum critical point in $BaCuSi_2O_6$," *Phys. Rev. B*, vol. 72, p. 100404, Sep 2005. [Online]. Available: http://link.aps.org/doi/10.1103/PhysRevB.72.100404

[80] C. Rüegg, D. F. McMorrow, B. Normand, H. M. Rønnow, S. E. Sebastian, I. R. Fisher, C. D. Batista, S. N. Gvasaliya, C. Niedermayer, and J. Stahn, "Multiple magnon modes and consequences for the bose-einstein condensed phase in $BaCuSi_2O_6$," *Phys. Rev. Lett.*, vol. 98, p. 017202, Jan 2007. [Online]. Available: http://link.aps.org/doi/10.1103/PhysRevLett.98.017202

[81] A. W. Sandvik, “Computational studies of quantum spin systems,” *AIP Conference Proceedings*, vol. 1297, no. 1, pp. 135–338, 2010. [Online]. Available: http://scitation.aip.org/content/aip/proceeding/aipcp/10.1063/1.3518900

[82] W. von der Linden, “Numerical many body physics,” Graz University of Technology, Institute of Theoretical and Computational Physics, lecturenotes 23, 2010. [Online]. Available: https://itp.tugraz.at/~evertz/CP/CP_mbook.pdf

[83] M. H. Anderson, J. R. Ensher, M. R. Matthews, C. E. Wieman, and E. A. Cornell, “Observation of bose-einstein condensation in a dilute atomic vapor,” *Science*, vol. 269, no. 5221, pp. 198–201, 1995. [Online]. Available: http://science.sciencemag.org/content/269/5221/198

[84] T. Matsubara and H. Matsuda, “A lattice model of liquid helium, I,” *Progress of Theoretical Physics*, vol. 16, no. 6, pp. 569–582, 1956. [Online]. Available: http://ptp.oxfordjournals.org/content/16/6/569.abstract

[85] S. Streib and P. Kopietz, “Hard-core boson approach to the spin $-\frac{1}{2}$ triangular-lattice antiferromagnet Cs_2CuCl_4 at finite temperatures in magnetic fields higher than the saturation field,” *Phys. Rev. B*, vol. 92, p. 094442, Sep 2015. [Online]. Available: http://link.aps.org/doi/10.1103/PhysRevB.92.094442

[86] K. Bernardet, G. G. Batrouni, J.-L. Meunier, G. Schmid, M. Troyer, and A. Dorneich, “Analytical and numerical study of hardcore bosons in two dimensions,” *Phys. Rev. B*, vol. 65, p. 104519, Feb 2002. [Online]. Available: http://link.aps.org/doi/10.1103/PhysRevB.65.104519

[87] T. Radu, H. Wilhelm, V. Yushankhai, D. Kovrizhin, R. Coldea, Z. Tylczynski, T. Lühmann, and F. Steglich, “Bose-einstein condensation of magnons in Cs_2CuCl_4,” *Phys. Rev. Lett.*, vol. 95, p. 127202, Sep 2005. [Online]. Available: http://link.aps.org/doi/10.1103/PhysRevLett.95.127202

[88] R. Parr and W. Yang, *Density-Functional Theory of Atoms and Molecules*, ser. International Series of Monographs on Chemistry. Oxford University

Press, USA, 1994. [Online]. Available: https://books.google.ca/books?id=mxiOngEACAAJ

[89] K. Capelle, “A bird’s-eye view of density-functional theory,” *Brazilian Journal of Physics*, vol. 36, no. 4a, pp. 1318–1343, 2006. [Online]. Available: http://www.scielo.br/scielo.php?pid=S0103-97332006000700035&script=sci_arttext&tlng=en

[90] K. Burke. (2007) The abc of dft. [Online]. Available: http://dft.uci.edu/doc/g1.pdf

[91] G. Radtke, A. Saúl, H. A. Dabkowska, G. M. Luke, and G. A. Botton, “Interplay between structural, electronic, and magnetic degrees of freedom in $Sr_3Cr_2O_8$,” *Phys. Rev. Lett.*, vol. 105, p. 036401, Jul 2010. [Online]. Available: http://link.aps.org/doi/10.1103/PhysRevLett.105.036401

[92] G. Radtke, A. Saúl, Y. Klein, and G. Rousse, “Magnetism of $Ba_4Ru_3O_{10}$ revealed by density functional calculations: Structural trimers behaving as coupled magnetic dimers,” *Phys. Rev. B*, vol. 87, p. 054436, Feb 2013. [Online]. Available: http://link.aps.org/doi/10.1103/PhysRevB.87.054436

[93] H. J. Xiang, E. J. Kan, S.-H. Wei, M.-H. Whangbo, and X. G. Gong, “Predicting the spin-lattice order of frustrated systems from first principles,” *Phys. Rev. B*, vol. 84, p. 224429, Dec 2011. [Online]. Available: http://link.aps.org/doi/10.1103/PhysRevB.84.224429

[94] U. Rössler, *Solid State Theory: An Introduction*. Springer Berlin Heidelberg, 2009. [Online]. Available: https://books.google.ca/books?id=qRsH7TWDjYEC

[95] M. Roy, “The n-electron wavefunction,” University of Leicester, lecturenotes 18, 2015. [Online]. Available: https://www2.le.ac.uk/departments/physics/people/mervynroy/lectures/pa4311/quantum-chemistry-summary.pdf

[96] P. Hohenberg and W. Kohn, “Inhomogeneous electron gas,” *Phys. Rev.*, vol. 136, pp. B864–B871, Nov 1964. [Online]. Available: http://link.aps.org/doi/10.1103/PhysRev.136.B864

[97] W. Kohn and L. J. Sham, “Self-consistent equations including exchange and correlation effects,” *Phys. Rev.*, vol. 140, pp. A1133–A1138, Nov 1965. [Online]. Available: http://link.aps.org/doi/10.1103/PhysRev.140.A1133

[98] W. Kohn, “Nobel lecture: Electronic structure of matter-wave functions and density functionals,” *Rev. Mod. Phys.*, vol. 71, pp. 1253–1266, Oct 1999. [Online]. Available: http://link.aps.org/doi/10.1103/RevModPhys.71.1253

[99] R. M. Dreizler and E. K. U. Gross, *Density functional theory: an approach to the quantum many-body problem*. Berlin: Springer, 1990. [Online]. Available: http://www.bibsonomy.org/bibtex/208d1c12d91ec41d2f44679bb01af1f5f/pbuczek

[100] D. M. Ceperley and B. J. Alder, “Ground state of the electron gas by a stochastic method,” *Phys. Rev. Lett.*, vol. 45, pp. 566–569, Aug 1980. [Online]. Available: http://link.aps.org/doi/10.1103/PhysRevLett.45.566

[101] J. P. Perdew and W. Yue, “Accurate and simple density functional for the electronic exchange energy: Generalized gradient approximation,” *Phys. Rev. B*, vol. 33, pp. 8800–8802, Jun 1986. [Online]. Available: http://link.aps.org/doi/10.1103/PhysRevB.33.8800

[102] J. P. Perdew, K. Burke, and M. Ernzerhof, “Generalized gradient approximation made simple,” *Phys. Rev. Lett.*, vol. 77, pp. 3865–3868, Oct 1996. [Online]. Available: http://link.aps.org/doi/10.1103/PhysRevLett.77.3865

[103] P. E. Blöchl, “Projector augmented-wave method,” *Phys. Rev. B*, vol. 50, pp. 17 953–17 979, Dec 1994. [Online]. Available: http://link.aps.org/doi/10.1103/PhysRevB.50.17953

[104] X. G. S. Botti, *Practical session IX ABINIT lectures*, ETSF Rhone-Alpes Associated Node, September 2004. [Online]. Available: https://www.hitpages.com/doc/4892643301523456/1

[105] H. J. Monkhorst and J. D. Pack, "Special points for brillouin-zone integrations," *Phys. Rev. B*, vol. 13, pp. 5188–5192, Jun 1976. [Online]. Available: http://link.aps.org/doi/10.1103/PhysRevB.13.5188

[106] M. Giantomassi, *Density Functional Theory in the ABINIT code*, ETSF, fnrs, Lyon, France, 2014. [Online]. Available: https://abinit14.sciencesconf.org/data/program/Lecture_May12_Giantomassi_pwbase_1.pdf

[107] D. R. Hamann, M. Schlüter, and C. Chiang, "Norm-conserving pseudopotentials," *Phys. Rev. Lett.*, vol. 43, pp. 1494–1497, Nov 1979. [Online]. Available: http://link.aps.org/doi/10.1103/PhysRevLett.43.1494

[108] [Online]. Available: http://www.abinit.org/downloads/psp-links

[109] L. Noodleman, "Valence bond description of antiferromagnetic coupling in transition metal dimers," *The Journal of Chemical Physics*, vol. 74, no. 10, pp. 5737–5743, 1981. [Online]. Available: http://scitation.aip.org/content/aip/journal/jcp/74/10/10.1063/1.440939

[110] V. Barone, A. GRAND, D. LUNEAU, P. REY, C. MINICHINO, and R. SUBRA, "Ab-initio study of ullmans nitroxide biradicals, exchange coupling versus structural characteristics analysis," *NEW JOURNAL OF CHEMISTRY*, vol. 17, pp. 545–549, 1993.

[111] G. A. Bain and J. F. Berry, "Diamagnetic corrections and pascal's constants," *Journal of Chemical Education*, vol. 85, no. 4, p. 532, 2008. [Online]. Available: http://dx.doi.org/10.1021/ed085p532

[112] W. Schnelle, J. Engelhardt, and E. Gmelin, "Specific heat capacity of apiezon N high vacuum grease and of duran borosilicate glass," *Cryogenics*, vol. 39, no. 3, pp. 271 – 275, 1999. [Online]. Available: http://www.sciencedirect.com/science/article/pii/S0011227599000351

[113] T. Giamarchi and A. M. Tsvelik, "Coupled ladders in a magnetic field," *Phys. Rev. B*, vol. 59, pp. 11 398–11 407, May 1999. [Online]. Available: http://link.aps.org/doi/10.1103/PhysRevB.59.11398

[114] O. Nohadani, S. Wessel, B. Normand, and S. Haas, "Universal scaling at field-induced magnetic phase transitions," *Phys. Rev. B*, vol. 69, p. 220402, Jun 2004. [Online]. Available: http://link.aps.org/doi/10.1103/PhysRevB.69.220402

[115] [Online]. Available: http://www.abinit.org/

[116] [Online]. Available: http://www.quantum-espresso.org/pseudopotentials/

[117] J. Kang, C. Lee, R. K. Kremer, and M.-H. Whangbo, "Consequences of the intrachain dimer-monomer spin frustration and the interchain dimer-monomer spin exchange in the diamond-chain compound azurite $Cu_3(CO_3)_2(OH)_2$," *Journal of Physics: Condensed Matter*, vol. 21, no. 39, p. 392201, 2009. [Online]. Available: http://stacks.iop.org/0953-8984/21/i=39/a=392201

[118] H.-J. Koo and M.-H. Whangbo, "Finite magnetization plateau from a two-dimensional antiferromagnet: Density functional analysis of the magnetic structure of $Cu_3(P_2O_6OH)_2$," *Inorganic Chemistry*, vol. 49, no. 20, pp. 9253–9256, 2010, pMID: 20853894. [Online]. Available: http://dx.doi.org/10.1021/ic100906s

[119] F. Wu, E. Kan, and M.-H. Whangbo, "On the importance of the interplaquette spin exchanges in Na_3RuO_4: Density functional theory analysis of the spin exchange and magnetic properties," *Inorganic Chemistry*, vol. 49, no. 6, pp. 3025–3028, 2010, pMID: 20146425. [Online]. Available: http://dx.doi.org/10.1021/ic902568v

[120] F. O. Kannemann and A. D. Becke, "Van der waals interactions in density-functional theory: Rare-gas diatomics," *Journal of Chemical Theory and Computation*, vol. 5, no. 4, pp. 719–727, 2009, pMID: 26609577. [Online]. Available: http://dx.doi.org/10.1021/ct800522r

Appendix I

Synthesis and recrystallization of NIT2Py

I.1 Synthesis of NIT2Py

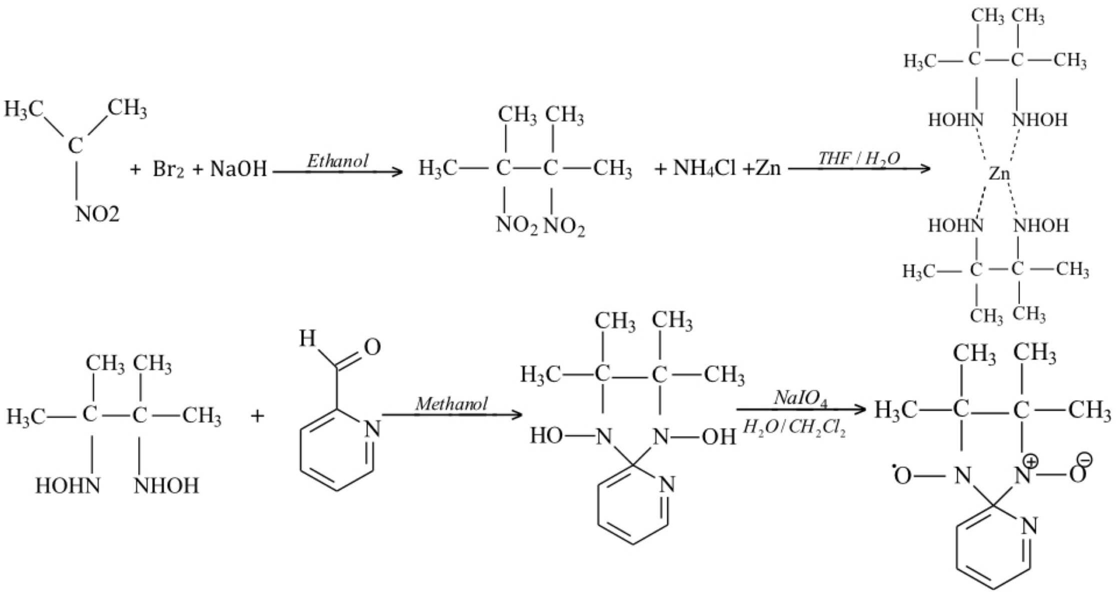

Figure I.1 – Schematic of the NIT2Py synthesis

I.2 X-ray results

A summary of the X-ray results of the α and β phases are given in Table. I.I.

I.3 Recrystallization of NIT2Py

Solvents such as methanol, ethanol, THF (tetrahydrofuran), dichloromethane, chloroform, and ethyl acetate, or solvent mixtures, can be used to make a saturation solution for NIT2Py. By using the slow evaporation method, different solvent mixtures were examined to identify the best mixture for elongating the crystallization process and provid-

Crystal Phase	α	β
Chemical formula	$C_{12}H_{16}N_3O_2$	$C_{12}H_{16}N_3O_2$
Crystal structure	Monoclinic	Monoclinic
Space group	$P2_{1/c}$	$P2_{1/c}$
Molecular weight (g/mol)	234.28	234.28
Lattice parameters (Å)	a=6.1471(2) b=30.061(1) c=12.9583(4)	a=6.2696(2) b=40.325(2) c=9.8488(3)
Angles (°)	α=90.00 β=100.269(2) γ=90.00	α= 90.00 β= 99.464(2) γ= 90.00
Z	8	8
Volume (Å^3)	2356.1(2)	2456.1(2)
R	0.0638	0.0523
Temperature (K)	150(2)	298(2)

Table I.I – X-ray results of the α and β phases are compared.

ing larger single crystals, and a mixture of dichloromethane and heptanes outperformed its rivals.

To recrystallize NIT2Py, we put the NIT2Py sample in a beaker, added about 15 ml of heptane to the sample, and then added dichloromethane drop by drop to observe the mixture becoming increasingly purple. The mixture was saturated after having added about 5 ml of dichloromethane. Next, we use a water bath to maintain the temperature of the solution at 30 C°. We attached the beaker to a motor that rotated it inside the bath and tested different rotation modes, such as constant rotation in one direction, and alternating clockwise and anticlockwise rotations. The beaker was sealed with a cap having a minute hole to ensure a very slow evaporation rate of the dichloromethane. Once the dichloromethane had completely evaporated, we observed that needle-shaped crystals had formed in the beaker, as shown in the Fig. I.2(a). We subsequently kept the beaker in the fume hood until all of the heptane had evaporated and the needle-shaped crystals were dry, as shown in Fig. I.2(b). The next time we attempted recrystallized NIT2Py, we used a couple of single crystals from the previous sample as seeds to grow

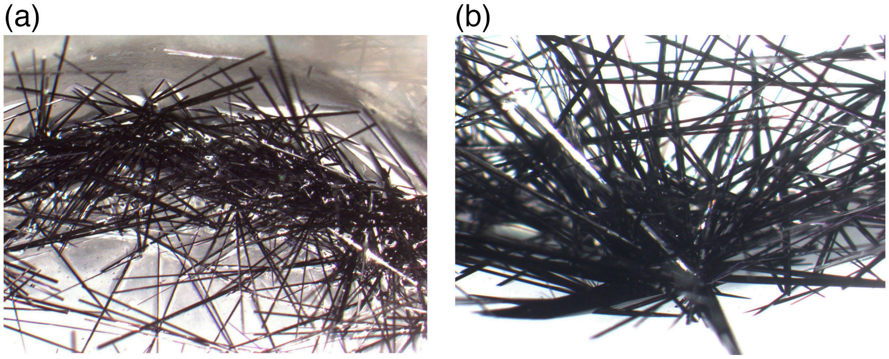

Figure I.2 – NIT2Py recrystallization carried out by means of the slow evaporation method with a solvent mixture composed of 15 ml of heptane and 5 ml of dichloromethane, and a constant temperature of 30 C°. The resulting needle-shaped crystals of NIT2Py are shown (a) before and (b) after evaporation of the heptane.

crystals and added the same solvent solution. The beaker containing the mixture was this time rotated in a cold bath because decreasing the temperature reduces the evaporation rate and allowed us to obtain larger crystals. The beaker was again sealed with a cap having only a tiny hole and a motor was used to rotate it in one direction in a cold bath with a stable temperature of 10 C°. After a couple of days, we noticed that a jelly liquid remained in the beaker and no crystals had formed. So, we added 5 ml more dichloromethane and increased the bath temperature to 20 C°. However, still no crystal had formed after full evaporation of the solution.

The next time, we only added 20 ml of dichloromethane and used no heptanes, and the beaker was rotated in a bath of 20 C°. After about six days, we obtained larger needle-shaped crystals, as shown in the Fig. I.3(a) and (b).

We tried another method of recrystallization consisting of first dissolving NIT2Py in 5 ml of dichloromethane in Container 1, and then proceeding to place that container in a second container (2) which held 15 ml of heptane. Container 2 was sealed off from the outside atmosphere, but Container 1 remained unsealed inside Container 2. We then put these containers in a controlled temperature of 30 C° for 10 days. The large crystal obtained are shown in Fig. I.4(a) and (b). The X-ray measurement of those crystals resulted in the discovery of a new metamorphic phase of NIT2Py. In the new phase, called β phase, the NIT2Py molecules are oriented differently in the unit cell than the

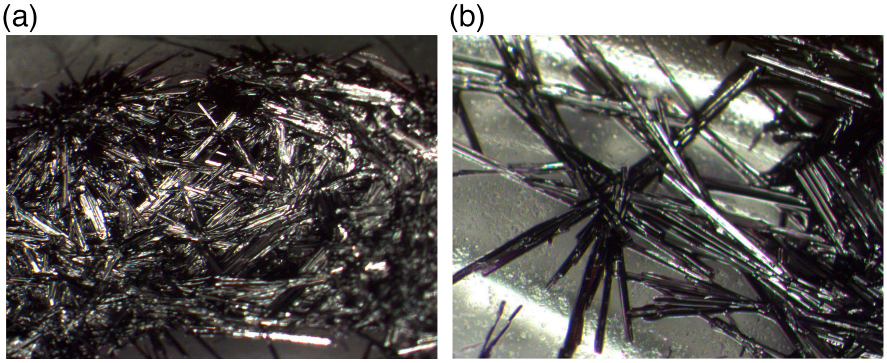

Figure I.3 – Recrystallization of NIT2Py carried out by slow evaporation method in which 20 ml of dichloromethane was used as the solvent, and rotation in one direction was applied to the beaker containing the sample that was placed in a cold bath of 20 C°.

molecules in the α phase.

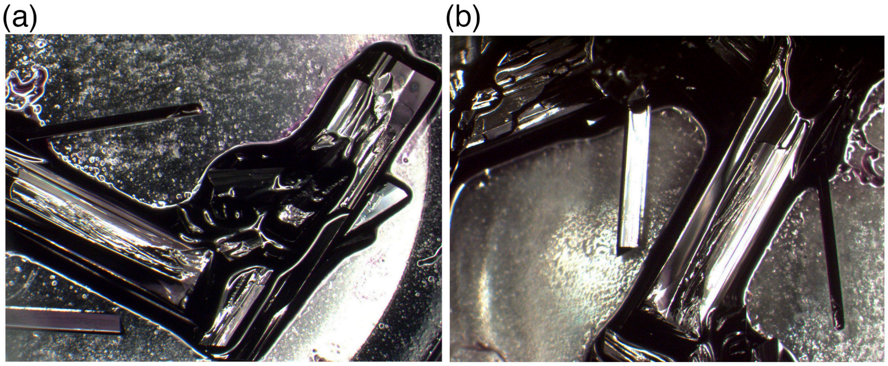

Figure I.4 – Crystals of a new NIT2py phase, the β phase, were grown using a slow evaporation technique including two containers in a temperature of 30 C°.

After examining different methods, we succeeded in growing large enough crystals by using about 5ml of dichloromethane and 15ml of Heptane, by slowing down the evaporation through the application of a narrow air flow into the round-bottom flask containing the mixture, and by placing the flask in a 30 C° water bath. The resulting large crystal are shown in Fig. I.5. X-ray measurements confirmed the crystal structure of the α phase.

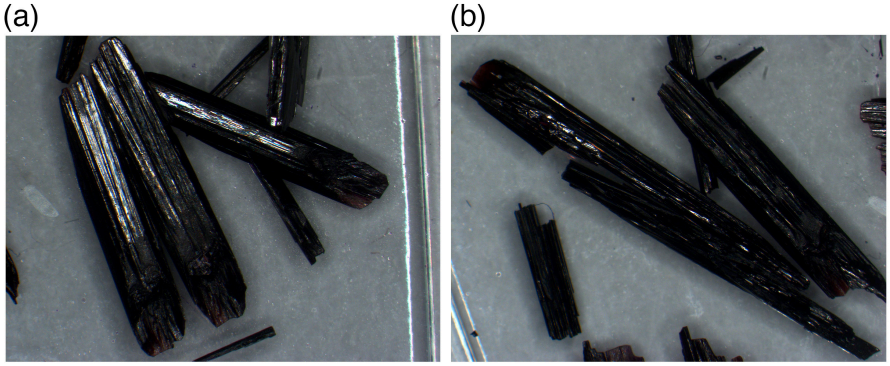

Figure I.5 – Large NIT2Py crystals of the α phase obtained by using airflow in a flask containing 75% Heptane (15ml) and 25% dichloromethane (5ml), and by placing the flask in a water bath of 30 C°.

Appendix II

Derivation of all the elements of the matrix Hamiltonian of a tetramer

First row:

$$\begin{aligned} H\left|+,+,+,+\right\rangle = & J_1(\frac{1}{4}\hbar^2\left|+,+,+,+\right\rangle + \frac{1}{4}\hbar^2\left|+,+,+,+\right\rangle) \\ & +J_2(\frac{1}{4}\hbar^2\left|+,+,+,+\right\rangle) = (\frac{1}{2}\hbar^2 J_1 + \frac{1}{4}\hbar^2 J_2)\left|+,+,+,+\right\rangle) \\ \langle +,+,+,+|H|+,+,+,+\rangle = & \langle 1|H|1\rangle = \frac{1}{2}\hbar^2 J_1 + \frac{1}{4}\hbar^2 J_2 \end{aligned} \tag{II.1}$$

It can be shown that the remaining components of the first row in the matrix are equal to zero $\langle 1|H|2\rangle = \langle 1|H|3\rangle = \cdots = \langle 1|H|16\rangle = 0$.

Second row:

$$\begin{aligned} H\left|+,+,+,-\right\rangle = & J_1(\frac{1}{4}\hbar^2\left|+,+,+,-\right\rangle + \frac{1}{2}\hbar^2\left|+,+,-,+\right\rangle \\ & +\frac{1}{4}\hbar^2\left|+,+,+,-\right\rangle) + J_2(\frac{1}{4}\hbar^2\left|+,+,+,-\right\rangle) \\ & =\frac{1}{2}\hbar^2 J_1\left|+,+,-,+\right\rangle + \frac{1}{4}\hbar^2 J_2\left|+,+,+,-\right\rangle) \end{aligned} \tag{II.2}$$

The non-zero terms in the second row:

$$\langle +,+,+,-|H|+,+,+,-\rangle = \langle 2|H|2\rangle = \frac{1}{4}\hbar^2 J_2. \tag{II.3}$$

$$\langle +,+,-,+|H|+,+,+,-\rangle = \langle 3|H|2\rangle = \frac{1}{2}\hbar^2 J_1. \tag{II.4}$$

Third row:

$$\begin{aligned} H\left|+,+,-,+\right\rangle = & J_1(\frac{1}{4}\hbar^2\left|+,+,-,+\right\rangle + \frac{1}{2}\hbar^2\left|+,+,+,-\right\rangle - \frac{1}{4}\hbar^2\left|+,+,-,+\right\rangle) \\ & +J_2(\frac{1}{2}\hbar^2\left|+,-,+,+\right\rangle - \frac{1}{4}\hbar^2\left|+,+,-,+\right\rangle) \\ & =\frac{1}{2}\hbar^2 J_1\left|+,+,+,-\right\rangle + \frac{1}{2}\hbar^2 J_2\left|+,-,+,+\right\rangle - \frac{1}{4}\hbar^2 J_2\left|+,+,-,+\right\rangle \end{aligned} \tag{II.5}$$

The non-zero terms in the third row:

$$\langle +,+,+,-|H|+,+,-,+\rangle = \langle 2|H|3\rangle = \frac{1}{2}\hbar^2 J_1 \tag{II.6}$$

$$\langle +,+,-,+|H|+,+,-,+\rangle = \langle 3|H|3\rangle = -\frac{1}{4}\hbar^2 J_2 \tag{II.7}$$

$$\langle +,-,+,+|H|+,+,-,+\rangle = \langle 4|H|3\rangle = \frac{1}{2}\hbar^2 J_2 \tag{II.8}$$

Fourth row:

$$\begin{aligned} H\,|+,-,+,+\rangle = {} & J_1(\frac{1}{2}\hbar^2\,|-,+,+,+\rangle - \frac{1}{4}\hbar^2\,|+,-,+,+\rangle + \frac{1}{4}\hbar^2\,|+,-,+,+\rangle) \\ & +J_2(\frac{1}{2}\hbar^2\,|+,+,-,+\rangle - \frac{1}{4}\hbar^2\,|+,-,+,+\rangle) \\ & =\frac{1}{2}\hbar^2 J_1\,|-,+,+,+\rangle + \frac{1}{2}\hbar^2 J_2\,|+,+,-,+\rangle - \frac{1}{4}\hbar^2 J_2\,|+,-,+,+\rangle \end{aligned} \tag{II.9}$$

The non-zero terms in the fourth row:

$$\langle +,+,-,+|H|+,-,+,+\rangle = \langle 3|H|4\rangle = -\frac{1}{4}\hbar^2 J_2 \tag{II.10}$$

$$\langle +,-,+,+|H|+,-,+,+\rangle = \langle 4|H|4\rangle = \frac{1}{2}\hbar^2 J_2 \tag{II.11}$$

$$\langle -,+,+,+|H|+,-,+,+\rangle = \langle 5|H|4\rangle = \frac{1}{2}\hbar^2 J_1 \tag{II.12}$$

Fifth row:

$$\begin{aligned} H\,|-,+,+,+\rangle = {} & J_1(\frac{1}{2}\hbar^2\,|+,-,+,+\rangle - \frac{1}{4}\hbar^2\,|-,+,+,+\rangle + \frac{1}{4}\hbar^2\,|-,+,+,+\rangle) \\ & +J_2(\frac{1}{4}\hbar^2\,|-,+,+,+\rangle) \\ & =\frac{1}{2}\hbar^2 J_1\,|+,-,+,+\rangle + \frac{1}{4}\hbar^2 J_2\,|-,+,+,+\rangle \end{aligned} \tag{II.13}$$

The non-zero terms in the fifth row:

$$\langle +,-,+,+|H|-,+,+,+\rangle = \langle 4|H|5\rangle = \frac{1}{4}\hbar^2 J_2 \tag{II.14}$$

$$\langle -,+,+,+|H|-,+,+,+\rangle = \langle 5|H|5\rangle = \frac{1}{2}\hbar^2 J_1 \tag{II.15}$$

Sixth row:

$$\begin{aligned} H\,|+,+,-,-\rangle = &J_1(\frac{1}{4}\hbar^2\,|+,+,-,-\rangle + \frac{1}{4}\hbar^2\,|+,+,-,-\rangle) \\ &+J_2(\frac{1}{2}\hbar^2\,|+,-,+,-\rangle - \frac{1}{4}\hbar^2\,|+,+,-,-\rangle) \\ &=(\frac{1}{2}\hbar^2 J_1 - \frac{1}{4}\hbar^2 J_2)\,|+,+,-,-\rangle + \frac{1}{2}\hbar^2 J_2\,|+,-,+,-\rangle \end{aligned} \tag{II.16}$$

The non-zero terms in the sixth row:

$$\langle +,+,-,-|H|+,+,-,-\rangle = \langle 6|H|6\rangle = \frac{1}{2}\hbar^2 J_1 - \frac{1}{4}\hbar^2 J_2 \tag{II.17}$$

$$\langle +,-,+,-|H|+,+,-,-\rangle = \langle 7|H|6\rangle = \frac{1}{2}\hbar^2 J_2 \tag{II.18}$$

In the seventh row:

$$\begin{aligned} H\,|+,-,+,-\rangle = &J_1(\frac{1}{2}\hbar^2\,|-,+,+,-\rangle - \frac{1}{4}\hbar^2\,|+,-,+,-\rangle + \frac{1}{2}\hbar^2\,|+,-,-,+\rangle \\ &-\frac{1}{4}\hbar^2\,|+,-,+,-\rangle) + J_2(\frac{1}{2}\hbar^2\,|+,+,-,-\rangle - \frac{1}{4}\hbar^2\,|+,-,+,-\rangle) \\ &=\frac{1}{2}\hbar^2 J_1\,|-,+,+,-\rangle + (-\frac{1}{2}\hbar^2 J_1 - \frac{1}{4}\hbar^2 J_2)\,|+,-,+,-\rangle \\ &+\frac{1}{2}\hbar^2 J_1\,|+,-,-,+\rangle + \frac{1}{2}\hbar^2 J_2\,|+,+,-,-\rangle \end{aligned} \tag{II.19}$$

The non-zero terms in the seventh row:

$$\langle +,+,-,-|H|+,-,+,-\rangle = \langle 6|H|7\rangle = \frac{1}{2}\hbar^2 J_2 \tag{II.20}$$

$$\langle +,-,+,-|H|+,-,+,-\rangle = \langle 7|H|7\rangle = -\frac{1}{2}\hbar^2 J_1 - \frac{1}{4}\hbar^2 J_2. \tag{II.21}$$

$$\langle +,-,-,+|H|+,-,+,-\rangle = \langle 8|H|7\rangle = \frac{1}{2}\hbar^2 J_1 \tag{II.22}$$

$$\langle -,+,+,-|H|+,-,+,-\rangle = \langle 9|H|7\rangle = \frac{1}{2}\hbar^2 J_1 \tag{II.23}$$

Eighth row:

$$\begin{aligned} H\,|+,-,-,+\rangle = J_1(&\frac{1}{2}\hbar^2\,|-,+,-,+\rangle - \frac{1}{4}\hbar^2\,|+,-,-,+\rangle + \frac{1}{2}\hbar^2\,|+,-,+,-\rangle \\ &-\frac{1}{4}\hbar^2\,|+,-,-,+\rangle) + J_2(\frac{1}{4}\hbar^2\,|+,-,-,+\rangle) \\ &= \frac{1}{2}\hbar^2 J_1\,|-,+,-,+\rangle + (-\frac{1}{2}\hbar^2 J_1 + \frac{1}{4}\hbar^2 J_2)\,|+,-,-,+\rangle \\ &+\frac{1}{2}\hbar^2 J_1\,|+,-,+,-\rangle \end{aligned} \tag{II.24}$$

The non-zero terms in the eighth row:

$$\langle +,-,+,-|H|+,-,-,+\rangle = \langle 7|H|8\rangle = \frac{1}{2}\hbar^2 J_1 \tag{II.25}$$

$$\langle +,-,-,+|H|+,-,-,+\rangle = \langle 8|H|8\rangle = -\frac{1}{2}\hbar^2 J_1 + \frac{1}{4}\hbar^2 J_2 \tag{II.26}$$

$$\langle -,+,-,+|H|+,-,-,+\rangle = \langle 10|H|8\rangle = \frac{1}{2}\hbar^2 J_1 \tag{II.27}$$

Ninth row:

$$\begin{aligned} H\,|-,+,+,-\rangle = J_1(&\frac{1}{2}\hbar^2\,|+,-,+,-\rangle - \frac{1}{4}\hbar^2\,|-,+,+,-\rangle + \frac{1}{2}\hbar^2\,|-,+,-,+\rangle \\ &-\frac{1}{4}\hbar^2\,|-,+,+,-\rangle) + J_2(\frac{1}{4}\hbar^2\,|-,+,+,-\rangle) \\ &= \frac{1}{2}\hbar^2 J_1\,|+,-,+,-\rangle + (-\frac{1}{2}\hbar^2 J_1 + \frac{1}{4}\hbar^2 J_2)\,|-,+,+,-\rangle + \frac{1}{2}\hbar^2 J_1\,|-,+,-,+\rangle \end{aligned} \tag{II.28}$$

The non-zero terms in the ninth row:

$$\langle +,-,+,-|H|-,+,+,-\rangle = \langle 7|H|9\rangle = \frac{1}{2}\hbar^2 J_1 \tag{II.29}$$

$$\langle -,+,+,-|H|-,+,+,-\rangle = \langle 9|H|9\rangle = -\frac{1}{2}\hbar^2 J_1 + \frac{1}{4}\hbar^2 J_2 \tag{II.30}$$

$$\langle -,+,-,+|H|-,+,+,-\rangle = \langle 10|H|9\rangle = \frac{1}{2}\hbar^2 J_1 \tag{II.31}$$

10th row:

$$\begin{aligned} H\,|-,+,-,+\rangle = J_1(&\frac{1}{2}\hbar^2\,|+,-,-,+\rangle - \frac{1}{4}\hbar^2\,|-,+,-,+\rangle + \frac{1}{2}\hbar^2\,|-,+,+,-\rangle \\ &-\frac{1}{4}\hbar^2\,|-,+,-,+\rangle) + J_2(\frac{1}{2}\hbar^2\,|-,-,+,+\rangle - \frac{1}{4}\hbar^2\,|-,+,-,+\rangle) \\ &= \frac{1}{2}\hbar^2 J_1\,|+,-,-,+\rangle + (-\frac{1}{2}\hbar^2 J_1 - \frac{1}{4}\hbar^2 J_2)\,|-,+,-,+\rangle \\ &+\frac{1}{2}\hbar^2 J_1\,|-,+,+,-\rangle + \frac{1}{2}\hbar^2 J_2\,|-,-,+,+\rangle \end{aligned} \tag{II.32}$$

The non-zero terms in the 10th row:

$$\langle +,-,-,+|H|-,+,-,+\rangle = \langle 8|H|10\rangle = \frac{1}{2}\hbar^2 J_1 \tag{II.33}$$

$$\langle -,+,+,-|H|-,+,-,+\rangle = \langle 9|H|10\rangle = \frac{1}{2}\hbar^2 J_1 \tag{II.34}$$

$$\langle -,+,-,+|H|-,+,-,+\rangle = \langle 10|H|10\rangle = -\frac{1}{2}\hbar^2 J_1 - \frac{1}{4}\hbar^2 J_2 \tag{II.35}$$

$$\langle -,-,+,+|H|-,+,-,+\rangle = \langle 11|H|10\rangle = \frac{1}{2}\hbar^2 J_2 \tag{II.36}$$

The 11th row:

$$\begin{aligned} H\,|-,-,+,+\rangle = J_1(&\frac{1}{4}\hbar^2\,|-,-,+,+\rangle + \frac{1}{4}\hbar^2\,|-,-,+,+\rangle \\ &+J_2(\frac{1}{2}\hbar^2\,|-,+,-,+\rangle - \frac{1}{4}\hbar^2\,|-,-,+,+\rangle) \\ &=(\frac{1}{2}\hbar^2 J_1 - \frac{1}{4}\hbar^2 J_2)\,|-,-,+,+\rangle + \frac{1}{2}\hbar^2 J_2\,|-,+,-,+\rangle \end{aligned} \tag{II.37}$$

The non-zero terms in the 11th row:

$$\langle -,+,-,+|H|-,-,+,+\rangle = \langle 10|H|11\rangle = \frac{1}{2}\hbar^2 J_2 \tag{II.38}$$

$$\langle -,-,+,+|H|-,-,+,+\rangle = \langle 11|H|11\rangle = \frac{1}{2}\hbar^2 J_1 - \frac{1}{4}\hbar^2 J_2 \tag{II.39}$$

The 12th row:

$$\begin{aligned} H\,|+,-,-,-\rangle = {} & J_1(\frac{1}{4}\hbar^2\,|-,+,-,-\rangle - \frac{1}{4}\hbar^2\,|+,-,-,-\rangle \\ & + \frac{1}{4}\hbar^2\,|+,-,-,-\rangle) + J_2(\frac{1}{4}\hbar^2\,|+,-,-,-\rangle) \\ = {} & \frac{1}{2}\hbar^2 J_1\,|-,+,-,-\rangle + \frac{1}{4}\hbar^2 J_2\,|+,-,-,-\rangle \end{aligned} \tag{II.40}$$

The non-zero terms in the 12th row:

$$\langle +,-,-,-|H|+,-,-,-\rangle = \langle 12|H|12\rangle = \frac{1}{4}\hbar^2 J_2 \tag{II.41}$$

$$\langle -,-,+,+|H|+,-,-,-\rangle = \langle 13|H|12\rangle = \frac{1}{2}\hbar^2 J_1 \tag{II.42}$$

The 13th row:

$$\begin{aligned} H\,|-,+,-,-\rangle = {} & J_1(\frac{1}{2}\hbar^2\,|+,-,-,-\rangle - \frac{1}{4}\hbar^2\,|-,+,-,-\rangle \\ & + \frac{1}{4}\hbar^2\,|-,+,-,-\rangle) + J_2(\frac{1}{2}\hbar^2\,|-,-,+,+\rangle - \frac{1}{4}\hbar^2\,|-,+,-,-\rangle) \\ = {} & \frac{1}{2}\hbar^2 J_1\,|+,-,-,-\rangle + \frac{1}{2}\hbar^2 J_2\,|-,-,+,-\rangle - \frac{1}{4}\hbar^2 J_2\,|-,+,-,-\rangle \end{aligned} \tag{II.43}$$

The non-zero terms in the 13th row:

$$\langle +,-,-,-|H|-,+,-,-\rangle = \langle 12|H|13\rangle = \frac{1}{2}\hbar^2 J_1 \tag{II.44}$$

$$\langle -,+,-,-|H|-,+,-,-\rangle = \langle 13|H|13\rangle = -\frac{1}{4}\hbar^2 J_2 \tag{II.45}$$

$$\langle -,-,+,-|H|-,+,-,-\rangle = \langle 14|H|13\rangle = \frac{1}{2}\hbar^2 J_2 \tag{II.46}$$

The 14th row:

$$\begin{aligned}H\left|-,-,+,-\right\rangle =& J_1(\frac{1}{4}\hbar^2\left|-,-,+,-\right\rangle+\frac{1}{2}\hbar^2\left|-,-,-,+\right\rangle\\ &-\frac{1}{4}\hbar^2\left|-,-,+,-\right\rangle)+J_2(\frac{1}{2}\hbar^2\left|-,+,-,-\right\rangle-\frac{1}{4}\hbar^2\left|-,-,+,-\right\rangle)\\ =&\frac{1}{2}\hbar^2J_1\left|-,-,-,+\right\rangle+\frac{1}{2}\hbar^2J_2\left|-,+,-,-\right\rangle-\frac{1}{4}\hbar^2J_2\left|-,-,+,-\right\rangle\end{aligned} \tag{II.47}$$

The non-zero terms in the 14th row:

$$\langle +,-,-,-|H|-,-,+,-\rangle = \langle 13|H|14\rangle = \frac{1}{2}\hbar^2 J_2 \tag{II.48}$$

$$\langle -,-,+,-|H|-,-,+,-\rangle = \langle 14|H|14\rangle = -\frac{1}{4}\hbar^2 J_2 \tag{II.49}$$

$$\langle -,-,-,+|H|-,-,+,-\rangle = \langle 15|H|14\rangle = \frac{1}{2}\hbar^2 J_1 \tag{II.50}$$

The 15th row:

$$\begin{aligned}H\left|-,-,-,+\right\rangle =& J_1(\frac{1}{4}\hbar^2\left|-,-,-,+\right\rangle+\frac{1}{2}\hbar^2\left|-,-,+,-\right\rangle\\ &-\frac{1}{4}\hbar^2\left|-,-,-,+\right\rangle)+J_2(\frac{1}{4}\hbar^2\left|-,-,-,+\right\rangle)\\ =&\frac{1}{2}\hbar^2J_1\left|-,-,+,-\right\rangle+\frac{1}{4}\hbar^2J_2\left|-,-,-,+\right\rangle\end{aligned} \tag{II.51}$$

The non-zero terms in the 15th row:

$$\langle -,-,+,-|H|-,-,-,+\rangle = \langle 14|H|15\rangle = \frac{1}{2}\hbar^2 J_1 \tag{II.52}$$

$$\langle -,-,-,+|H|-,-,-,+\rangle = \langle 15|H|15\rangle = \frac{1}{4}\hbar^2 J_2 \tag{II.53}$$

The 16th row:

$$\begin{aligned} H\left|-,-,-,-\right\rangle = & J_1(\frac{1}{4}\hbar^2\left|-,-,-,-\right\rangle + \frac{1}{4}\hbar^2\left|-,-,-,-\right\rangle) \\ & + J_2(\frac{1}{4}\hbar^2\left|-,-,-,-\right\rangle) \\ = & \frac{1}{2}\hbar^2 J_1\left|-,-,-,-\right\rangle + \frac{1}{4}\hbar^2 J_2\left|-,-,-,-\right\rangle \end{aligned} \tag{II.54}$$

The only non-zero term in the 16th row:

$$\langle -,-,-,-|H|-,-,-,- \rangle = \langle 16|H|16 \rangle = \frac{1}{2}\hbar^2 J_1 + \frac{1}{4}\hbar^2 J_2 \tag{II.55}$$

Appendix III

Spin configurations in the NIT2Py single cell

Number of molecules with distinct spin sign	Configs.		M_1	M_2	M_3	M_4	M_5	M_6	M_7	M_8
4 (4 molecules in symmetry group I)	Config. 1		-	-	-	-	+	+	+	+
	Crystalline symmetry	1	-	-	-	-	+	+	+	+
		2	-	-	-	-	+	+	+	+
		3	-	-	-	-	+	+	+	+
		4	-	-	-	-	+	+	+	+
	Spin reversal symmetry		+	+	+	+	-	-	-	-
			+	+	+	+	-	-	-	-
			+	+	+	+	-	-	-	-
			+	+	+	+	-	-	-	-
	Deg.		2							
4 (2 molecules in symmetry group I, and 2 molecules in symmetry group II)	Config. 2		+	-	+	-	+	-	+	-
	Crystalline symmetry	1	+	-	+	-	+	-	+	-
		2	-	+	-	+	-	+	-	+
		3	-	+	-	+	-	+	-	+
		4	+	-	+	-	+	-	+	-
	Spin reversal symmetry		-	+	-	+	-	+	-	+
			+	-	+	-	+	-	+	-
			+	-	+	-	+	-	+	-
			-	+	-	+	-	+	-	+
	Deg.		2							
4 (2 molecules in symmetry group I, and 2 molecules in symmetry group II)	Config. 3		-	+	-	+	+	-	+	-
	Crystalline symmetry	1	-	+	-	+	+	-	+	-
		2	+	-	+	-	-	+	-	+
		3	+	-	+	-	-	+	-	+
		4	-	+	-	+	+	-	+	-
	Spin reversal symmetry		+	-	+	-	-	+	-	+
			-	+	-	+	+	-	+	-
			-	+	-	+	+	-	+	-
			+	-	+	-	-	+	-	+
	Deg.		2							
4 (2 molecules in symmetry group I, and 2 molecules in symmetry group II)	Config. 4		-	+	+	-	-	+	+	-
	Crystalline symmetry	1	-	+	+	-	-	+	+	-
		2	+	-	-	+	+	-	-	+
		3	-	+	+	-	-	+	+	-
		4	+	-	-	+	+	-	-	+
	Spin reversal symmetry		+	-	-	+	+	-	-	+
			-	+	+	-	-	+	+	-
			+	-	-	+	+	-	-	+
			-	+	+	-	-	+	+	-
	Deg.		2							
4 (2 molecules in symmetry group I, and 2 molecules in symmetry group II)	Config. 5		-	-	+	+	+	+	-	-
	Crystalline symmetry	1	-	-	+	+	+	+	-	-
		2	-	-	+	+	+	+	-	-
		3	+	+	-	-	-	-	+	+
		4	+	+	-	-	-	-	+	+
	Spin reversal symmetry		+	+	-	-	-	-	+	+
			+	+	-	-	-	-	+	+
			-	-	+	+	+	+	-	-
			-	-	+	+	+	+	-	-
	Deg.		2							
4 (3 molecules in symmetry group I, and 1 molecule in symmetry group II)	Config. 6		-	+	-	-	+	+	+	-
	Crystalline symmetry	1	-	+	-	-	+	+	+	-
		2	+	-	-	-	+	+	-	+
		3	-	-	+	-	-	+	+	+
		4	-	-	-	+	+	-	+	+
	Spin reversal symmetry		+	-	+	+	-	-	-	+
			-	+	+	+	-	-	+	-
			+	+	-	+	+	-	-	-
			+	+	+	-	-	+	-	-
	Deg.		8							

4 (3 molecules in symmetry group I, and 1 molecule in symmetry group II)	Config. 7		-	-	-	+	+	+	-	+
	Crystalline symmetry	1	-	-	-	+	+	+	-	+
		2	-	-	+	-	+	+	+	-
		3	+	-	-	-	+	-	+	+
		4	-	+	-	-	-	+	+	+
	Spin reversal symmetry		+	+	+	-	-	-	+	-
			+	+	-	+	-	-	-	+
			-	+	+	+	-	+	-	-
			+	-	+	+	+	-	-	-
	Deg.		8							

4 (2 molecules in symmetry group I, and 2 molecules in symmetry group II)	Config. 8		-	+	-	+	+	+	-	-
	Crystalline symmetry	1	-	+	-	+	+	+	-	-
		2	+	-	+	-	+	+	-	-
		3	+	-	+	-	-	-	+	+
		4	-	+	-	+	-	-	+	+
	Spin reversal symmetry		+	-	+	-	-	-	+	+
			-	+	-	+	-	-	+	+
			-	+	-	+	+	+	-	-
			+	-	+	-	+	+	-	-
	Deg.		4							

4 (2 molecules in symmetry group I, and 2 molecules in symmetry group II)	Config. 9		-	+	-	+	+	-	-	+
	Crystalline symmetry	1	-	+	-	+	+	-	-	+
		2	+	-	+	-	-	+	+	-
		3	+	-	+	-	+	-	-	+
		4	-	+	-	+	-	+	+	-
	Spin reversal symmetry		+	-	+	-	-	+	+	-
			-	+	-	+	+	-	-	+
			-	+	-	+	-	+	+	-
			+	-	+	-	+	-	-	+
	Deg.		4							

4 (2 molecules in symmetry group I, and 2 molecules in symmetry group II)	Config. 10		-	-	+	+	+	-	-	+
	Crystalline symmetry	1	-	-	+	+	+	-	-	+
		2	-	-	+	+	-	+	+	-
		3	+	+	-	-	+	-	-	+
		4	+	+	-	-	-	+	+	-
	Spin reversal symmetry		+	+	-	-	-	+	+	-
			+	+	-	-	+	-	-	+
			-	-	+	+	-	+	+	-
			-	-	+	+	+	-	-	+
	Deg.		4							

4 (3 molecules in symmetry group I, and 1 molecule in symmetry group II)	Config. 11		-	-	-	+	-	+	+	+
	Crystalline symmetry	1	-	-	-	+	-	+	+	+
		2	-	-	+	-	+	-	+	+
		3	+	-	-	-	+	+	+	-
		4	-	+	-	-	+	+	-	+
	Spin reversal symmetry		+	+	+	-	+	-	-	-
			+	+	-	+	-	+	-	-
			-	+	+	+	-	-	-	+
			+	-	+	+	-	-	+	-
	Deg.		8							

4 (3 molecules in symmetry group I, and 1 molecule in symmetry group II)	Config. 12		-	-	-	+	+	+	+	-
	Crystalline symmetry	1	-	-	-	+	+	+	+	-
		2	-	-	+	-	+	+	-	+
		3	+	-	-	-	-	+	+	+
		4	-	+	-	-	+	-	+	+
	Spin reversal symmetry		+	+	+	-	-	-	-	+
			+	+	-	+	-	-	+	-
			-	+	+	+	+	-	-	-
			+	-	+	+	-	+	-	-
	Deg.		8							

4 (2 molecules in symmetry group I, and 2 molecules in symmetry group II)	Config. 13		-	-	+	+	-	-	+	+
	Crystalline symmetry	1	-	-	+	+	-	-	+	+
		2	-	-	+	+	-	-	+	+
		3	+	+	-	-	+	+	-	-
		4	+	+	-	-	+	+	-	-
	Spin reversal symmetry		+	+	-	-	+	+	-	-
			+	+	-	-	+	+	-	-
			-	-	+	+	-	-	+	+
			-	-	+	+	-	-	+	+
	Deg.		2							

4 (2 molecules in symmetry group I, and 2 molecules in symmetry group II)	Config. 14		-	-	+	+	-	+	-	+
	Crystalline symmetry	1	-	-	+	+	-	+	-	+
		2	-	-	+	+	+	-	+	-
		3	+	+	-	-	+	-	+	-
		4	+	+	-	-	-	+	-	+
	Spin reversal symmetry		+	+	-	-	+	-	+	-
			+	+	-	-	-	+	-	+
			-	-	+	+	-	+	-	+
			-	-	+	+	+	-	+	-
	Deg.		4							

4 (2 molecules in symmetry group I, and 2 molecules in symmetry group II)	Config. 15		-	+	+	-	-	-	+	+
	Crystalline symmetry	1	-	+	+	-	-	-	+	+
		2	+	-	-	+	-	-	+	+
		3	-	+	+	-	+	+	-	-
		4	+	-	-	+	+	+	-	-
	Spin reversal symmetry		+	-	-	+	+	+	-	-
			-	+	+	-	+	+	-	-
			+	-	-	+	-	-	+	+
			-	+	+	-	-	-	+	+
	Deg.		4							

4 (2 molecules in symmetry group I, and 2 molecules in symmetry group II)	Config. 16		-	+	+	-	-	+	-	+
	Crystalline symmetry	1	-	+	+	-	-	+	-	+
		2	+	-	-	+	+	-	+	-
		3	-	+	+	-	+	-	+	-
		4	+	-	-	+	-	+	-	+
	Spin reversal symmetry		+	-	-	+	+	-	+	-
			-	+	+	-	-	+	-	+
			+	-	-	+	-	+	-	+
			-	+	+	-	+	-	+	-
	Deg.		4							

4 (2 molecules in symmetry group I, and 2 molecules in symmetry group II)	Config. 17		-	+	+	-	+	-	-	+
	Crystalline symmetry	1	-	+	+	-	+	-	-	+
		2	+	-	-	+	-	+	+	-
		3	-	+	+	-	+	-	-	+
		4	+	-	-	+	-	+	+	-
	Spin reversal symmetry		+	-	-	+	-	+	+	-
			-	+	+	-	+	-	-	+
			+	-	-	+	-	+	+	-
			-	+	+	-	+	-	-	+
	Deg.		2							

Appendix IV

Spin configurations in the NIT2Py $2 \times 1 \times 1$ supercell

Configurations		M_1	M_2	M_3	M_4	M_5	M_6	M_7	M_8	M_9	M_{10}	M_{11}	M_{12}	M_{13}	M_{14}	M_{15}	M_{16}
Config. 1		-	-	-	-	+	+	+	+	+	+	+	+	-	-	-	-
Crystalline symmetry	1	-	-	-	-	+	+	+	+	+	+	+	+	-	-	-	-
	2	-	-	-	-	+	+	+	+	+	+	+	+	-	-	-	-
	3	-	-	-	-	+	+	+	+	+	+	+	+	-	-	-	-
	4	-	-	-	-	+	+	+	+	+	+	+	+	-	-	-	-
	5	+	+	+	+	-	-	-	-	-	-	-	-	+	+	+	+
	6	+	+	+	+	-	-	-	-	-	-	-	-	+	+	+	+
	7	+	+	+	+	-	-	-	-	-	-	-	-	+	+	+	+
	8	+	+	+	+	-	-	-	-	-	-	-	-	+	+	+	+
Spin reversal symmetry		+	+	+	+	-	-	-	-	-	-	-	-	+	+	+	+
		+	+	+	+	-	-	-	-	-	-	-	-	+	+	+	+
		+	+	+	+	-	-	-	-	-	-	-	-	+	+	+	+
		+	+	+	+	-	-	-	-	-	-	-	-	+	+	+	+
		-	-	-	-	+	+	+	+	+	+	+	+	-	-	-	-
		-	-	-	-	+	+	+	+	+	+	+	+	-	-	-	-
		-	-	-	-	+	+	+	+	+	+	+	+	-	-	-	-
		-	-	-	-	+	+	+	+	+	+	+	+	-	-	-	-
Deg.		2															
Config. 2		-	-	-	-	+	+	+	+	-	-	-	-	+	+	+	+
Crystalline symmetry	1	-	-	-	-	+	+	+	+	-	-	-	-	+	+	+	+
	2	-	-	-	-	+	+	+	+	-	-	-	-	+	+	+	+
	3	-	-	-	-	+	+	+	+	-	-	-	-	+	+	+	+
	4	-	-	-	-	+	+	+	+	-	-	-	-	+	+	+	+
	5	-	-	-	-	+	+	+	+	-	-	-	-	+	+	+	+
	6	-	-	-	-	+	+	+	+	-	-	-	-	+	+	+	+
	7	-	-	-	-	+	+	+	+	-	-	-	-	+	+	+	+
	8	-	-	-	-	+	+	+	+	-	-	-	-	+	+	+	+
Spin reversal symmetry		+	+	+	+	-	-	-	-	+	+	+	+	-	-	-	-
		+	+	+	+	-	-	-	-	+	+	+	+	-	-	-	-
		+	+	+	+	-	-	-	-	+	+	+	+	-	-	-	-
		+	+	+	+	-	-	-	-	+	+	+	+	-	-	-	-
		+	+	+	+	-	-	-	-	+	+	+	+	-	-	-	-
		+	+	+	+	-	-	-	-	+	+	+	+	-	-	-	-
		+	+	+	+	-	-	-	-	+	+	+	+	-	-	-	-
		+	+	+	+	-	-	-	-	+	+	+	+	-	-	-	-
Deg.		2															
Config. 3		+	-	+	-	+	-	+	-	-	+	-	+	-	+	-	+
Crystalline symmetry	1	+	-	+	-	+	-	+	-	-	+	-	+	-	+	-	+
	2	+	-	+	-	+	-	+	-	-	+	-	+	-	+	-	+
	3	-	+	-	+	-	+	-	+	+	-	+	-	+	-	+	-
	4	-	+	-	+	-	+	-	+	+	-	+	-	+	-	+	-
	5	+	-	+	-	+	-	+	-	-	+	-	+	-	+	-	+
	6	+	-	+	-	+	-	+	-	-	+	-	+	-	+	-	+
	7	+	-	+	-	+	-	+	-	-	+	-	+	-	+	-	+
	8	-	+	-	+	-	+	-	+	+	-	+	-	+	-	+	-
Spin reversal symmetry		-	+	-	+	-	+	-	+	+	-	+	-	+	-	+	-
		+	-	+	-	+	-	+	-	-	+	-	+	-	+	-	+
		+	-	+	-	+	-	+	-	-	+	-	+	-	+	-	+
		-	+	-	+	-	+	-	+	+	-	+	-	+	-	+	-
		-	+	-	+	-	+	-	+	+	-	+	-	+	-	+	-
		-	+	-	+	-	+	-	+	+	-	+	-	+	-	+	-
		+	-	+	-	+	-	+	-	-	+	-	+	-	+	-	+
		+	-	+	-	+	-	+	-	-	+	-	+	-	+	-	+
Deg.		2															
Config. 4		+	-	+	-	+	-	+	-	+	-	+	-	+	-	+	-
Crystalline symmetry	1	+	-	+	-	+	-	+	-	+	-	+	-	+	-	+	-
	2	-	+	-	+	-	+	-	+	-	+	-	+	-	+	-	+
	3	-	+	-	+	-	+	-	+	-	+	-	+	-	+	-	+
	4	+	-	+	-	+	-	+	-	+	-	+	-	+	-	+	-
	5	-	+	-	+	-	+	-	+	-	+	-	+	-	+	-	+
	6	-	+	-	+	-	+	-	+	-	+	-	+	-	+	-	+
	7	+	-	+	-	+	-	+	-	+	-	+	-	+	-	+	-
	8	+	-	+	-	+	-	+	-	+	-	+	-	+	-	+	-
Spin reversal symmetry		-	+	-	+	-	+	-	+	-	+	-	+	-	+	-	+
		+	-	+	-	+	-	+	-	+	-	+	-	+	-	+	-
		+	-	+	-	+	-	+	-	+	-	+	-	+	-	+	-
		-	+	-	+	-	+	-	+	-	+	-	+	-	+	-	+
		+	-	+	-	+	-	+	-	+	-	+	-	+	-	+	-
		+	-	+	-	+	-	+	-	+	-	+	-	+	-	+	-
		-	+	-	+	-	+	-	+	-	+	-	+	-	+	-	+
		-	+	-	+	-	+	-	+	-	+	-	+	-	+	-	+
Deg.		2															
Config. 5		-	+	-	+	+	-	+	-	+	-	+	-	-	+	-	+
Crystalline symmetry	1	-	+	-	+	+	-	+	-	+	-	+	-	-	+	-	+
	2	+	-	+	-	-	+	-	+	-	+	-	+	+	-	+	-
	3	+	-	+	-	-	+	-	+	-	+	-	+	+	-	+	-
	4	-	+	-	+	+	-	+	-	+	-	+	-	-	+	-	+
	5	-	+	-	+	+	-	+	-	+	-	+	-	-	+	-	+
	6	-	+	-	+	+	-	+	-	+	-	+	-	-	+	-	+
	7	+	-	+	-	-	+	-	+	-	+	-	+	+	-	+	-
	8	+	-	+	-	-	+	-	+	-	+	-	+	+	-	+	-
Spin reversal		+	-	+	-	-	+	-	+	-	+	-	+	+	-	+	-

symmetry		-	+	-	+	+	-	+	-	+	-	+	-	-	+	-	+
		-	+	-	+	+	-	+	-	+	-	+	-	-	+	-	+
		+	-	+	-	-	+	-	+	-	+	-	+	+	-	+	-
		+	-	+	-	-	+	-	+	-	+	-	+	+	-	+	-
		+	-	+	-	-	+	-	+	-	+	-	+	+	-	+	-
		-	+	-	+	+	-	+	-	+	-	+	-	-	+	-	+
		-	+	-	+	+	-	+	-	+	-	+	-	-	+	-	+
Deg.		2															
Config. 6		-	+	-	+	+	-	+	-	-	+	-	+	+	-	+	-
Crystalline symmetry	1	-	+	-	+	+	-	+	-	-	+	-	+	+	-	+	-
	2	+	-	+	-	-	+	-	+	+	-	+	-	-	+	-	+
	3	+	-	+	-	-	+	-	+	+	-	+	-	-	+	-	+
	4	-	+	-	+	+	-	+	-	-	+	-	+	+	-	+	-
	5	+	-	+	-	-	+	-	+	+	-	+	-	-	+	-	+
	6	+	-	+	-	-	+	-	+	+	-	+	-	-	+	-	+
	7	-	+	-	+	+	-	+	-	-	+	-	+	+	-	+	-
	8	-	+	-	+	+	-	+	-	-	+	-	+	+	-	+	-
Spin reversal symmetry		+	-	+	-	-	+	-	+	+	-	+	-	-	+	-	+
		-	+	-	+	+	-	+	-	-	+	-	+	+	-	+	-
		-	+	-	+	+	-	+	-	-	+	-	+	+	-	+	-
		+	-	+	-	-	+	-	+	+	-	+	-	-	+	-	+

		-	+	-	+	+	-	+	-	-	+	-	+	+	-	+	-
		-	+	-	+	+	-	+	-	-	+	-	+	+	-	+	-
		+	-	+	-	-	+	-	+	+	-	+	-	-	+	-	+
		+	-	+	-	-	+	-	+	+	-	+	-	-	+	-	+
Deg.		2															
Config. 7		-	+	+	-	-	+	+	-	+	-	-	+	+	-	-	+
Crystalline symmetry	1	-	+	+	-	-	+	+	-	+	-	-	+	+	-	-	+
	2	+	-	-	+	+	-	-	+	-	+	+	-	-	+	+	-
	3	-	+	+	-	-	+	+	-	+	-	-	+	+	-	-	+
	4	+	-	-	+	+	-	-	+	-	+	+	-	-	+	+	-
	5	+	-	-	+	+	-	-	+	-	+	+	-	-	+	+	-
	6	-	+	+	-	-	+	+	-	+	-	-	+	+	-	-	+
	7	+	-	-	+	+	-	-	+	-	+	+	-	-	+	+	-
	8	-	+	+	-	-	+	+	-	+	-	-	+	+	-	-	+
Spin reversal symmetry		+	-	-	+	+	-	-	+	-	+	+	-	-	+	+	-
		-	+	+	-	-	+	+	-	+	-	-	+	+	-	-	+
		+	-	-	+	+	-	-	+	-	+	+	-	-	+	+	-
		-	+	+	-	-	+	+	-	+	-	-	+	+	-	-	+
		-	+	+	-	-	+	+	-	+	-	-	+	+	-	-	+
		+	-	-	+	+	-	-	+	-	+	+	-	-	+	+	-
		-	+	+	-	-	+	+	-	+	-	-	+	+	-	-	+

		+	-	-	+	+	-	-	+	-	+	+	-	-	+	+	-
Deg.		2															
Config. 8		-	+	+	-	-	+	+	-	-	+	+	-	-	+	+	-
Crystalline symmetry	1	-	+	+	-	-	+	+	-	-	+	+	-	-	+	+	-
	2	+	-	-	+	+	-	-	+	+	-	-	+	+	-	-	+
	3	-	+	+	-	-	+	+	-	-	+	+	-	-	+	+	-
	4	+	-	-	+	+	-	-	+	+	-	-	+	+	-	-	+
	5	-	+	+	-	-	+	+	-	-	+	+	-	-	+	+	-
	6	+	-	-	+	+	-	-	+	+	-	-	+	+	-	-	+
	7	-	+	+	-	-	+	+	-	-	+	+	-	-	+	+	-
	8	+	-	-	+	+	-	-	+	+	-	-	+	+	-	-	+
Spin reversal symmetry		+	-	-	+	+	-	-	+	+	-	-	+	+	-	-	+
		-	+	+	-	-	+	+	-	-	+	+	-	-	+	+	-
		+	-	-	+	+	-	-	+	+	-	-	+	+	-	-	+
		-	+	+	-	-	+	+	-	-	+	+	-	-	+	+	-
		+	-	-	+	+	-	-	+	+	-	-	+	+	-	-	+
		-	+	+	-	-	+	+	-	-	+	+	-	-	+	+	-
		+	-	-	+	+	-	-	+	+	-	-	+	+	-	-	+
		-	+	+	-	-	+	+	-	-	+	+	-	-	+	+	-
Deg.		2															
Config. 9		-	-	+	+	+	+	-	-	+	+	-	-	-	-	+	+

Crystalline symmetry	1	-	-	+	+	+	+	-	-	+	+	-	-	-	-	+	+
	2	-	-	+	+	+	+	-	-	+	+	-	-	-	-	+	+
	3	+	+	-	-	-	-	+	+	-	-	+	+	+	+	-	-
	4	+	+	-	-	-	-	+	+	-	-	+	+	+	+	-	-
	5	-	-	+	+	+	+	-	-	+	+	-	-	-	-	+	+
	6	+	+	-	-	-	-	+	+	-	-	+	+	+	+	-	-
	7	+	+	-	-	-	-	+	+	-	-	+	+	+	+	-	-
	8	-	-	+	+	+	+	-	-	+	+	-	-	-	-	+	+
Spin reversal symmetry		+	+	-	-	-	-	+	+	-	-	+	+	+	+	-	-
		+	+	-	-	-	-	+	+	-	-	+	+	+	+	-	-
		-	-	+	+	+	+	-	-	+	+	-	-	-	-	+	+
		-	-	+	+	+	+	-	-	+	+	-	-	-	-	+	+
		+	+	-	-	-	-	+	+	-	-	+	+	+	+	-	-
		-	-	+	+	+	+	-	-	+	+	-	-	-	-	+	+
		-	-	+	+	+	+	-	-	+	+	-	-	-	-	+	+
		+	+	-	-	-	-	+	+	-	-	+	+	+	+	-	-
Deg.		2															
Config. 10		-	-	+	+	+	+	-	-	-	-	+	+	+	+	-	-
Crystalline symmetry	1	-	-	+	+	+	+	-	-	-	-	+	+	+	+	-	-
	2	-	-	+	+	+	+	-	-	-	-	+	+	+	+	-	-
	3	+	+	-	-	-	-	+	+	+	+	-	-	-	-	+	+

	4	+	+	-	-	-	-	+	+	+	+	-	-	-	-	+	+
	5	+	+	-	-	-	-	+	+	+	+	-	-	-	-	+	+
	6	-	-	+	+	+	+	-	-	-	-	+	+	+	+	-	-
	7	-	-	+	+	+	+	-	-	-	-	+	+	+	+	-	-
	8	+	+	-	-	-	-	+	+	+	+	-	-	-	-	+	+
Spin reversal symmetry		+	+	-	-	-	-	+	+	+	+	-	-	-	-	+	+
		+	+	-	-	-	-	+	+	+	+	-	-	-	-	+	+
		-	-	+	+	+	+	-	-	-	-	+	+	+	+	-	-
		-	-	+	+	+	+	-	-	-	-	+	+	+	+	-	-
		-	-	+	+	+	+	-	-	-	-	+	+	+	+	-	-
		+	+	-	-	-	-	+	+	+	+	-	-	-	-	+	+
		+	+	-	-	-	-	+	+	+	+	-	-	-	-	+	+
		-	-	+	+	+	+	-	-	-	-	+	+	+	+	-	-
Deg.		2															
Config. 11		-	+	-	-	+	+	+	-	+	-	+	+	-	-	-	+
Crystalline symmetry	1	-	+	-	-	+	+	+	-	+	-	+	+	-	-	-	+
	2	+	-	-	-	+	+	-	+	-	+	+	+	-	-	+	-
	3	-	-	+	-	-	+	+	+	+	+	-	+	+	-	-	-
	4	-	-	-	+	+	-	+	+	+	+	+	-	-	+	-	-
	5	+	+	-	+	+	-	-	-	-	-	+	-	-	+	+	+
	6	-	+	+	+	-	-	+	-	+	-	-	-	+	+	-	+

	7	+	-	+	+	-	-	-	+	-	+	-	-	+	+	+	-
	8	+	+	+	-	-	+	-	-	-	-	-	+	+	-	+	+
Spin reversal symmetry		+	-	+	+	-	-	-	+	-	+	-	-	+	+	+	-
		-	+	+	+	-	-	+	-	+	-	-	-	+	+	-	+
		+	+	-	+	+	-	-	-	-	-	+	-	-	+	+	+
		+	+	+	-	-	+	-	-	-	-	-	+	+	-	+	+
		-	-	+	-	-	+	+	+	+	+	-	+	+	-	-	-
		+	-	-	-	+	+	-	+	-	+	+	+	-	-	+	-
		-	+	-	-	+	+	+	-	+	-	+	+	-	-	-	+
		-	-	-	+	+	-	+	+	+	+	+	-	-	+	-	-
Deg.		8															
Config. 12		-	+	-	-	+	+	+	-	-	+	-	-	+	+	+	-
Crystalline symmetry	1	-	+	-	-	+	+	+	-	-	+	-	-	+	+	+	-
	2	+	-	-	-	+	+	-	+	+	-	-	-	+	+	-	+
	3	-	-	+	-	-	+	+	+	-	-	+	-	-	+	+	+
	4	-	-	-	+	+	-	+	+	-	-	-	+	+	-	+	+
	5	-	-	+	-	-	+	+	+	-	-	+	-	-	+	+	+
	6	+	-	-	-	+	+	-	+	+	-	-	-	+	+	-	+
	7	-	+	-	-	+	+	+	-	-	+	-	-	+	+	+	-
	8	-	-	-	+	+	-	+	+	-	-	-	+	+	-	+	+
Spin reversal		+	-	+	+	-	-	-	+	+	-	+	+	-	-	-	+

symmetry		-	+	+	+	-	-	+	-	-	+	+	+	-	-	+	-
		+	+	-	+	+	-	-	-	+	+	-	+	+	-	-	-
		+	+	+	-	-	+	-	-	+	+	+	-	-	+	-	-
		+	+	-	+	+	-	-	-	+	+	-	+	+	-	-	-
		-	+	+	+	-	-	+	-	-	+	+	+	-	-	+	-
		+	-	+	+	-	-	-	+	+	-	+	+	-	-	-	+
		+	+	+	-	-	+	-	-	+	+	+	-	-	+	-	-
Deg.		8															
Config. 13		-	-	-	+	+	+	-	+	+	+	+	-	-	-	+	-
Crystalline symmetry	1	-	-	-	+	+	+	-	+	+	+	+	-	-	-	+	-
	2	-	-	+	-	+	+	+	-	+	+	-	+	-	-	-	+
	3	+	-	-	-	+	-	+	+	-	+	+	+	-	+	-	-
	4	-	+	-	-	-	+	+	+	+	-	+	+	+	-	-	-
	5	-	+	+	+	-	+	-	-	+	-	-	-	+	-	+	+
	6	+	+	-	+	-	-	-	+	-	-	+	-	+	+	+	-
	7	+	+	+	-	-	-	+	-	-	-	-	+	+	+	-	+
	8	+	-	+	+	+	-	-	-	-	+	-	-	-	+	+	+
Spin reversal symmetry		+	+	+	-	-	-	+	-	-	-	-	+	+	+	-	+
		+	+	-	+	-	-	-	+	-	-	+	-	+	+	+	-
		-	+	+	+	-	+	-	-	+	-	-	-	+	-	+	+
		+	-	+	+	+	-	-	-	-	+	-	-	-	+	+	+

		+	-	-	-	+	-	+	+	-	+	+	+	-	+	-	-
		-	-	+	-	+	+	+	-	+	+	-	+	-	-	-	+
		-	-	-	+	+	+	-	+	+	+	+	-	-	-	+	-
		-	+	-	-	-	+	+	+	+	-	+	+	+	-	-	-
Deg.		8															
Config. 14		-	-	-	+	+	+	-	+	-	-	-	+	+	+	-	+
Crystalline symmetry	1	-	-	-	+	+	+	-	+	-	-	-	+	+	+	-	+
	2	-	-	+	-	+	+	+	-	-	-	+	-	+	+	+	-
	3	+	-	-	-	+	-	+	+	+	-	-	-	+	-	+	+
	4	-	+	-	-	-	+	+	+	-	+	-	-	-	+	+	+
	5	+	-	-	-	+	-	+	+	+	-	-	-	+	-	+	+
	6	-	-	+	-	+	+	+	-	-	-	+	-	+	+	+	-
	7	-	-	-	+	+	+	-	+	-	-	-	+	+	+	-	+
	8	-	+	-	-	-	+	+	+	-	+	-	-	-	+	+	+
Spin reversal symmetry		+	+	+	-	-	-	+	-	+	+	+	-	-	-	+	-
		+	+	-	+	-	-	-	+	+	+	-	+	-	-	-	+
		-	+	+	+	-	+	-	-	-	+	+	+	-	+	-	-
		+	-	+	+	+	-	-	-	+	-	+	+	+	-	-	-
		-	+	+	+	-	+	-	-	-	+	+	+	-	+	-	-
		+	+	-	+	-	-	-	+	+	+	-	+	-	-	-	+
		+	+	+	-	-	-	+	-	+	+	+	-	-	-	+	-

		+	-	+	+	+	-	-	-	+	-	+	+	+	-	-	-
Deg.		8															
Config. 15		-	+	-	+	+	+	-	-	+	-	+	-	-	-	+	+
Crystalline symmetry	1	-	+	-	+	+	+	-	-	+	-	+	-	-	-	+	+
	2	+	-	+	-	+	+	-	-	-	+	-	+	-	-	+	+
	3	+	-	+	-	-	-	+	+	-	+	-	+	+	+	-	-
	4	-	+	-	+	-	-	+	+	+	-	+	-	+	+	-	-
	5	-	+	-	+	+	+	-	-	+	-	+	-	-	-	+	+
	6	-	+	-	+	-	-	+	+	+	-	+	-	+	+	-	-
	7	+	-	+	-	-	-	+	+	-	+	-	+	+	+	-	-
	8	+	-	+	-	+	+	-	-	-	+	-	+	-	-	+	+
Spin reversal symmetry		+	-	+	-	-	-	+	+	-	+	-	+	+	+	-	-
		-	+	-	+	-	-	+	+	+	-	+	-	+	+	-	-
		-	+	-	+	+	+	-	-	+	-	+	-	-	-	+	+
		+	-	+	-	+	+	-	-	-	+	-	+	-	-	+	+
		+	-	+	-	-	-	+	+	-	+	-	+	+	+	-	-
		+	-	+	-	+	+	-	-	-	+	-	+	-	-	+	+
		-	+	-	+	+	+	-	-	+	-	+	-	-	-	+	+
		-	+	-	+	-	-	+	+	+	-	+	-	+	+	-	-
Deg.		4															
Config. 16		-	+	-	+	+	+	-	-	-	+	-	+	+	+	-	-

Crystalline symmetry	1	-	+	-	+	+	+	-	-	-	+	-	+	+	+	-	-
	2	+	-	+	-	+	+	-	-	+	-	+	-	+	+	-	-
	3	+	-	+	-	-	-	+	+	+	-	+	-	-	-	+	+
	4	-	+	-	+	-	-	+	+	-	+	-	+	-	-	+	+
	5	+	-	+	-	-	-	+	+	+	-	+	-	-	-	+	+
	6	+	-	+	-	+	+	-	-	+	-	+	-	+	+	-	-
	7	-	+	-	+	+	+	-	-	-	+	-	+	+	+	-	-
	8	-	+	-	+	-	-	+	+	-	+	-	+	-	-	+	+
Spin reversal symmetry		+	-	+	-	-	-	+	+	+	-	+	-	-	-	+	+
		-	+	-	+	-	-	+	+	-	+	-	+	-	-	+	+
		-	+	-	+	+	+	-	-	-	+	-	+	+	+	-	-
		+	-	+	-	+	+	-	-	+	-	+	-	+	+	-	-
		-	+	-	+	+	+	-	-	-	+	-	+	+	+	-	-
		-	+	-	+	-	-	+	+	-	+	-	+	-	-	+	+
		+	-	+	-	-	-	+	+	+	-	+	-	-	-	+	+
		+	-	+	-	+	+	-	-	+	-	+	-	+	+	-	-
Deg.		4															
Config. 17		-	+	-	+	+	-	-	+	-	+	-	+	+	-	-	+
Crystalline symmetry	1	-	+	-	+	+	-	-	+	-	+	-	+	+	-	-	+
	2	+	-	+	-	-	+	+	-	+	-	+	-	-	+	+	-
	3	+	-	+	-	+	-	-	+	+	-	+	-	+	-	-	+

	4	-	+	-	+	-	+	+	-	-	+	-	+	-	+	+	-
	5	+	-	+	-	+	-	-	+	+	-	+	-	+	-	-	+
	6	+	-	+	-	-	+	+	-	+	-	+	-	-	+	+	-
	7	-	+	-	+	+	-	-	+	-	+	-	+	+	-	-	+
	8	-	+	-	+	-	+	+	-	-	+	-	+	-	+	+	-
Spin reversal symmetry		+	-	+	-	-	+	+	-	+	-	+	-	-	+	+	-
		-	+	-	+	+	-	-	+	-	+	-	+	+	-	-	+
		-	+	-	+	-	+	+	-	-	+	-	+	-	+	+	-
		+	-	+	-	+	-	-	+	+	-	+	-	+	-	-	+
		-	+	-	+	-	+	+	-	-	+	-	+	-	+	+	-
		-	+	-	+	+	-	-	+	-	+	-	+	+	-	-	+
		+	-	+	-	-	+	+	-	+	-	+	-	-	+	+	-
		+	-	+	-	+	-	-	+	+	-	+	-	+	-	-	+
Deg.		4															
Config. 18		-	-	+	+	+	-	-	+	+	+	-	-	-	+	+	-
Crystalline symmetry	1	-	-	+	+	+	-	-	+	+	+	-	-	-	+	+	-
	2	-	-	+	+	-	+	+	-	+	+	-	-	+	-	-	+
	3	+	+	-	-	+	-	-	+	-	-	+	+	-	+	+	-
	4	+	+	-	-	-	+	+	-	-	-	+	+	+	-	-	+
	5	-	-	+	+	-	+	+	-	+	+	-	-	+	-	-	+
	6	+	+	-	-	+	-	-	+	-	-	+	+	-	+	+	-

	7	+	+	-	-	-	+	+	-	-	-	+	+	+	-	-	+
	8	-	-	+	+	+	-	-	+	+	+	-	-	-	+	+	-
Spin reversal symmetry		+	+	-	-	-	+	+	-	-	-	+	+	+	-	-	+
		+	+	-	-	+	-	-	+	-	-	+	+	-	+	+	-
		-	-	+	+	-	+	+	-	+	+	-	-	+	-	-	+
		-	-	+	+	+	-	-	+	+	+	-	-	-	+	+	-
		+	+	-	-	+	-	-	+	-	-	+	+	-	+	+	-
		-	-	+	+	-	+	+	-	+	+	-	-	+	-	-	+
		-	-	+	+	+	-	-	+	+	+	-	-	-	+	+	-
		+	+	-	-	-	+	+	-	-	-	+	+	+	-	-	+
Deg.		4															
Config. 19		-	-	+	+	+	-	-	+	-	-	+	+	+	-	-	+
Crystalline symmetry	1	-	-	+	+	+	-	-	+	-	-	+	+	+	-	-	+
	2	-	-	+	+	-	+	+	-	-	-	+	+	-	+	+	-
	3	+	+	-	-	+	-	-	+	+	+	-	-	+	-	-	+
	4	+	+	-	-	-	+	+	-	+	+	-	-	-	+	+	-
	5	+	+	-	-	+	-	-	+	+	+	-	-	+	-	-	+
	6	-	-	+	+	-	+	+	-	-	-	+	+	-	+	+	-
	7	-	-	+	+	+	-	-	+	-	-	+	+	+	-	-	+
	8	+	+	-	-	-	+	+	-	+	+	-	-	-	+	+	-
Spin reversal		+	+	-	-	-	+	+	-	+	+	-	-	-	+	+	-

symmetry		+	+	-	-	+	-	-	+	+	+	-	-	+	-	-	+
		-	-	+	+	-	+	+	-	-	-	+	+	-	+	+	-
		-	-	+	+	+	-	-	+	-	-	+	+	+	-	-	+
		-	-	+	+	-	+	+	-	-	-	+	+	-	+	+	-
		+	+	-	-	+	-	-	+	+	+	-	-	+	-	-	+
		+	+	-	-	-	+	+	-	+	+	-	-	-	+	+	-
		-	-	+	+	+	-	-	+	-	-	+	+	+	-	-	+
Deg.		4															
Config. 20		-	-	-	+	-	+	+	+	-	-	-	+	-	+	+	+
Crystalline symmetry	1	-	-	-	+	-	+	+	+	-	-	-	+	-	+	+	+
	2	-	-	+	-	+	-	+	+	-	-	+	-	+	-	+	+
	3	+	-	-	-	+	+	+	-	+	-	-	-	+	+	+	-
	4	-	+	-	-	+	+	-	+	-	+	-	-	+	+	-	+
	5	+	-	-	-	+	+	+	-	+	-	-	-	+	+	+	-
	6	-	-	+	-	+	-	+	+	-	-	+	-	+	-	+	+
	7	-	-	-	+	-	+	+	+	-	-	-	+	-	+	+	+
	8	-	+	-	-	+	+	-	+	-	+	-	-	+	+	-	+
Spin reversal symmetry		+	+	+	-	+	-	-	-	+	+	+	-	+	-	-	-
		+	+	-	+	-	+	-	-	+	+	-	+	-	+	-	-
		-	+	+	+	-	-	-	+	-	+	+	+	-	-	-	+
		+	-	+	+	-	-	+	-	+	-	+	+	-	-	+	-
		-	+	+	+	-	-	-	+	-	+	+	+	-	-	-	+
		+	+	-	+	-	+	-	-	+	+	-	+	-	+	-	-
		+	+	+	-	+	-	-	-	+	+	+	-	+	-	-	-
		+	-	+	+	-	-	+	-	+	-	+	+	-	-	+	-
Deg.		8															
Config. 21		-	-	-	+	+	+	+	-	+	+	+	-	-	-	-	+
Crystalline symmetry	1	-	-	-	+	+	+	+	-	+	+	+	-	-	-	-	+
	2	-	-	+	-	+	+	-	+	+	+	-	+	-	-	+	-
	3	+	-	-	-	-	+	+	+	-	+	+	+	+	-	-	-
	4	-	+	-	-	+	-	+	+	+	-	+	+	-	+	-	-
	5	-	+	+	+	+	-	-	-	+	-	-	-	-	+	+	+
	6	+	+	-	+	-	-	+	-	-	-	+	-	+	+	-	+
	7	+	+	+	-	-	-	-	+	-	-	-	+	+	+	+	-
	8	+	-	+	+	-	+	-	-	-	+	-	-	+	-	+	+
Spin reversal symmetry		+	+	+	-	-	-	-	+	-	-	-	+	+	+	+	-
		+	+	-	+	-	-	+	-	-	-	+	-	+	+	-	+
		-	+	+	+	+	-	-	-	+	-	-	-	-	+	+	+
		+	-	+	+	-	+	-	-	-	+	-	-	+	-	+	+
		+	-	-	-	-	+	+	+	-	+	+	+	+	-	-	-
		-	-	+	-	+	+	-	+	+	+	-	+	-	-	+	-
		-	-	-	+	+	+	+	-	+	+	+	-	-	-	-	+
		-	+	-	-	+	-	+	+	+	-	+	+	-	+	-	-
Deg.		8															
Config. 22		-	-	-	+	+	+	+	-	-	-	-	+	+	+	+	-
Crystalline symmetry	1	-	-	-	+	+	+	+	-	-	-	-	+	+	+	+	-
	2	-	-	+	-	+	+	-	+	-	-	+	-	+	+	-	+
	3	+	-	-	-	-	+	+	+	+	-	-	-	-	+	+	+
	4	-	+	-	-	+	-	+	+	-	+	-	-	+	-	+	+
	5	+	-	-	-	-	+	+	+	+	-	-	-	-	+	+	+
	6	-	-	+	-	+	+	-	+	-	-	+	-	+	+	-	+
	7	-	-	-	+	+	+	+	-	-	-	-	+	+	+	+	-
	8	-	+	-	-	+	-	+	+	-	+	-	-	+	-	+	+
Spin reversal symmetry		+	+	+	-	-	-	-	+	+	+	+	-	-	-	-	+
		+	+	-	+	-	-	+	-	+	+	-	+	-	-	+	-
		-	+	+	+	+	-	-	-	-	+	+	+	+	-	-	-
		+	-	+	+	-	+	-	-	+	-	+	+	-	+	-	-
		-	+	+	+	+	-	-	-	-	+	+	+	+	-	-	-
		+	+	-	+	-	-	+	-	+	+	-	+	-	-	+	-
		+	+	+	-	-	-	-	+	+	+	+	-	-	-	-	+
		+	-	+	+	-	+	-	-	+	-	+	+	-	+	-	-
Deg.		8															
Config. 23		-	-	+	+	-	-	+	+	+	+	-	-	+	+	-	-
Crystalline symmetry	1	-	-	+	+	-	-	+	+	+	+	-	-	+	+	-	-
	2	-	-	+	+	-	-	+	+	+	+	-	-	+	+	-	-
	3	+	+	-	-	+	+	-	-	-	-	+	+	-	-	+	+
	4	+	+	-	-	+	+	-	-	-	-	+	+	-	-	+	+
	5	-	-	+	+	-	-	+	+	+	+	-	-	+	+	-	-
	6	+	+	-	-	+	+	-	-	-	-	+	+	-	-	+	+
	7	+	+	-	-	+	+	-	-	-	-	+	+	-	-	+	+
	8	-	-	+	+	-	-	+	+	+	+	-	-	+	+	-	-
Spin reversal symmetry		+	+	-	-	+	+	-	-	-	-	+	+	-	-	+	+
		+	+	-	-	+	+	-	-	-	-	+	+	-	-	+	+
		-	-	+	+	-	-	+	+	+	+	-	-	+	+	-	-
		-	-	+	+	-	-	+	+	+	+	-	-	+	+	-	-
		+	+	-	-	+	+	-	-	-	-	+	+	-	-	+	+
		-	-	+	+	-	-	+	+	+	+	-	-	+	+	-	-
		-	-	+	+	-	-	+	+	+	+	-	-	+	+	-	-
		+	+	-	-	+	+	-	-	-	-	+	+	-	-	+	+
Deg.		2															
Config. 24		-	-	+	+	-	-	+	+	-	-	+	+	-	-	+	+
Crystalline symmetry	1	-	-	+	+	-	-	+	+	-	-	+	+	-	-	+	+
	2	-	-	+	+	-	-	+	+	-	-	+	+	-	-	+	+
	3	+	+	-	-	+	+	-	-	+	+	-	-	+	+	-	-
	4	+	+	-	-	+	+	-	-	+	+	-	-	+	+	-	-
	5	+	+	-	-	+	+	-	-	+	+	-	-	+	+	-	-
	6	-	-	+	+	-	-	+	+	-	-	+	+	-	-	+	+
	7	-	-	+	+	-	-	+	+	-	-	+	+	-	-	+	+
	8	+	+	-	-	+	+	-	-	+	+	-	-	+	+	-	-
Spin reversal symmetry		+	+	-	-	+	+	-	-	+	+	-	-	+	+	-	-
		+	+	-	-	+	+	-	-	+	+	-	-	+	+	-	-
		-	-	+	+	-	-	+	+	-	-	+	+	-	-	+	+
		-	-	+	+	-	-	+	+	-	-	+	+	-	-	+	+
		-	-	+	+	-	-	+	+	-	-	+	+	-	-	+	+
		+	+	-	-	+	+	-	-	+	+	-	-	+	+	-	-
		+	+	-	-	+	+	-	-	+	+	-	-	+	+	-	-
		-	-	+	+	-	-	+	+	-	-	+	+	-	-	+	+
Deg.		2															
Config. 25		-	-	+	+	-	+	-	+	+	+	-	-	+	-	+	-
Crystalline symmetry	1	-	-	+	+	-	+	-	+	+	+	-	-	+	-	+	-
	2	-	-	+	+	+	-	+	-	+	+	-	-	-	+	-	+
	3	+	+	-	-	+	-	+	-	-	-	+	+	-	+	-	+
	4	+	+	-	-	-	+	-	+	-	-	+	+	+	-	+	-
	5	-	-	+	+	-	+	-	+	+	+	-	-	+	-	+	-
	6	+	+	-	-	-	+	-	+	-	-	+	+	+	-	+	-
	7	+	+	-	-	+	-	+	-	-	-	+	+	-	+	-	+
	8	-	-	+	+	+	-	+	-	+	+	-	-	-	+	-	+
Spin reversal symmetry		+	+	-	-	+	-	+	-	-	-	+	+	-	+	-	+
		+	+	-	-	-	+	-	+	-	-	+	+	+	-	+	-
		-	-	+	+	-	+	-	+	+	+	-	-	+	-	+	-
		-	-	+	+	+	-	+	-	+	+	-	-	-	+	-	+
		+	+	-	-	+	-	+	-	-	-	+	+	-	+	-	+
		-	-	+	+	+	-	+	-	+	+	-	-	-	+	-	+
		-	-	+	+	-	+	-	+	+	+	-	-	+	-	+	-
		+	+	-	-	-	+	-	+	-	-	+	+	+	-	+	-
Deg.		4															
Config. 26		-	-	+	+	-	+	-	+	-	-	+	+	-	+	-	+
Crystalline symmetry	1	-	-	+	+	-	+	-	+	-	-	+	+	-	+	-	+
	2	-	-	+	+	+	-	+	-	-	-	+	+	+	-	+	-
	3	+	+	-	-	+	-	+	-	+	+	-	-	+	-	+	-
	4	+	+	-	-	-	+	-	+	+	+	-	-	-	+	-	+
	5	+	+	-	-	+	-	+	-	+	+	-	-	+	-	+	-
	6	-	-	+	+	+	-	+	-	-	-	+	+	+	-	+	-
	7	-	-	+	+	-	+	-	+	-	-	+	+	-	+	-	+
	8	+	+	-	-	-	+	-	+	+	+	-	-	-	+	-	+
Spin reversal		+	+	-	-	+	-	+	-	+	+	-	-	+	-	+	-

symmetry		+	+	-	-	-	+	-	+	+	+	-	-	-	+	-	+
		-	-	+	+	-	+	-	+	-	-	+	+	-	+	-	+
		-	-	+	+	+	-	+	-	-	-	+	+	+	-	+	-
		-	-	+	+	-	+	-	+	-	-	+	+	-	+	-	+
		+	+	-	-	-	+	-	+	+	+	-	-	-	+	-	+
		+	+	-	-	+	-	+	-	+	+	-	-	+	-	+	-
		-	-	+	+	+	-	+	-	-	-	+	+	+	-	+	-
Deg.		4															
Config. 27		-	+	+	-	-	-	+	+	+	-	-	+	+	+	-	-
Crystalline symmetry	1	-	+	+	-	-	-	+	+	+	-	-	+	+	+	-	-
	2	+	-	-	+	-	-	+	+	-	+	+	-	+	+	-	-
	3	-	+	+	-	+	+	-	-	+	-	-	+	-	-	+	+
	4	+	-	-	+	+	+	-	-	-	+	+	-	-	-	+	+
	5	+	-	-	+	-	-	+	+	-	+	+	-	+	+	-	-
	6	-	+	+	-	+	+	-	-	+	-	-	+	-	-	+	+
	7	+	-	-	+	+	+	-	-	-	+	+	-	-	-	+	+
	8	-	+	+	-	-	-	+	+	+	-	-	+	+	+	-	-
Spin reversal symmetry		+	-	-	+	+	+	-	-	-	+	+	-	-	-	+	+
		-	+	+	-	+	+	-	-	+	-	-	+	-	-	+	+
		+	-	-	+	-	-	+	+	-	+	+	-	+	+	-	-
		-	+	+	-	-	-	+	+	+	-	-	+	+	+	-	-

		-	+	+	-	+	+	-	-	+	-	-	+	-	-	+	+
		+	-	-	+	-	-	+	+	-	+	+	-	+	+	-	-
		-	+	+	-	-	-	+	+	+	-	-	+	+	+	-	-
		+	-	-	+	+	+	-	-	-	+	+	-	-	-	+	+
Deg.		4															
Config. 28		-	+	+	-	-	-	+	+	-	+	+	-	-	-	+	+
Crystalline symmetry	1	-	+	+	-	-	-	+	+	-	+	+	-	-	-	+	+
	2	+	-	-	+	-	-	+	+	+	-	-	+	-	-	+	+
	3	-	+	+	-	+	+	-	-	-	+	+	-	+	+	-	-
	4	+	-	-	+	+	+	-	-	+	-	-	+	+	+	-	-
	5	-	+	+	-	+	+	-	-	-	+	+	-	+	+	-	-
	6	+	-	-	+	-	-	+	+	+	-	-	+	-	-	+	+
	7	-	+	+	-	-	-	+	+	-	+	+	-	-	-	+	+
	8	+	-	-	+	+	+	-	-	+	-	-	+	+	+	-	-
Spin reversal symmetry		+	-	-	+	+	+	-	-	+	-	-	+	+	+	-	-
		-	+	+	-	+	+	-	-	-	+	+	-	+	+	-	-
		+	-	-	+	-	-	+	+	+	-	-	+	-	-	+	+
		-	+	+	-	-	-	+	+	-	+	+	-	-	-	+	+
		+	-	-	+	-	-	+	+	+	-	-	+	-	-	+	+
		-	+	+	-	+	+	-	-	-	+	+	-	+	+	-	-
		+	-	-	+	+	+	-	-	+	-	-	+	+	+	-	-

		-	+	+	-	-	-	+	+	-	+	+	-	-	-	+	+
Deg.		4															
Config. 29		-	+	+	-	-	+	-	+	+	-	-	+	+	-	+	-
Crystalline symmetry	1	-	+	+	-	-	+	-	+	+	-	-	+	+	-	+	-
	2	+	-	-	+	+	-	+	-	-	+	+	-	-	+	-	+
	3	-	+	+	-	+	-	+	-	+	-	-	+	-	+	-	+
	4	+	-	-	+	-	+	-	+	-	+	+	-	+	-	+	-
	5	+	-	-	+	-	+	-	+	-	+	+	-	+	-	+	-
	6	-	+	+	-	-	+	-	+	+	-	-	+	+	-	+	-
	7	+	-	-	+	+	-	+	-	-	+	+	-	-	+	-	+
	8	-	+	+	-	+	-	+	-	+	-	-	+	-	+	-	+
Spin reversal symmetry		+	-	-	+	+	-	+	-	-	+	+	-	-	+	-	+
		-	+	+	-	-	+	-	+	+	-	-	+	+	-	+	-
		+	-	-	+	-	+	-	+	-	+	+	-	+	-	+	-
		-	+	+	-	+	-	+	-	+	-	-	+	-	+	-	+
		-	+	+	-	+	-	+	-	+	-	-	+	-	+	-	+
		+	-	-	+	+	-	+	-	-	+	+	-	-	+	-	+
		-	+	+	-	-	+	-	+	+	-	-	+	+	-	+	-
		+	-	-	+	-	+	-	+	-	+	+	-	+	-	+	-
Deg.		4															
Config. 30		-	+	+	-	-	+	-	+	-	+	+	-	-	+	-	+

Crystalline symmetry	1	-	+	+	-	-	+	-	+	-	+	+	-	-	+	-	+
	2	+	-	-	+	+	-	+	-	+	-	-	+	+	-	+	-
	3	-	+	+	-	+	-	+	-	-	+	+	-	+	-	+	-
	4	+	-	-	+	-	+	-	+	+	-	-	+	-	+	-	+
	5	-	+	+	-	+	-	+	-	-	+	+	-	+	-	+	-
	6	+	-	-	+	+	-	+	-	+	-	-	+	+	-	+	-
	7	-	+	+	-	-	+	-	+	-	+	+	-	-	+	-	+
	8	+	-	-	+	-	+	-	+	+	-	-	+	-	+	-	+
Spin reversal symmetry		+	-	-	+	+	-	+	-	+	-	-	+	+	-	+	-
		-	+	+	-	-	+	-	+	-	+	+	-	-	+	-	+
		+	-	-	+	-	+	-	+	+	-	-	+	-	+	-	+
		-	+	+	-	+	-	+	-	-	+	+	-	+	-	+	-
		+	-	-	+	-	+	-	+	+	-	-	+	-	+	-	+
		-	+	+	-	-	+	-	+	-	+	+	-	-	+	-	+
		+	-	-	+	+	-	+	-	+	-	-	+	+	-	+	-
		-	+	+	-	+	-	+	-	-	+	+	-	+	-	+	-
Deg.		4															
Config. 31		-	+	+	-	+	-	-	+	+	-	-	+	-	+	+	-
Crystalline symmetry	1	-	+	+	-	+	-	-	+	+	-	-	+	-	+	+	-
	2	+	-	-	+	-	+	+	-	-	+	+	-	+	-	-	+
	3	-	+	+	-	+	-	-	+	+	-	-	+	-	+	+	-

	4	+	-	-	+	-	+	+	-	-	+	+	-	+	-	-	+
	5	+	-	-	+	-	+	+	-	-	+	+	-	+	-	-	+
	6	-	+	+	-	+	-	-	+	+	-	-	+	-	+	+	-
	7	+	-	-	+	-	+	+	-	-	+	+	-	+	-	-	+
	8	-	+	+	-	+	-	-	+	+	-	-	+	-	+	+	-
Spin reversal symmetry		+	-	-	+	-	+	+	-	-	+	+	-	+	-	-	+
		-	+	+	-	+	-	-	+	+	-	-	+	-	+	+	-
		+	-	-	+	-	+	+	-	-	+	+	-	+	-	-	+
		-	+	+	-	+	-	-	+	+	-	-	+	-	+	+	-
		-	+	+	-	+	-	-	+	+	-	-	+	-	+	+	-
		+	-	-	+	-	+	+	-	-	+	+	-	+	-	-	+
		-	+	+	-	+	-	-	+	+	-	-	+	-	+	+	-
		+	-	-	+	-	+	+	-	-	+	+	-	+	-	-	+
Deg.		2															
Config. 32		-	+	+	-	+	-	-	+	-	+	+	-	+	-	-	+
Crystalline symmetry	1	-	+	+	-	+	-	-	+	-	+	+	-	+	-	-	+
	2	+	-	-	+	-	+	+	-	+	-	-	+	-	+	+	-
	3	-	+	+	-	+	-	-	+	-	+	+	-	+	-	-	+
	4	+	-	-	+	-	+	+	-	+	-	-	+	-	+	+	-
	5	-	+	+	-	+	-	-	+	-	+	+	-	+	-	-	+
	6	+	-	-	+	-	+	+	-	+	-	-	+	-	+	+	-

	7	-	+	+	-	+	-	-	+	-	+	+	-	+	-	-	+
	8	+	-	-	+	-	+	+	-	+	-	-	+	-	+	+	-
Spin reversal symmetry		+	-	-	+	-	+	+	-	+	-	-	+	-	+	+	-
		-	+	+	-	+	-	-	+	-	+	+	-	+	-	-	+
		+	-	-	+	-	+	+	-	+	-	-	+	-	+	+	-
		-	+	+	-	+	-	-	+	-	+	+	-	+	-	-	+
		+	-	-	+	-	+	+	-	+	-	-	+	-	+	+	-
		-	+	+	-	+	-	-	+	-	+	+	-	+	-	-	+
		+	-	-	+	-	+	+	-	+	-	-	+	-	+	+	-
		-	+	+	-	+	-	-	+	-	+	+	-	+	-	-	+
Deg.		2															

Appendix V

All the possible interactions in the $2 \times 1 \times 1$ supercell

J	Symmetry equivalent J	$\mathbf{S}_i\cdot \mathbf{S}_j$	Symmetry Operator 1	Symmetry Operator 2	Symmetry Operator 3	Symmetry Operator 4	Symmetry Operator 5	Symmetry Operator 6	Symmetry Operator 7	Symmetry Operator 8
J_1	-	$\mathbf{S}_1\cdot \mathbf{S}_2$	$\mathbf{S}_1\cdot \mathbf{S}_2$	$\mathbf{S}_2\cdot \mathbf{S}_1$	$\mathbf{S}_4\cdot \mathbf{S}_3$	$\mathbf{S}_3\cdot \mathbf{S}_4$	$\mathbf{S}_{12}\cdot \mathbf{S}_{11}$	$\mathbf{S}_{10}\cdot \mathbf{S}_9$	$\mathbf{S}_9\cdot \mathbf{S}_{10}$	$\mathbf{S}_{11}\cdot \mathbf{S}_{12}$
J_2	-	$\mathbf{S}_1\cdot \mathbf{S}_3$	$\mathbf{S}_1\cdot \mathbf{S}_3$	$\mathbf{S}_2\cdot \mathbf{S}_4$	$\mathbf{S}_4\cdot \mathbf{S}_2$	$\mathbf{S}_3\cdot \mathbf{S}_1$	$\mathbf{S}_{12}\cdot \mathbf{S}_{10}$	$\mathbf{S}_{10}\cdot \mathbf{S}_{12}$	$\mathbf{S}_9\cdot \mathbf{S}_{11}$	$\mathbf{S}_{11}\cdot \mathbf{S}_9$
J_3	-	$\mathbf{S}_1\cdot \mathbf{S}_4$	$\mathbf{S}_1\cdot \mathbf{S}_4$	$\mathbf{S}_2\cdot \mathbf{S}_3$	$\mathbf{S}_4\cdot \mathbf{S}_1$	$\mathbf{S}_3\cdot \mathbf{S}_2$	$\mathbf{S}_{12}\cdot \mathbf{S}_9$	$\mathbf{S}_{10}\cdot \mathbf{S}_{11}$	$\mathbf{S}_9\cdot \mathbf{S}_{12}$	$\mathbf{S}_{11}\cdot \mathbf{S}_{10}$
J_4	-	$\mathbf{S}_1\cdot \mathbf{S}_5$	$\mathbf{S}_1\cdot \mathbf{S}_5$	$\mathbf{S}_2\cdot \mathbf{S}_6$	$\mathbf{S}_4\cdot \mathbf{S}_8$	$\mathbf{S}_3\cdot \mathbf{S}_7$	$\mathbf{S}_{12}\cdot \mathbf{S}_{16}$	$\mathbf{S}_{10}\cdot \mathbf{S}_{14}$	$\mathbf{S}_9\cdot \mathbf{S}_{13}$	$\mathbf{S}_{11}\cdot \mathbf{S}_{15}$
J_5	-	$\mathbf{S}_1\cdot \mathbf{S}_6$	$\mathbf{S}_1\cdot \mathbf{S}_6$	$\mathbf{S}_2\cdot \mathbf{S}_5$	$\mathbf{S}_4\cdot \mathbf{S}_7$	$\mathbf{S}_3\cdot \mathbf{S}_8$	$\mathbf{S}_{12}\cdot \mathbf{S}_{15}$	$\mathbf{S}_{10}\cdot \mathbf{S}_{13}$	$\mathbf{S}_9\cdot \mathbf{S}_{14}$	$\mathbf{S}_{11}\cdot \mathbf{S}_{16}$
J_6	-	$\mathbf{S}_1\cdot \mathbf{S}_7$	$\mathbf{S}_1\cdot \mathbf{S}_7$	$\mathbf{S}_2\cdot \mathbf{S}_8$	$\mathbf{S}_4\cdot \mathbf{S}_6$	$\mathbf{S}_3\cdot \mathbf{S}_5$	$\mathbf{S}_{12}\cdot \mathbf{S}_{14}$	$\mathbf{S}_{10}\cdot \mathbf{S}_{16}$	$\mathbf{S}_9\cdot \mathbf{S}_{15}$	$\mathbf{S}_{11}\cdot \mathbf{S}_{13}$
J_7	-	$\mathbf{S}_1\cdot \mathbf{S}_8$	$\mathbf{S}_1\cdot \mathbf{S}_8$	$\mathbf{S}_2\cdot \mathbf{S}_7$	$\mathbf{S}_4\cdot \mathbf{S}_5$	$\mathbf{S}_3\cdot \mathbf{S}_6$	$\mathbf{S}_{12}\cdot \mathbf{S}_{13}$	$\mathbf{S}_{10}\cdot \mathbf{S}_{15}$	$\mathbf{S}_9\cdot \mathbf{S}_{16}$	$\mathbf{S}_{11}\cdot \mathbf{S}_{14}$
J_8	-	$\mathbf{S}_1\cdot \mathbf{S}_9$	$\mathbf{S}_1\cdot \mathbf{S}_9$	$\mathbf{S}_2\cdot \mathbf{S}_{10}$	$\mathbf{S}_4\cdot \mathbf{S}_{12}$	$\mathbf{S}_3\cdot \mathbf{S}_{11}$	$\mathbf{S}_{12}\cdot \mathbf{S}_4$	$\mathbf{S}_{10}\cdot \mathbf{S}_2$	$\mathbf{S}_9\cdot \mathbf{S}_1$	$\mathbf{S}_{11}\cdot \mathbf{S}_3$
J_9	-	$\mathbf{S}_1\cdot \mathbf{S}_{10}$	$\mathbf{S}_1\cdot \mathbf{S}_{10}$	$\mathbf{S}_2\cdot \mathbf{S}_9$	$\mathbf{S}_4\cdot \mathbf{S}_{11}$	$\mathbf{S}_3\cdot \mathbf{S}_{12}$	$\mathbf{S}_{12}\cdot \mathbf{S}_3$	$\mathbf{S}_{10}\cdot \mathbf{S}_1$	$\mathbf{S}_9\cdot \mathbf{S}_2$	$\mathbf{S}_{11}\cdot \mathbf{S}_4$
J_{10}	-	$\mathbf{S}_1\cdot \mathbf{S}_{11}$	$\mathbf{S}_1\cdot \mathbf{S}_{11}$	$\mathbf{S}_2\cdot \mathbf{S}_{12}$	$\mathbf{S}_4\cdot \mathbf{S}_{10}$	$\mathbf{S}_3\cdot \mathbf{S}_9$	$\mathbf{S}_{12}\cdot \mathbf{S}_2$	$\mathbf{S}_{10}\cdot \mathbf{S}_4$	$\mathbf{S}_9\cdot \mathbf{S}_3$	$\mathbf{S}_{11}\cdot \mathbf{S}_1$
J_{11}	-	$\mathbf{S}_1\cdot \mathbf{S}_{12}$	$\mathbf{S}_1\cdot \mathbf{S}_{12}$	$\mathbf{S}_2\cdot \mathbf{S}_{11}$	$\mathbf{S}_4\cdot \mathbf{S}_9$	$\mathbf{S}_3\cdot \mathbf{S}_{10}$	$\mathbf{S}_{12}\cdot \mathbf{S}_1$	$\mathbf{S}_{10}\cdot \mathbf{S}_3$	$\mathbf{S}_9\cdot \mathbf{S}_4$	$\mathbf{S}_{11}\cdot \mathbf{S}_2$
J_{12}	-	$\mathbf{S}_1\cdot \mathbf{S}_{13}$	$\mathbf{S}_1\cdot \mathbf{S}_{13}$	$\mathbf{S}_2\cdot \mathbf{S}_{14}$	$\mathbf{S}_4\cdot \mathbf{S}_{16}$	$\mathbf{S}_3\cdot \mathbf{S}_{15}$	$\mathbf{S}_{12}\cdot \mathbf{S}_8$	$\mathbf{S}_{10}\cdot \mathbf{S}_6$	$\mathbf{S}_9\cdot \mathbf{S}_5$	$\mathbf{S}_{11}\cdot \mathbf{S}_7$
J_{13}	-	$\mathbf{S}_1\cdot \mathbf{S}_{14}$	$\mathbf{S}_1\cdot \mathbf{S}_{14}$	$\mathbf{S}_2\cdot \mathbf{S}_{13}$	$\mathbf{S}_4\cdot \mathbf{S}_{15}$	$\mathbf{S}_3\cdot \mathbf{S}_{16}$	$\mathbf{S}_{12}\cdot \mathbf{S}_7$	$\mathbf{S}_{10}\cdot \mathbf{S}_5$	$\mathbf{S}_9\cdot \mathbf{S}_6$	$\mathbf{S}_{11}\cdot \mathbf{S}_8$
J_{14}	-	$\mathbf{S}_1\cdot \mathbf{S}_{15}$	$\mathbf{S}_1\cdot \mathbf{S}_{15}$	$\mathbf{S}_2\cdot \mathbf{S}_{16}$	$\mathbf{S}_4\cdot \mathbf{S}_{14}$	$\mathbf{S}_3\cdot \mathbf{S}_{13}$	$\mathbf{S}_{12}\cdot \mathbf{S}_6$	$\mathbf{S}_{10}\cdot \mathbf{S}_8$	$\mathbf{S}_9\cdot \mathbf{S}_7$	$\mathbf{S}_{11}\cdot \mathbf{S}_5$
J_{15}	-	$\mathbf{S}_1\cdot \mathbf{S}_{16}$	$\mathbf{S}_1\cdot \mathbf{S}_{16}$	$\mathbf{S}_2\cdot \mathbf{S}_{15}$	$\mathbf{S}_4\cdot \mathbf{S}_{13}$	$\mathbf{S}_3\cdot \mathbf{S}_{14}$	$\mathbf{S}_{12}\cdot \mathbf{S}_5$	$\mathbf{S}_{10}\cdot \mathbf{S}_7$	$\mathbf{S}_9\cdot \mathbf{S}_8$	$\mathbf{S}_{11}\cdot \mathbf{S}_6$
J_{16}	J_3	$\mathbf{S}_2\cdot \mathbf{S}_3$	$\mathbf{S}_2\cdot \mathbf{S}_3$	$\mathbf{S}_1\cdot \mathbf{S}_4$	$\mathbf{S}_3\cdot \mathbf{S}_2$	$\mathbf{S}_4\cdot \mathbf{S}_1$	$\mathbf{S}_{11}\cdot \mathbf{S}_{10}$	$\mathbf{S}_9\cdot \mathbf{S}_{12}$	$\mathbf{S}_{10}\cdot \mathbf{S}_{11}$	$\mathbf{S}_{12}\cdot \mathbf{S}_9$
J_{17}	J_2	$\mathbf{S}_2\cdot \mathbf{S}_4$	$\mathbf{S}_2\cdot \mathbf{S}_4$	$\mathbf{S}_1\cdot \mathbf{S}_3$	$\mathbf{S}_3\cdot \mathbf{S}_1$	$\mathbf{S}_4\cdot \mathbf{S}_2$	$\mathbf{S}_{11}\cdot \mathbf{S}_9$	$\mathbf{S}_9\cdot \mathbf{S}_{11}$	$\mathbf{S}_{10}\cdot \mathbf{S}_{12}$	$\mathbf{S}_{12}\cdot \mathbf{S}_{10}$
J_{18}	J_5	$\mathbf{S}_2\cdot \mathbf{S}_5$	$\mathbf{S}_2\cdot \mathbf{S}_5$	$\mathbf{S}_1\cdot \mathbf{S}_6$	$\mathbf{S}_3\cdot \mathbf{S}_8$	$\mathbf{S}_4\cdot \mathbf{S}_7$	$\mathbf{S}_{11}\cdot \mathbf{S}_{16}$	$\mathbf{S}_9\cdot \mathbf{S}_{14}$	$\mathbf{S}_{10}\cdot \mathbf{S}_{13}$	$\mathbf{S}_{12}\cdot \mathbf{S}_{15}$
J_{19}	J_4	$\mathbf{S}_2\cdot \mathbf{S}_6$	$\mathbf{S}_2\cdot \mathbf{S}_6$	$\mathbf{S}_1\cdot \mathbf{S}_5$	$\mathbf{S}_3\cdot \mathbf{S}_7$	$\mathbf{S}_4\cdot \mathbf{S}_8$	$\mathbf{S}_{11}\cdot \mathbf{S}_{15}$	$\mathbf{S}_9\cdot \mathbf{S}_{13}$	$\mathbf{S}_{10}\cdot \mathbf{S}_{14}$	$\mathbf{S}_{12}\cdot \mathbf{S}_{16}$
J_{20}	J_7	$\mathbf{S}_2\cdot \mathbf{S}_7$	$\mathbf{S}_2\cdot \mathbf{S}_7$	$\mathbf{S}_1\cdot \mathbf{S}_8$	$\mathbf{S}_3\cdot \mathbf{S}_6$	$\mathbf{S}_4\cdot \mathbf{S}_5$	$\mathbf{S}_{11}\cdot \mathbf{S}_{14}$	$\mathbf{S}_9\cdot \mathbf{S}_{16}$	$\mathbf{S}_{10}\cdot \mathbf{S}_{15}$	$\mathbf{S}_{12}\cdot \mathbf{S}_{13}$
J_{21}	J_6	$\mathbf{S}_2\cdot \mathbf{S}_8$	$\mathbf{S}_2\cdot \mathbf{S}_8$	$\mathbf{S}_1\cdot \mathbf{S}_7$	$\mathbf{S}_3\cdot \mathbf{S}_5$	$\mathbf{S}_4\cdot \mathbf{S}_6$	$\mathbf{S}_{11}\cdot \mathbf{S}_{13}$	$\mathbf{S}_9\cdot \mathbf{S}_{15}$	$\mathbf{S}_{10}\cdot \mathbf{S}_{16}$	$\mathbf{S}_{12}\cdot \mathbf{S}_{14}$
J_{22}	J_9	$\mathbf{S}_2\cdot \mathbf{S}_9$	$\mathbf{S}_2\cdot \mathbf{S}_9$	$\mathbf{S}_1\cdot \mathbf{S}_{10}$	$\mathbf{S}_3\cdot \mathbf{S}_{12}$	$\mathbf{S}_4\cdot \mathbf{S}_{11}$	$\mathbf{S}_{11}\cdot \mathbf{S}_4$	$\mathbf{S}_9\cdot \mathbf{S}_2$	$\mathbf{S}_{10}\cdot \mathbf{S}_1$	$\mathbf{S}_{12}\cdot \mathbf{S}_3$
J_{23}	J_8	$\mathbf{S}_2\cdot \mathbf{S}_{10}$	$\mathbf{S}_2\cdot \mathbf{S}_{10}$	$\mathbf{S}_1\cdot \mathbf{S}_9$	$\mathbf{S}_3\cdot \mathbf{S}_{11}$	$\mathbf{S}_4\cdot \mathbf{S}_{12}$	$\mathbf{S}_{11}\cdot \mathbf{S}_3$	$\mathbf{S}_9\cdot \mathbf{S}_1$	$\mathbf{S}_{10}\cdot \mathbf{S}_2$	$\mathbf{S}_{12}\cdot \mathbf{S}_4$
J_{24}	J_{11}	$\mathbf{S}_2\cdot \mathbf{S}_{11}$	$\mathbf{S}_2\cdot \mathbf{S}_{11}$	$\mathbf{S}_1\cdot \mathbf{S}_{12}$	$\mathbf{S}_3\cdot \mathbf{S}_{10}$	$\mathbf{S}_4\cdot \mathbf{S}_9$	$\mathbf{S}_{11}\cdot \mathbf{S}_2$	$\mathbf{S}_9\cdot \mathbf{S}_4$	$\mathbf{S}_{10}\cdot \mathbf{S}_3$	$\mathbf{S}_{12}\cdot \mathbf{S}_1$
J_{25}	J_{10}	$\mathbf{S}_2\cdot \mathbf{S}_{12}$	$\mathbf{S}_2\cdot \mathbf{S}_{12}$	$\mathbf{S}_1\cdot \mathbf{S}_{11}$	$\mathbf{S}_3\cdot \mathbf{S}_9$	$\mathbf{S}_4\cdot \mathbf{S}_{10}$	$\mathbf{S}_{11}\cdot \mathbf{S}_1$	$\mathbf{S}_9\cdot \mathbf{S}_3$	$\mathbf{S}_{10}\cdot \mathbf{S}_4$	$\mathbf{S}_{12}\cdot \mathbf{S}$
J_{26}	J_{13}	$\mathbf{S}_2\cdot \mathbf{S}_{13}$	$\mathbf{S}_2\cdot \mathbf{S}_{13}$	$\mathbf{S}_1\cdot \mathbf{S}_{14}$	$\mathbf{S}_3\cdot \mathbf{S}_{16}$	$\mathbf{S}_4\cdot \mathbf{S}_{15}$	$\mathbf{S}_{11}\cdot \mathbf{S}_8$	$\mathbf{S}_9\cdot \mathbf{S}_6$	$\mathbf{S}_{10}\cdot \mathbf{S}_5$	$\mathbf{S}_{12}\cdot \mathbf{S}_7$
J_{27}	J_{12}	$\mathbf{S}_2\cdot \mathbf{S}_{14}$	$\mathbf{S}_2\cdot \mathbf{S}_{14}$	$\mathbf{S}_1\cdot \mathbf{S}_{13}$	$\mathbf{S}_3\cdot \mathbf{S}_{15}$	$\mathbf{S}_4\cdot \mathbf{S}_{16}$	$\mathbf{S}_{11}\cdot \mathbf{S}_7$	$\mathbf{S}_9\cdot \mathbf{S}_5$	$\mathbf{S}_{10}\cdot \mathbf{S}_6$	$\mathbf{S}_{12}\cdot \mathbf{S}_8$
J_{28}	J_{15}	$\mathbf{S}_2\cdot \mathbf{S}_{15}$	$\mathbf{S}_2\cdot \mathbf{S}_{15}$	$\mathbf{S}_1\cdot \mathbf{S}_{16}$	$\mathbf{S}_3\cdot \mathbf{S}_{14}$	$\mathbf{S}_4\cdot \mathbf{S}_{13}$	$\mathbf{S}_{11}\cdot \mathbf{S}_6$	$\mathbf{S}_9\cdot \mathbf{S}_8$	$\mathbf{S}_{10}\cdot \mathbf{S}_7$	$\mathbf{S}_{12}\cdot \mathbf{S}_5$
J_{29}	J_{14}	$\mathbf{S}_2\cdot \mathbf{S}_{16}$	$\mathbf{S}_2\cdot \mathbf{S}_{16}$	$\mathbf{S}_1\cdot \mathbf{S}_{15}$	$\mathbf{S}_3\cdot \mathbf{S}_{13}$	$\mathbf{S}_4\cdot \mathbf{S}_{14}$	$\mathbf{S}_{11}\cdot \mathbf{S}_5$	$\mathbf{S}_9\cdot \mathbf{S}_7$	$\mathbf{S}_{10}\cdot \mathbf{S}_8$	$\mathbf{S}_{12}\cdot \mathbf{S}_6$
J_{30}	J_1	$\mathbf{S}_3\cdot \mathbf{S}_4$	$\mathbf{S}_3\cdot \mathbf{S}_4$	$\mathbf{S}_4\cdot \mathbf{S}_3$	$\mathbf{S}_2\cdot \mathbf{S}_1$	$\mathbf{S}_1\cdot \mathbf{S}_2$	$\mathbf{S}_{10}\cdot \mathbf{S}_9$	$\mathbf{S}_{12}\cdot \mathbf{S}_{11}$	$\mathbf{S}_{11}\cdot \mathbf{S}_{12}$	$\mathbf{S}_9\cdot \mathbf{S}_{10}$
J_{31}	J_6	$\mathbf{S}_3\cdot \mathbf{S}_5$	$\mathbf{S}_3\cdot \mathbf{S}_5$	$\mathbf{S}_4\cdot \mathbf{S}_6$	$\mathbf{S}_2\cdot \mathbf{S}_8$	$\mathbf{S}_1\cdot \mathbf{S}_7$	$\mathbf{S}_{10}\cdot \mathbf{S}_{16}$	$\mathbf{S}_{12}\cdot \mathbf{S}_{14}$	$\mathbf{S}_{11}\cdot \mathbf{S}_{13}$	$\mathbf{S}_9\cdot \mathbf{S}_{15}$
J_{32}	J_7	$\mathbf{S}_3\cdot \mathbf{S}_6$	$\mathbf{S}_3\cdot \mathbf{S}_6$	$\mathbf{S}_4\cdot \mathbf{S}_5$	$\mathbf{S}_2\cdot \mathbf{S}_7$	$\mathbf{S}_1\cdot \mathbf{S}_8$	$\mathbf{S}_{10}\cdot \mathbf{S}_{15}$	$\mathbf{S}_{12}\cdot \mathbf{S}_{13}$	$\mathbf{S}_{11}\cdot \mathbf{S}_{14}$	$\mathbf{S}_9\cdot \mathbf{S}_{16}$

J_{33}	J_{4}	$\mathbf{S}_{3}\cdot\mathbf{S}_{7}$	$\mathbf{S}_{3}\cdot\mathbf{S}_{7}$	$\mathbf{S}_{4}\cdot\mathbf{S}_{8}$	$\mathbf{S}_{2}\cdot\mathbf{S}_{6}$	$\mathbf{S}_{1}\cdot\mathbf{S}_{5}$	$\mathbf{S}_{10}\cdot\mathbf{S}_{14}$	$\mathbf{S}_{12}\cdot\mathbf{S}_{16}$	$\mathbf{S}_{11}\cdot\mathbf{S}_{15}$	$\mathbf{S}_{9}\cdot\mathbf{S}_{13}$
J_{34}	J_{5}	$\mathbf{S}_{3}\cdot\mathbf{S}_{8}$	$\mathbf{S}_{3}\cdot\mathbf{S}_{8}$	$\mathbf{S}_{4}\cdot\mathbf{S}_{7}$	$\mathbf{S}_{2}\cdot\mathbf{S}_{5}$	$\mathbf{S}_{1}\cdot\mathbf{S}_{6}$	$\mathbf{S}_{10}\cdot\mathbf{S}_{13}$	$\mathbf{S}_{12}\cdot\mathbf{S}_{15}$	$\mathbf{S}_{11}\cdot\mathbf{S}_{16}$	$\mathbf{S}_{9}\cdot\mathbf{S}_{14}$
J_{35}	J_{10}	$\mathbf{S}_{3}\cdot\mathbf{S}_{9}$	$\mathbf{S}_{3}\cdot\mathbf{S}_{9}$	$\mathbf{S}_{4}\cdot\mathbf{S}_{10}$	$\mathbf{S}_{2}\cdot\mathbf{S}_{12}$	$\mathbf{S}_{1}\cdot\mathbf{S}_{11}$	$\mathbf{S}_{10}\cdot\mathbf{S}_{4}$	$\mathbf{S}_{12}\cdot\mathbf{S}_{2}$	$\mathbf{S}_{11}\cdot\mathbf{S}_{1}$	$\mathbf{S}_{9}\cdot\mathbf{S}_{3}$
J_{36}	J_{11}	$\mathbf{S}_{3}\cdot\mathbf{S}_{10}$	$\mathbf{S}_{3}\cdot\mathbf{S}_{10}$	$\mathbf{S}_{4}\cdot\mathbf{S}_{9}$	$\mathbf{S}_{2}\cdot\mathbf{S}_{11}$	$\mathbf{S}_{1}\cdot\mathbf{S}_{12}$	$\mathbf{S}_{10}\cdot\mathbf{S}_{3}$	$\mathbf{S}_{12}\cdot\mathbf{S}_{1}$	$\mathbf{S}_{11}\cdot\mathbf{S}_{2}$	$\mathbf{S}_{9}\cdot\mathbf{S}_{4}$
J_{37}	J_{8}	$\mathbf{S}_{3}\cdot\mathbf{S}_{11}$	$\mathbf{S}_{3}\cdot\mathbf{S}_{11}$	$\mathbf{S}_{4}\cdot\mathbf{S}_{12}$	$\mathbf{S}_{2}\cdot\mathbf{S}_{10}$	$\mathbf{S}_{1}\cdot\mathbf{S}_{9}$	$\mathbf{S}_{10}\cdot\mathbf{S}_{2}$	$\mathbf{S}_{12}\cdot\mathbf{S}_{4}$	$\mathbf{S}_{11}\cdot\mathbf{S}_{3}$	$\mathbf{S}_{9}\cdot\mathbf{S}_{1}$
J_{38}	J_{9}	$\mathbf{S}_{3}\cdot\mathbf{S}_{12}$	$\mathbf{S}_{3}\cdot\mathbf{S}_{12}$	$\mathbf{S}_{4}\cdot\mathbf{S}_{11}$	$\mathbf{S}_{2}\cdot\mathbf{S}_{9}$	$\mathbf{S}_{1}\cdot\mathbf{S}_{10}$	$\mathbf{S}_{10}\cdot\mathbf{S}_{1}$	$\mathbf{S}_{12}\cdot\mathbf{S}_{3}$	$\mathbf{S}_{11}\cdot\mathbf{S}_{4}$	$\mathbf{S}_{9}\cdot\mathbf{S}_{2}$
J_{39}	J_{14}	$\mathbf{S}_{3}\cdot\mathbf{S}_{13}$	$\mathbf{S}_{3}\cdot\mathbf{S}_{13}$	$\mathbf{S}_{4}\cdot\mathbf{S}_{14}$	$\mathbf{S}_{2}\cdot\mathbf{S}_{16}$	$\mathbf{S}_{1}\cdot\mathbf{S}_{15}$	$\mathbf{S}_{10}\cdot\mathbf{S}_{8}$	$\mathbf{S}_{12}\cdot\mathbf{S}_{6}$	$\mathbf{S}_{11}\cdot\mathbf{S}_{5}$	$\mathbf{S}_{9}\cdot\mathbf{S}_{7}$
J_{40}	J_{15}	$\mathbf{S}_{3}\cdot\mathbf{S}_{14}$	$\mathbf{S}_{3}\cdot\mathbf{S}_{14}$	$\mathbf{S}_{4}\cdot\mathbf{S}_{13}$	$\mathbf{S}_{2}\cdot\mathbf{S}_{15}$	$\mathbf{S}_{1}\cdot\mathbf{S}_{16}$	$\mathbf{S}_{10}\cdot\mathbf{S}_{7}$	$\mathbf{S}_{12}\cdot\mathbf{S}_{5}$	$\mathbf{S}_{11}\cdot\mathbf{S}_{6}$	$\mathbf{S}_{9}\cdot\mathbf{S}_{8}$
J_{41}	J_{12}	$\mathbf{S}_{3}\cdot\mathbf{S}_{15}$	$\mathbf{S}_{3}\cdot\mathbf{S}_{15}$	$\mathbf{S}_{4}\cdot\mathbf{S}_{16}$	$\mathbf{S}_{2}\cdot\mathbf{S}_{14}$	$\mathbf{S}_{1}\cdot\mathbf{S}_{13}$	$\mathbf{S}_{10}\cdot\mathbf{S}_{6}$	$\mathbf{S}_{12}\cdot\mathbf{S}_{8}$	$\mathbf{S}_{11}\cdot\mathbf{S}_{7}$	$\mathbf{S}_{9}\cdot\mathbf{S}_{5}$
J_{42}	J_{13}	$\mathbf{S}_{3}\cdot\mathbf{S}_{16}$	$\mathbf{S}_{3}\cdot\mathbf{S}_{16}$	$\mathbf{S}_{4}\cdot\mathbf{S}_{15}$	$\mathbf{S}_{2}\cdot\mathbf{S}_{13}$	$\mathbf{S}_{1}\cdot\mathbf{S}_{14}$	$\mathbf{S}_{10}\cdot\mathbf{S}_{5}$	$\mathbf{S}_{12}\cdot\mathbf{S}_{7}$	$\mathbf{S}_{11}\cdot\mathbf{S}_{8}$	$\mathbf{S}_{9}\cdot\mathbf{S}_{6}$
J_{43}	J_{7}	$\mathbf{S}_{4}\cdot\mathbf{S}_{5}$	$\mathbf{S}_{4}\cdot\mathbf{S}_{5}$	$\mathbf{S}_{3}\cdot\mathbf{S}_{6}$	$\mathbf{S}_{1}\cdot\mathbf{S}_{8}$	$\mathbf{S}_{2}\cdot\mathbf{S}_{7}$	$\mathbf{S}_{9}\cdot\mathbf{S}_{16}$	$\mathbf{S}_{11}\cdot\mathbf{S}_{14}$	$\mathbf{S}_{12}\cdot\mathbf{S}_{13}$	$\mathbf{S}_{10}\cdot\mathbf{S}_{15}$
J_{44}	J_{6}	$\mathbf{S}_{4}\cdot\mathbf{S}_{6}$	$\mathbf{S}_{4}\cdot\mathbf{S}_{6}$	$\mathbf{S}_{3}\cdot\mathbf{S}_{5}$	$\mathbf{S}_{1}\cdot\mathbf{S}_{7}$	$\mathbf{S}_{2}\cdot\mathbf{S}_{8}$	$\mathbf{S}_{9}\cdot\mathbf{S}_{15}$	$\mathbf{S}_{11}\cdot\mathbf{S}_{13}$	$\mathbf{S}_{12}\cdot\mathbf{S}_{14}$	$\mathbf{S}_{10}\cdot\mathbf{S}_{16}$
J_{45}	J_{5}	$\mathbf{S}_{4}\cdot\mathbf{S}_{7}$	$\mathbf{S}_{4}\cdot\mathbf{S}_{7}$	$\mathbf{S}_{3}\cdot\mathbf{S}_{8}$	$\mathbf{S}_{1}\cdot\mathbf{S}_{6}$	$\mathbf{S}_{2}\cdot\mathbf{S}_{5}$	$\mathbf{S}_{9}\cdot\mathbf{S}_{14}$	$\mathbf{S}_{11}\cdot\mathbf{S}_{16}$	$\mathbf{S}_{12}\cdot\mathbf{S}_{15}$	$\mathbf{S}_{10}\cdot\mathbf{S}_{13}$
J_{46}	J_{4}	$\mathbf{S}_{4}\cdot\mathbf{S}_{8}$	$\mathbf{S}_{4}\cdot\mathbf{S}_{8}$	$\mathbf{S}_{3}\cdot\mathbf{S}_{7}$	$\mathbf{S}_{1}\cdot\mathbf{S}_{5}$	$\mathbf{S}_{2}\cdot\mathbf{S}_{6}$	$\mathbf{S}_{9}\cdot\mathbf{S}_{13}$	$\mathbf{S}_{11}\cdot\mathbf{S}_{15}$	$\mathbf{S}_{12}\cdot\mathbf{S}_{16}$	$\mathbf{S}_{10}\cdot\mathbf{S}_{14}$
J_{47}	J_{11}	$\mathbf{S}_{4}\cdot\mathbf{S}_{9}$	$\mathbf{S}_{4}\cdot\mathbf{S}_{9}$	$\mathbf{S}_{3}\cdot\mathbf{S}_{10}$	$\mathbf{S}_{1}\cdot\mathbf{S}_{12}$	$\mathbf{S}_{2}\cdot\mathbf{S}_{11}$	$\mathbf{S}_{9}\cdot\mathbf{S}_{4}$	$\mathbf{S}_{11}\cdot\mathbf{S}_{2}$	$\mathbf{S}_{12}\cdot\mathbf{S}_{1}$	$\mathbf{S}_{10}\cdot\mathbf{S}_{3}$
J_{48}	J_{10}	$\mathbf{S}_{4}\cdot\mathbf{S}_{10}$	$\mathbf{S}_{4}\cdot\mathbf{S}_{10}$	$\mathbf{S}_{3}\cdot\mathbf{S}_{9}$	$\mathbf{S}_{1}\cdot\mathbf{S}_{11}$	$\mathbf{S}_{2}\cdot\mathbf{S}_{12}$	$\mathbf{S}_{9}\cdot\mathbf{S}_{3}$	$\mathbf{S}_{11}\cdot\mathbf{S}_{1}$	$\mathbf{S}_{12}\cdot\mathbf{S}_{2}$	$\mathbf{S}_{10}\cdot\mathbf{S}_{4}$
J_{49}	J_{9}	$\mathbf{S}_{4}\cdot\mathbf{S}_{11}$	$\mathbf{S}_{4}\cdot\mathbf{S}_{11}$	$\mathbf{S}_{3}\cdot\mathbf{S}_{12}$	$\mathbf{S}_{1}\cdot\mathbf{S}_{10}$	$\mathbf{S}_{2}\cdot\mathbf{S}_{9}$	$\mathbf{S}_{9}\cdot\mathbf{S}_{2}$	$\mathbf{S}_{11}\cdot\mathbf{S}_{4}$	$\mathbf{S}_{12}\cdot\mathbf{S}_{3}$	$\mathbf{S}_{10}\cdot\mathbf{S}_{1}$
J_{50}	J_{8}	$\mathbf{S}_{4}\cdot\mathbf{S}_{12}$	$\mathbf{S}_{4}\cdot\mathbf{S}_{12}$	$\mathbf{S}_{3}\cdot\mathbf{S}_{11}$	$\mathbf{S}_{1}\cdot\mathbf{S}_{9}$	$\mathbf{S}_{2}\cdot\mathbf{S}_{10}$	$\mathbf{S}_{9}\cdot\mathbf{S}_{1}$	$\mathbf{S}_{11}\cdot\mathbf{S}_{3}$	$\mathbf{S}_{12}\cdot\mathbf{S}_{4}$	$\mathbf{S}_{10}\cdot\mathbf{S}_{2}$
J_{51}	J_{15}	$\mathbf{S}_{4}\cdot\mathbf{S}_{13}$	$\mathbf{S}_{4}\cdot\mathbf{S}_{13}$	$\mathbf{S}_{3}\cdot\mathbf{S}_{14}$	$\mathbf{S}_{1}\cdot\mathbf{S}_{16}$	$\mathbf{S}_{2}\cdot\mathbf{S}_{15}$	$\mathbf{S}_{9}\cdot\mathbf{S}_{8}$	$\mathbf{S}_{11}\cdot\mathbf{S}_{6}$	$\mathbf{S}_{12}\cdot\mathbf{S}_{5}$	$\mathbf{S}_{10}\cdot\mathbf{S}_{7}$
J_{52}	J_{14}	$\mathbf{S}_{4}\cdot\mathbf{S}_{14}$	$\mathbf{S}_{4}\cdot\mathbf{S}_{14}$	$\mathbf{S}_{3}\cdot\mathbf{S}_{13}$	$\mathbf{S}_{1}\cdot\mathbf{S}_{15}$	$\mathbf{S}_{2}\cdot\mathbf{S}_{16}$	$\mathbf{S}_{9}\cdot\mathbf{S}_{7}$	$\mathbf{S}_{11}\cdot\mathbf{S}_{5}$	$\mathbf{S}_{12}\cdot\mathbf{S}_{6}$	$\mathbf{S}_{10}\cdot\mathbf{S}_{8}$
J_{53}	J_{13}	$\mathbf{S}_{4}\cdot\mathbf{S}_{15}$	$\mathbf{S}_{4}\cdot\mathbf{S}_{15}$	$\mathbf{S}_{3}\cdot\mathbf{S}_{16}$	$\mathbf{S}_{1}\cdot\mathbf{S}_{14}$	$\mathbf{S}_{2}\cdot\mathbf{S}_{13}$	$\mathbf{S}_{9}\cdot\mathbf{S}_{6}$	$\mathbf{S}_{11}\cdot\mathbf{S}_{8}$	$\mathbf{S}_{12}\cdot\mathbf{S}_{7}$	$\mathbf{S}_{10}\cdot\mathbf{S}_{5}$
J_{54}	J_{12}	$\mathbf{S}_{4}\cdot\mathbf{S}_{16}$	$\mathbf{S}_{4}\cdot\mathbf{S}_{16}$	$\mathbf{S}_{3}\cdot\mathbf{S}_{15}$	$\mathbf{S}_{1}\cdot\mathbf{S}_{13}$	$\mathbf{S}_{2}\cdot\mathbf{S}_{14}$	$\mathbf{S}_{9}\cdot\mathbf{S}_{5}$	$\mathbf{S}_{11}\cdot\mathbf{S}_{7}$	$\mathbf{S}_{12}\cdot\mathbf{S}_{8}$	$\mathbf{S}_{10}\cdot\mathbf{S}_{6}$
J_{55}	-	$\mathbf{S}_{5}\cdot\mathbf{S}_{6}$	$\mathbf{S}_{5}\cdot\mathbf{S}_{6}$	$\mathbf{S}_{6}\cdot\mathbf{S}_{5}$	$\mathbf{S}_{8}\cdot\mathbf{S}_{7}$	$\mathbf{S}_{7}\cdot\mathbf{S}_{8}$	$\mathbf{S}_{16}\cdot\mathbf{S}_{15}$	$\mathbf{S}_{14}\cdot\mathbf{S}_{13}$	$\mathbf{S}_{13}\cdot\mathbf{S}_{14}$	$\mathbf{S}_{15}\cdot\mathbf{S}_{16}$
J_{56}	-	$\mathbf{S}_{5}\cdot\mathbf{S}_{7}$	$\mathbf{S}_{5}\cdot\mathbf{S}_{7}$	$\mathbf{S}_{6}\cdot\mathbf{S}_{8}$	$\mathbf{S}_{8}\cdot\mathbf{S}_{6}$	$\mathbf{S}_{7}\cdot\mathbf{S}_{5}$	$\mathbf{S}_{16}\cdot\mathbf{S}_{14}$	$\mathbf{S}_{14}\cdot\mathbf{S}_{16}$	$\mathbf{S}_{13}\cdot\mathbf{S}_{15}$	$\mathbf{S}_{15}\cdot\mathbf{S}_{13}$
J_{57}	-	$\mathbf{S}_{5}\cdot\mathbf{S}_{8}$	$\mathbf{S}_{5}\cdot\mathbf{S}_{8}$	$\mathbf{S}_{6}\cdot\mathbf{S}_{7}$	$\mathbf{S}_{8}\cdot\mathbf{S}_{5}$	$\mathbf{S}_{7}\cdot\mathbf{S}_{6}$	$\mathbf{S}_{16}\cdot\mathbf{S}_{13}$	$\mathbf{S}_{14}\cdot\mathbf{S}_{15}$	$\mathbf{S}_{13}\cdot\mathbf{S}_{16}$	$\mathbf{S}_{15}\cdot\mathbf{S}_{14}$
J_{58}	J_{12}	$\mathbf{S}_{5}\cdot\mathbf{S}_{9}$	$\mathbf{S}_{5}\cdot\mathbf{S}_{9}$	$\mathbf{S}_{6}\cdot\mathbf{S}_{10}$	$\mathbf{S}_{8}\cdot\mathbf{S}_{12}$	$\mathbf{S}_{7}\cdot\mathbf{S}_{11}$	$\mathbf{S}_{16}\cdot\mathbf{S}_{4}$	$\mathbf{S}_{14}\cdot\mathbf{S}_{2}$	$\mathbf{S}_{13}\cdot\mathbf{S}_{1}$	$\mathbf{S}_{15}\cdot\mathbf{S}_{3}$
J_{59}	J_{13}	$\mathbf{S}_{5}\cdot\mathbf{S}_{10}$	$\mathbf{S}_{5}\cdot\mathbf{S}_{10}$	$\mathbf{S}_{6}\cdot\mathbf{S}_{9}$	$\mathbf{S}_{8}\cdot\mathbf{S}_{11}$	$\mathbf{S}_{7}\cdot\mathbf{S}_{12}$	$\mathbf{S}_{16}\cdot\mathbf{S}_{3}$	$\mathbf{S}_{14}\cdot\mathbf{S}_{1}$	$\mathbf{S}_{13}\cdot\mathbf{S}_{2}$	$\mathbf{S}_{15}\cdot\mathbf{S}_{4}$
J_{60}	J_{14}	$\mathbf{S}_{5}\cdot\mathbf{S}_{11}$	$\mathbf{S}_{5}\cdot\mathbf{S}_{11}$	$\mathbf{S}_{6}\cdot\mathbf{S}_{12}$	$\mathbf{S}_{8}\cdot\mathbf{S}_{10}$	$\mathbf{S}_{7}\cdot\mathbf{S}_{9}$	$\mathbf{S}_{16}\cdot\mathbf{S}_{2}$	$\mathbf{S}_{14}\cdot\mathbf{S}_{4}$	$\mathbf{S}_{13}\cdot\mathbf{S}_{3}$	$\mathbf{S}_{15}\cdot\mathbf{S}_{1}$
J_{61}	J_{15}	$\mathbf{S}_{5}\cdot\mathbf{S}_{12}$	$\mathbf{S}_{5}\cdot\mathbf{S}_{12}$	$\mathbf{S}_{6}\cdot\mathbf{S}_{11}$	$\mathbf{S}_{8}\cdot\mathbf{S}_{9}$	$\mathbf{S}_{7}\cdot\mathbf{S}_{10}$	$\mathbf{S}_{16}\cdot\mathbf{S}_{1}$	$\mathbf{S}_{14}\cdot\mathbf{S}_{3}$	$\mathbf{S}_{13}\cdot\mathbf{S}_{4}$	$\mathbf{S}_{15}\cdot\mathbf{S}_{2}$
J_{62}	-	$\mathbf{S}_{5}\cdot\mathbf{S}_{13}$	$\mathbf{S}_{5}\cdot\mathbf{S}_{13}$	$\mathbf{S}_{6}\cdot\mathbf{S}_{14}$	$\mathbf{S}_{8}\cdot\mathbf{S}_{16}$	$\mathbf{S}_{7}\cdot\mathbf{S}_{15}$	$\mathbf{S}_{16}\cdot\mathbf{S}_{8}$	$\mathbf{S}_{14}\cdot\mathbf{S}_{6}$	$\mathbf{S}_{13}\cdot\mathbf{S}_{5}$	$\mathbf{S}_{15}\cdot\mathbf{S}_{7}$
J_{63}	-	$\mathbf{S}_{5}\cdot\mathbf{S}_{14}$	$\mathbf{S}_{5}\cdot\mathbf{S}_{14}$	$\mathbf{S}_{6}\cdot\mathbf{S}_{13}$	$\mathbf{S}_{8}\cdot\mathbf{S}_{15}$	$\mathbf{S}_{7}\cdot\mathbf{S}_{16}$	$\mathbf{S}_{16}\cdot\mathbf{S}_{7}$	$\mathbf{S}_{14}\cdot\mathbf{S}_{5}$	$\mathbf{S}_{13}\cdot\mathbf{S}_{6}$	$\mathbf{S}_{15}\cdot\mathbf{S}_{8}$
J_{64}	-	$\mathbf{S}_{5}\cdot\mathbf{S}_{15}$	$\mathbf{S}_{5}\cdot\mathbf{S}_{15}$	$\mathbf{S}_{6}\cdot\mathbf{S}_{16}$	$\mathbf{S}_{8}\cdot\mathbf{S}_{14}$	$\mathbf{S}_{7}\cdot\mathbf{S}_{13}$	$\mathbf{S}_{16}\cdot\mathbf{S}_{6}$	$\mathbf{S}_{14}\cdot\mathbf{S}_{8}$	$\mathbf{S}_{13}\cdot\mathbf{S}_{7}$	$\mathbf{S}_{15}\cdot\mathbf{S}_{5}$
J_{65}	-	$\mathbf{S}_{5}\cdot\mathbf{S}_{16}$	$\mathbf{S}_{5}\cdot\mathbf{S}_{16}$	$\mathbf{S}_{6}\cdot\mathbf{S}_{15}$	$\mathbf{S}_{8}\cdot\mathbf{S}_{13}$	$\mathbf{S}_{7}\cdot\mathbf{S}_{14}$	$\mathbf{S}_{16}\cdot\mathbf{S}_{5}$	$\mathbf{S}_{14}\cdot\mathbf{S}_{7}$	$\mathbf{S}_{13}\cdot\mathbf{S}_{8}$	$\mathbf{S}_{15}\cdot\mathbf{S}_{6}$
J_{66}	J_{57}	$\mathbf{S}_{6}\cdot\mathbf{S}_{7}$	$\mathbf{S}_{6}\cdot\mathbf{S}_{7}$	$\mathbf{S}_{5}\cdot\mathbf{S}_{8}$	$\mathbf{S}_{7}\cdot\mathbf{S}_{6}$	$\mathbf{S}_{8}\cdot\mathbf{S}_{5}$	$\mathbf{S}_{15}\cdot\mathbf{S}_{14}$	$\mathbf{S}_{13}\cdot\mathbf{S}_{16}$	$\mathbf{S}_{14}\cdot\mathbf{S}_{15}$	$\mathbf{S}_{16}\cdot\mathbf{S}_{13}$
J_{67}	J_{56}	$\mathbf{S}_{6}\cdot\mathbf{S}_{8}$	$\mathbf{S}_{6}\cdot\mathbf{S}_{8}$	$\mathbf{S}_{5}\cdot\mathbf{S}_{7}$	$\mathbf{S}_{7}\cdot\mathbf{S}_{5}$	$\mathbf{S}_{8}\cdot\mathbf{S}_{6}$	$\mathbf{S}_{15}\cdot\mathbf{S}_{13}$	$\mathbf{S}_{13}\cdot\mathbf{S}_{15}$	$\mathbf{S}_{14}\cdot\mathbf{S}_{16}$	$\mathbf{S}_{16}\cdot\mathbf{S}_{14}$

J_{68}	J_{13}	$S_6 \cdot S_9$	$S_6 \cdot S_9$	$S_5 \cdot S_{10}$	$S_7 \cdot S_{12}$	$S_8 \cdot S_{11}$	$S_{15} \cdot S_4$	$S_{13} \cdot S_2$	$S_{14} \cdot S_1$	$S_{16} \cdot S_3$
J_{69}	J_{12}	$S_6 \cdot S_{10}$	$S_6 \cdot S_{10}$	$S_5 \cdot S_9$	$S_7 \cdot S_{11}$	$S_8 \cdot S_{12}$	$S_{15} \cdot S_3$	$S_{13} \cdot S_1$	$S_{14} \cdot S_2$	$S_{16} \cdot S_4$
J_{70}	J_{15}	$S_6 \cdot S_{11}$	$S_6 \cdot S_{11}$	$S_5 \cdot S_{12}$	$S_7 \cdot S_{10}$	$S_8 \cdot S_9$	$S_{15} \cdot S_2$	$S_{13} \cdot S_4$	$S_{14} \cdot S_3$	$S_{16} \cdot S_1$
J_{71}	J_{14}	$S_6 \cdot S_{12}$	$S_6 \cdot S_{12}$	$S_5 \cdot S_{11}$	$S_7 \cdot S_9$	$S_8 \cdot S_{10}$	$S_{15} \cdot S_1$	$S_{13} \cdot S_3$	$S_{14} \cdot S_4$	$S_{16} \cdot S_2$
J_{72}	J_{63}	$S_6 \cdot S_{13}$	$S_6 \cdot S_{13}$	$S_5 \cdot S_{14}$	$S_7 \cdot S_{16}$	$S_8 \cdot S_{15}$	$S_{15} \cdot S_8$	$S_{13} \cdot S_6$	$S_{14} \cdot S_5$	$S_{16} \cdot S_7$
J_{73}	J_{62}	$S_6 \cdot S_{14}$	$S_6 \cdot S_{14}$	$S_5 \cdot S_{13}$	$S_7 \cdot S_{15}$	$S_8 \cdot S_{16}$	$S_{15} \cdot S_7$	$S_{13} \cdot S_5$	$S_{14} \cdot S_6$	$S_{16} \cdot S_8$
J_{74}	J_{65}	$S_6 \cdot S_{15}$	$S_6 \cdot S_{15}$	$S_5 \cdot S_{16}$	$S_7 \cdot S_{14}$	$S_8 \cdot S_{13}$	$S_{15} \cdot S_6$	$S_{13} \cdot S_8$	$S_{14} \cdot S_7$	$S_{16} \cdot S_5$
J_{75}	J_{64}	$S_6 \cdot S_{16}$	$S_6 \cdot S_{16}$	$S_5 \cdot S_{15}$	$S_7 \cdot S_{13}$	$S_8 \cdot S_{14}$	$S_{15} \cdot S_5$	$S_{13} \cdot S_7$	$S_{14} \cdot S_8$	$S_{16} \cdot S_6$
J_{76}	J_{55}	$S_7 \cdot S_8$	$S_7 \cdot S_8$	$S_8 \cdot S_7$	$S_6 \cdot S_5$	$S_5 \cdot S_6$	$S_{14} \cdot S_{13}$	$S_{16} \cdot S_{15}$	$S_{15} \cdot S_{16}$	$S_{13} \cdot S_{14}$
J_{77}	J_{14}	$S_7 \cdot S_9$	$S_7 \cdot S_9$	$S_8 \cdot S_{10}$	$S_6 \cdot S_{12}$	$S_5 \cdot S_{11}$	$S_{14} \cdot S_4$	$S_{16} \cdot S_2$	$S_{15} \cdot S_1$	$S_{13} \cdot S_3$
J_{78}	J_{15}	$S_7 \cdot S_{10}$	$S_7 \cdot S_{10}$	$S_8 \cdot S_9$	$S_6 \cdot S_{11}$	$S_5 \cdot S_{12}$	$S_{14} \cdot S_3$	$S_{16} \cdot S_1$	$S_{15} \cdot S_2$	$S_{13} \cdot S_4$
J_{79}	J_{12}	$S_7 \cdot S_{11}$	$S_7 \cdot S_{11}$	$S_8 \cdot S_{12}$	$S_6 \cdot S_{10}$	$S_5 \cdot S_9$	$S_{14} \cdot S_2$	$S_{16} \cdot S_4$	$S_{15} \cdot S_3$	$S_{13} \cdot S_1$
J_{80}	J_{13}	$S_7 \cdot S_{12}$	$S_7 \cdot S_{12}$	$S_8 \cdot S_{11}$	$S_6 \cdot S_9$	$S_5 \cdot S_{10}$	$S_{14} \cdot S_1$	$S_{16} \cdot S_3$	$S_{15} \cdot S_4$	$S_{13} \cdot S_2$
J_{81}	J_{64}	$S_7 \cdot S_{13}$	$S_7 \cdot S_{13}$	$S_8 \cdot S_{14}$	$S_6 \cdot S_{16}$	$S_5 \cdot S_{15}$	$S_{14} \cdot S_8$	$S_{16} \cdot S_6$	$S_{15} \cdot S_5$	$S_{13} \cdot S_7$
J_{82}	J_{65}	$S_7 \cdot S_{14}$	$S_7 \cdot S_{14}$	$S_8 \cdot S_{13}$	$S_6 \cdot S_{15}$	$S_5 \cdot S_{16}$	$S_{14} \cdot S_7$	$S_{16} \cdot S_5$	$S_{15} \cdot S_6$	$S_{13} \cdot S_8$
J_{83}	J_{62}	$S_7 \cdot S_{15}$	$S_7 \cdot S_{15}$	$S_8 \cdot S_{16}$	$S_6 \cdot S_{14}$	$S_5 \cdot S_{13}$	$S_{14} \cdot S_6$	$S_{16} \cdot S_8$	$S_{15} \cdot S_7$	$S_{13} \cdot S_5$
J_{84}	J_{63}	$S_7 \cdot S_{16}$	$S_7 \cdot S_{16}$	$S_8 \cdot S_{15}$	$S_6 \cdot S_{13}$	$S_5 \cdot S_{14}$	$S_{14} \cdot S_5$	$S_{16} \cdot S_7$	$S_{15} \cdot S_8$	$S_{13} \cdot S_6$
J_{85}	J_{15}	$S_8 \cdot S_9$	$S_8 \cdot S_9$	$S_7 \cdot S_{10}$	$S_5 \cdot S_{12}$	$S_6 \cdot S_{11}$	$S_{13} \cdot S_4$	$S_{15} \cdot S_2$	$S_{16} \cdot S_1$	$S_{14} \cdot S_3$
J_{86}	J_{14}	$S_8 \cdot S_{10}$	$S_8 \cdot S_{10}$	$S_7 \cdot S_9$	$S_5 \cdot S_{11}$	$S_6 \cdot S_{12}$	$S_{13} \cdot S_3$	$S_{15} \cdot S_1$	$S_{16} \cdot S_2$	$S_{14} \cdot S_4$
J_{87}	J_{13}	$S_8 \cdot S_{11}$	$S_8 \cdot S_{11}$	$S_7 \cdot S_{12}$	$S_5 \cdot S_{10}$	$S_6 \cdot S_9$	$S_{13} \cdot S_2$	$S_{15} \cdot S_4$	$S_{16} \cdot S_3$	$S_{14} \cdot S_1$
J_{88}	J_{12}	$S_8 \cdot S_{12}$	$S_8 \cdot S_{12}$	$S_7 \cdot S_{11}$	$S_5 \cdot S_9$	$S_6 \cdot S_{10}$	$S_{13} \cdot S_1$	$S_{15} \cdot S_3$	$S_{16} \cdot S_4$	$S_{14} \cdot S_2$
J_{89}	J_{65}	$S_8 \cdot S_{13}$	$S_8 \cdot S_{13}$	$S_7 \cdot S_{14}$	$S_5 \cdot S_{16}$	$S_6 \cdot S_{15}$	$S_{13} \cdot S_8$	$S_{15} \cdot S_6$	$S_{16} \cdot S_5$	$S_{14} \cdot S_7$
J_{90}	J_{64}	$S_8 \cdot S_{14}$	$S_8 \cdot S_{14}$	$S_7 \cdot S_{13}$	$S_5 \cdot S_{15}$	$S_6 \cdot S_{16}$	$S_{13} \cdot S_7$	$S_{15} \cdot S_5$	$S_{16} \cdot S_6$	$S_{14} \cdot S_8$
J_{91}	J_{63}	$S_8 \cdot S_{15}$	$S_8 \cdot S_{15}$	$S_7 \cdot S_{16}$	$S_5 \cdot S_{14}$	$S_6 \cdot S_{13}$	$S_{13} \cdot S_6$	$S_{15} \cdot S_8$	$S_{16} \cdot S_7$	$S_{14} \cdot S_5$
J_{92}	J_{62}	$S_8 \cdot S_{16}$	$S_8 \cdot S_{16}$	$S_7 \cdot S_{15}$	$S_5 \cdot S_{13}$	$S_6 \cdot S_{14}$	$S_{13} \cdot S_5$	$S_{15} \cdot S_7$	$S_{16} \cdot S_8$	$S_{14} \cdot S_6$
J_{93}	J_1	$S_9 \cdot S_{10}$	$S_9 \cdot S_{10}$	$S_{10} \cdot S_9$	$S_{12} \cdot S_{11}$	$S_{11} \cdot S_{12}$	$S_4 \cdot S_3$	$S_2 \cdot S_1$	$S_1 \cdot S_2$	$S_3 \cdot S_4$
J_{94}	J_2	$S_9 \cdot S_{11}$	$S_9 \cdot S_{11}$	$S_{10} \cdot S_{12}$	$S_{12} \cdot S_{10}$	$S_{11} \cdot S_9$	$S_4 \cdot S_2$	$S_2 \cdot S_4$	$S_1 \cdot S_3$	$S_3 \cdot S_1$
J_{95}	J_3	$S_9 \cdot S_{12}$	$S_9 \cdot S_{12}$	$S_{10} \cdot S_{11}$	$S_{12} \cdot S_9$	$S_{11} \cdot S_{10}$	$S_4 \cdot S_1$	$S_2 \cdot S_3$	$S_1 \cdot S_4$	$S_3 \cdot S_2$
J_{96}	J_4	$S_9 \cdot S_{13}$	$S_9 \cdot S_{13}$	$S_{10} \cdot S_{14}$	$S_{12} \cdot S_{16}$	$S_{11} \cdot S_{15}$	$S_4 \cdot S_8$	$S_2 \cdot S_6$	$S_1 \cdot S_5$	$S_3 \cdot S_7$
J_{97}	J_5	$S_9 \cdot S_{14}$	$S_9 \cdot S_{14}$	$S_{10} \cdot S_{13}$	$S_{12} \cdot S_{15}$	$S_{11} \cdot S_{16}$	$S_4 \cdot S_7$	$S_2 \cdot S_5$	$S_1 \cdot S_6$	$S_3 \cdot S_8$
J_{98}	J_6	$S_9 \cdot S_{15}$	$S_9 \cdot S_{15}$	$S_{10} \cdot S_{16}$	$S_{12} \cdot S_{14}$	$S_{11} \cdot S_{13}$	$S_4 \cdot S_6$	$S_2 \cdot S_8$	$S_1 \cdot S_7$	$S_3 \cdot S_5$
J_{99}	J_7	$S_9 \cdot S_{16}$	$S_9 \cdot S_{16}$	$S_{10} \cdot S_{15}$	$S_{12} \cdot S_{13}$	$S_{11} \cdot S_{14}$	$S_4 \cdot S_5$	$S_2 \cdot S_7$	$S_1 \cdot S_8$	$S_3 \cdot S_6$
J_{100}	J_3	$S_{10} \cdot S_{11}$	$S_{10} \cdot S_{11}$	$S_9 \cdot S_{12}$	$S_{11} \cdot S_{10}$	$S_{12} \cdot S_9$	$S_3 \cdot S_2$	$S_1 \cdot S_4$	$S_2 \cdot S_3$	$S_4 \cdot S_1$
J_{101}	J_2	$S_{10} \cdot S_{12}$	$S_{10} \cdot S_{12}$	$S_9 \cdot S_{11}$	$S_{11} \cdot S_9$	$S_{12} \cdot S_{10}$	$S_3 \cdot S_1$	$S_1 \cdot S_3$	$S_2 \cdot S_4$	$S_4 \cdot S_2$
J_{102}	J_5	$S_{10} \cdot S_{13}$	$S_{10} \cdot S_{13}$	$S_9 \cdot S_{14}$	$S_{11} \cdot S_{16}$	$S_{12} \cdot S_{15}$	$S_3 \cdot S_8$	$S_1 \cdot S_6$	$S_2 \cdot S_5$	$S_4 \cdot S_7$

J_{103}	J_4	$S_{10}\cdot S_{14}$	$S_{10}\cdot S_{14}$	$S_9\cdot S_{13}$	$S_{11}\cdot S_{15}$	$S_{12}\cdot S_{16}$	$S_3\cdot S_7$	$S_1\cdot S_5$	$S_2\cdot S_6$	$S_4\cdot S_8$
J_{104}	J_7	$S_{10}\cdot S_{15}$	$S_{10}\cdot S_{15}$	$S_9\cdot S_{16}$	$S_{11}\cdot S_{14}$	$S_{12}\cdot S_{13}$	$S_3\cdot S_6$	$S_1\cdot S_8$	$S_2\cdot S_7$	$S_4\cdot S_5$
J_{105}	J_6	$S_{10}\cdot S_{16}$	$S_{10}\cdot S_{16}$	$S_9\cdot S_{15}$	$S_{11}\cdot S_{13}$	$S_{12}\cdot S_{14}$	$S_3\cdot S_5$	$S_1\cdot S_7$	$S_2\cdot S_8$	$S_4\cdot S_6$
J_{106}	J_1	$S_{11}\cdot S_{12}$	$S_{11}\cdot S_{12}$	$S_{12}\cdot S_{11}$	$S_{10}\cdot S_9$	$S_9\cdot S_{10}$	$S_2\cdot S_1$	$S_4\cdot S_3$	$S_3\cdot S_4$	$S_1\cdot S_2$
J_{107}	J_6	$S_{11}\cdot S_{13}$	$S_{11}\cdot S_{13}$	$S_{12}\cdot S_{14}$	$S_{10}\cdot S_{16}$	$S_9\cdot S_{15}$	$S_2\cdot S_8$	$S_4\cdot S_6$	$S_3\cdot S_5$	$S_1\cdot S_7$
J_{108}	J_7	$S_{11}\cdot S_{14}$	$S_{11}\cdot S_{14}$	$S_{12}\cdot S_{13}$	$S_{10}\cdot S_{15}$	$S_9\cdot S_{16}$	$S_2\cdot S_7$	$S_4\cdot S_5$	$S_3\cdot S_6$	$S_1\cdot S_8$
J_{109}	J_4	$S_{11}\cdot S_{15}$	$S_{11}\cdot S_{15}$	$S_{12}\cdot S_{16}$	$S_{10}\cdot S_{14}$	$S_9\cdot S_{13}$	$S_2\cdot S_6$	$S_4\cdot S_8$	$S_3\cdot S_7$	$S_1\cdot S_5$
J_{110}	J_5	$S_{11}\cdot S_{16}$	$S_{11}\cdot S_{16}$	$S_{12}\cdot S_{15}$	$S_{10}\cdot S_{13}$	$S_9\cdot S_{14}$	$S_2\cdot S_5$	$S_4\cdot S_7$	$S_3\cdot S_8$	$S_1\cdot S_6$
J_{111}	J_7	$S_{12}\cdot S_{13}$	$S_{12}\cdot S_{13}$	$S_{11}\cdot S_{14}$	$S_9\cdot S_{16}$	$S_{10}\cdot S_{15}$	$S_1\cdot S_8$	$S_3\cdot S_6$	$S_4\cdot S_5$	$S_2\cdot S_7$
J_{112}	J_6	$S_{12}\cdot S_{14}$	$S_{12}\cdot S_{14}$	$S_{11}\cdot S_{13}$	$S_9\cdot S_{56}$	$S_{10}\cdot S_{16}$	$S_1\cdot S_7$	$S_3\cdot S_5$	$S_4\cdot S_6$	$S_2\cdot S_8$
J_{113}	J_5	$S_{12}\cdot S_{15}$	$S_{12}\cdot S_{15}$	$S_{11}\cdot S_{16}$	$S_9\cdot S_{14}$	$S_{10}\cdot S_{13}$	$S_1\cdot S_6$	$S_3\cdot S_8$	$S_4\cdot S_7$	$S_2\cdot S_5$
J_{114}	J_4	$S_{12}\cdot S_{16}$	$S_{12}\cdot S_{16}$	$S_{11}\cdot S_{15}$	$S_9\cdot S_{13}$	$S_{10}\cdot S_{14}$	$S_1\cdot S_5$	$S_3\cdot S_7$	$S_4\cdot S_8$	$S_2\cdot S_6$
J_{115}	J_{55}	$S_{13}\cdot S_{14}$	$S_{13}\cdot S_{14}$	$S_{14}\cdot S_{13}$	$S_{16}\cdot S_{15}$	$S_{15}\cdot S_{16}$	$S_8\cdot S_7$	$S_6\cdot S_5$	$S_5\cdot S_6$	$S_7\cdot S_7$
J_{116}	J_{56}	$S_{13}\cdot S_{15}$	$S_{13}\cdot S_{15}$	$S_{14}\cdot S_{16}$	$S_{16}\cdot S_{14}$	$S_{15}\cdot S_{13}$	$S_8\cdot S_6$	$S_6\cdot S_8$	$S_5\cdot S_7$	$S_7\cdot S_5$
J_{117}	J_{57}	$S_{13}\cdot S_{16}$	$S_{13}\cdot S_{16}$	$S_{14}\cdot S_{15}$	$S_{16}\cdot S_{13}$	$S_{15}\cdot S_{14}$	$S_8\cdot S_5$	$S_6\cdot S_7$	$S_5\cdot S_8$	$S_7\cdot S_6$
J_{118}	J_{57}	$S_{14}\cdot S_{15}$	$S_{14}\cdot S_{15}$	$S_{13}\cdot S_{16}$	$S_{15}\cdot S_{14}$	$S_{16}\cdot S_{13}$	$S_7\cdot S_6$	$S_5\cdot S_8$	$S_6\cdot S_7$	$S_8\cdot S_5$
J_{119}	J_{56}	$S_{14}\cdot S_{16}$	$S_{14}\cdot S_{16}$	$S_{13}\cdot S_{15}$	$S_{15}\cdot S_{13}$	$S_{16}\cdot S_{14}$	$S_7\cdot S_5$	$S_5\cdot S_7$	$S_6\cdot S_8$	$S_8\cdot S_6$
J_{120}	J_{55}	$S_{15}\cdot S_{16}$	$S_{15}\cdot S_{16}$	$S_{16}\cdot S_{15}$	$S_{14}\cdot S_{13}$	$S_{13}\cdot S_{14}$	$S_6\cdot S_5$	$S_8\cdot S_7$	$S_7\cdot S_8$	$S_5\cdot S_6$

Appendix VI

ABINIT Information

ABINIT version: 7.11.0

VI.1 Input file to calculate the total energy of configuration 3 (- + - + + - + -)

iscf **17** # SCF cycle, Pulay mixing of the density based on the npulayit previous iterations

ixc **11** # Use the Perdew-Burke-Ernzerhof GGA

ecut **15** # Energy cutoff of 15 Ha

pawecutdg **30** # PAW Energy cutoff for the double grid of 30 Ha

istwfk **∗1** # It defines the choice of storage of waveFunction at each k-point in ABINIT. When it is set to 1, the time-reversal symmetry is not used.

prtdensph **1** # It gives us a rough approximation of a local magnetic moment by calculating the difference between the spin up and spin down densities.

Definition of the SCF procedure:

nstep **100** # Maximal number of SCF cycles

diemac **4.0** # Model dielectric macroscopic constant is a practical help to speed-up the SCF procedure

optforces **1** # It calculates the forces at each SCF iteration, and hence we can use forces as criterion to stop the SCF cycles.

Definition of the k-point grid:

kptopt **1** # Option for the automatic generation of k-points, taking into account the symmetry

ngkpt **4 1 2** # This is a 4x1x2 grid based on the primitive vectors

nshiftk **1** # Number of shifts for k-point grids to be utilized to create the full grid of k points

***shiftk* 0.5 0.5 0.5** # Shift for k-points. When we are not dealing with a FCC nor a BCC lattice, a preferred k-point sampling is usually done by forming Monkhorst-Pack grids by using nshiftk=1 and shiftk 0.5 0.5 0.5.

***toldfe* 1.0*d* − 8** # Tolerance on the difference of total energy. When this value is reached twice, the SCF cycle will stop.

Definition of the unit cell:

acell* 6.1471 30.0605 12.9583 *angstrom # Cell lattice vector scaling. It provides us with the length scales by which dimensionless primitive translations (in rprim) are to be multiplied.

***angdeg* 90 100.269 90** # It produces the angles between the directions of the primitive vectors of the unit cell in degrees.

Definition of the atom types:

***ntypat* 4** # There are four types of atoms in a NIT2Py molecule: Hydrogen, Carbon, Nitrogen, Oxygen.

***znucl* 1 6 7 8** # The keyword "znucl" refers to the atomic number of the types of atoms. Here, we have Hydrogen (znucl 1), Carbon (znucl 6), Nitrogen (znucl 7), and Oxygen (znucl 8). Note that, the pseudopotentials mentioned in the "files" file must correspond to the types of atoms.

Definition of the atoms:

***natom* 264** # There are 264 atoms in a NIT2Py single cell.

typat # Type of atom is an array providing an integer label to each atom in the unit cell to indicate its type. There are 33 atoms in every NIT2Py molecule, and thus there are 33 type of atoms in each array. 1 referes to H, 2 to C, 3 to N, and 4 to O. It must be consistent with the atomic locations defined in xred , xcart or xangst. It has to be in agreement with the way the input of pseudopotentials are ordered. Moreover, it must correspond to the nuclear charge of the elements, given by the array znucl.

2 1 2 1 2 1 2 1 2 2 2 2 1 1 1 2 1 1 1 2 2 1 1 1 2 1 1 1 3 3 3 4 4
2 1 2 1 2 1 2 1 2 2 2 2 1 1 1 2 1 1 1 2 2 1 1 1 2 1 1 1 3 3 3 4 4
2 1 2 1 2 1 2 1 2 2 2 2 1 1 1 2 1 1 1 2 2 1 1 1 2 1 1 1 3 3 3 4 4
2 1 2 1 2 1 2 1 2 2 2 2 1 1 1 2 1 1 1 2 2 1 1 1 2 1 1 1 3 3 3 4 4
2 1 2 1 2 1 2 1 2 2 2 2 1 1 1 2 1 1 1 2 2 1 1 1 2 1 1 1 3 3 3 4 4
2 1 2 1 2 1 2 1 2 2 2 2 1 1 1 2 1 1 1 2 2 1 1 1 2 1 1 1 3 3 3 4 4
2 1 2 1 2 1 2 1 2 2 2 2 1 1 1 2 1 1 1 2 2 1 1 1 2 1 1 1 3 3 3 4 4
2 1 2 1 2 1 2 1 2 2 2 2 1 1 1 2 1 1 1 2 2 1 1 1 2 1 1 1 3 3 3 4 4

xcart # It gives the cartesian coordinates of atoms within unit cell. Here, we give the coordinates of 264 atoms related to eight molecules in the NIT2Py unit cell.

spinat # It gives the beginning electronic spin-magnetization for each atom in units of $\hbar/2$. We define the z-component of each atom (0 0 z-component). Here, we show only three examples, and do not bring the total of 264 lines of all the atoms. But, in the real code, one needs to define the array of (0 0 z-component) for all the atoms.

0 0 1 # Spin up, for the N and O atoms of the ONCNO branch of each molecule.
0 0 -1 # Spin down, for the N and O atoms of the ONCNO branch of each molecule.
0 0 0 # Spin zero for the remaining atoms.

Definition of the magnetic system:

***nsppol*2** # If the number of spin polarization is set to 2, we have a spin-polarized (collinear) calculation with separate and different wavefunctions for spin-up and spin-down electrons for each band and k-point.

***nspden*2** # If the number of spin-density components is set as 2, we have a scalar magnetization with the axis fixed along the z direction. In this case, the density matrix is diagonal, and we have different spin-up and spin-down values.

Definition of the Parallelisation:

***paral_kgb*1** # Parallelisation over k-points, G-vectors and bands.

***npfft*6** # It provides the number of processors between which the job over the FFT level is shared.

***npkpt*8** # It gives the number of processors at the k-point level.

VI.2 Defining two magnetic systems

(1) A spin-polarized (collinear magnetization) system

Different wavefunctions for the spin up and spin down corresponding to each k-point.

nsppol=2 → A collinear magnetization.

nspden=2 → A scalar magnetization is fixed along the z axis which leads to a diagonalized density matrix comprised of distinct magnitudes for the spin up and spin down.

nspinor=1 → A scalar wavefunction.

(2) An AFM system

nsppol=1, *nspden*=2, *nspinor*=1

Table VI.I – Some input variables of ABINIT used in this research [115]

Input parameter	Description
ixc=11	GGA, x-only part of PBE GGA functional
xangs	Cartesian atomic coordinates in Angstrom
xred	Reduced atomic coordinates
xcart	Cartesian atomic coordinates in Bohr atomic units
rprim	Real space primitive vectors
acell	Cell lattice vector scaling
angdeg	Angles between lattice constants
znucl	Charge of the nuclei
typat	Array of atom types
typat	Array of atom types
ngkpt	Number of k-points in each of the three dimensions of k-point grid
kpt	k-point array
kptopt	k-point option
nshiftk	Number of shifts of k-point grid
shiftk	Shifting value of the k-points in each dimension of k-point grid
nspden	Number of spin-density components.
nspinor	Number of spinorial components of the wavefunctions
nsppol	Number of spin polarization
spinat	Preliminary electronic spin-magnetization in an $\hbar/2$ unit
ionmov=2	Structural optimization using BFGS minimization
ntime	Structural optimization number
toldff	Tolerance on the diference of forces
optforces=1	To calculate the force in each iteration
tolmxf	Maximal tolerance of the force below which the BFGS iterations ends
ecut	Energy cutoff
pawecutdg	Energy cutoff for the double grid
ndtset	Number of datasets
ecut+	Increasing value of cutoff in each datastep
occopt=2	Occupation option, k-points can have a different number of bands and different occupancies
occ	Band occupancy
prtdensph	To evaluate the integral of the density inside of a sphere around an atom for the spin up and down components
optcell=0	To neglect the optimization of the cell shape and dimensions
diemac	Model dielectric macroscopic constant
diemix	Model dielectric mixing factor
diemixmag	Model dielectric mixing factor for the magnetization
magconon=1	A Lagrangian constraint on the direction of the magnetization
magcon-lambda	Amplitude of the Lagrangian constraint on the direction of the magnetization
ratsph	Radii of the atomic sphere(s)
nsym	Number of symmetry operators